The University of Nottingham

UNITED KINGDOM · CHINA · MALAYSIA

Integrated Passive Filter Inductors for Motor Drive Applications

M. Raza Khowja, MSc

Thesis submitted to the University of Nottingham for the degree of Doctor of Philosophy, July 2017.

To

My respected Parents,

And

My beloved Wife, Gulrukh

Abstract

Passive elements such as filter inductors and capacitors occupy a significant amount of space in motor drives and have added penalties of increased system losses and weight. Traditionally, the filters are designed and introduced separately after the drive system components have been defined. This leads to discrete sub-systems which require a functional and structural integration to make efficient and power dense overall system. Such power dense system is the prerequisite in aerospace and marine applications. Therefore, the main focus of this thesis is to look at an integrated approach to design and optimize the filter inductor, both from functional and physical point of integration.

Two novel integrative approaches for passive filter inductor are presented in this thesis along with a detailed literature review of passive filters that are being used at present. The first approach is a functional integration of passive filter inductor which uses the inherent motor magnetics to act as a filter inductance instead of introducing a separate filter inductor between the inverter and motor terminals. The mathematical and FE models of the integrated motor have been made using $MATLAB^{®}-Simulink$ and $MagNet-Infolytica$ finite element tool to predict and compare its overall performance with the conventional motor drive system. For the purpose of comparing these two systems, a separate EE core filter inductor is designed and sized using "Area Product" approach. Subsequently, the optimization of the integrated motor is presented in terms of torque ripple, total losses, weight and volume which is then compared with the conventional motor drive. For the purpose of experimental verification, the existing $HEMAS$ motor is modified and tested on a DDS motor drive system.

In addition, the concept of motor-shaped inductors are presented which provided an effective structural integration as the inductor can be embedded within the housing of existing motor or generator. The motor-shaped inductors include: motor-shaped rotational inductor and motor-shaped rotor-less inductor. The design procedure of both motor-shaped inductors is explained which is followed by the design optimization process. The design optimization of motor-shaped inductors have been carried out whilst considering various slot-pole combinations and winding configurations which is then compared with the conventional EE core inductor in terms of total losses, weight and AC copper resistance. To validate it experimentally, 12 slots 2 poles rotational

inductor is manufactured at The University of Nottingham, UK which is tested on a 49 kW, 20,000 rpm induction motor drive system. The results have been presented at different rotor speeds and supply frequencies. Subsequently, the performance of both rotational inductor and conventional EE core inductor have been compared in terms of synchronous inductance, power losses, DC and AC resistance, power quality, weight and volume.

Acknowledgements

I would especially like to thank my supervisors Professor Chris Gerada and Dr. Gaurang Vakil for the confidence, guidance and invaluable help they have provided me during the course of my doctorate studies. They have been an imaginative support to me during my research studies. The understanding they have always given has been truly remarkable. I feel privileged and honoured to have them as my supervisors. I am forever grateful, thank both of you.

I would also like to thank Dr. Chintan Patel for his crucial help, exclusively during the experimentation stages of this PhD project as the experimental stage of this project was one of the toughest part which I could not have done it without his guidance and support.

My sincere appreciations also go to Dr. Martin Jones and Dr. Alberto Castellazzi for acting as my external and internal examiner for my PhD viva voice. In particular, my special thanks to my internal examiner for giving me helpful remarks and making constructive criticism during my first and second year PhD reviews.

Also, presenting gratitude to my colleagues within the Power Electronics, Machines and Control (PEMC) Research Group I thank you for your support and encouragement during many aspects of this research. In particular, I would like to thank Syed Quadir, Shafiq Odhano, Asad Fayaz, Usman Nasir, Zain Hassan, Adam Walker, Anubrata Dey and Shajjad Chowdhury.

I would also like to thank The University of Nottingham for the opportunity to undertake my PhD course within their world class PEMC Research Group. Indeed, immense thanks must go to the University's International Office and Clean Sky-I JTI Project for funding this research, without which none of this would be imaginable.

As an expression of my most sincere appreciation, I would like to thank my uncle and Aunt Dr. Ashiq Turabee and Mehjabeen Turabee, without your support this milestone of my life would not be possible. My cousins, Azra Turabee, Zohra Turabee, Aiza Turabee and Asad Turabee, you all have been a wonderful part of my life. Thank you for always being there as helping hands in all matter during my UK visit.

My siblings, Sana and Sadaf, thank you for your priceless help and support when it was needed. Living away from home has always been hard and tough but your love made it feel easy.

Lastly, and most importantly, my deepest love and thanks to my dearest parents Mr. Akbar Ali Khowja and Najma Akbar for their unconditional love, support, motivation and sacrifices. Without these two outstanding figures, this thesis would never have been written. In the end, I would like to thank all other family members and friends for their love and support throughout my life.

Abbreviations

2D	Two dimensional
AC	Alternating Current
CM	Common Mode
CNW	Concentrated Windings
DL	Double Layer
DW	Distributed Winding
DC	Direct Current
DM	Differential Mode
DSP	Digital Signal Processing
DDS	Drivetrain Diagnostic Simulator
ESI	Electronic Smoothing Inductor
EMI	Electromagnetic Interference
EMC	Electromagnetic Compatibility
FFT	Fast Fourier Transform
FPGA	Field Programmable Gate Array
FE	Finite Element
FEA	Finite Element Analysis
HEMAS	Helicopter Electromechanical Actuation System
IGBT	Insulated Gate Bipolar Junction Transistor
KHz	Kilo-hertz
KV	Kill-volts
L	Inductive Filter
LC	Inductive-Capacitive-Inductive Filter
LCL	Inductive-Capacitive Filter
PWM	Pulse Width Modulation
PMSM	Permanent Magnet Synchronous Motor
RLC	Resistive-Inductive-Capacitive Filter
RMS	Root Mean Square
RPM	Revolutions per minute
RT	Rotational Inductor
RL	Rotor-less Inductor

SL	Single Layer
THD	Total Harmonic Distortion
VSI	Voltage Source Inverter

Symbols & Acronyms

$A_{p,1ph}$	Single phase area product
$A_{p,3ph}$	Three phase area product
A_c	Iron core area of EE core inductor
A_g	Airgap length of EE core inductor
B_{max}	Peak flux density
B_w	Back iron width
C_f	Filter capacitance
C_b	Base capacitance
C_{dc}	DC side capacitance
D_{sh}	Shaft diameter
E_m	No-load motor voltage
E_1	Filter branch no-load voltage
E_{abc}	Three phase no-load voltage
E_2	Motor branch no-load voltage
f_s	Fundamental frequency in Hz
f_{sw}	Switching frequency in Hz
f_{res}	Resonance frequency in Hz
f_{ripple}	Ripple frequency in Hz
f_{max}	Maximum frequency that control loop is able to reject
F	Window width
G	Window height
I_{rms}	RMS current through inductor
i_{abc}	Three phase motor current
i_M	motor current with external inductor
i_F	filter inductor current with external inductor
i_1	Filter branch current
i_2	Motor branch current
i_c	RC branch current
J_{rms}	RMS current density
J	Motor-load inertia
K_w	Waveform Factor

K_F	Fill Factor
L_s	Synchronous Inductance
L_{limb}	Limb Length (or width)
L_{stack}	Stack Length
L_1	Converter side inductance
L_2	Grid side inductance
L_{dc}	DC side inductance
L_b	Base inductance
L_F	External filter inductance
L_1	Filter branch inductance
L_2	Motor branch inductance
L_m	Motor side inductance for RLC output filter
L_g	Airgap length of Motor-shaped inductor
N	Turns per slot
P	Number of Poles
$P_{m,loss}$	Total motor loss
P_{in}	Measured input power
P_{copper}	Total copper loss
P_{dc}	DC copper loss
P_{ac}	AC copper loss
pp	Pole pair
R_m	motor phase resistance
R_1	Filter branch resistance
R_2	Motor branch resistance
R_f	Damping Resistance
R_w	Rotor width
S_o	Slot opening
S_{oh}	Slot opening height
T_{a1}	Torque due to filter branch
T_{a2}	Torque due to motor branch
T_{em}	Electromagnetic torque
T_{load}	Mechanical load torque

T_{out}	Measured or estimated output torque
T_w	Tooth width
t_{cr}	Critical rise time of inverter
V_{rms}	RMS voltage across inductor
V_c	Inverter terminal voltage
V_m	Motor terminal voltage
$V_{C,abc}$	Three phase inverter terminal voltage
$V_{m,abc}$	Three phase motor terminal voltage
v_o	ESI output voltage
v_e	ESI voltage
v_r	ESI input voltage
W_a	Window area of EE core inductor
X_{L1}	Inductance reactance of filter branch
X_{L2}	Inductance reactance of motor branch
ω_{res}	Resonance frequency in rad/s
ω_s	Fundamental frequency in rad/s
ω_e	Electrical fundamental frequency in rad/s
ω_r	Measured rotor speed in rad/s
ψ_m	No-load flux linkage of the motor
ψ_1	No-load flux linkage of filter branch
ψ_1	No-load flux linkage of motor branch
θ_e	Rotor position
α	Phase shift angle between filter and motor branch currents

Table of Contents

List of Figures

List of Tables

Chapter 6

CHAPTER

1

INTRODUCTION

This chapter starts off by giving a brief introduction about the background and motivation of the research work that has been carried out in this thesis; emphasizing the requirements of passive filter for AC drives in the recent past. The chapter also includes the brief introduction about different types of the magnetic cores and its physical layouts used for conventional inductors along with the objectives of the presented research work. The chapter is concluded by giving a thesis structure and a list of research publication resulting from this project.

1.1 BACKGROUND AND MOTIVATION

Traditional motor drives structure similar to the one shown in Figure 1.1, have been in use for years. The complete motor drive involves a grid generator, power modulators (converter and inverter), filters (input, output and DC link) and an electric motor. Three filtering stages are required to get a smooth operation of a complete drive system whose purpose is to prevent the harmonics getting injected into the network. Input grid filters mitigate the harmonics which is generated by the grid generator and the power converter. DC link filters, also known as smoothing filters are used to shape the DC link voltage and current; and the output filters are employed to reduce the effect of harmonics induced by the power inverter and the electric motor.

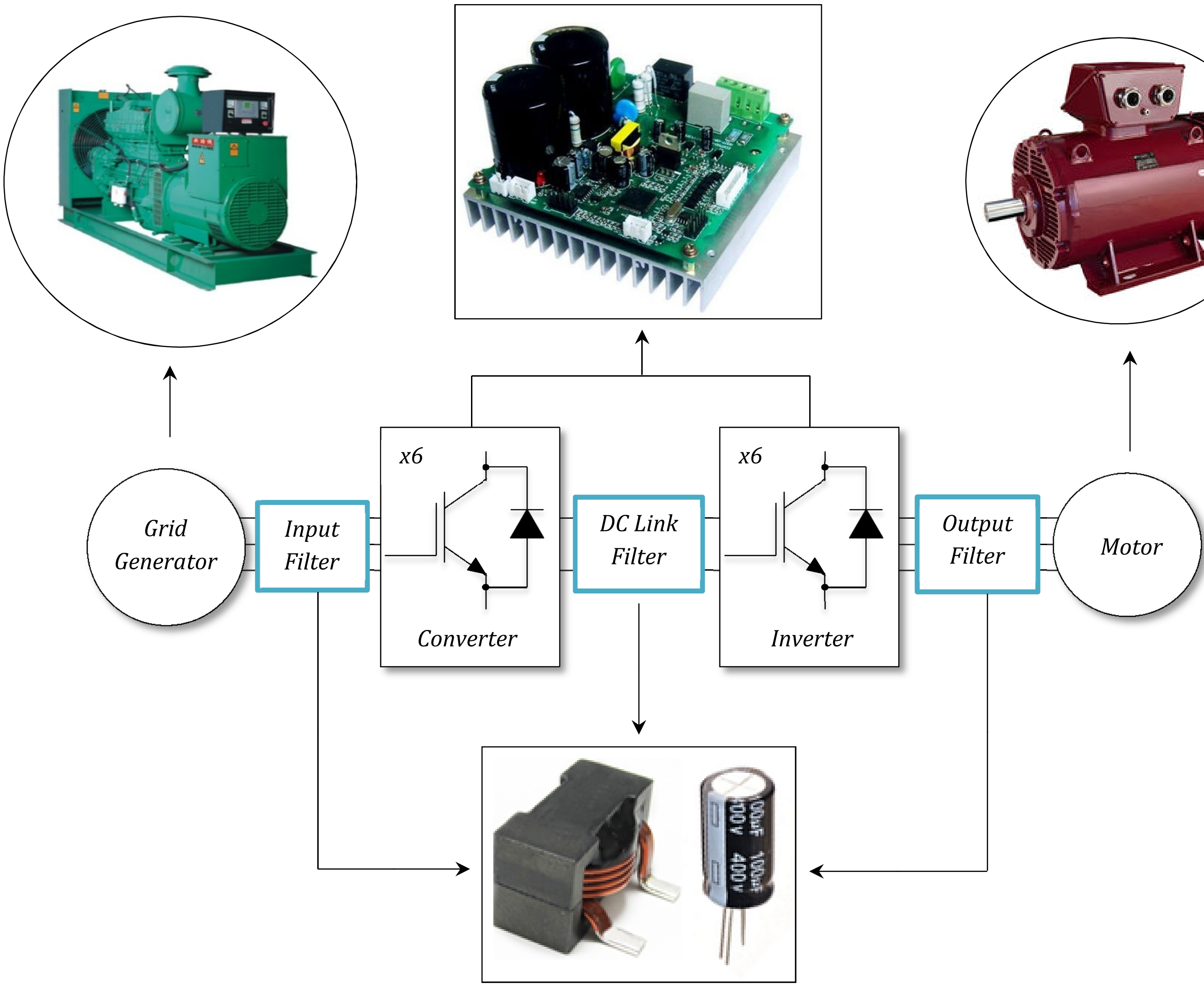

Figure 1.1: Classical motor drives system

The low order harmonics induced by the motor and generator, and the switching harmonics generated by the power modules increases the power losses inside the electrical machine. This leads to the temperature rise, reduced efficiency, increased noise, vibration and reduced life [1].

The output of the inverter generates a voltage gradient (dv/dt) of about 6 $KV/\mu s$ or even more. High voltage gradient (dv/dt) results in a high frequency conducted and radiated emissions, motor insulation stress, leakage currents, bearing stress, acoustic noise, core losses and skin-effect losses in the motor windings. Depending on the specific application, the eradication of some of these consequences is necessary [2, 3].

In some industrial applications, inverter and motor are separated by long distance cables. The pulses with high voltage gradient (dv/dt) on the long lines behave like a travelling wave which results in the voltage reflections. This voltage reflection can cause the voltage to overshoot at the motor terminals. In such a case, motor insulation may lead to an ultimate failure if the preventive measures are not taken into account in the form of filters [4, 5].

The passive elements such as filter inductors and capacitors occupy a significant amount of space in motor drives and have added penalties of potential higher losses and weight. In classical motor drives, filters are designed and introduced externally after the drive system components have been defined. This leads to a discrete sub-system which in turn results in a bulky overall system. In order to overcome this issue, this project looks at an integrative approach to design and optimize the filter inductors, both from the functional and physical point of view [6, 7].

There are many prospects of integrating the passive filter components in motor drives system. The use of integrated approach in motor drives allows functional and structural integration of different drive components into one component that results in a compact design, fewer manufacturing tasks, reduced losses and its associated weight, volume and cost. Therefore, applications where high power density is needed, the use of integrated approach present to be the best solution [6-9].

1.2 PHYSICAL LAYOUTS FOR INDUCTOR CORE:

The wide range of core structure is being used in the industries to manufacture the filter inductors as shown in Figure 1.2 and Figure 1.3. The traditional magnetic and non-magnetic cores for inductor are air core, Tape wound, powder and laminated cores.

1.2.1 Air Core

Air core does not use a magnetic core. The coils are wound on non-magnetic former such as plastic, ceramic or just an air (coreless) as shown in Figure 1.2(a). The drawback of this core is that they are less permeable in nature compared to magnetic core, however, are often used in high frequency applications since they are free from magnetic core losses that depend on the square of the frequency [10, 11].

(a) Single Phase Air Core Inductor

(b) Single Phase Toroidal Core Inductor

(c) Single Phase EE Core Inductor

(d) Single Phase Laminated EI Core

Figure 1.2: Physical Layout for filter inductor

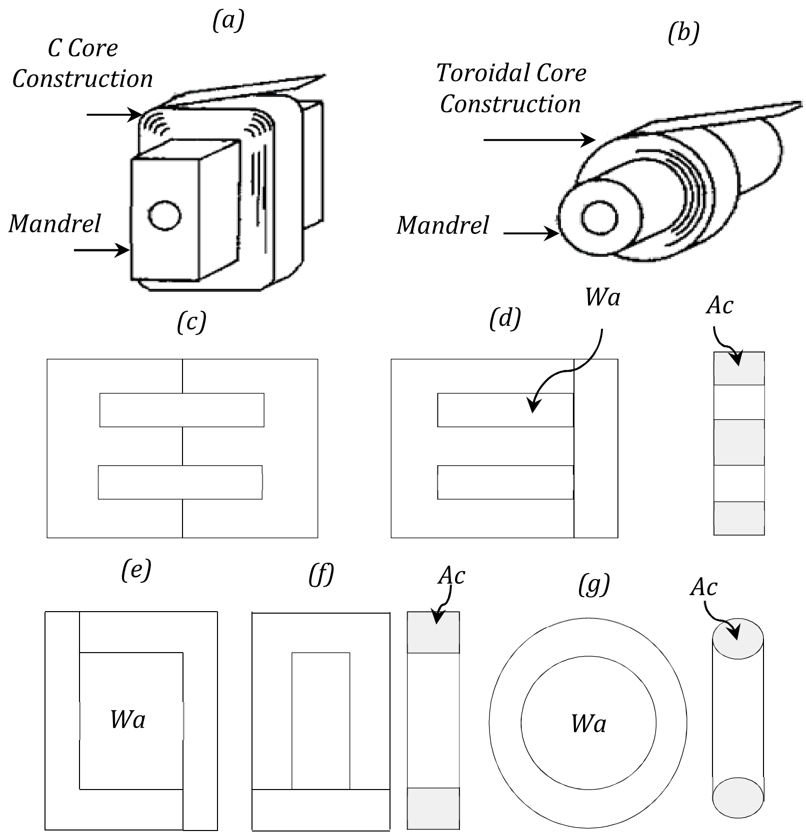

Figure 1.3: Magnetic Cores for filter inductor

1.2.2 Tape Wound Core

Tape wound cores are made by winding around a mandrel, a magnetic material in the form of preslit tape as shown in Figure 1.3(a) and Figure 1.3(b). The benefit of using such type of core is that flux is parallel to the direction of rolling magnetic material that provides the full utilization of material with maximum flux for a given field strength. Tape wound core can be constructed in C, EE or toroid shapes (Figure 1.3(a) and Figure 1.3(b)) [10].

1.2.3 Powder Core

Powder cores are very unique in construction. They have integrated small airgap evenly distributed throughout the core material. This acts in a similar way as a core with airgap which prevents the magnetic core from saturating at higher levels of current. They come in a variety of materials and are very stable with temperature. The powder core can be available in the toroid, EI or EE shape off the shelf [10].

1.2.4 Laminated Core

Laminated cores are one of the most commonly used cores in power electronics and drive applications. They comprise of stamped and pressed steel sheets separated by an insulation coating between the sheets as shown in Figure 1.2(d). The coating reduces the eddy currents between the sheets [10]. The laminated cores can be EE, EI, LL, UI and toroid in construction as shown in Figure 1.3(c) to Figure 1.3(g).

1.3 MAGNETIC CORE DESIGN FOR INDUCTORS

The design of an AC inductor requires the calculation of apparent power capability. According to the area product approach used in [10, 12, 13], the apparent power handling capability of an inductor is related to the area product (A_p), by a relationship which is given as,

$$A_{p,1ph} = W_a A_c = \frac{V_{rms}.I_{rms} \times 10^4}{K_w\, K_F\, B_{max}\, f_s\, J_{rms}} [cm^4] \tag{1.1}$$

where K_w is the waveform coefficient (K_w= $2\pi/\sqrt{2}$ =4.44 for sine wave), K_F is the window fill factor, $V_{rms}.I_{rms}$ is the RMS apparent power handling of an inductor in VA, B_{max} is the peak operating flux density in Tesla, f_s is the supply frequency in Hz, J_{rms} is the RMS current density in A/cm^2, W_a is the window area in cm^2 and A_c is the core cross-sectional area in cm^2.

For 3 phase inductor design, the area product is different from the one indicated in (1.1). Since there are two window areas (W_a) and three iron areas (A_c), the window utilization is different and area product (A_p) changes to,

$$A_{p,3ph} = 3.\left(\frac{W_a}{2}\right).A_c = 1.5\, A_{p,1ph}\ \ [cm^4] \tag{1.2}$$

The expression (1.1) can be rewritten by substituting the expression of induced voltage across the inductor. Therefore, the area product is,

$$W_a A_c = \frac{I_{rms}.\omega_s.L_s.I_{rms} \times 10^4}{K_w\, K_F\, B_{max}\, f_s\, J_{rms}} [cm^4] \tag{1.3}$$

$$W_a A_c = \frac{2\pi\, I_{rms}^2 . L_s \times 10^4}{K_w\, K_F\, B_{max}\, J_{rms}} [cm^4] \tag{1.3}$$

Where, ω_s is the electrical frequency in rad/s, L_s is the synchronous inductance of the inductor and K_w is the waveform coefficient (K_w= $1/\sqrt{2} = 0.707$). It is clear from equation (1.3) that the area product is independent of the supply frequency which means inductor size does not depends on frequency of the supply current. However, the core power loss completely depends on the supply frequency.

"*Suppose that the design specification of the frequency is changed from 100 Hz to 1 MHz. In such a case, we select the same core as that for 100 Hz following the same procedure as discussed above. This leads to core loss 52 times larger, which is not acceptable from an efficiency point of view. Therefore, it is necessary to reset maximum flux density (B_{max}) to a lower value, which requires trial-and-error effor*ts" *[12].*

1.3.1 Typical Requirement for Inductor Design

As can be seen from Eq. (1.1) that the factors such as flux density, supply frequency, current density and the window fill factor (which defines the maximum space occupied by the copper windings in the window) influence the inductor area product. It can be observed from Eq. (1.1) that the physical parameters of the inductor equate to the electrical parameters. The core area A_c indicates the flux conduction capabilities whereas parameter W_a indicates the current conduction capabilities of an inductor [10].

1.3.2 Inductor Sizing Constraints

While designing an inductor, it is important to take the limitations of flux density and current density into account. It is very clear from (1.1) that the area product is inversely related to the operating flux density and current density of an inductor. Flux density in the core is limited by material saturation whereas the current density in the conductor is limited by the thermal limit of the inductor. High flux and current densities will result in a lower area product and hence lower overall weight. However, this comes at the expense of potential higher core and copper losses which results in higher operating temperatures which is clearly a trade-off between weight and loss [10].

1.3.3 Inductor Sizing Calculation

The area product approach can be practically implemented for EE, EI or toroidal core depending on the application of an inductor. The physical layout for EE core inductor and the algorithm of calculating inductor size are shown in Figure 1.4 and Figure 1.5 respectively. As stated earlier, the sizing of an inductor greatly depends upon its apparent power handling capability, which in turn depends on the area product of the window and core. Initially, the specifications of required inductance, peak flux density, fill factor, RMS current and RMS current density have to be selected to compute the area product. To determine the copper and iron core area, window-to-core area ratio (W_a/A_c) of the inductor can be assumed. The window-to-core area ratio indicates a trade-off between core and copper losses. The core length ratio (L_{stack}/L_{limb}) and window aspect ratio (G/F) can then assume in order to set the lengths of the core and window respectively. It has been suggested in [10] to set a low window to core area ratio (W_a/A_c) in order to keep the fringing flux at minimum level. The value of window aspect ratio is typically varies between 3 to 4 based on the core manufacturer [10] and the value of core length ratio is application specific. Subsequently, the turns per phase must be determined based on the specified voltage across the inductor. In the end, airgap can be calculated to get a required inductance of an inductor.

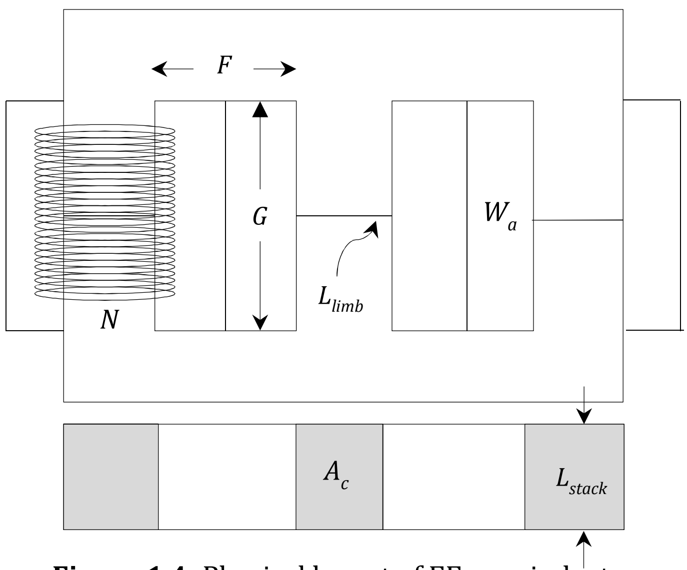

Figure 1.4: Physical layout of EE core inductor

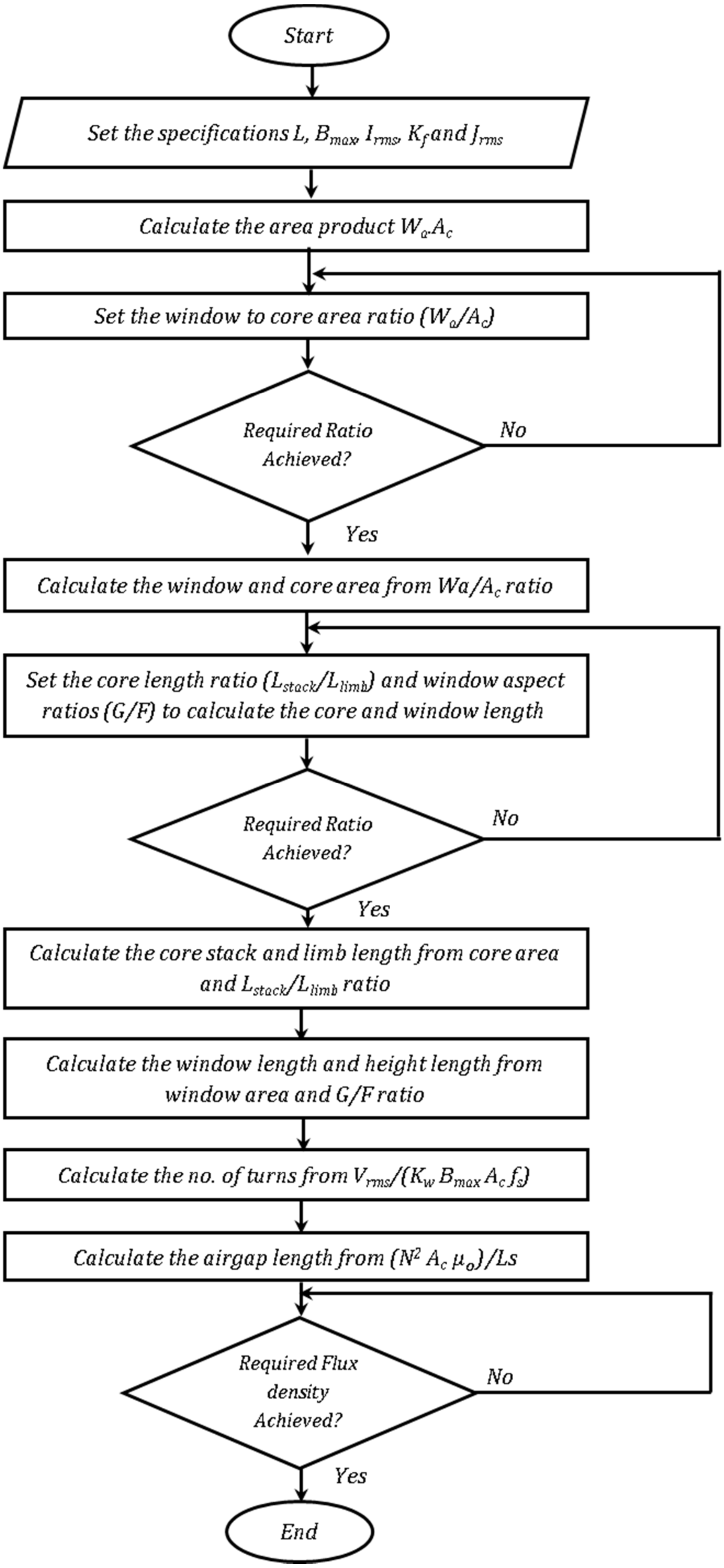

Figure 1.5: EE Core Inductor Design Algorithm

1.4 RESEARCH GOALS AND THESIS STRUCTURE:

The goal of this research is to transform the traditional way of manufacturing and integrating filter inductor into motor drives to get a high power dense integrated drive both structurally and functionally. As stated earlier, the passive filter inductor occupies a significant amount of space in traditional motor drives and have penalties of higher losses and its associated weight. Filter inductor is introduced separately after the drive system components have been fixed which leads to a discrete subsystem. This discrete subsystem ultimately requires to be fully integrated into a single unit to prevent the drive system from becoming bulky and lossy.

To achieve the research goals, this thesis is structured into seven chapters. A brief overview of the contents of each chapter is outlined below,

Chapter 2 gives an insight into passive filter topologies which is used to smooth out the harmonics from the voltage and current waveforms in motor drives system. Input filters, output filters, and DC link filters are reviewed that are being used in conventional motor drives at present. Also, the literature review on the functional and structural integration of passive filters are presented.

Chapter 3 presents a concept of permanent magnet synchronous motor (PMSM) with integrated output filter inductor. A detailed analytical model of the motor with an integrated inductor is presented, taking switching effect and modulation into account. The design procedure for external EE core inductor and the practical implementation of the integrated inductor is discussed. The analytical results of the motor with integrated inductor are analyzed and compared with the motor with external inductor. Subsequently, the motor with external and integrated inductor are validated with finite element analysis (FEA) and their FEA based performance comparison is presented. In the end, integrated inductance is optimized and the effect of varying the integrated inductance is investigated.

Chapter 4 gives a description of the experimental rig and test setup for the integrated motor proposed in chapter 3. The experimental results of the motor with external and integrated inductor are presented respectively. The experimental comparison between the motor with external inductor and motor with integrated inductor has been made.

Finally, the chapter is concluded by giving a comprehensive experimental characterization of the motor with the integrated inductor.

Chapter 5 introduces an idea behind the integrated motor-shaped inductors. The motor-shaped rotational and rotor-less inductors are explored and demonstrated in this chapter. The design method of transforming EE core inductor into motor-shaped inductor is discussed. Afterwards, design optimization of motor-shaped inductors in terms of losses and associated weight has been done, taking into consideration of different slot-pole combinations and winding configurations. The chapter finishes with a comparative analysis of EE core and motor-shaped inductors.

Chapter 6 validates the concept of integrated motor-shaped rotational inductor proposed in chapter 5. The experimental results of the rotational inductor in terms of power losses at different rotor speeds and supply frequencies are presented. Successively, the performance of both rotational inductor and conventional EE core inductor are compared in terms of synchronous inductance, power losses, DC and AC resistance, power quality, weight, and volume.

Chapter 7 enlists the conclusive remarks drawn from this work with suggestions on areas where improvements can be made. The appendices include the basics of magnetic circuits, a method to calculate the 3-phase inductances, technical specifications and construction drawings.

1.5 NOVELTY & CONTRIBUTION OF THE THESIS:

1.5.1 Novelty of the Thesis:

The thesis presents:

- novel options for integrating passive filter inductor embedded inside the electrical machine both from functional and physical point of view.

- functional integration uses the motor inherent magnetics which eventually act as a filter inductance for RLC output filter applications in motor drive systems. This leads to elimination of added inductor losses and its associated mass and volume.

- physical integration which encompasses: motor-shaped rotational and rotor-less inductors. Rotational inductor rotates at synchronous speed of the stator magnetic field thereby reducing the rotor iron losses due to no rotor magnetic induction. Both rotational and rotor-less inductors share the existing motor/generator housing which allow us to design at high current density.

- the high current density inductor design which offer enoumous reduction in weight and volume which is pre-requisite for aerospace and marine applications.

1.5.2 Contribution of the Thesis:

The work carried out in this thesis has resulted in four international conference publications. The work published in these papers is presented in chapters 3, 4, 5 and 6 respectively. The key contribution of this thesis includes: design, development, simulation, testing and practical verification of novel integrated passive filter inductors for motor drive applications. The published papers are:

- M. Raza Khowja, C. Gerada, G. Vakil, P. Wheeler and C. Patel, "Integrated output filter inductor for permanent magnet motor drives," *IECON 2016 - 42nd Annual Conference of the IEEE Industrial Electronics Society*, Florence, 2016

- M. Raza Khowja, C. Gerada, G. Vakil, P. Wheeler and C. Patel, "Novel integrative options for passive filter inductor in high speed AC drives," *IECON 2016 - 42nd Annual Conference of the IEEE Industrial Electronics Society*, Florence, 2016

- M. Raza Khowja, C. Gerada, G. Vakil, C. Patel and P. Wheeler, "Design optimization of integrated rotational inductors for high-speed AC drive applications," *2017 IEEE International Electrical Machine & Drives Conference (IEMDC),* Miami FL, USA, 2017

- M. Raza Khowja, C. Gerada, G. Vakil, C. Patel and P. Wheeler, "Design optimization of integrated rotor-less inductors for high-speed AC drive applications," *2017 IEEE Workshop on Electrical Machines Design, Control and Diagnosis (WEMDCD)*, Nottingham, United Kingdom, 2017

1.5.2.1 Journal Publications:

The first draft of the enlisted journal publications have been prepared and being reviewed by the supervisors before the submission.

- M. Raza Khowja, C. Gerada, C. Patel, G. Vakil, S.A. Odhano, A. Walker and P. Wheeler, "Experimental Verification of Permanent Manget Motor with Integrated Filter Inductor,"
- M. Raza Khowja, C. Gerada, G. Vakil, R. Abebe, C. Patel and P. Wheeler, "Experimental Validation of Integrated Motor-shaped Rotational Inductor,"
- M. Raza Khowja, R. Abebe, Chris Gerada, G. Vakil, A. Walker, C. Patel "Integrated Passive Filters – An overview of the Modern Technolgies,"

1.6 SUMMARY:

This chapter presented an introduction about the project background, motivation and goals by highlighting the need of integration technologies in the motor drives system. The chapter also underlined the structure of the thesis and the contribution of the work that has been carried out as a part of this project.

The next chapter presents the reviewed literature in detail on passive filters topologies that are being used in the industry at present with emphasis on its structural integration.

1.7 REFERENCES:

[1] C. Hong, W. Fengxiang, and Z. Tao, "Research on repression method of harmonics for high-speed motor power supply," in *Electrical Machines and Systems, 2007. ICEMS. International Conference on*, 2007, pp. 610-613.

[2] N. Hanigovszki, J. Landkildehus, and F. Blaabjerg, "Output filters for AC adjustable speed drives," in *APEC 07 - Twenty-Second Annual IEEE Applied Power Electronics Conference and Exposition*, 2007, pp. 236-242.

[3] K. Han-Jong, L. Geun-Ho, J. Cheol-Ho, and L. Jea-Pil, "Cost-effective design of an inverter output reactor in ASD applications," *IEEE Transactions on Industrial Electronics,* vol. 48, pp. 1128-1135, 2001.

[4] A. v. Jouanne and P. N. Enjeti, "Design considerations for an inverter output filter to mitigate the effects of long motor leads in ASD applications," *IEEE Transactions on Industry Applications,* vol. 33, pp. 1138-1145, 1997.

[5] A. v. Jouanne, D. A. Rendusara, P. N. Enjeti, and J. W. Gray, "Filtering techniques to minimize the effect of long motor leads on PWM inverter-fed AC motor drive systems," *IEEE Transactions on Industry Applications,* vol. 32, pp. 919-926, 1996.

[6] M. R. Khowja, C. Gerada, G. Vakil, P. Wheeler, and C. Patel, "Novel Integrative Options for Passive Filter Inductor in High Speed AC Drives," in *Industrial Electronics Society, IECON 2016 - 42nd Annual Conference of the IEEE*, 2016.

[7] M. R. Khowja, C. Gerada, G. Vakil, P. Wheeler, and C. Patel, "Integrated Output Filter Inductor for Permanent Magnet Motor Drives," in *Industrial Electronics Society, IECON 2016 - 42nd Annual Conference of the IEEE*, 2016.

[8] J. Popovic-Gerber, M. Gerber, and B. Ferreira, "Integrated filter in electrolytic capacitor technology for implementation in high power density industrial drives," in *2008 IEEE Power Electronics Specialists Conference*, 2008, pp. 2968-2974.

[9] G. V. Robert Abebe, Giovanni Lo Calzo, Thmas Cox, Simon, Lambert, Mark Johnson, Chris Gerada, Barrie Mecrow, "Integrated motor drives: state of the art and future trends," *IET Electric Power Applications,* 2016.

[10] C. W. T. Mclyman, *Transformer and Inductor Design Handbook*, Fourth ed.

[11] R. Meere, N. Wang, T. O. Donnell, S. Kulkarni, S. Roy, and S. C. O. Mathuna, "Magnetic-Core and Air-Core Inductors on Silicon: A Performance Comparison up to 100 MHz," *IEEE Transactions on Magnetics,* vol. 47, pp. 4429-4432, 2011.

[12] M. K. Kazimierczuk and H. Sekiya, "Design of AC resonant inductors using area product method," in *2009 IEEE Energy Conversion Congress and Exposition*, 2009, pp. 994-1001.

[13] H. Nijende, N. Frohleke, and J. Bocker, "Optimized size design of integrated magnetic components using area product approach," in *Power Electronics and Applications, 2005 European Conference on*, 2005, pp. 10 pp.-P.10.

CHAPTER

2

PASSIVE FILTERS FOR MOTOR DRIVES

The variable frequency drives system is one of the major sources of harmonics, which drastically affects the power quality of the system. Implementing the technology of variable frequency drives potentially improve the energy efficiency. However, the use of such technology results in unwanted harmonics injection which leads to high losses and instability in the power system [1-6]. This chapter deals with the application of passive filters in motor drives system to smooth out the voltage and current waveforms. Input filters, DC link filters and output filters are described from the functional point of view. The chapter also presents the layout of structural integration of passive filter inductor being used at present.

2.1 GRID SIDE FILTERS:

The grid side filters, also known as grid input filters are desired in motor drives system to smooth the grid input current and satisfy the electromagnetic compatibility (EMC) standards. The input currents drawn from the grid have the high order switching ripples along with a desirable fundamental component [7-9].

Three types of input filter are being employed to reduce the harmonics of grid current and hence, improve the power quality and meet the grid standards. They include: L filter, LC filter and LCL filter.

2.1.1 L Filter:

In L type filter [10-17] as illustrated in Figure 2.1, a large amount of inductance is desired to attenuate the switching frequency component which increases the size and hence, cost of the inductor counterparts. Furthermore, the excessive voltage drop across the filter inductor prevents it from being used for the grid applications [18]. The selection of filter inductance (L_1) is based on the allowable maximum current ripple at the switching frequency [13, 19, 20] which is given by,

$$L_1 = \frac{v_{dc}}{6 f_{sw} \Delta i_{max}} \tag{2.1}$$

where v_{dc} is the DC link voltage, f_{sw} is the switching frequency of the converter and Δi_{max} is the maximum current ripple of the converter which is a rough estimation recommended by an empirical relation. A 20% current ripple of the rated current is considered acceptable in [13, 17] and a 10% ripple of the rated current is preferred in [20] for the design of grid side inductor (L_1). It is recommended in [9], the filter inductance (L_1) is selected such that the voltage drop across it should not exceed 5% of the input voltage. Again the value of current ripple and voltage drop across the inductor is application specific and governed by targeted application requirement.

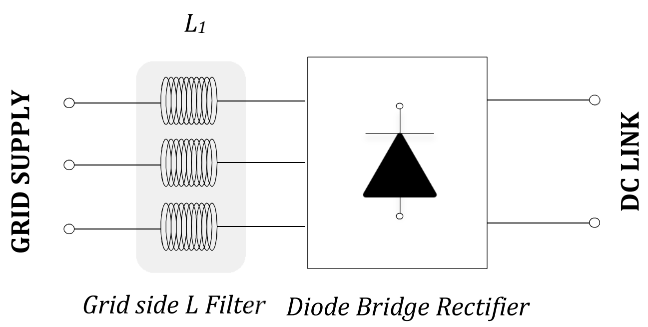

Figure 2.1: L Type Grid Side Filter

2.1.2 LC AND LCL Filter:

On the contrary, higher order LC filter [18, 21, 22] and LCL filter [10-13, 15, 18-21, 23-30] as shown in Figure 2.2(a) and Figure 2.2(b) delivers two or three times higher attenuation than a simple L type filter depending on the selection of filter's resonance frequency. This reduces the amount of inductance required for the filter that in turn results in reduction of size and cost [10, 13, 14, 16-18].

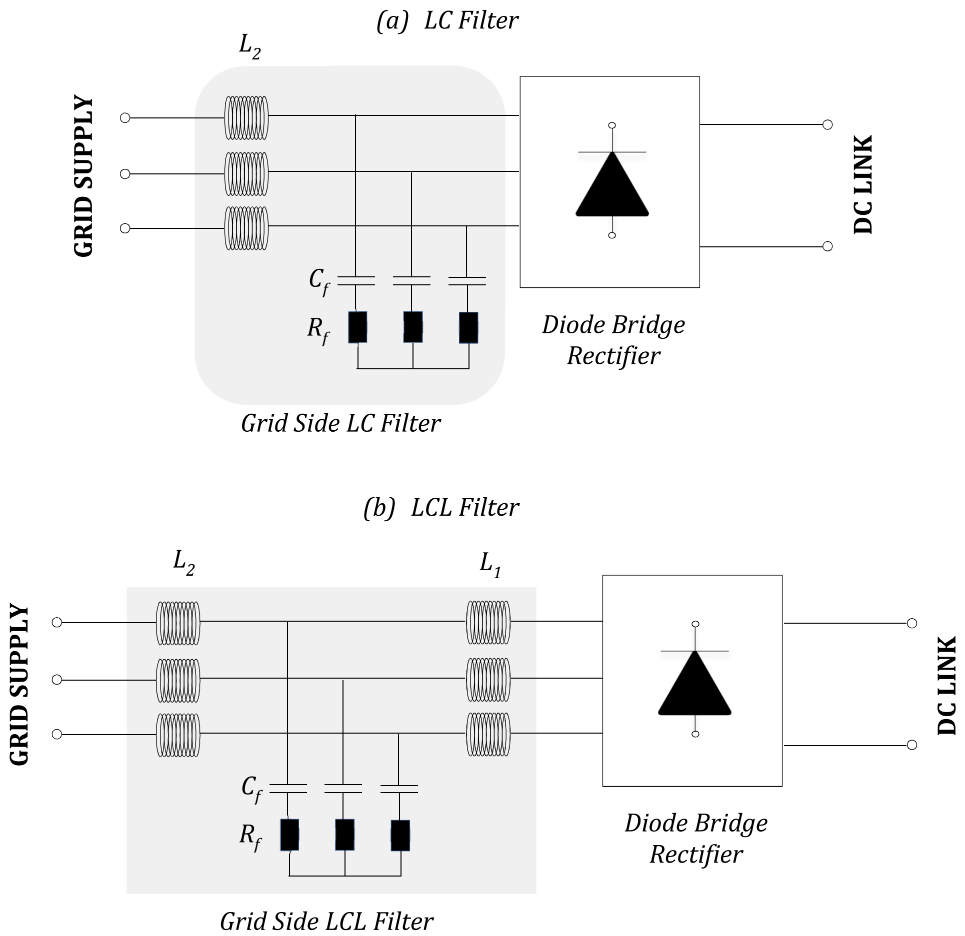

Figure 2.2: LC and LCL Type Grid Side Filter

The design of the converter side inductance (L_1) follows the same procedure [13] as discussed in section 2.1.1. For the design of the filter capacitance (C_f), the reactive power desired by the filter capacitor is typically set to 2−5% of the base capacitance at rated conditions in [18-20] whereas, a design factor for reactive power of 15% is used in [13]. The maximum filter capacitance as a percentage (y) of base capacitance is given by the following expression [13, 18, 20],

$$C_f = (y\%)\,\frac{S}{2\pi f_o V_{rms}^2} \tag{2.2}$$

where S is the apparent power rating of the converter, y is the filter capacitance design factor in percentage, f_o is grid fundamental frequency and V_{rms} is the grid line-to-line RMS voltage. The grid side inductance L_2 can be calculated from the limit of total inductance. The total inductance (L_1+L_2) should not exceed 10% of base inductance which restricts the voltage drop across both inductances. The base inductance is defined by,

$$L_b = \frac{V_{rms}^2}{2\pi f_o S} \tag{2.2}$$

With the filter parameters (L_1, C_f and L_2) determined, it is essential to confirm the range of resonance frequency [19]. Typically, the resonance frequency is half of the switching frequency and at least 10 times higher than the grid fundamental frequency [13, 20]. Therefore, the resonance frequency must lie in the range of the following equation [13, 19, 20, 26],

$$10f_o < f_{res} < 0.5f_{sw} \tag{2.3}$$

In order to avoid the resonance between the filter components, the damping is achieved by connecting a damping resistance (R_f) in series with the filter capacitance (C_f). The damping resistance (R_f) attenuates the ripple on the switching frequency and hence dampens the oscillations caused at the resonance. The value of the damping resistance (R_f) can be determined using following relation [20],

$$R_f = \frac{1}{3\omega_{res}C_f} \tag{2.4}$$

2.2 DC LINK FILTERS:

The DC current drawn by the voltage source inverter contains significant amount of switching pulsations in voltage and current waveforms. The DC link input filters, also known as smoothing filters are employed to reduce the amount of switching fluctuations that oscillates between its average dc values. The pulsating component of the DC link voltage and current has to be limited to a low value in order to meet the electro-magnetic compatibility (EMC) requirements. This is achieved by the use of DC link inductor and capacitor, the details of which are described in section 2.2.1 [31].

2.2.1 LC Filter

The LC resonance circuit as shown in Figure 2.3 is used to improve the power quality of the DC link. The inductor basically helps to limit the switching ripples in the current waveform, whereas the capacitor serves to reduce the amount of voltage oscillations across the input terminals of the voltage source inverter. The criteria and procedure [31, 32] of selecting DC side L and C components is discussed below,

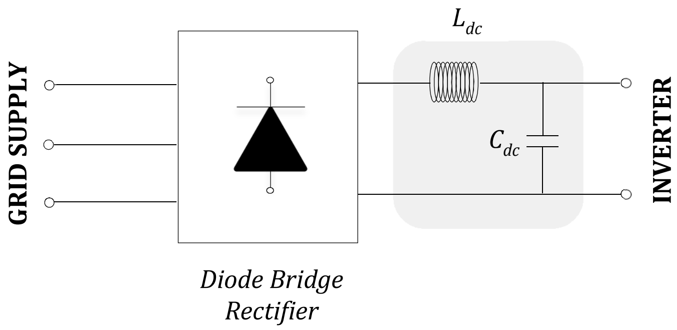

Figure 2.3: DC side LC Filter

The DC side filter capacitance needed to absorb the voltage fluctuations can be calculated by using an energy based equation of the capacitor [32]. The energy supplied by the filter capacitor and the required filter capacitance are defined by,

$$W_C = \frac{P_{inv}}{f_{ripple}} = \frac{1}{2} C_{dc}(V_{max}^2 - V_{min}^2) \tag{2.5}$$

$$C_{dc} = \frac{2P_{inv}}{f_{ripple} \times (V_{max}^2 - V_{min}^2)} \tag{2.6}$$

Where, C_{dc} is the DC side filter capacitance, P_{inv} is the inverter capacity in KW, f_{ripple} is the ripple frequency of diode bridge rectifier and V_{max}, V_{min} are the magnitude of maximum and minimum voltage ripple at the DC link respectively. The minimum allowable voltage (V_{min}) at the DC link has to be calculated with the limitation of maximum allowable ripple voltage (V_{ripple}), which is given as,

$$V_{min} = V_{max} - V_{ripple} \tag{2.7}$$

Once filter capacitance (C_{dc}) is assessed using (2.6), the filter inductance (L_{dc}) can be estimated by selecting the resonance frequency of the DC link filter [31]. The resonance frequency of the DC link filter must be lower than switching frequency of the inverter. In the case of six-step inverter, the resonance frequency must satisfy the given equation,

$$f_{res} < 6f_{sw} \tag{2.8}$$

In the case of PWM inverters, the resonance frequency must satisfy the given equation,

$$f_{res} < 2Nf_{sw} \tag{2.8}$$

where, N is the number of pulses per half-cycle in the line-to-line voltage of the inverter output. In [31], the dc side filter inductance (L_{dc}) is selected by keeping the resonance frequency one-fifth of the inverter switching frequency.

2.2.2 Electronic Smoothing Inductor (ESI) System

The DC side inductance occupies considerable amount of space in motor drives system which increases its size and weight. In order to overcome this issue, the electronic smoothing inductor (ESI) was initially introduced in [33] and the control strategy has been improved in [4, 33-39]. In [33], the classical DC side inductor as shown in Figure 2.3 is replaced by an ESI system as shown in Figure 2.4(a). The ESI system consists of a DC side inductor, two diodes, two MOSFETs and a DC link capacitor. The ESI system is able to control the output DC current of diode bridge rectifier and makes it possible to reduce both voltage ripple across the inverter and current harmonics present in the grid.

The ESI voltage (v_e) is the difference of rectifier output voltage (v_r) and the inverter input voltage (v_o). The gate signals of MOSFETs produced by the PWM control are shown in Figure 2.4(b). The inductor current (i_L) is controlled at a constant DC value by operating switch T_1 and T_2 with variable duty cycle. When switches T_1 and T_2 are turned ON, the DC link capacitor (C) discharges and inductor current (i_L) increases. On the contrary, DC link capacitor (C) will charge and inductor current (i_L) decreases when switches T_1 and T_2 are turned OFF. In the period when either of the switch T_1 or T_2 is turned ON, inductor current (i_L) will not flow in DC link capacitor (C). Therefore, DC link capacitor (C) is charged when voltage across ESI is positive and discharge when voltage across ESI is negative [34, 36-39].

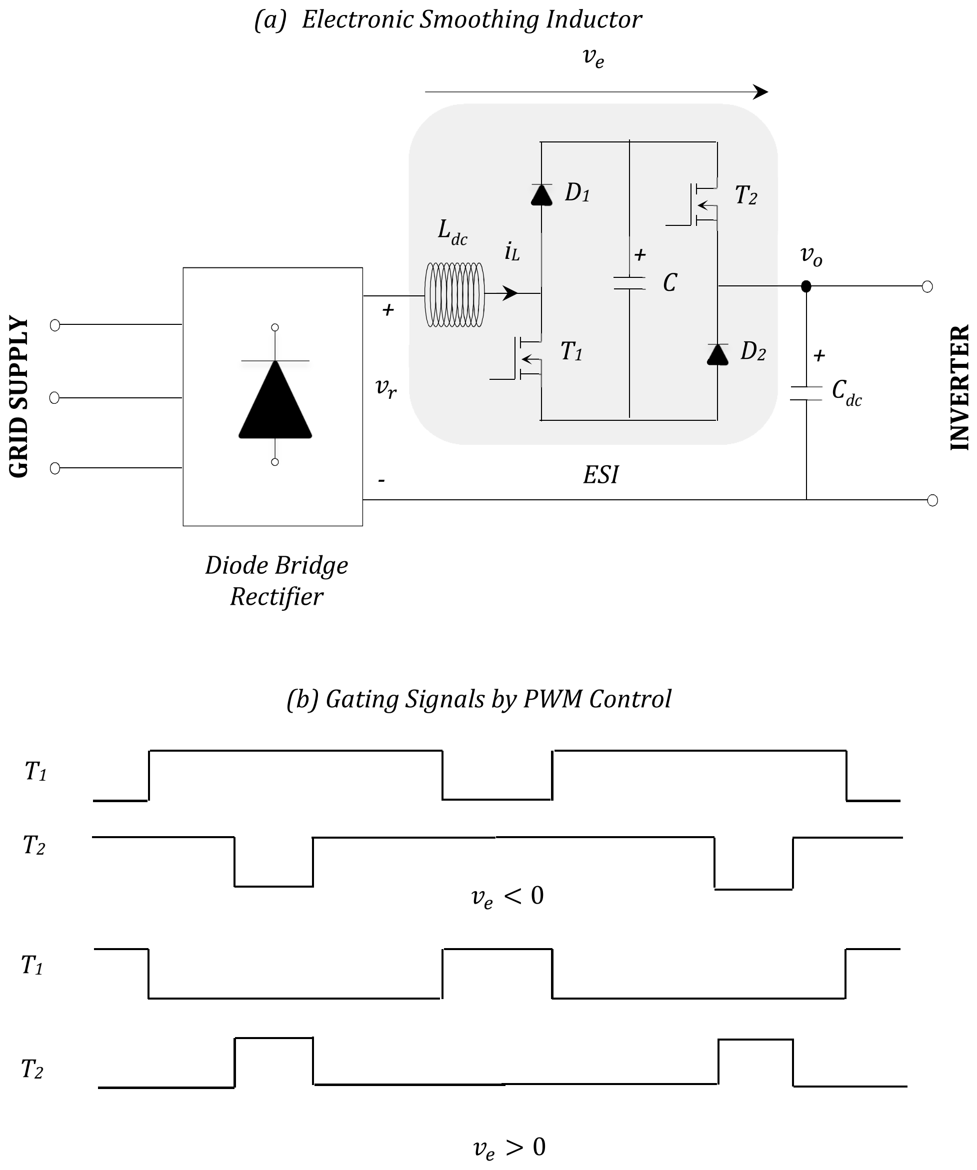

Figure 2.4: Electronic Smoothing Inductor (ESI) System

In ESI system, the DC side inductance is chosen just as equation (2.9) such that the amplitude of the current ripple is $\pm 15\%$ of DC side inductor current (i_L) at the rated operating condition [37, 38] whereas the amplitude of the current ripple is selected as $\pm 20\%$ of DC side inductor current (i_L) in [34, 39].

$$L_{DC} = \frac{\left(\sqrt{3}/_2\right) \times v_{inp} - (v_o - v_c)}{0.3 \times i_L \times 2f_{sw}} \times D_{max} \tag{2.9}$$

where, i_L is the average value of the inductor current, D_{max} is the maximum duty cycle, v_{inp} is the grid voltage, v_o is the inverter terminal input voltage, v_c is the voltage across DC link capacitor in the ESI system.

2.2 OUTPUT PASSIVE FILTERS

In inverter-driven AC machines, voltage source inverter (VSI) can generate a high voltage gradient (dv/dt) of around 10 $KV/\mu s$ across the motor terminals. The inverter output voltage with high (dv/dt) propagate through the motor cable that behaves like a transmission line and voltage overshoots appears at the motor terminals. High voltage gradient (dv/dt) results in an increase high frequency conducted and radiated emissions, motor insulation stress, leakage currents, bearing stress, acoustic noise, core losses and skin-effect losses in the motor windings. Depending on the specific application, the eradication of some of these concerns becomes mandatory [40-48].

The output filters are employed to eliminate the steep PWM voltage pulses from appearing on the motor terminals. Four output filter solutions that are commonly being used in industrial applications which are outlined below [40],

2.2.1 Output Choke

The output chokes are also known as series reactors or output inductors is a kind of (dv/dt) filter without a capacitor as shown in Figure 2.5 [40, 42, 43, 49, 50] but have the drawback of causing voltage overshoots with a very poor damping which increases the risk of “voltage doubling” across the motor terminals [40]. The chokes are inserted as three phase coils between inverter and the motor terminals to provide additional inductance to the system. Output chokes are often used to reduce the high (dv/dt) stress on the motor insulation. However, these are not effective enough to reduce the bearing stress, high frequency emissions, leakage currents and acoustic noise [40, 50].

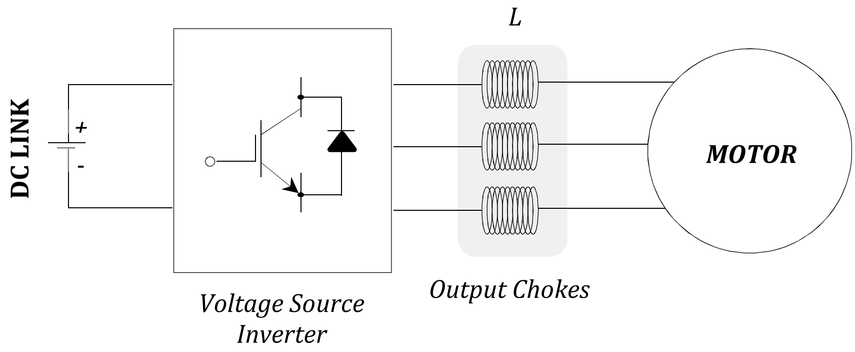

Figure 2.5: Output chokes

The degree of suppression is almost proportional to the value of output chokes which leads to increase in cost, volume and weight, and deteriorates the power factor of the drive system. Moreover, the series reactor will introduce the significant amount voltage drop at the fundamental frequency which reduces the ability of the machine to produce the rated torque. Nevertheless, due to its simple functional and physical structure, the output chokes are often adopted in applications where motors are built with poor insulation [40] and where the motor is designed with lower winding inductance to provide enough inductance to control the drive. Output chokes are not always enough to eliminate the high frequency harmonics from the inverter output voltage due to its functional limitations. Therefore, LC filters are the most commonly used compared to output chokes when it comes to mitigate the high frequencies [50].

2.2.2 LC Filter

It is well known that the PWM inverter injects the high frequency electromagnetic interference (EMI) noises: that flows within the power-feeding paths known as differential-mode (DM) noise, and that flows between the power conversion system and the ground known as common-mode (CM) noise [51]. The effect of high frequency (EMI) excites the parasitic capacitances (i.e. the capacitance between the motor windings and the ground; and the capacitance between $IGBT$ inverter and its heat sink) which leads to severe serious problems such as radiated and conducted high frequency emissions, shaft voltage and bearing currents, motor over voltage and reduced life of the motor insulation [40, 52-54].

2.2.2.1 Common-mode Filter:

Common-mode (CM) LC filter as shown in Figure 2.6 is consists of three common-mode inductors and three common-mode capacitors. They are used to reduce conducted and radiated high frequencies (above 150 kHz) common-mode noise from the motor cable. The resonance frequency of common-mode filter is usually selected higher than the switching frequency which reduces its overall size and provides a cost effective solution [40, 49, 55, 56]. The criterion of selecting resonance frequency is given by (2.10) where f_{re} is the high frequency emission getting eliminated from the system.

$$f_{sw} < f_{res} < f_{re} \tag{2.10}$$

In terms of design, author of [50] suggests that the CM inductor must be designed in a way that the core does not saturates as the saturation of the core may lead to excessive amount of CM current through the parasitic capacitances. Therefore, the maximum flux density in the core at fundamental frequency must limit below the saturation flux density of the core material.

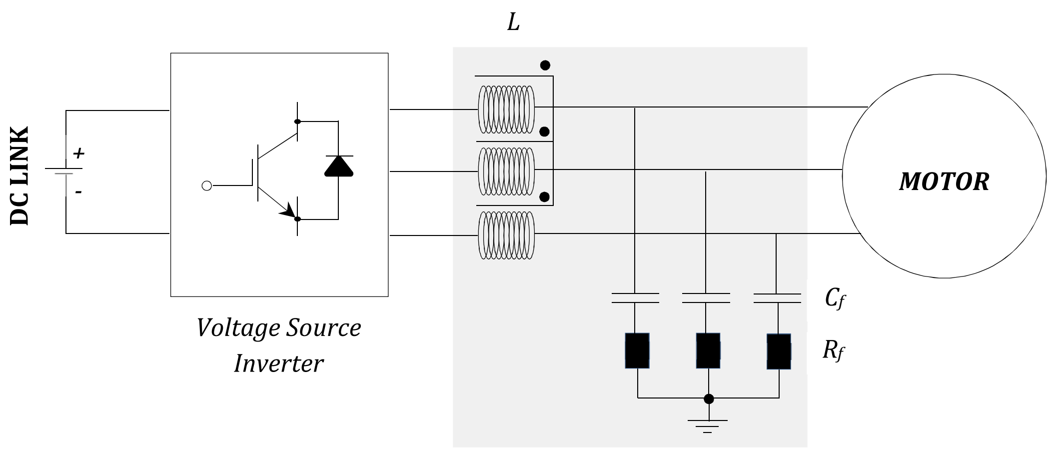

Figure 2.6: Common-mode Filter

2.2.2.2 *Differential Mode* $^{dv}/_{dt}$ *Filter:*

Differential mode (dv/dt) filter (LC or RLC) as shown in Figure 2.7 has been used to reduce the differential mode dv/dt on the motor terminals to protect insulation of the motor cables. However, dv/dt filters are not effective solutions for reducing leakage current, induced shaft voltage, high frequency emissions and acoustic noise [40, 43]. Filter resistors are often used to overdamp the ringing oscillations caused by long cables between inverter and motor terminals [42, 55]. The resonance frequency of this kind of filter is also greater than the switching frequency [40].

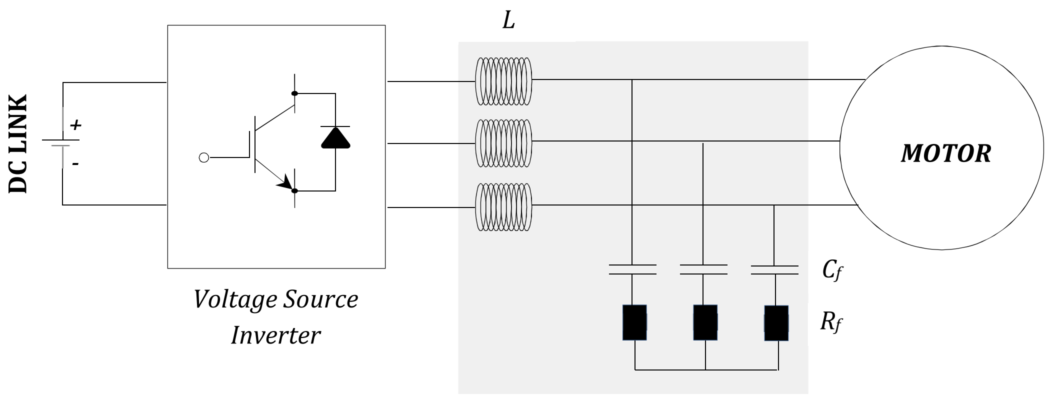

Figure 2.7: Differential-mode dv/dt or sine-wave Filter

The resonance frequency is chosen using the relation (2.11) where t_{cr} is the critical rise-time. Based on the relationship shown in [42], critical rise time corresponding to a 20% motor side overvoltage for a cable length of 15m, 30m and 60m, the critical rise time (t_{cr}) is approximately 1.5 μs, 2.5 μs and 3.5 μs respectively [42, 55].

$$f_{res} = \frac{1}{2t_{cr}} \tag{2.11}$$

The values of L and C can be selected with the help of RLC network transfer function for 3 dB attenuation at a given resonance frequency (2.11). The damping resistor (R_f) is picked to critically damped the filter circuit using characteristic impedance of the cable which is given as [42, 55],

$$R_f \geq \sqrt{\frac{4L_f}{C_f}} \tag{2.12}$$

A number of articles have been published to improve the functional performance of dv/dt filters [48, 55, 57, 58]. In paper [55], the neutral point of the filter capacitors is connected to the midpoint of DC link as shown in Figure 2.8 which significantly reduces both common-mode and differential-mode effects i.e. the voltage over shoots on the motor terminals, high frequency leakage currents and induced shaft voltages. Another paper [57] presented a similar [55] filter design which is practicable for the applications where midpoint of DC link is not accessible. Two star points are obtained with six resistors and six capacitors that are connected to the positive and negative terminal of the DC buses respectively.

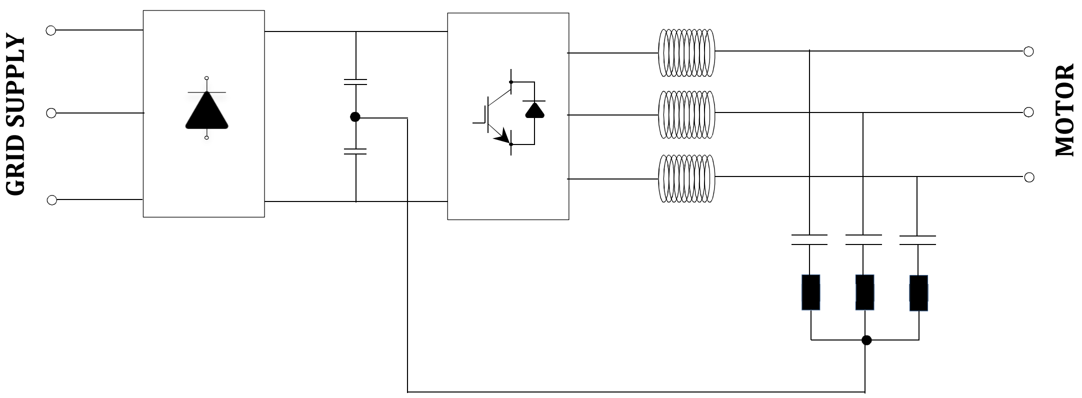

Figure 2.8: dv/dt with RLC filter connection to DC Link Midpoint

The author of [58] proposed a diode clamping filter design shown in Figure 2.9 which uses six clamping diodes to connect each phase to both positive and negative DC buses. The approach effectively reduces the dv/dt of the inverter output voltage and, in addition, eliminates the effect of ringing oscillations at the motor terminals.

The work presented in [48] also reduces the motor terminals over voltage considerably by connecting the neutral point of filter capacitors between the two diodes across the DC bus as shown in Figure 2.10.

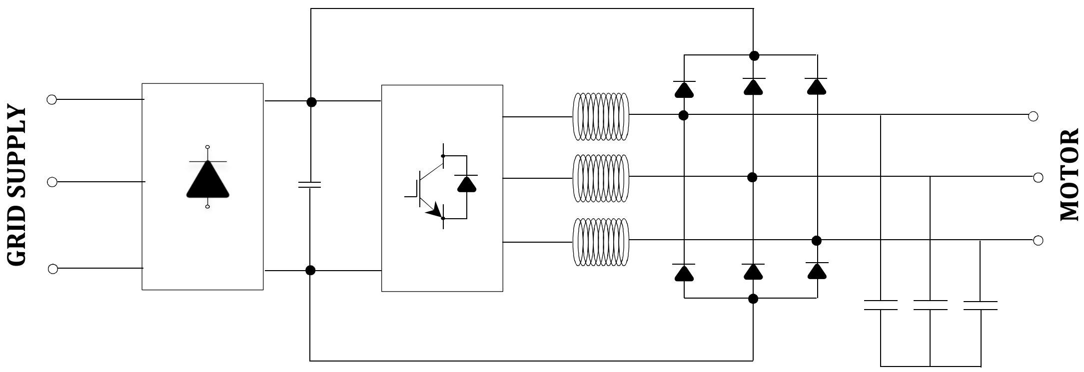

Figure 2.9: Diode Clamp dv/dt Filter with Six Diodes

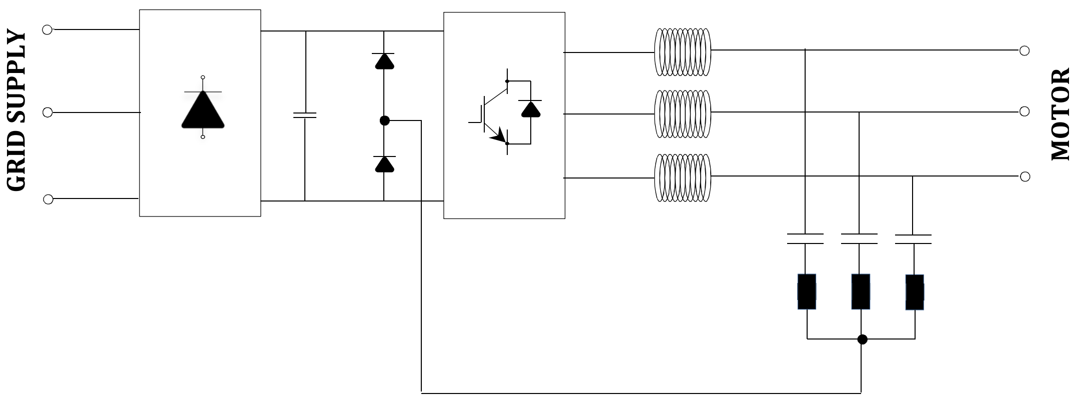

Figure 2.10: Diode Clamp dv/dt Filter with Two Diodes

2.2.2.3 Differential Mode Sine-wave Filter:

The sine-wave filter is also a differential-mode filter as shown in Figure 2.7 but have the resonance frequency well below the switching frequency. There are numerous guidelines in the literature to choose the resonance frequency. In [40, 59-61], it has been suggested to pick resonance frequency one-third of the switching frequency to have enough attenuation at the switching frequency. This provides an attenuation of about 18 dB at the switching frequency [40]. On the other hand, the resonance frequency must be at least ten times higher than the fundamental output frequency in order to avoid the resonance with the motor impedance around the fundamental frequency [40, 60]. Therefore, the criterion for selecting resonance frequency is given as,

$$10f_{out} < f_c < \frac{1}{3}f_{sw} \tag{2.13}$$

The selection of filter capacitance (C_f) is based on the resonance between the filter capacitance and motor windings. In [62], it is recommended that the filter capacitance should be selected such that resonance between the motor winding and the filter capacitance does not interfere with the control loop of the drive system. Therefore,

$$C_f \leq \frac{1}{(2\pi\, f_{max})^2 . L_m} \tag{2.14}$$

Where, L_m is the inductance of the motor windings and f_{max} is the maximum frequency that control loop is able to reject. When sine-wave filters are employed, the voltage across the motor terminals is no longer contain PWM pulses which leads to near sinusoidal power being fed to the motor i.e. no voltage overshoot arises at the motor terminals, reduced motor losses with reduced acoustic noise due to PWM switching [40, 63].

A variety of sinusoidal filters have been presented [59, 64, 65] that can not only reduce common-mode currents but can also reduce differential-mode effects. In [64], six diodes are employed to link phases to positive and negative DC bus terminals as shown in Figure 2.11. The topology reduces the high voltage gradient at the motor terminals and remove voltage spikes due to ringing oscillation. The major benefit when compared to RLC filter is smaller filter size and lower power losses.

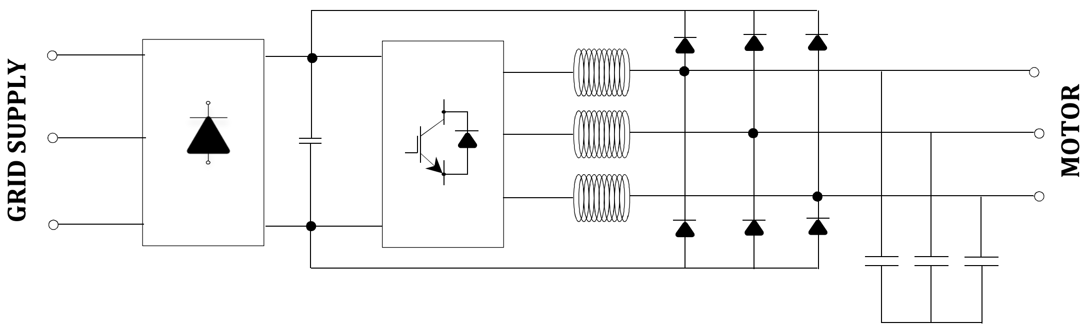

Figure 2.11: Diode Clamp Sine-wave Filter with connections to DC Link

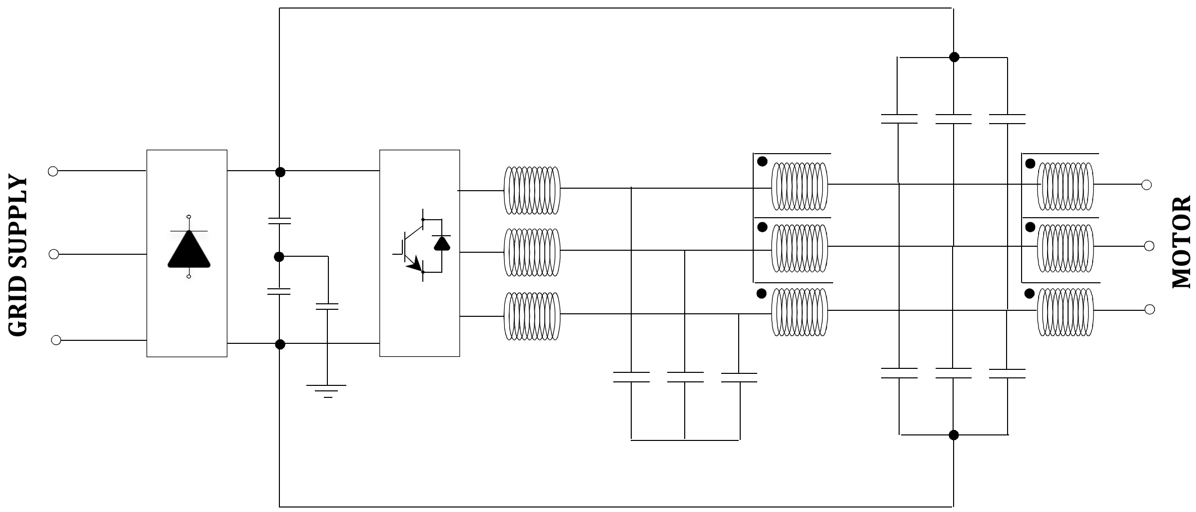

Figure 2.12: Sine-wave "All Cure" Filter

The author of [59] introduced an "all-cure filter" as shown Figure 2.12. The filter consists of separate differential-mode and common-mode filters and the star points of both common-mode capacitors are connected with positive and negative terminals of the DC bus. The right-hand side common-mode inductor is added to filter out the high-frequencies beyond 150 kHz. The left-hand side common-mode inductor is used to mitigate the switching frequency harmonics. This filter topology effectively reduces stress on the motor insulation, bearing currents, acoustic noise, and high-frequency emissions to the mains.

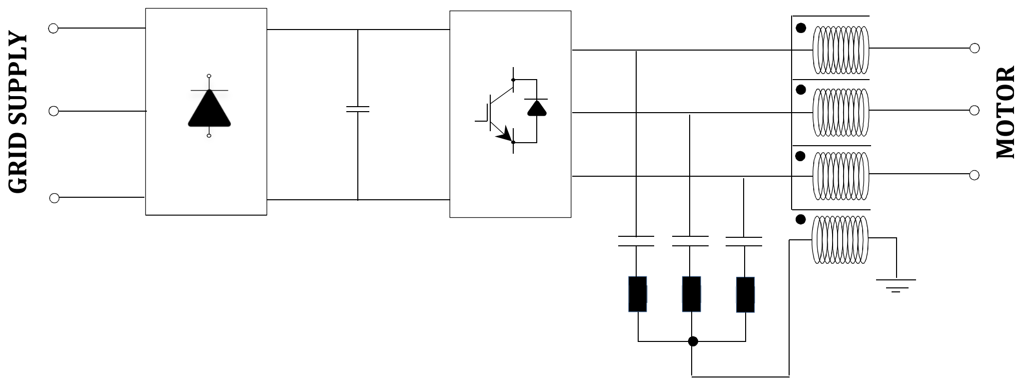

Figure 2.13: CM Filter with Artificial Point Connected to the Ground

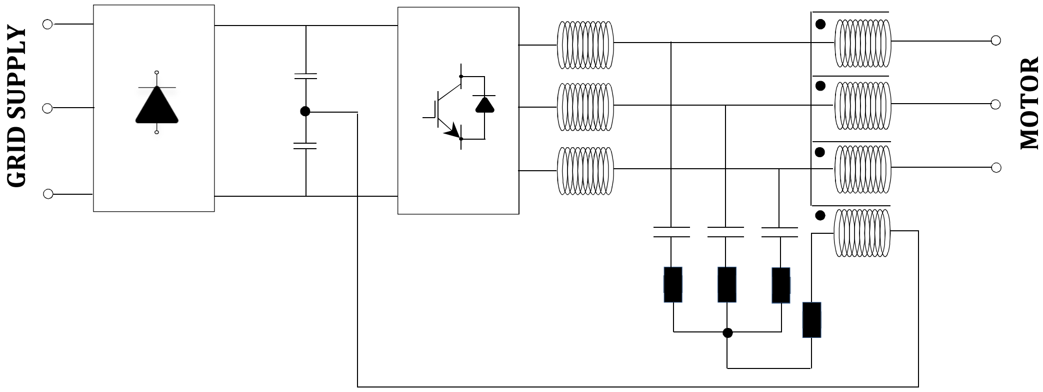

Figure 2.14: CM and DM Filter with CM Transformer

Several output filters have also been proposed in the literature which is based on the common-mode transformer [64, 66]. Paper [64] proposed an output filter which replaces the common-mode inductor with potential-type suppression transformer as shown in Figure 2.13. The star point of shunt capacitors and resistors is connected to the ground through an additional fourth winding of the common-mode transformer. The voltage across a neutral point generates a common-mode current through the fourth winding. The common-mode current induces a voltage which is equal to the common-mode voltage across the other windings which cancels out the common-mode voltage at the motor terminals.

A similar concept of output filter with a separate differential-mode filter inductor is presented in [66] as shown in Figure 2.14. This topology is consists of a differential-mode filter inductance and a common-mode transformer with its fourth winding connected with the mid-point of the DC bus. In comparison, this approach requires one capacitor less than the approach used in [65] but it needs one extra transformer winding in the common-mode transformer. However, the analysis of the common-mode circuit is more complicated for the filter presented in [66] as that presented in [65].

2.3 INTEGRATED PASSIVE FILTERS:

Traditional motor drive structure similar to the one shown in Figure 1.1, has been in use for many years which utilizes the physical structure of passive inductor as indicated in section 1.2. The power electronics and drive industries are shifting more towards integration of passive components to gain the benefits such as compact design, reduction in cost, mass, size and fewer manufacturing process. In recent times, there has been a shift from traditional passive elements into integrated package enclosed within the drive's system [67-70]. Therefore, applications where high power density is required, the use of the integrative options present to be the best solution [71, 72].

There are few studies aimed at achieving the goals of integrating passive inductor inside the machine. In [67, 69, 70], the perspectives on the integrated filter inductors are presented, that motivates for the drive integration on a system level. The design of integrated filter inductor that may be required for power factor correction application is presented in [69] as shown in

Figure **2.15**. The paper modified the stator laminations to increase the stator back iron which acts as an integrated filter inductor. This modification of stator lamination increases the outer diameter of the motor which in turn increases the overall weight and size of the motor. However, the integrated inductor design does not interact with the magnetic field of the motor itself.

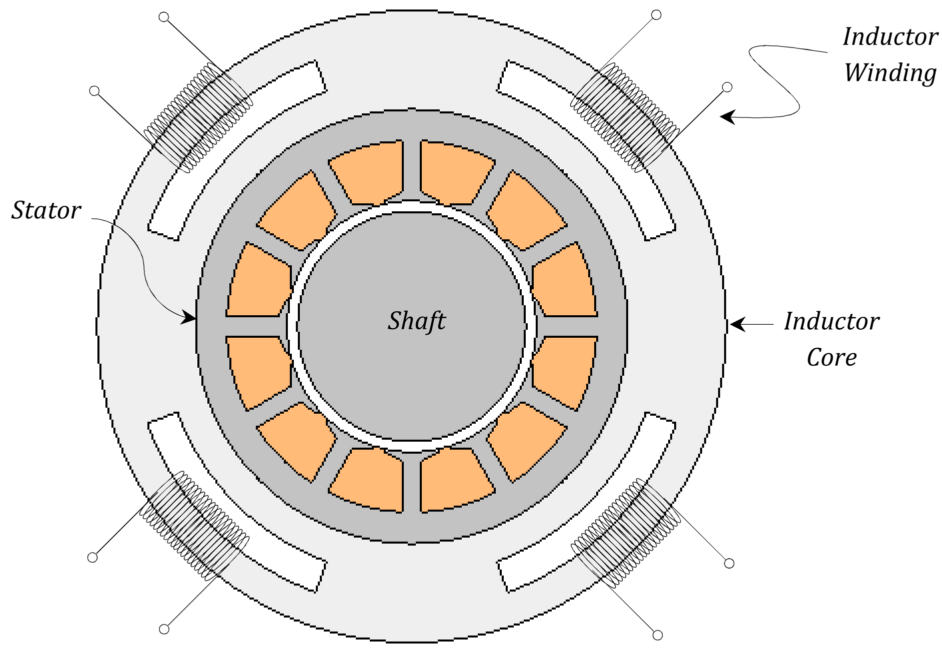

Figure 2.15: Integrated Filter Inductor [69]

In another publication [67, 70], the complete stator back iron is used as a magnetic component for one or more discrete inductors or transformers as shown in

Figure **2.16**. This is done by integrating toroidal winding which drives alternating magnetic ring flux in the back of the stator core. This ring flux shares the back iron with main motor flux. The ring flux always travel in one direction at the back of the core whereas main flux at any instant has as much flux going anti-clockwise in the back of the core as is going clockwise. The drawback of this approach is that the presence of ring flux due to inductor winding will affect the main motor flux if the stator back iron of the machine is operating above the linear region for a given soft magnetic material.

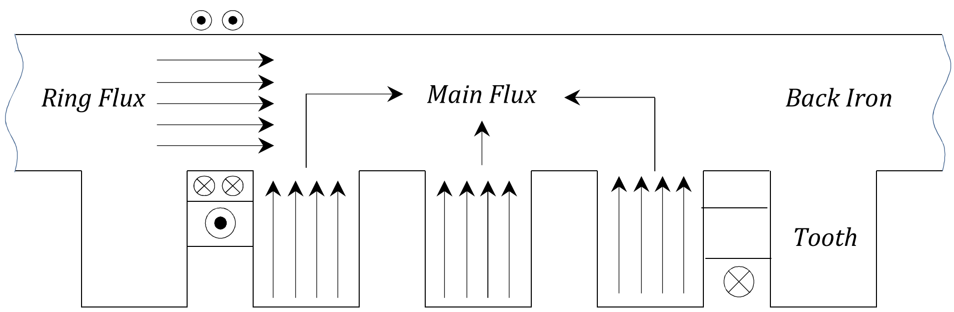

Figure 2.16: Integrated Filter Inductor [67, 70]

The paper [73] presents a structural integration of grid side passive LCL filter into the permanent magnet synchronous machine which achieves high power density. Both inductors are wound into the outermost slots of the double slot machine as shown in Figure 2.17. The proposed integrated inductor is iteratively optimised in terms of iron and copper weight and compared with the traditional separate inductor. The integrated filter inductors on the outermost slots are free from cross-coupling of magnetic fields between the main machine and filter winding. This is possible by adopting different pole numbers of filter winding to that of torque producing motor windings.

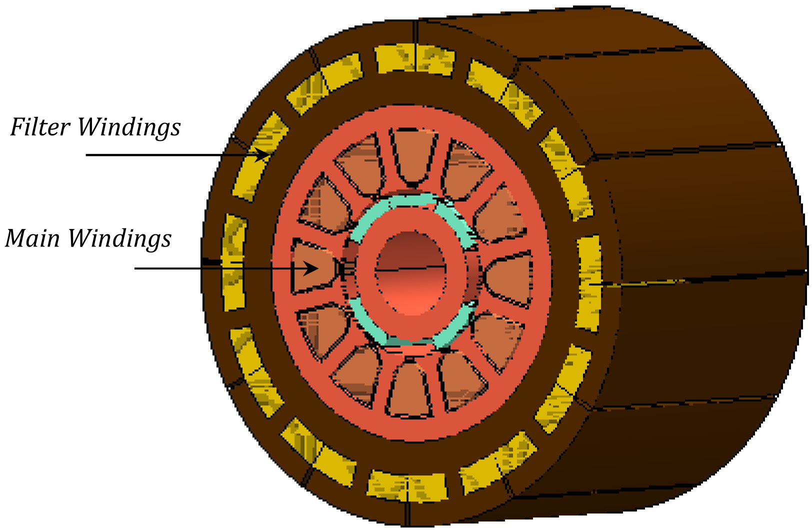

Figure 2.17: An Electrical Machine with integrated grid-side LCL filter

Different pole number combinations for the main machine and filter windings result in either balanced or unbalanced magnetic poles. Therefore, for the balance case, pole numbers of main machine and filter windings must be separated by a multiple of two pole pairs. This will allow both magnetic fields rotate at a different speed and hence minimum flux linking between them. The approach is validated through Finite Element Method by energizing both windings simultaneously at different supply frequency. The results showed the minimum cross-coupling between the filter and main torque producing winding.

Article [74] designs a passive DC link inductor to reduce the grid side harmonics, DC side voltage ripple, current stress of the DC link capacitors and stress on rectifier side diodes. The design of separate DC link inductor as shown in Figure 2.18(a) is shifted to an integrated structure on a single magnetic core. It has been advised that the inductor can be integrated by directing the flux either in the middle leg or outer leg as shown in Figure 2.18(b) and Figure 2.18(c) respectively. All inductor designs (Figure 2.18(a)-(c)) can be constructed to have the same amount of inductance depending on the design specifications.

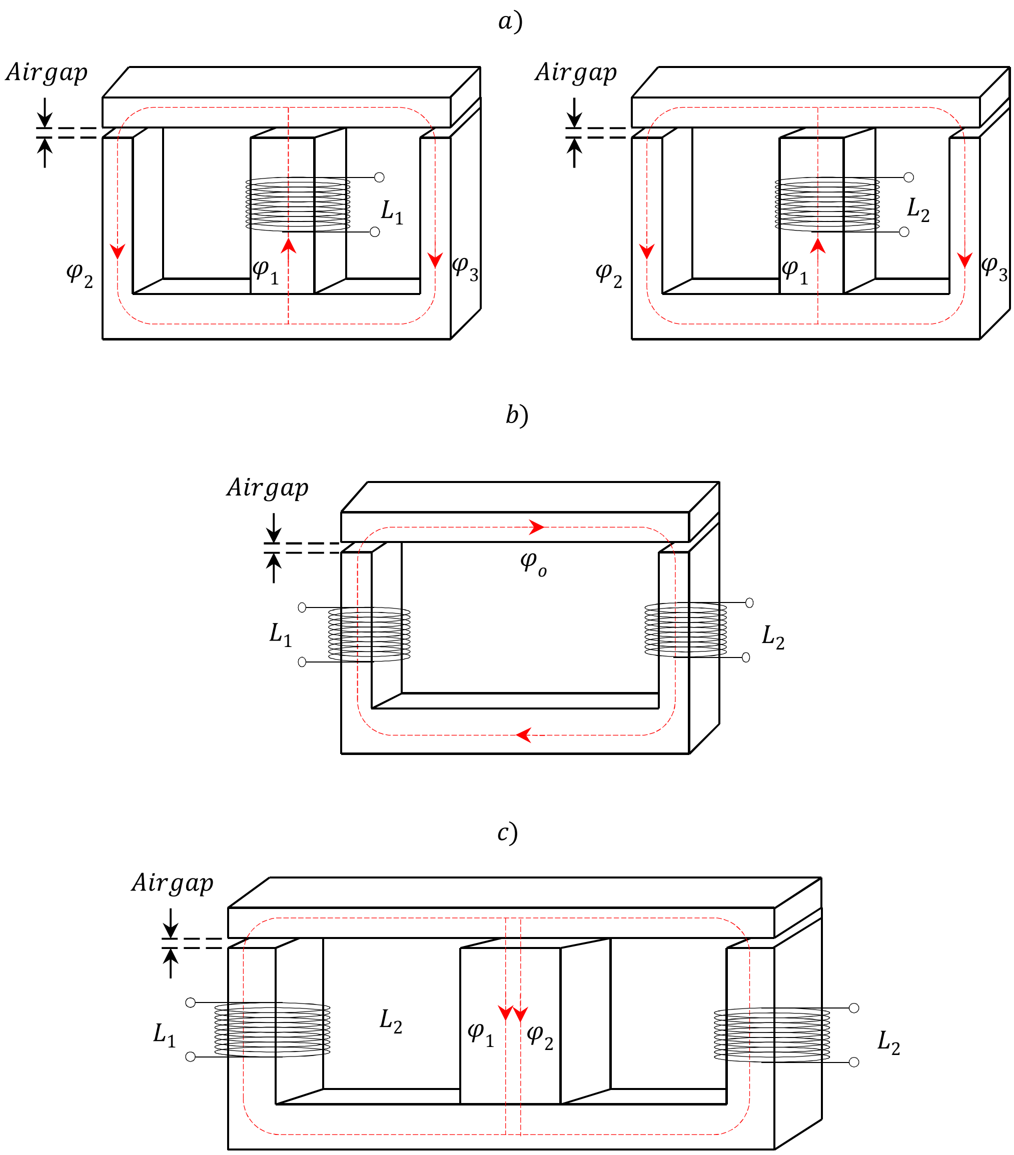

Figure 2.18: Integrated Filter Inductor [74]

Several studies have been considered to integrate both passive inductor and capacitor into same component [75-83]. The principle of electromagnetic integration is used to integrate the capacitance in the same magnetic component as that of the inductor. In [75-81], the planar LC filter is integrated which consists of alternating layers of magnetic material, conductors, dielectrics and insulation which results in integrated LC structure. The LC winding is a dielectric substrate with conductor windings directly deposited on both sides, thus resulting in a distributed inductance and capacitance structure as shown in Figure 2.19(a). By properly connecting the four terminals A, B, C and D of the LC winding, different equivalent structures can be obtained such as equivalent LC series resonator, parallel resonator or low-pass filter. This is shown in Figure 2.19(b).

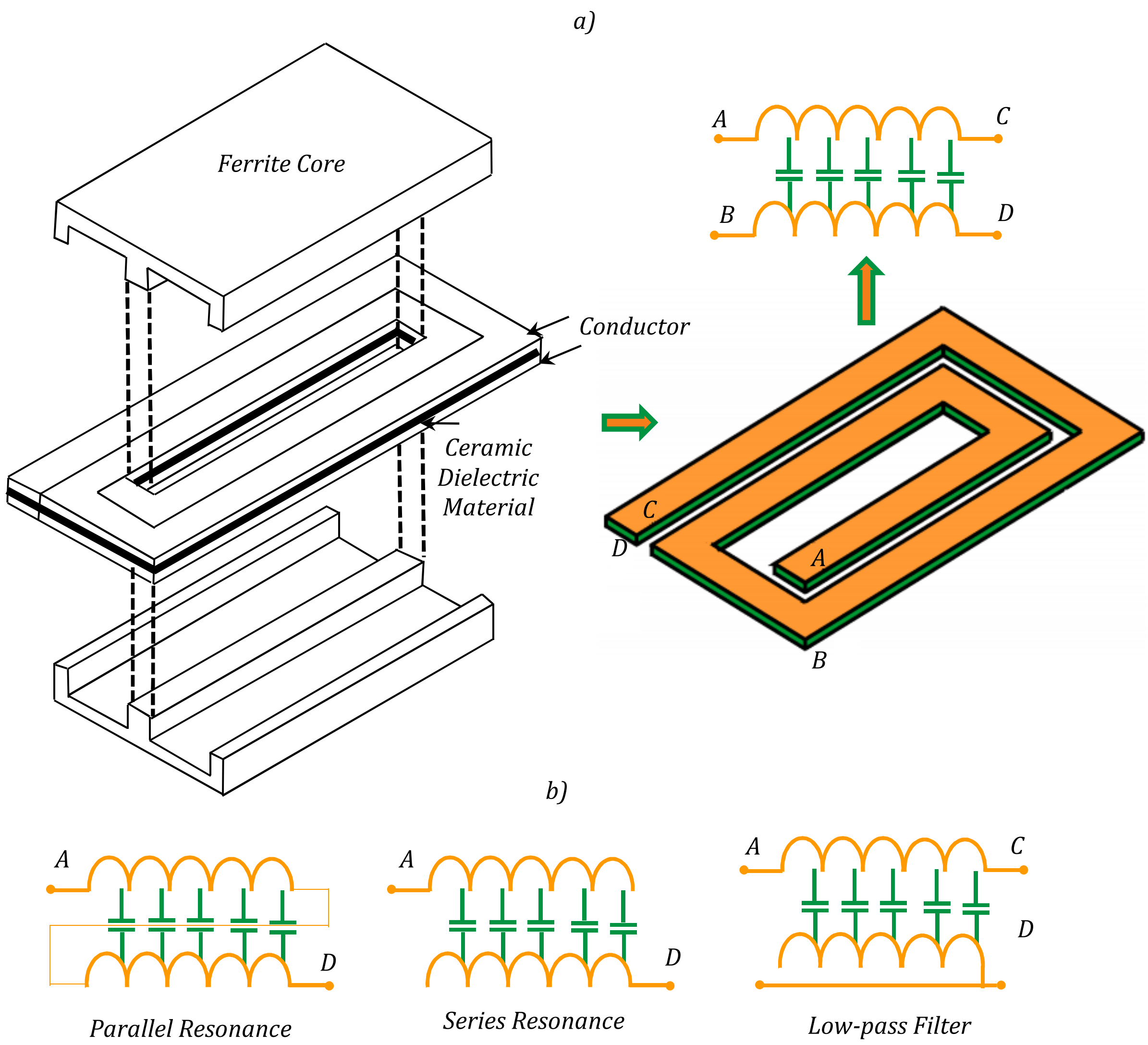

Figure 2.19: Integrated Planar LC Filter [75-81]

The same principle of [75-81] is applied in articles [82, 83] for EMI filter applications. The principle of electromagnetic integration increases the capacitance in the winding by introducing a dielectric layer between the windings. The distributed capacitance is implemented in a traditional way i.e. the anode and cathode foil are etched with aluminum oxide dielectric layers. On the other hand, the inductor is made by using the cathode and anode aluminum foils of the capacitor to implement the windings wound around the magnetic core as shown in Figure

2.20(a). The inductor windings are packed in a can, which has a hole in the middle for the magnetic core as shown in Figure 2.20(b). It has shown that the volume of the integrated EMI filter is reduced significantly by 45% when compared to the discrete EMI filter while satisfying the EMC standards.

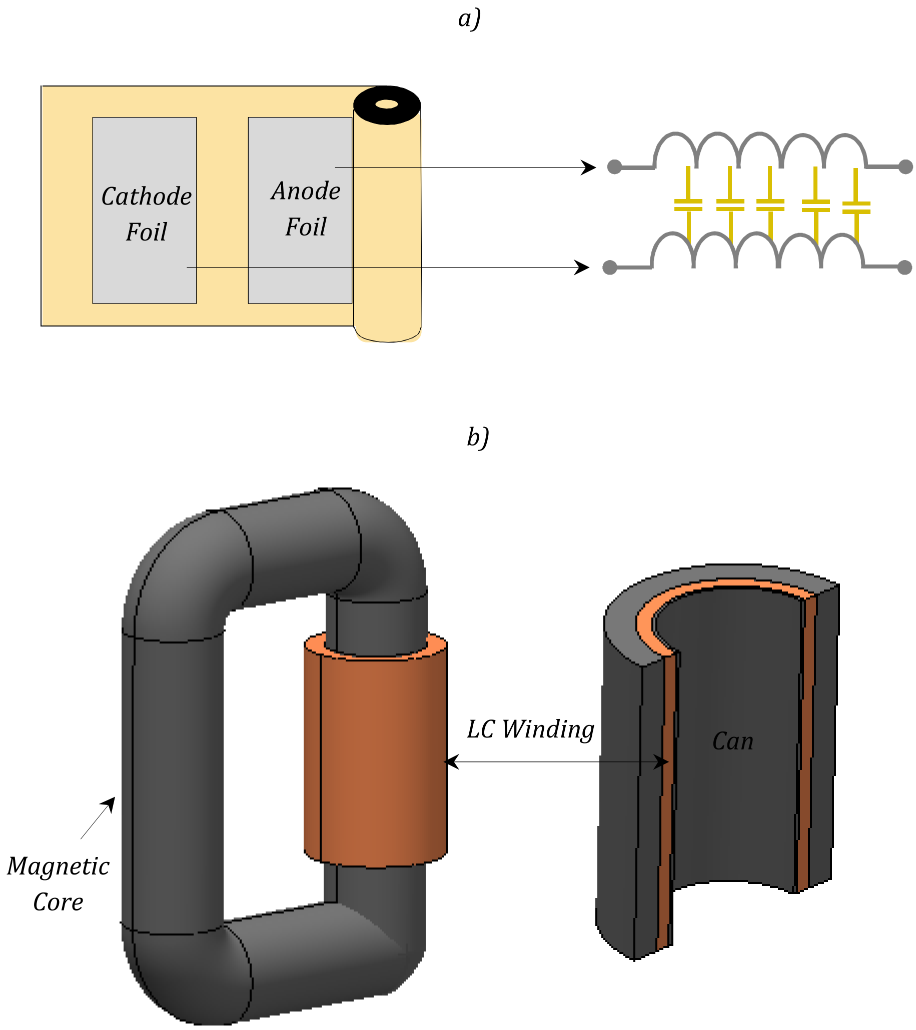

Figure 2.20: Integrated Planar LC Filter [75-81]

2.4 SUMMARY:

A comprehensive review of the passive filters used in the motor drives system is provided in this chapter. Classification of those passive filters such as gird side input filters, DC link filters, and output filters is provided along with a brief description of their functionality, design rules and design process. The layout of the passive filters from a physical point of view is also discussed. Finally, different options for passive filters integration documented in literature is presented.

2.5 REFERENCES:

[1] W. Gray and F. Haydock, "Industrial power quality considerations when installing adjustable speed drive systems," in *Cement Industry Technical Conference, 1995. XXXVII Conference Record., 1995 IEEE*, 1995, pp. 17-33.

[2] D. Kumar and F. Zare, "Harmonic Analysis of Grid Connected Power Electronic Systems in Low Voltage Distribution Networks," *IEEE Journal of Emerging and Selected Topics in Power Electronics,* vol. 4, pp. 70-79, 2016.

[3] P. Davari, Y. Yang, F. Zare, and F. Blaabjerg, "A Multipulse Pattern Modulation Scheme for Harmonic Mitigation in Three-Phase Multimotor Drives," *IEEE Journal of Emerging and Selected Topics in Power Electronics,* vol. 4, pp. 174-185, 2016.

[4] P. Davari, F. Zare, and F. Blaabjerg, "A smart current modulation scheme for harmonic reduction in three-phase motor drive applications," in *Power Electronics and Applications (EPE'15 ECCE-Europe), 2015 17th European Conference on*, 2015, pp. 1-10.

[5] P. Davari, Y. Yang, F. Zare, and F. Blaabjerg, "A novel harmonic elimination approach in three-phase multi-motor drives," in *2015 IEEE Energy Conversion Congress and Exposition (ECCE)*, 2015, pp. 7001-7008.

[6] P. Davari, F. Zare, and F. Blaabjerg, "Pulse Pattern-Modulated Strategy for Harmonic Current Components Reduction in Three-Phase AC–DC Converters," *IEEE Transactions on Industry Applications,* vol. 52, pp. 3182-3192, 2016.

[7] L. Huber and D. Borojevic, "Space vector modulated three-phase to three-phase matrix converter with input power factor correction," *IEEE Transactions on Industry Applications,* vol. 31, pp. 1234-1246, 1995.

[8] A. K. Sahoo, K. Basu, and N. Mohan, "Systematic Input Filter Design of Matrix Converter by Analytical Estimation of RMS Current Ripple," *IEEE Transactions on Industrial Electronics,* vol. 62, pp. 132-143, 2015.

[9] H. She, H. Lin, X. Wang, and L. Yue, "Damped input filter design of matrix converter," in *2009 International Conference on Power Electronics and Drive Systems (PEDS)*, 2009, pp. 672-677.

[10] M. A. Elsaharty, "Passive L and LCL filter design method for grid-connected inverters," in *2014 IEEE Innovative Smart Grid Technologies - Asia (ISGT ASIA)*, 2014, pp. 13-18.

[11] F. L. Paukner, E. G. Carati, R. Cardoso, C. M. O. Stein, and J. P. d. Costa, "Dynamic behavior of the PV Grid-connected inverter based on L and LCL filter with active damping control," in *2015 IEEE 13th Brazilian Power Electronics Conference and 1st Southern Power Electronics Conference (COBEP/SPEC)*, 2015, pp. 1-6.

[12] J. Scoltock, T. Geyer, and U. Madawala, "Model Predictive Direct Current Control for a grid-connected converter: LCL-filter versus L-filter," in *Industrial Technology (ICIT), 2013 IEEE International Conference on*, 2013, pp. 576-581.

[13] J. M. Sosa, G. Escobar, P. R. Mart, x00Ed, R. nez, guez, V. G, x00E, zquez, M. A. Ju, rez, and M. Diosdado, "Comparative evaluation of L and LCL filters in transformerless grid tied converters for active power injection," in *Power, Electronics and Computing (ROPEC), 2014 IEEE International Autumn Meeting on*, 2014, pp. 1-6.

[14] J. M. Sosa, G. Escobar, P. R. Mart, x00Ed, R. nez, guez, V. G, x00E, zquez, M. A. Ju, rez, A. A. Vald, F. z, ndez, and M. Diosdado, "Control law for transformerless converters connected to the grid through an L filter," in *Power, Electronics and Computing (ROPEC), 2014 IEEE International Autumn Meeting on*, 2014, pp. 1-6.

[15] K. M. Tsang and W. L. Chan, "Coupled inductor filter with frequency notching characteristics for grid interface," *IET Power Electronics,* vol. 7, pp. 1934-1943, 2014.

[16] R. Xie, X. Hao, X. Yang, L. Huang, C. Wang, and Y. Yang, "Stability analysis of single-phase grid-connected inverter with L-filter," in *2014 IEEE Energy Conversion Congress and Exposition (ECCE)*, 2014, pp. 5626-5630.

[17] W. Yao, Z. Lu, H. Long, and B. Li, "Research on grid-connected interleaved inverter with L filter," in *Future Energy Electronics Conference (IFEEC), 2013 1st International*, 2013, pp. 87-92.

[18] R. N. Beres, X. Wang, M. Liserre, F. Blaabjerg, and C. L. Bak, "A Review of Passive Power Filters for Three-Phase Grid-Connected Voltage-Source Converters," *IEEE Journal of Emerging and Selected Topics in Power Electronics,* vol. 4, pp. 54-69, 2016.

[19] Y. Jiao and F. C. Lee, "LCL Filter Design and Inductor Current Ripple Analysis for a Three-Level NPC Grid Interface Converter," *IEEE Transactions on Power Electronics,* vol. 30, pp. 4659-4668, 2015.

[20] A. Reznik, Marcelo, and G. Simões, "LCL Filter Design and Performance Analysis for Grid-Interconnected Systems," *IEEE Transactions on Industry Applications,* vol. 50, pp. 1225-1232, 2014.

[21] G. L. Calzo, A. Lidozzi, L. Solero, and F. Crescimbini, "LC Filter Design for On-Grid and Off-Grid Distributed Generating Units," *IEEE Transactions on Industry Applications,* vol. 51, pp. 1639-1650, 2015.

[22] S. Liu, B. Ge, Y. Liu, H. Abu-Rub, R. S. Balog, and H. Sun, "Modeling, Analysis, and Parameters Design of LC-Filter-Integrated Quasi-Z-Source Indirect Matrix Converter," *IEEE Transactions on Power Electronics,* vol. 31, pp. 7544-7555, 2016.

[23] T. Erika and D. G. Holmes, "Grid current regulation of a three-phase voltage source inverter with an LCL input filter," *IEEE Transactions on Power Electronics,* vol. 18, pp. 888-895, 2003.

[24] H. G. Jeong, K. B. Lee, S. Choi, and W. Choi, "Performance Improvement of LCL-Filter-Based Grid-Connected Inverters Using Power Transformation," *IEEE Transactions on Power Electronics,* vol. 25, pp. 1320-1330, 2010.

[25] M. Sanatkar-Chayjani and M. Monfared, "Design of LCL and LLCL filters for single-phase grid connected converters," *IET Power Electronics,* vol. 9, pp. 1971-1978, 2016.

[26] S. Sen, K. Yenduri, and P. Sensarma, "Step-by-step design and control of LCL filter based three phase grid-connected inverter," in *Industrial Technology (ICIT), 2014 IEEE International Conference on*, 2014, pp. 503-508.

[27] Y. Tang, W. Yao, P. C. Loh, and F. Blaabjerg, "Design of LCL Filter with LCL Resonance Frequencies Beyond the Nyquist Frequency for Grid-Connected Converters," *IEEE Journal of Emerging and Selected Topics in Power Electronics,* vol. 4, pp. 3-14, 2016.

[28] J. Xu, S. Xie, and T. Tang, "Improved control strategy with grid-voltage feedforward for LCL-filter-based inverter connected to weak grid," *IET Power Electronics,* vol. 7, pp. 2660-2671, 2014.

[29] M. Zabaleta, E. Burguete, D. Madariaga, I. Zubimendi, M. Zubiaga, and I. Larrazabal, "LCL Grid Filter Design of a Multimegawatt Medium-Voltage Converter for Offshore Wind Turbine Using SHEPWM Modulation," *IEEE Transactions on Power Electronics,* vol. 31, pp. 1993-2001, 2016.

[30] X. Zheng, L. Xiao, Y. Lei, and Z. Wang, "Optimisation of LCL filter based on closed-loop total harmonic distortion calculation model of the grid-connected inverter," *IET Power Electronics,* vol. 8, pp. 860-868, 2015.

[31] K. S. Rajashekara, V. Rajagopalan, A. Sevigny, and J. Vithayathil, "DC Link Filter Design Considerations in Three-Phase Voltage Source Inverter-Fed Induction Motor Drive System," *IEEE Transactions on Industry Applications,* vol. IA-23, pp. 673-680, 1987.

[32] P. A. Gath and M. Lucas, "Designing LC filters for AC-motor drives," in *Industry Applications Conference, 1995. Thirtieth IAS Annual Meeting, IAS '95., Conference Record of the 1995 IEEE*, 1995, pp. 1050-1052 vol.2.

[33] H. Ertl and J. W. Kolar, "A constant output current three-phase diode bridge rectifier employing a novel "Electronic Smoothing Inductor"," *IEEE Transactions on Industrial Electronics,* vol. 52, pp. 454-461, 2005.

[34] Y. V. Singh, P. O. Rasmussuen, and T. O. Andersen, "Performance improvement of three phase rectifier by employing electronic smoothing inductor," in *IECON 2014 - 40th Annual Conference of the IEEE Industrial Electronics Society*, 2014, pp. 1713-1719.

[35] C. Galea and L. Asiminoaei, "New topology of electronic smoothing inductor used in three phase electric drives," in *Electrical Power Quality and Utilisation (EPQU), 2011 11th International Conference on*, 2011, pp. 1-6.

[36] Y. V. Singh, P. O. Rasmussen, T. O. Andersen, and H. Shaker, "Modeling and control of three phase rectifier with electronic smoothing inductor," in *IECON 2011 - 37th Annual Conference on IEEE Industrial Electronics Society*, 2011, pp. 1450-1455.

[37] Y. V. Singh, P. O. Rasmussen, and T. O. Anderson, "Three-phase electric drive with modified electronic smoothing inductor," in *2010 IEEE Energy Conversion Congress and Exposition*, 2010, pp. 4199-4203.

[38] K. Mino, M. L. Heldwein, and J. W. Kolar, "Ultra compact three-phase rectifier with electronic smoothing inductor," in *Twentieth Annual IEEE Applied Power*

Electronics Conference and Exposition, 2005. APEC 2005., 2005, pp. 522-528 Vol. 1.

[39] Y. V. Singh, P. O. Rasmussuen, and T. O. Andersen, "Robust and reliable rectifier based on electronic inductor with improved performance," in *Power Electronics, Drives and Energy Systems (PEDES), 2014 IEEE International Conference on*, 2014, pp. 1-5.

[40] N. Hanigovszki, J. Landkildehus, and F. Blaabjerg, "Output filters for AC adjustable speed drives," in *APEC 07 - Twenty-Second Annual IEEE Applied Power Electronics Conference and Exposition*, 2007, pp. 236-242.

[41] K. Han-Jong, L. Geun-Ho, J. Cheol-Ho, and L. Jea-Pil, "Cost-effective design of an inverter output reactor in ASD applications," *IEEE Transactions on Industrial Electronics,* vol. 48, pp. 1128-1135, 2001.

[42] A. v. Jouanne and P. N. Enjeti, "Design considerations for an inverter output filter to mitigate the effects of long motor leads in ASD applications," *IEEE Transactions on Industry Applications,* vol. 33, pp. 1138-1145, 1997.

[43] A. v. Jouanne, D. A. Rendusara, P. N. Enjeti, and J. W. Gray, "Filtering techniques to minimize the effect of long motor leads on PWM inverter-fed AC motor drive systems," *IEEE Transactions on Industry Applications,* vol. 32, pp. 919-926, 1996.

[44] N. Hanigovszki, J. Landkildehus, G. Spiazzi, and F. Blaabjerg, "An EMC evaluation of the use of unshielded motor cables in AC adjustable speed drive applications," *IEEE Transactions on Power Electronics,* vol. 21, pp. 273-281, 2006.

[45] L. A. Saunders, G. L. Skibinski, S. T. Evon, and D. L. Kempkes, "Riding the reflected wave-IGBT drive technology demands new motor and cable considerations," in *Petroleum and Chemical Industry Conference, 1996, Record of Conference Papers. The Institute of Electrical and Electronics Engineers Incorporated Industry Applications Society 43rd Annual*, 1996, pp. 75-84.

[46] A. v. Jouanne, P. Enjeti, and W. Gray, "Application issues for PWM adjustable speed AC motor drives," *IEEE Industry Applications Magazine,* vol. 2, pp. 10-18, 1996.

[47] T. G. Habetler, R. Naik, and T. A. Nondahl, "Design and implementation of an inverter output LC filter used for dv/dt reduction," *IEEE Transactions on Power Electronics,* vol. 17, pp. 327-331, 2002.

[48] N. Hanigovszki, J. Poulsen, and F. Blaabjerg, "A novel output filter topology to reduce motor overvoltage," *IEEE Transactions on Industry Applications,* vol. 40, pp. 845-852, 2004.

[49] J. P. Strom, M. Koski, H. Muittari, and P. Silventoinen, "Analysis and filtering of common mode and shaft voltages in adjustable speed AC drives," in *Power Electronics and Applications, 2007 European Conference on*, 2007, pp. 1-10.

[50] J. Salomaki, "SENSORLESS CONTROL OF AC DRIVES EQUIPPED WITH AN INVERTER OUTPUT FILTER," PhD, Department of Electrical and Communications Engineering, Power Electronics Laboratory, Helsinki University of Technology, 2007.

[51] S. Wang, Y. Y. Maillet, F. Wang, D. Boroyevich, and R. Burgos, "Investigation of Hybrid EMI Filters for Common-Mode EMI Suppression in a Motor Drive System," *IEEE Transactions on Power Electronics,* vol. 25, pp. 1034-1045, 2010.

[52] R. M. Tallam, G. L. Skibinski, T. A. Shudarek, and R. A. Lukaszewski, "Integrated Differential-Mode and Common-Mode Filter to Mitigate the Effects of Long Motor Leads on AC Drives," *IEEE Transactions on Industry Applications,* vol. 47, pp. 2075-2083, 2011.

[53] M. C. D. Piazza, A. Ragusa, and G. Vitale, "Effects of Common-Mode Active Filtering in Induction Motor Drives for Electric Vehicles," *IEEE Transactions on Vehicular Technology,* vol. 59, pp. 2664-2673, 2010.

[54] M. H. Hedayati, A. B. Acharya, and V. John, "Common-Mode Filter Design for PWM Rectifier-Based Motor Drives," *IEEE Transactions on Power Electronics,* vol. 28, pp. 5364-5371, 2013.

[55] D. A. Rendusara and P. N. Enjeti, "An improved inverter output filter configuration reduces common and differential modes dv/dt at the motor terminals in PWM drive systems," *IEEE Transactions on Power Electronics,* vol. 13, pp. 1135-1143, 1998.

[56] D. Rendusara and P. Enjeti, "New inverter output filter configuration reduces common mode and differential mode dv/dt at the motor terminals in PWM drive systems," in *Power Electronics Specialists Conference, 1997. PESC '97 Record., 28th Annual IEEE*, 1997, pp. 1269-1275 vol.2.

[57] L. Palma and P. Enjeti, "An inverter output filter to mitigate dV/dt effects in PWM drive system," in *Applied Power Electronics Conference and Exposition, 2002. APEC 2002. Seventeenth Annual IEEE*, 2002, pp. 550-556 vol.1.

[58] K. Sung-Jun and S. Seung-Ki, "A novel filter design for suppression of high voltage gradient in voltage-fed PWM inverter," in *Applied Power Electronics Conference and Exposition, 1997. APEC '97 Conference Proceedings 1997., Twelfth Annual*, 1997, pp. 122-127 vol.1.

[59] N. Hanigovszki, "EMC output filters for adjustable speed drives," Ph.D, Aalborg University, Aalborg, Denmark, 2005.

[60] R. Picatoste, M. Butcher, and A. Masi, "Sine wave filter for stepper motor drives working with long cables," in *Electrical Machines (ICEM), 2012 XXth International Conference on*, 2012, pp. 1075-1081.

[61] J. K. Steinke, "Use of an LC filter to achieve a motor-friendly performance of the PWM voltage source inverter," *IEEE Transactions on Energy Conversion,* vol. 14, pp. 649-654, 1999.

[62] Y. Sozer, D. A. Torrey, and S. Reva, "New inverter output filter topology for PWM motor drives," *IEEE Transactions on Power Electronics,* vol. 15, pp. 1007-1017, 2000.

[63] P. T. Finlayson, "Output filters for PWM drives with induction motors," *IEEE Industry Applications Magazine,* vol. 4, pp. 46-52, 1998.

[64] Y. Murai, T. Kubota, and Y. Kawase, "Leakage current reduction for a high-frequency carrier inverter feeding an induction motor," *IEEE Transactions on Industry Applications,* vol. 28, pp. 858-863, 1992.

[65] H. Akagi, H. Hasegawa, and T. Doumoto, "Design and performance of a passive EMI filter for use with a voltage-source PWM inverter having sinusoidal output voltage and zero common-mode voltage," *IEEE Transactions on Power Electronics,* vol. 19, pp. 1069-1076, 2004.

[66] X. Chen, D. Xu, F. Liu, and J. Zhang, "A Novel Inverter-Output Passive Filter for Reducing Both Differential- and Common-Mode dv/dt at the Motor Terminals in PWM Drive Systems," *IEEE Transactions on Industrial Electronics,* vol. 54, pp. 419-426, 2007.

[67] S. D. Garvey, W. T. Norris, and M. T. Wright, "The role of integrated passive components in protecting motor windings," *IEE Proceedings - Electric Power Applications,* vol. 147, pp. 367-370, 2000.

[68] G. V. Robert Abebe, Giovanni Lo Calzo, Thmas Cox, Simon, Lambert, Mark Johnson, Chris Gerada, Barrie Mecrow, "Integrated motor drives: state of the art and future trends," *IET Electric Power Applications,* 2016.

[69] B. M. Nee and P. L. Chapman, "Integrated Filter Elements in Electric Drives," in *2007 IEEE Vehicle Power and Propulsion Conference*, 2007, pp. 148-153.

[70] Y. I. Nakajima, Tomoya Mizukoshi, Yukio Sato, Sho Zushi, Yusuke, "Integrated Capacitor Type Stator," United States Patent US 8,049,383 B2, 2000.

[71] M. R. Khowja, C. Gerada, G. Vakil, P. Wheeler, and C. Patel, "Novel Integrative Options for Passive Filter Inductor in High Speed AC Drives," in *Industrial Electronics Society, IECON 2015 - 42nd Annual Conference of the IEEE*, 2016.

[72] M. R. Khowja, C. Gerada, G. Vakil, P. Wheeler, and C. Patel, "Integrated Output Filter Inductor for Permanent Magnet Motor Drives," in *Industrial Electronics Society, IECON 2015 - 42nd Annual Conference of the IEEE*, 2016.

[73] M. A. Mohamed, S. M. Lambert, B. C. Mecrow, D. J. Atkinson, and A. C. Smith, "An electrical machine with integrated drive LCL filter components," in *8th IET International Conference on Power Electronics, Machines and Drives (PEMD 2016)*, 2016, pp. 1-6.

[74] Z. Vrankovic, L. Wei, C. Winterhalter, and B. Y. Hong, "The influence of the DC link inductor design on the rectifier voltage stress in an adjustable speed drive during a mains voltage surge," in *2009 IEEE Energy Conversion Congress and Exposition*, 2009, pp. 3653-3659.

[75] F. Luo, R. Robutel, S. Wang, F. Wang, and D. Boroyevich, "Integrated Input EMI Filter for a 2 kW DC-fed 3-phase Motor Drive," in *Applied Power Electronics Conference and Exposition, 2009. APEC 2009. Twenty-Fourth Annual IEEE*, 2009, pp. 325-329.

[76] C. Rengang, J. D. v. Wyk, S. Wang, and W. G. Odendaal, "Planar electromagnetic integration technologies for integrated EMI filters," in *Industry Applications Conference, 2003. 38th IAS Annual Meeting. Conference Record of the*, 2003, pp. 1582-1588 vol.3.

[77] C. Rengang, W. Shuo, J. D. v. Wyk, and W. G. Odendaal, "Integration of EMI filter for distributed power system (DPS) front-end converter," in *Power Electronics Specialist Conference, 2003. PESC '03. 2003 IEEE 34th Annual*, 2003, pp. 296-300 vol.1.

[78] L. Zhao, J. T. Strydom, and J. D. v. Wyk, "Wide band modeling of integrated power passive structures: the series resonator," in *Power Electronics Specialists Conference, 2002. pesc 02. 2002 IEEE 33rd Annual*, 2002, pp. 1283-1288 vol.3.

[79] Z. Lingyin, J. T. Strydom, and J. D. V. Wyk, "An alternative planar multi-cell structure integrated reactive module," in *Industry Applications Conference, 2001. Thirty-Sixth IAS Annual Meeting. Conference Record of the 2001 IEEE*, 2001, pp. 2217-2223 vol.4.

[80] C. Rengang, J. T. Strydom, and J. D. v. Wyk, "Design of planar integrated passive module for zero-voltage-switched asymmetrical half-bridge PWM converter," *IEEE Transactions on Industry Applications,* vol. 39, pp. 1648-1655, 2003.

[81] J. T. Strydom, J. D. v. Wyk, and J. A. Ferreira, "Some limits of integrated LCT modules for resonant converters at 1 MHz," in *Industry Applications Conference, 1999. Thirty-Fourth IAS Annual Meeting. Conference Record of the 1999 IEEE*, 1999, pp. 1411-1417 vol.2.

[82] J. Popovic-Gerber, M. Gerber, and B. Ferreira, "Integrated filter in electrolytic capacitor technology for implementation in high power density industrial drives," in *2008 IEEE Power Electronics Specialists Conference*, 2008, pp. 2968-2974.

[83] J. Popovic, J. A. Ferreira, M. B. Gerber, A. Konig, and R. d. Doncker, "Integration technologies for high power density power electronic converters for AC drives," in *International Symposium on Power Electronics, Electrical Drives, Automation and Motion, 2006. SPEEDAM 2006.*, 2006, pp. 634-639.

CHAPTER

3

PMSM WITH INTEGRATED FILTER INDUCTOR

3.1 INTRODUCTION

This chapter proposes a functional integration of passive filter inductor as an inverter RLC output filter for PMSM drives. The RLC output filter is the most common type of filter which is used to filter out the switching harmonics from the motor terminals thus reducing the PWM stress on the motor winding insulation. The proposed motor with integrated filter inductor minimises the need of external filter inductor in the traditional motor drive system, which is usually placed separately (or externally) between the inverter and the motor.

A brief introduction of the proposed motor with integrated filter inductor and its practical implementation is provided in this chapter. Along with this, the design procedure of external EE core filter inductor and integrated filter inductor is discussed. The vector controlled mathematical modelling of the proposed motor is also presented that takes into account switching and modulation effects. The $MATLAB/Simulink$ results based on vector controlled mathematical models in all operating modes, i.e. when motor is operating without output filter, with traditional output filter and with proposed output filter, are presented. Subsequently, the performance based on FEA for both motors with external and integrated filter inductor are presented. This is then followed by comparative analysis of the motor with and without integrated filter inductor in terms of mean electromagnetic torque, torque ripple, motor losses, filter inductor losses, and its weight and volume. At the end, optimization of the filter branch windings has been done to improve the performance of the integrated motor in terms of reducing total losses and output torque ripple.

3.2 PMSM WITH INTEGRATED FILTER INDUCTOR

Instead of introducing an external filter inductor, the integrated filter inductor utilizes the motor inherent magnetics as filter inductance. This filter inductor is usually located aside with the motor which introduces additional filter inductor losses and its associated weight and size added with the drive's system. Figure 3.1(a) and Figure 3.1(b) shows both traditional drives and proposed integrated drive respectively. It can be observed that the proposed motor with integrated filter inductor does not include an external inductor, thus eliminating added filter inductor losses and its weight and volume. Filter capacitor and damping resistor are connected between the motor windings to form a RLC output filter using the magnetics of the motor winding. The value of the filter inductance can be varied by varying the proportion of the motor windings once the filter capacitance is decided using the method detailed in chapter 2 and paper [1].

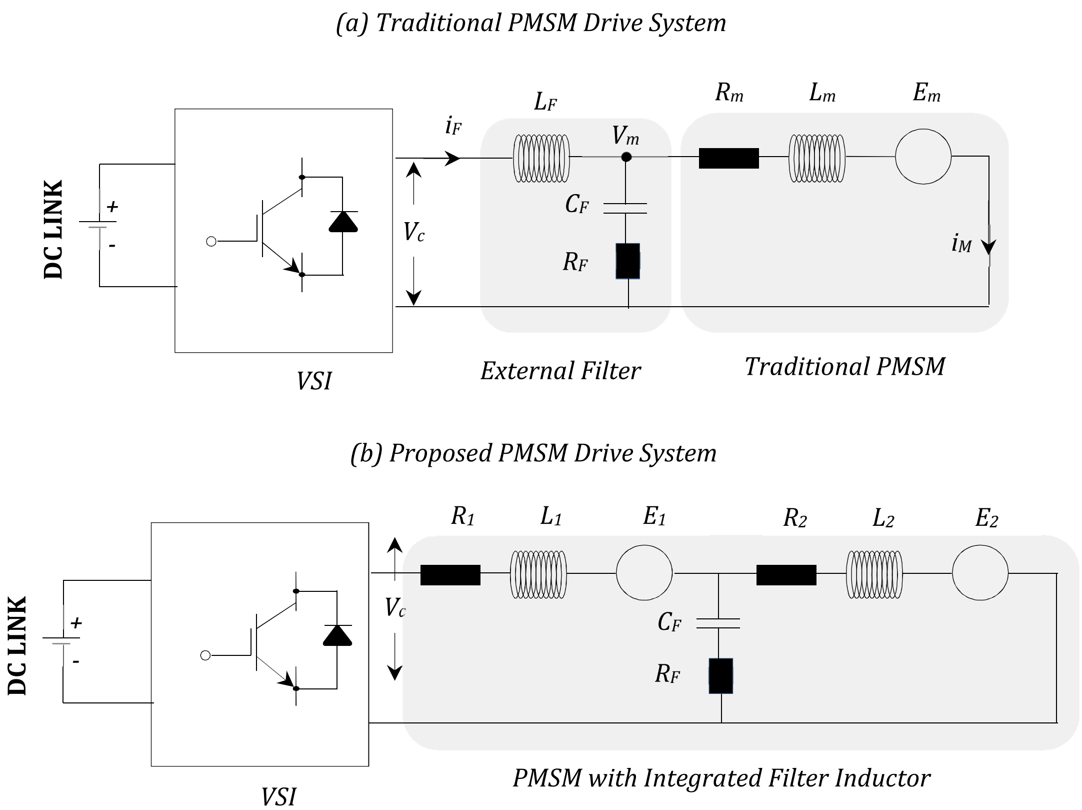

Figure 3.1: Traditional and Integrated PMSM Drives

3.2.1 Filter and Motor Branch

The proposed motor with integrated filter inductor is separated into two branches; filter branch and the motor branch as shown in Figure 3.2(a) and Figure 3.2(b). The windings in the motor branch will experience the filtered sinusoidal currents and voltages due to the filtering effect from the filter branch which behaves as a RLC output filter. On the other hand, the currents with PWM switching components will flow through the filter branch winding, which is the fraction of the entire motor windings.

a) Filter Branch

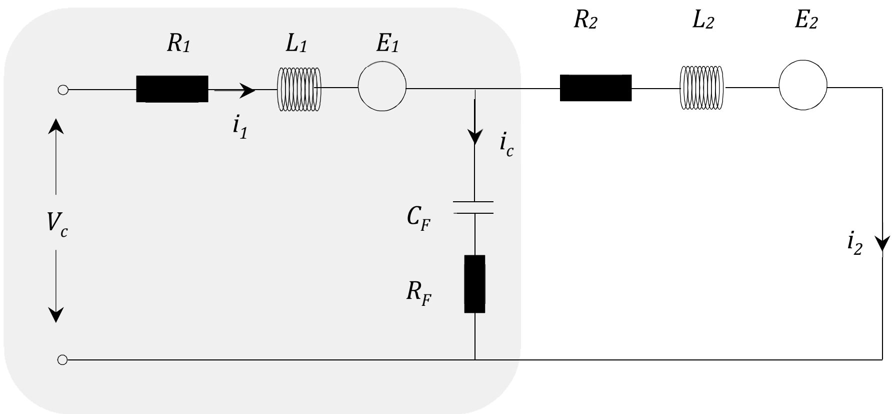

b) Motor Branch

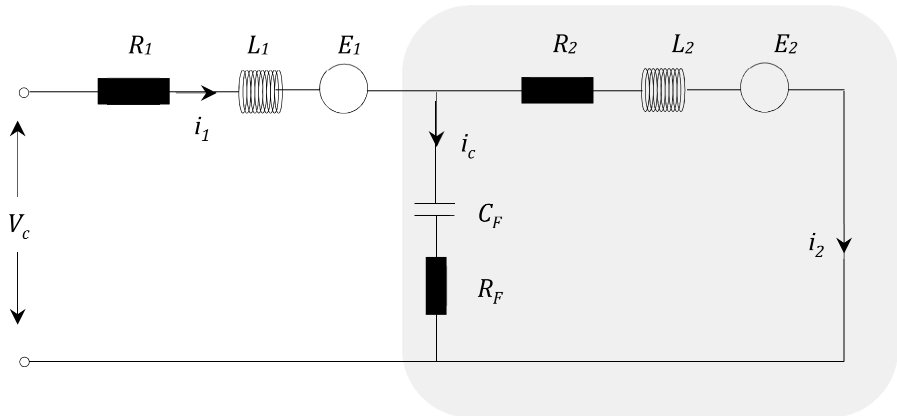

Figure 3.2: Filter and Motor Branch

3.2.2 *Practical Implementation of the Filter Branch*

The existing HEMAS motor was chosen to validate the concept of the motor with integrated filter inductor. The motor is single layer concentrated wound machine and was chosen to have a redundancy in the system which leads to two 3-phase units operating independendly. Each 3-phase unit is magnetically coupled and electrically isolated. Figure 3.3 shows the practical implementation of the filter branch. The filter branch uses a part of motor windings as a filter windings. This filter inductance forms a part of integrated RLC filter that attenuates the harmonic frequencies (switching frequency and its side bands) for a defined resonance frequency. In Figure 3.3, the vectors $A1$, $B1$ and $C1$ represent the filter branch, whereas the vectors $A2$, $B2$ and $C2$ correspond to the motor branch. The value of filter inductance is fixed by the filter design process which is half of the entire motor windings in this case. However, the filter branch winding can be less than half of the entire motor winding and this is decided based on the inductance required for the motor drive to attenuate the switching frequency component.

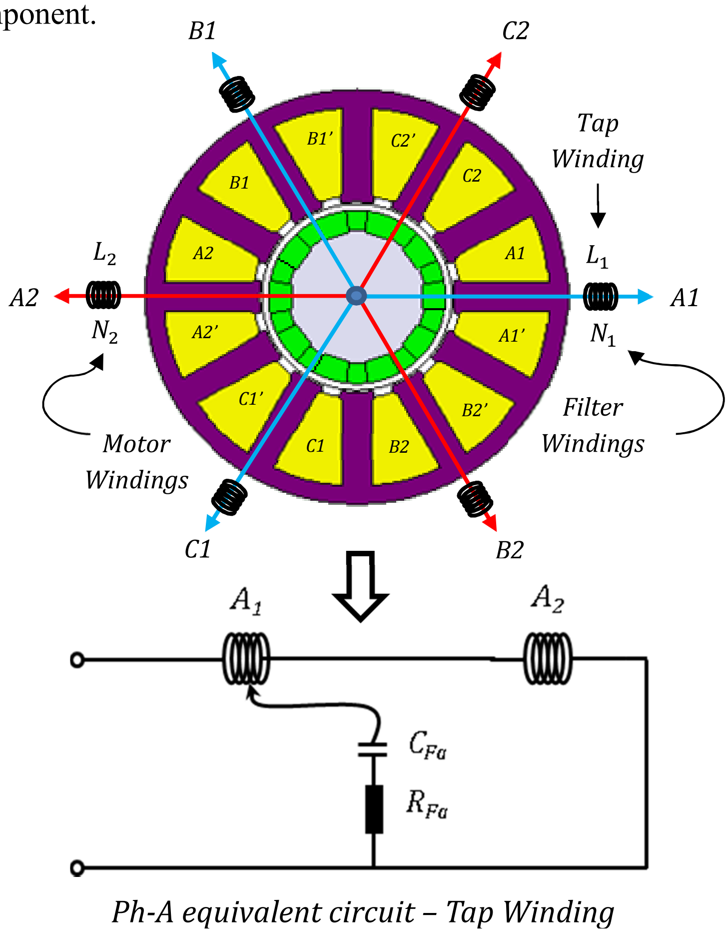

Figure 3.3: Practical Implementation of the Filter Branch and Motor Branch in PMSM

3.3 ANALYTICAL MODEL OF PMSM WITH INTEGRATED FILTER INDUCTOR

A detailed vector control model of the proposed motor with integrated filter inductor, taking into account modulation and device switching has been developed using $MATLAB/Simulink$ and is shown in Figure 3.5. 12 slots, 5 pole-pairs surface mounted permanent magnet motor is considered as shown in Figure 3.3. The motor drive specifications are shown in Table I.

Table I: Motor Drive Specifications

PARAMETERS	VALUES	UNITS
DC Bus Voltage	200	V
RMS Line Voltage	141.42	V
Fundamental Frequency	0.175	kHz
Switching Frequency	10	
Current Loop Frequency	1	
Motor Connections	STAR	-
No. of Turns per phase	2×46	-
Operating Torque	1.5	Nm
Maximum Torque	2×4	Nm
Operating Speed	2100	RPM
Phase Resistance	2×0.21	Ω
Phase Inductance	2×1.3	mH
Operating Peak Current	5.85	A
Maximum Peak Current	31	A
No-load Flux Linkage	2×0.017122	Wb.T
Motor Inertia	2×1.65	Kg.m^2

The motor has a base operating speed of 2100 RPM and mechanical load torque of 1.5Nm with the peak current of 5.85A. An RLC output filter is designed using the procedure as explained in [1] and chapter 2. The resonance frequency is fixed to 2 kHz, whereas the maximum frequency to avoid the resonance between the filter capacitance and motor inductance is 1.2 kHz [1]. Based on the chosen resonance frequency, the design of RLC output filter is given below:

- The RLC output filter is designed by specifying the resonance frequency of the filter, damping conditions and the resonance between the filter capacitance and the motor inherent inductance.
- Based on the method shown in section 2.2.2, the filter capacitance can be calculated as:

$$C_F \leq \frac{1}{(2\pi\, f_{max})^2 . L_m} \leq \frac{1}{(2\pi\, .\, 1200)^2 .\ 0.0026} \leq 6.77\ \mu F$$

- To avoid the reosance between filter capacitance and motor inductance is the filter capacitance is selected as 5 μF.
- Since the resonance frequency of the is chosen as 2000 Hz therefore, the filter inductance is estimated using the relation:

$$L_F = \frac{1}{(2\pi\, f_{res})^2 . L_m} = \frac{1}{(2\pi\, .\, 2000)^2 .\ 0.000005} = 1.27\ mH$$

- The damping resistance of 2Ω is chosen using trial and error method in the MATLAB simulation.

The bode plot of the RLC output filter is shown in Figure 3.4. The magnitude and phase response of the output filter is plotted against the frequency. As expected, the cut-off frequency is 2000 Hz at which the filter resonance occurs. Both magnitude and phase changes after the cut-off frequency thereby providing the attenuation to the motor voltage which resulted in surpass high frequency switching component into through RC branch instead of flowing through the motor branch.

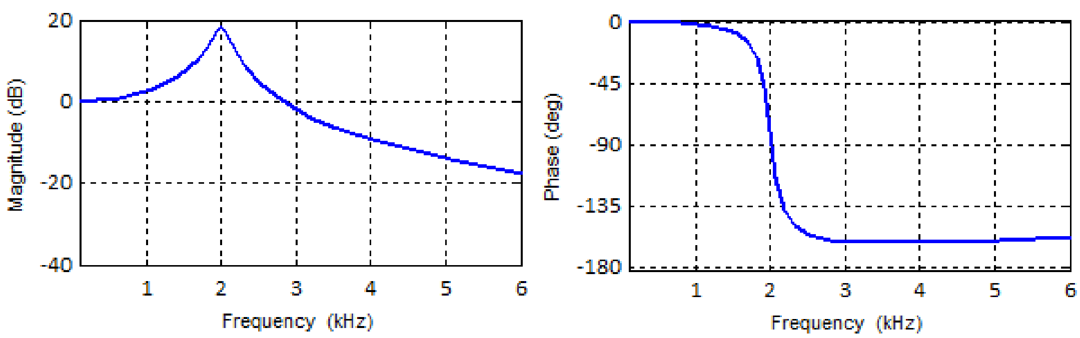

Figure 3.4: Bode Diagram of RLC output Filter

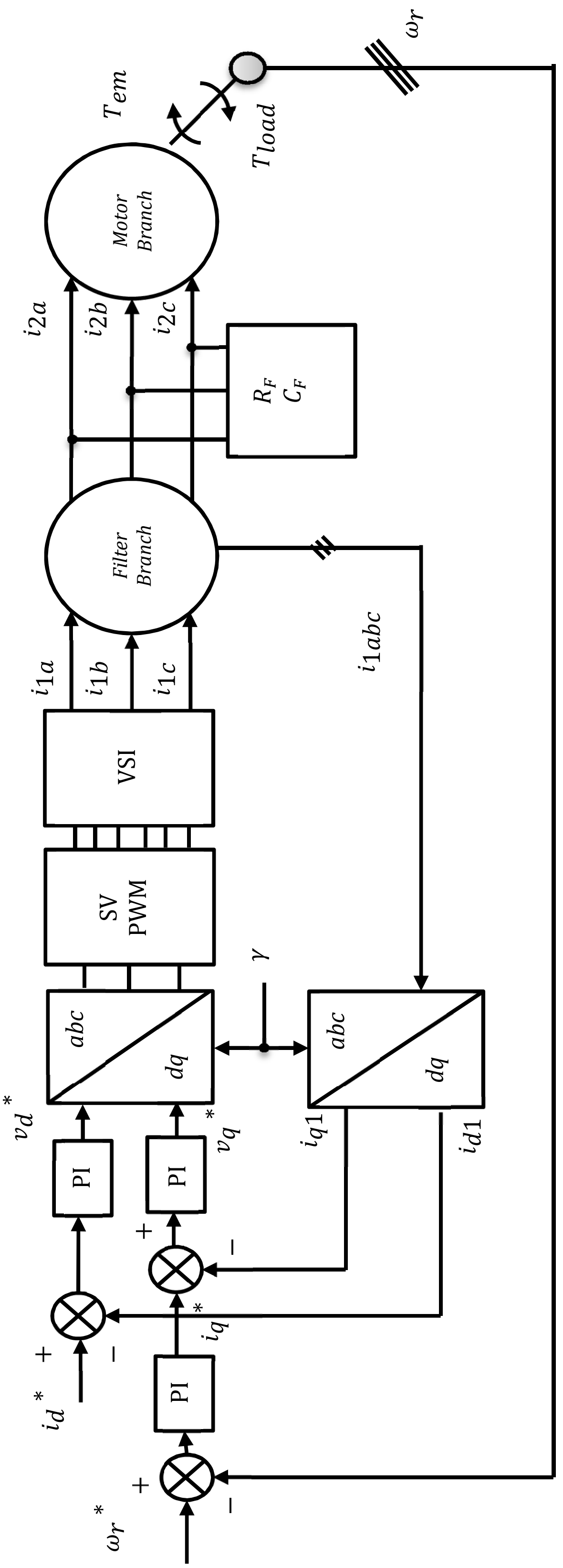

Figure 3.5: Block Diagram of Control System for the Motor with Integrated Inductor

3.3.1 Mathematical Model in a-b-c Reference Frame

The motor with integrated filter inductor is modelled in this section with the assupmtions of linear magnetic saturation, sinusoildal distribution of flux linakge, phase resistance and phase inductance without end winding effects taken into account. The mathematical model is based on the abc reference frame. The abc currents are transformed into $d-q$ reference frame for control purpose. As the number of turns in filter branch and motor branch are identical, i.e. 50% of the total number of turns, the filter branch currents are controlled to produce maximum torque of the filter branch. The motor branch can also be controlled to produce the maximum torque if the current sensors are placed in the motor branch. The filter capacitor and damping resistor are connected in between the filter and motor branch. It should be noted that, inserting filter capacitance and resistance between the filter branch and the motor branch will introduce a slight phase shift between two branch currents, i.e. i_{1abc} and i_{2abc}. The mathematical equations needed to model the proposed motor with integrated filter inductor can be obtained by using per phase equivalent circuit. The per-phase equivalent circuit of the proposed motor with integrated filter inductor is shown in Figure 3.6.

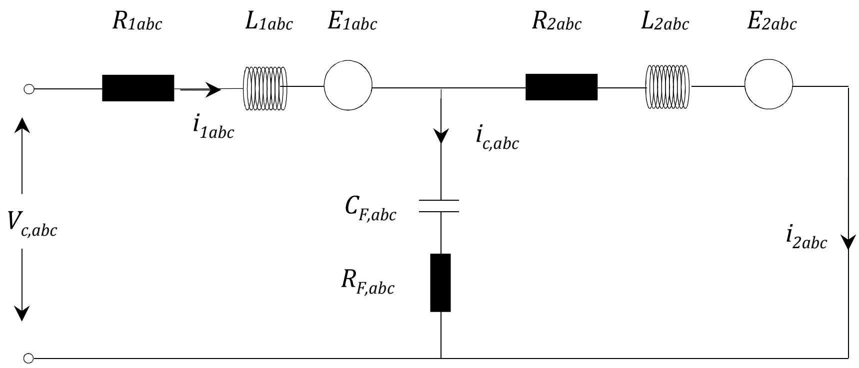

Figure 3.6: Equivalent Circuit of PMSM with Integrated Filter Inductor

By applying KVL on the filter branch, the filter branch voltage can be determined by,

$$V_{ca}(t) = R_1 i_{1a} + L_1 \frac{d}{dt} i_{1a} + \frac{d}{dt}\psi_1 \cos\theta_e$$

$$+ \frac{1}{C_F}\int (i_{1a} - i_{2a})dt + R_F\,(i_{1a} - i_{2a}) \tag{3.1}$$

Converting (3.1) into s-domain by applying Laplace transformation on both sides, the filter branch voltage can be given as,

$$V_{ca}(s) = R_1 i_{1a} + L_1 i_{1a} s - \omega_e \psi_1 \sin\theta_e + \frac{1}{C_F s}(i_{1a} - i_{2a}) + R_F(i_{1a} - i_{2a}) \qquad (3.2)$$

Solving for i_{1a},

$$i_{1a} = \frac{1}{sL_1}\left(V_{ca} + \omega_e \psi_1 \sin\theta_e - R_1 i_{1a} - R_F i_{1a} + R_f i_{2a} - \frac{1}{sC_F} i_{1a} + \frac{1}{sC_F} i_{2a}\right) \quad (3.3)$$

The current of phase b and c with 120^0 phase shifts are,

$$i_{1b} = \frac{1}{sL_1}\left(V_{cb} + \omega_e \psi_1 \sin\left(\theta_e + \frac{2\pi}{3}\right) - R_1 i_{1b} - R_F i_{1b} + R_F i_{2b} - \frac{1}{sC_F} i_{1b} + \frac{1}{sC_F} i_{2b}\right) \qquad (3.4)$$

$$i_{1c} = \frac{1}{sL_1}\left(V_{cc} + \omega_e \psi_1 \sin\left(\theta_e + \frac{2\pi}{3}\right) - R_1 i_{1c} - R_F i_{1c} + R_F i_{2c} - \frac{1}{sC_F} i_{1c} + \frac{1}{sC_F} i_{2c}\right) \qquad (3.5)$$

Similarly, the motor branch can be calculated as,

$$0 = R_2 i_{2a} + L_2 \frac{d}{dt} i_{2a} + \frac{d}{dt}\psi_2 \cos\theta_e + \frac{1}{C_F}\int (i_{2a} - i_{1a})dt + R_F\,(i_{2a} - i_{1a}) \qquad (3.6)$$

Converting (3.6) into s-domain by applying Laplace transformation on both sides, the motor branch current can be given as,

$$0 = R_2 i_{2a} + L_2 i_{2a} s - \omega_e \psi_2\, sin\,\theta_e + \frac{1}{C_F s}(i_{2a} - i_{1a}) + R_F(i_{2a} - i_{1a}) \qquad (3.7)$$

Solving for i_{2a},

$$i_{2a} = \frac{1}{sL_2}\left(0 + \omega_e \psi_2 \sin\theta_e - R_2 i_{2a} - R_F i_{2a} + R_F i_{1a} - \frac{1}{sC_F} i_{2a} + \frac{1}{sC_F} i_{1a}\right) \quad (3.8)$$

The current of phase b and c with 120^0 phase shifts are,

$$i_{2b} = \frac{1}{sL_2}\left(0 + \omega_e \psi_2 \sin\left(\theta_e + \frac{2\pi}{3}\right) - R_2 i_{2b} - R_F i_{2b} + R_F i_{1b} - \frac{1}{sC_F} i_{2b} + \frac{1}{sC_F} i_{1b}\right) \tag{3.9}$$

$$i_{2c} = \frac{1}{sL_2}\left(0 + \omega_e \psi_2 \sin\left(\theta_e + \frac{2\pi}{3}\right) - R_2 i_{2c} - R_F i_{2c} + R_F i_{1c} - \frac{1}{sC_F} i_{2c} + \frac{1}{sC_F} i_{1c}\right) \tag{3.10}$$

3.3.2 Per-Phase Phasor Representation

The per-phase equivalent circuit and the phasor diagram of the proposed motor with integrated filter inductor are shown in Figure 3.6 and Figure 3.7 respectively. The filter branch and motor branch voltage equations for steady state analysis can be given as,

$$\overline{V_1} = \overline{i_1}R_1 + \overline{i_1}X_{L1} + \overline{E_1} \tag{3.11}$$

$$\overline{V_2} = \overline{i_2}R_2 + \overline{i_2}X_{L2} + \overline{E_2} = \overline{i_c}R_f + \overline{i_c}X_c \tag{3.12}$$

Therefore, the voltage across inverter terminal can be determined by,

$$\overline{V_c} = \overline{V_1} + \overline{V_2} \tag{3.13}$$

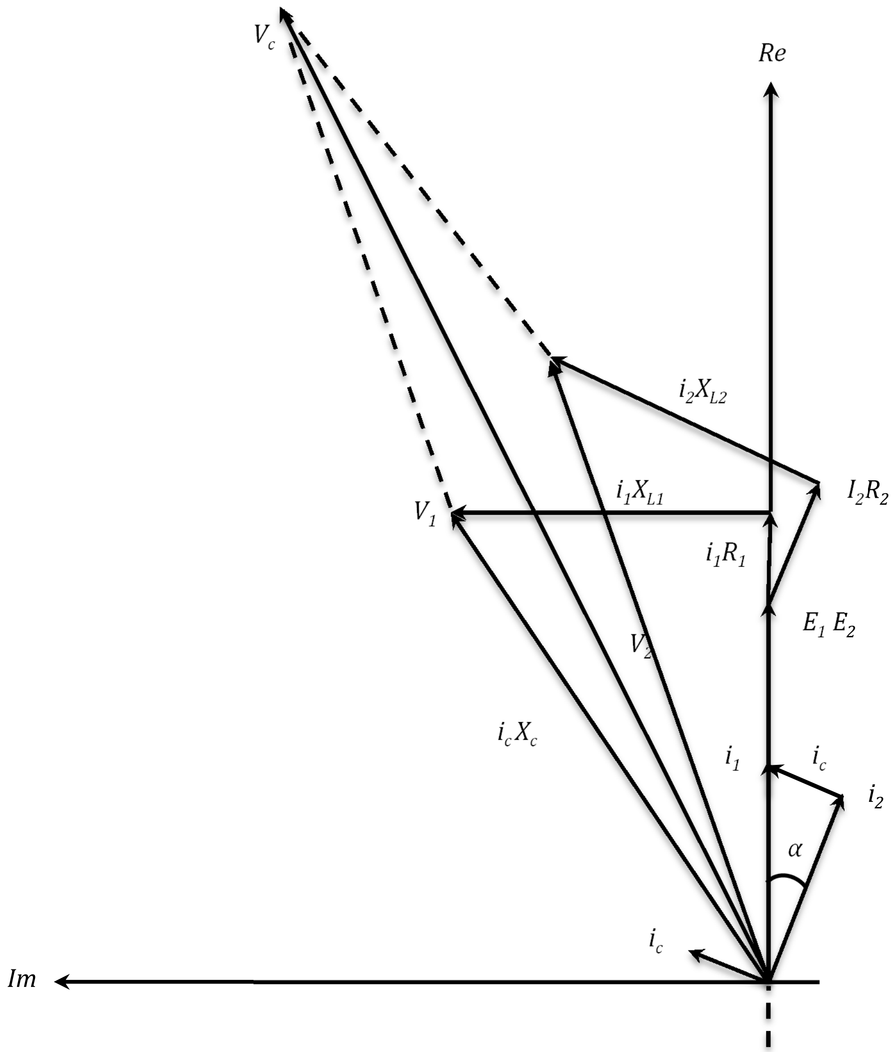

Figure 3.7: Per-phase Phasor of PMSM with Integrated Filter Inductor

The back-EMF of filter branch (E_1) and the back-EMF of motor branch (E_2) are taken as reference to realize the phasor representation of the motor with integrated filter inductor. Since the current through the filter branch (i_1) is controlled, the resistive voltage drop of the filter winding ($i_1 * R_1$) is in phase with filter branch back-EMF (E_1), whereas the reactive voltage drop of filter winding ($i_1 * X_1$) is displaced 90^0 with respect to the current in the filter winding (i_1). The inverter voltage (V_c) is the resultant phasor of filter and motor branch windings. Since the current in the motor branch winding (i_2) is left uncontrolled, the current through the filter branch winding (i_1) is leading the current through motor branch winding (i_2) due to the addition of filter capacitance and damping resistance. The active and reactive drop for the motor branch is in phase and orthogonal with respect to the current in the motor branch windings (i_2) respectively and the voltage across the motor branch (V_2) is the resultant phasor of all voltage drops in the motor branch. Capacitor current (i_c) is leading the voltage across motor branch (V_2) by less than 90^0 due to the damping resistance. The phasor summation of current through the capacitor (i_c) and motor winding (i_2) will form the filter branch current (i_1). Filter branch current (i_1) is phase shifted (leading) to motor branch current (i_2) by an angle (α). The phase shift angle (α) between the filter branch current and motor branch current can be defined as,

$$\alpha = cos^{-1}\left(\frac{i_1^2 + i_2^2 - i_c^2}{2\, i_1 i_2}\right) \tag{3.14}$$

3.3.3 Electromagnetic Torque Developed by the LCL PMSM

The electromagnetic torque developed by the conventional surface mounted permanent magnet motor can be calculated by cross product as,

$$T_{em} = \frac{pp}{2}\psi_{m,abc} \times i_{m,abc} \tag{3.15}$$

Where, $\psi_m$is the peak no-load flux linkage and i_a is the peak value of the fundamental motor current when integrated filter inductor is not considered, i.e. 100% motor branch and 0% filter branch. From the equivalent circuit of proposed motor, shown in Figure 3.6(a), equation (3.15) is not applicable to estimate the electromagnetic torque developed by the motor with integrated filter inductor. There are now two torque components developed by the motor with integrated filter inductor,

- Torque due to the filter branch windings, (T_{a1}) and,
- Torque due to the motor branch windings, (T_{a2})

Therefore, the electromagnetic torque developed by the motor with integrated filter inductor can be given as,

$$T_{em} = T_{a1} + T_{a2} \tag{3.16}$$

$$T_{em} = \frac{pp}{2}(\psi_{m1,abc} \times i_{1,abc}\cos(0) + \psi_{m2,abc} \times i_{2,abc}\cos\alpha) \tag{3.17}$$

The electromagnetic torque in terms of $d - q$ components can be derived as,

$$T_{em} = 3\frac{pp}{2}(\psi_{m1}i_{q1} + \psi_{m2}i_{q2}) \tag{3.18}$$

This electromagnetic torque (T_{em}) will cause the speed response that can be given by,

$$\omega_r = \frac{1}{Js}(T_{em} - T_{load}) \tag{3.19}$$

3.4 DESIGN OF FILTER INDUCTORS

3.4.1 *External Filter Inductor Design*

To size the inductor, a design process as stated in section 1.3 is used. The area product approach is the most commonly used design method to size the transformers and inductors. To drive the motor (as defined in Table I) with an RLC output filter, the inductor is sized up by specifying the required inductance, maximum flux density, RMS current, window fill factor, RMS current density and the type of the core material, where the details of which are given in Table II.

Based on the design specifications given in Table II, the area product can be estimated by,

$$A_{p,3ph} = W_a A_c = 1.5 \times 2\pi \frac{I_{rms}^2 . L_s \times 10^4}{K_w\, K_F\, B_{max}\, J_{rms}} = 27.1\ cm^4 \tag{3.20}$$

Table II: External Filter Inductor Specifications

PARAMETERS	VALUES	UNIT
Core Material	Non-oriented Silicon Steel M – 15	-
Required Inductance	1.3	mH
RMS Current	12.73	A
Maximum Flux Density	1.3	T
Window Fill Factor	0.5	-
Waveform Coefficient	$1/\sqrt{2}$	-
RMS Current Density	235.66	A/cm^2

The window to core area ratio (W_a/A_c) is assumed as 0.25 as suggested in [2] to have smallest ratio. Therefore, the window and core areas can be calculated as,

$$W_a = \sqrt{\frac{0.25 \times A_{p,3ph}}{1.5}} = 2.125\ cm^2 \tag{3.21}$$

$$A_c = \frac{W_a}{0.25} = \frac{2.125}{0.25} = 8.5\ cm^2 \tag{3.22}$$

The core stack to limb length ratio is assumed as 15.5. Thus, the limb and stack length can be calculated as,

$$L_{limb} = \sqrt{\frac{A_c}{15.5}} = 0.743\ cm \tag{3.23}$$

$$L_{stack} = 15.5 \times L_{limb} = 11.5\ cm \tag{3.24}$$

The window height to width is assumed to be 3 based on the 3-phase cores designs detailed in [2]. So, the window height and width can be calculated as,

$$F = \sqrt{\frac{W_a}{3}} = 1.19\ cm \tag{3.23}$$

$$G = 3 \times F = 3.57\ cm \tag{3.24}$$

The number of turns required to support the voltage across inductor based on the given inductance is,

$$N = \frac{V_{rms} \times 10^4}{K_F\ B_{max}\ f_s\ A_c} = 19.7 \approx 20\ T \tag{3.25}$$

The air gap length to get the required inductance is,

$$L_g = \frac{\left(4\pi \times 10^{-7}\right) N^2 A_c}{L_s} = 0.033\ cm \tag{3.26}$$

The fringing flux factor is calculated as 1.05 for the above inductor design using the method detailed in [2] and Appendix A. The fringing factor of 1.05 does not change the original inductor design and therefore neglected for this analysis.

$$FF = \left(1 + \frac{L_g}{\sqrt{A_{core}}} ln\left(\frac{2G}{L_g}\right)\right) = 1.05 \tag{3.27}$$

The EE cores with silicon steel magnetic material were chosen [3, 4] for the application of RLC output filter. The FE model was developed in $MagNet - Infolytica$ to validate the inductance and the degree of saturation in the core material. The $2D$ cross-section of the filter inductor is shown in Figure 3.8(a) and its flux distribution plot is shown in Figure 3.6(b). The flux density and inductance results are shown in Table III. It can be seen that the values obtained from FE simulation for inductance and maximum flux density in the limb closely match the specified ones in the design procedure.

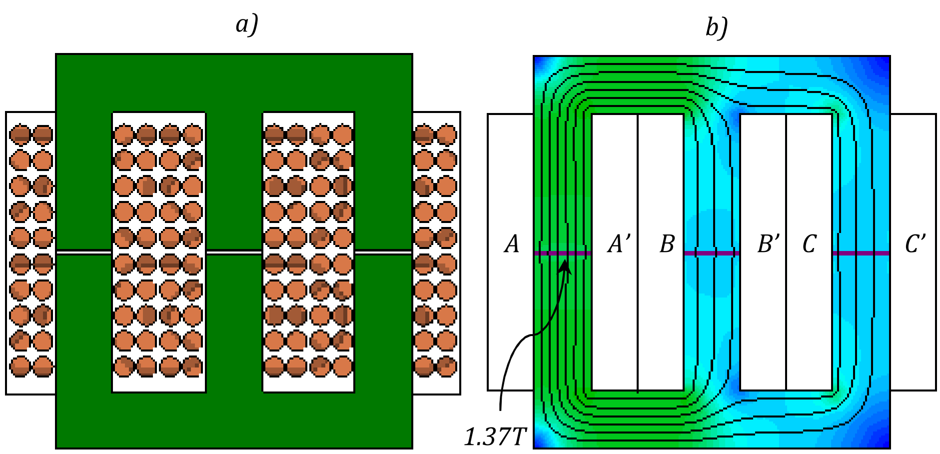

Figure 3.8: Cross-section and Flux Distribution of External EE Core Inductor

Table III: FE Validation of Inductance and Flux Density

PARAMETERS	FINITE ELEMENT	DESIGNED	UNITS
Synchronous Inductance	1.28	1.3	mH
Maximum Flux Density	1.35	1.4	T

3.4.2 *Integrated Filter Inductor Design*

The integrated filter inductor is implemented using the principle as explained in section 3.2. The practical implementation of the integrated filter is shown in Figure 3.9. Initially, the motor has a total inductance of 2.6mH and 92 turns per phase. The required inductance of 1.3mH is considered for filter branch leaving 1.3mH for the motor branch. The filter branch is not tapped since the required inductance is exactly half of the total inductance of the motor winding.

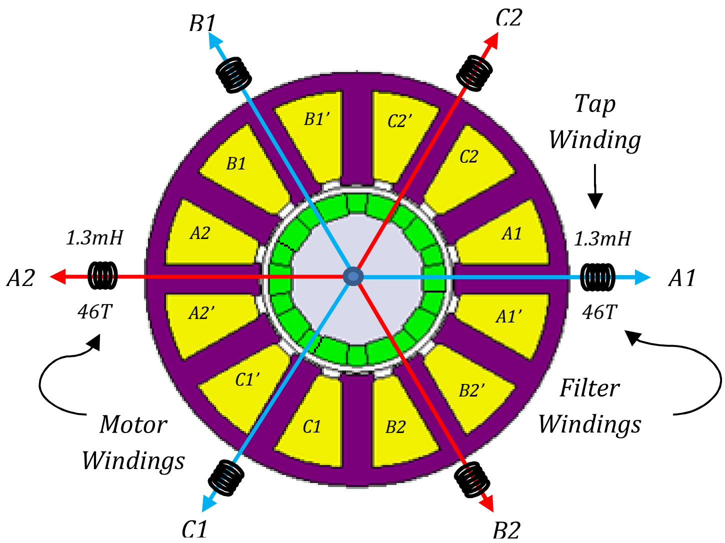

Figure 3.9: Practical Design of Integrated Filter Inductor

3.5 MATLAB & FEA SIMULATION RESULTS

This section presents the simulation results for the traditional motor and proposed motor with integrated filter inductor, which is driven by the voltage source inverter with switching and modulation effects taken into account. The space vector modulation strategy is considered for both traditional and proposed motors. The simulation tests have been conducted on "$MATLAB - Simulink$" R2012a version and its corresponding 3 phase motor currents are injected into finite element package "$MagNet - Infolytica$" to validate and compare the performance of the proposed motor with the traditional one. In both the cases, motors are operating at a speed of 2100 rpm and the mechanical loading of 1.5 Nm. The simulation results without output filter, with integrated and traditional filter are presented in the next sections.

3.5.1 Results for the Motor without Output Filter

3.5.1.1 Simulink Results

Simulink results are analyzed when the motor shown in Figure 3.9 is operating alone i.e. voltage source inverter drives the motor without output filter. Figure 3.10 and Figure 3.11 shows the motor terminal voltage and the currents through the motor windings respectively. The FFT of the motor terminal voltage and current is shown in Figure 3.12 and Figure 3.13 respectively. The first dominant switching component of motor voltage is at 20 kHz frequency, which is 80.03% of the fundamental component. The motor voltage THD is 186%. On the other hand, motor current also contains the first dominant switching component is at 20kHz, which is 2.05% of the fundamental component. The motor current THD is 3.28%.

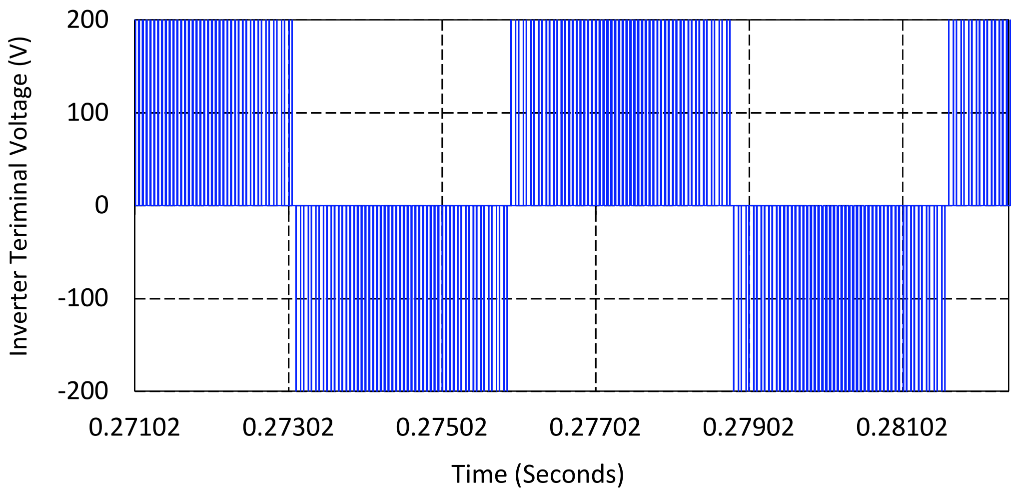

Figure 3.10: Line-to-line Motor Terminals Voltage without Filter (V_{AB})

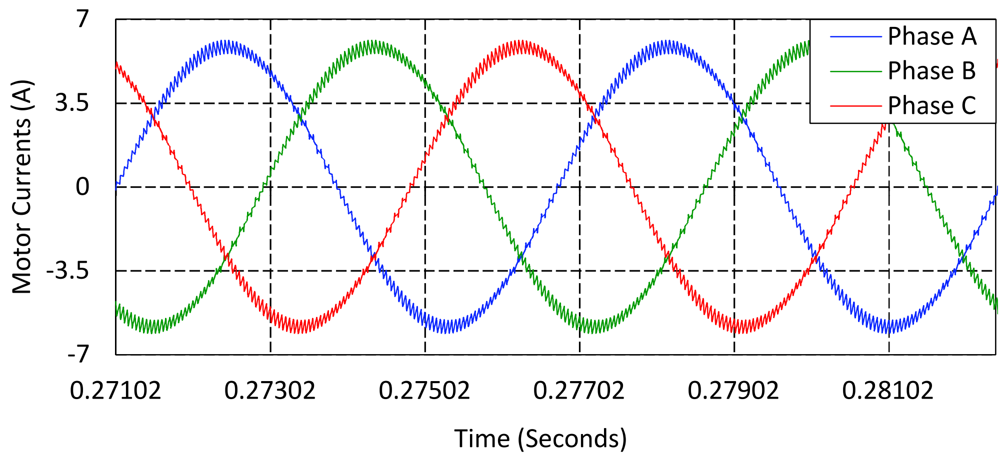

Figure 3.11: Motor Current without Filter

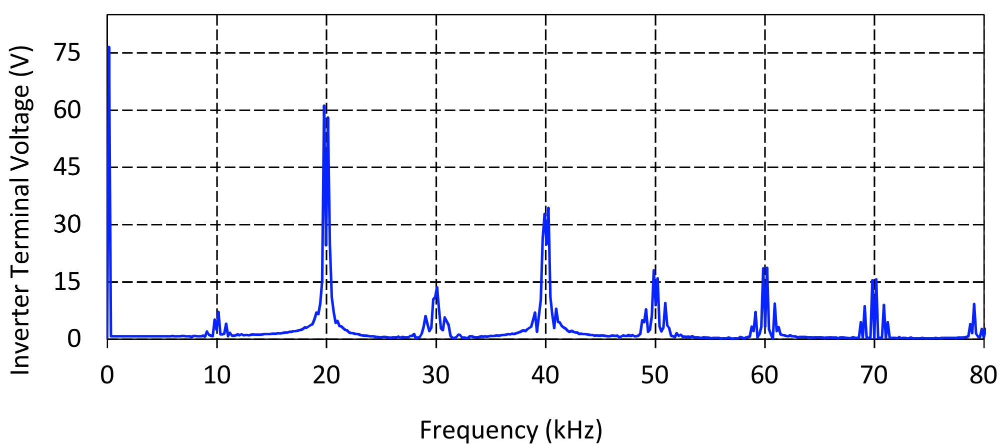

Figure 3.12: FFT of Motor Terminal Voltage without Filter

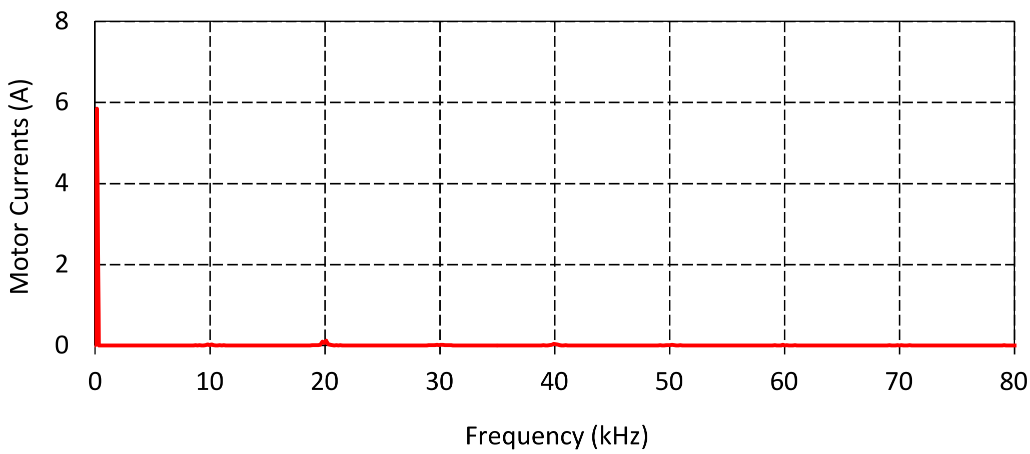

Figure 3.13: FFT of Motor Current without Filter

3.5.1.2 Finite Element Results

Result in Figure 3.14 shows the electromagnetic torque developed by 2the motor without output filter when the motor is driven by the currents illustrated in Figure 3.11. Table IV shows the torque ripple frequency, mean electromagnetic torque developed by the motor and the torque ripple under different loading conditions followed by total motor losses at rated torque of 1.5Nm.

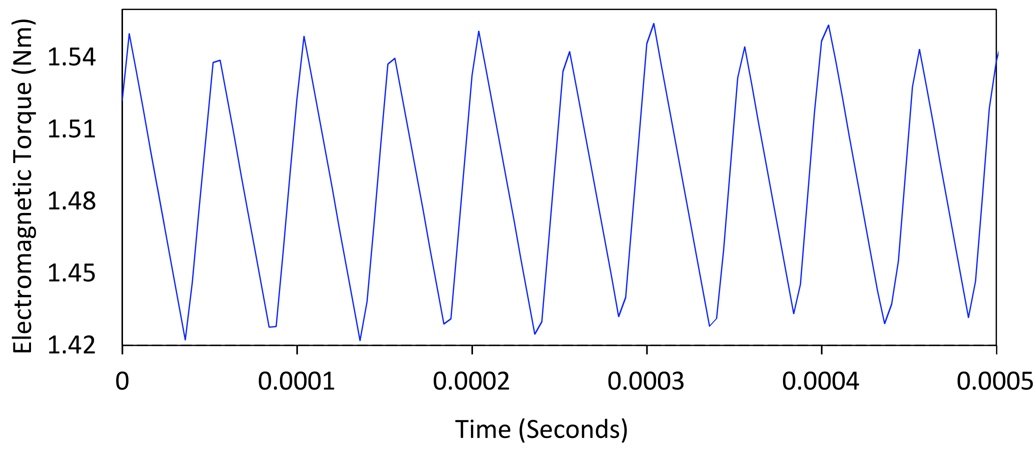

Figure 3.14: Electromagnetic Torque without Output Filter

Table IV: FEA Based Performance of the motor without Output Filter

PARAMETERS	VALUES	UNITS
Torque Ripple Frequency	20	kHz
Mean Torque at Loading of 1.5, 3 and 4.5Nm	1.49	Nm
	2.99	Nm
	4.49	Nm
Torque Ripple at T_{load} = 1.5Nm	9.55	%
Torque Ripple at T_{load} = 3.0Nm	5.35	%
Torque Ripple at T_{load} = 4.5Nm	4.25	%
Total Motor Losses (at 1.5Nm)	32	W

3.5.2 Results for the Motor with Integrated Filter Inductor

3.5.2.1 Simulink Results

Results in this section analyze the effectiveness and performance of the motor with integrated filter inductor in the steady state condition. Figure 3.15 and Figure 3.16

shows the line voltage across the inverter terminals ($V_{c,abc}$) and the line voltage across the motor branch winding ($V_{2,abc}$) respectively, whereas the current through the filter branch ($i_{1,abc}$) and the motor branch current ($i_{2,abc}$) are shown in Figure 3.17 and Figure 3.18 respectively.

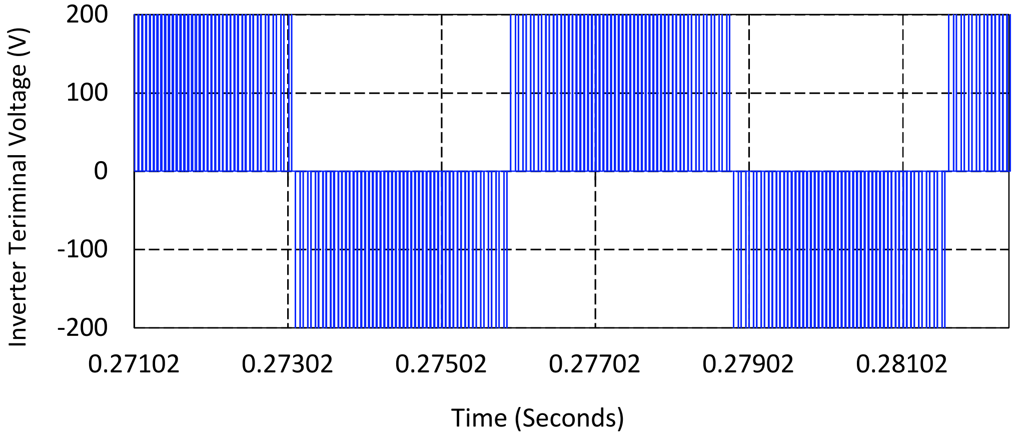

Figure 3.15: Line-to-line Inverter Terminals Voltage with Integrated Filter (V_{AB}) (i.e. line-to-line voltage across the filter branch)

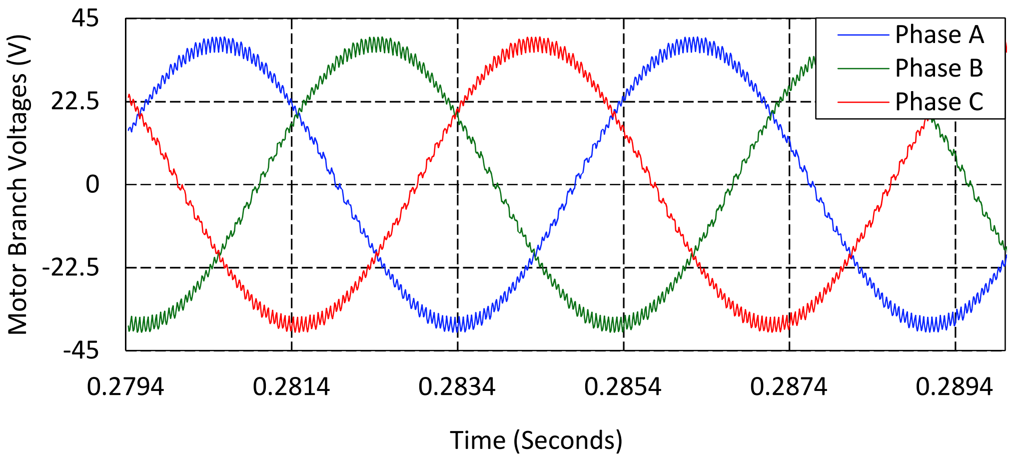

Figure 3.16: Line-to-line Motor Branch Voltage with Integrated Filter

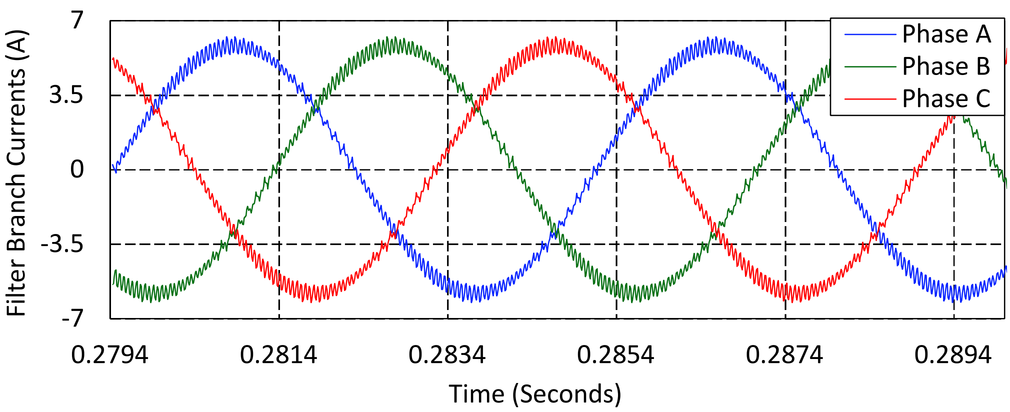

Figure 3.17: Filter Branch Currents with Integrated Filter

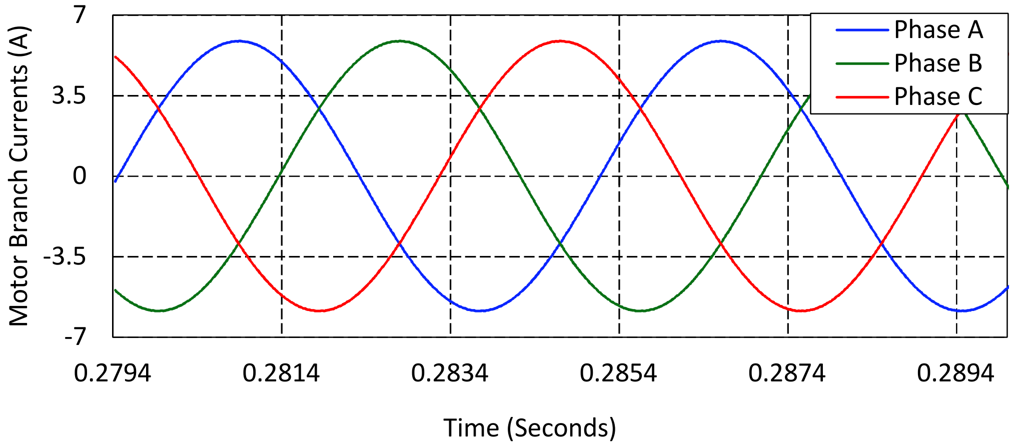

Figure 3.18: Motor Branch Currents with Integrated Filter

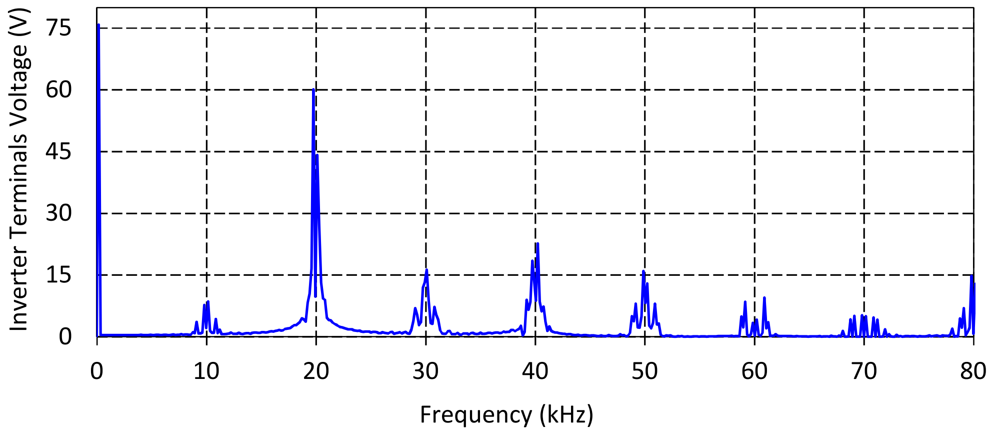

Figure 3.19: FFT of Inverter Terminal Voltage with Integrated Filter

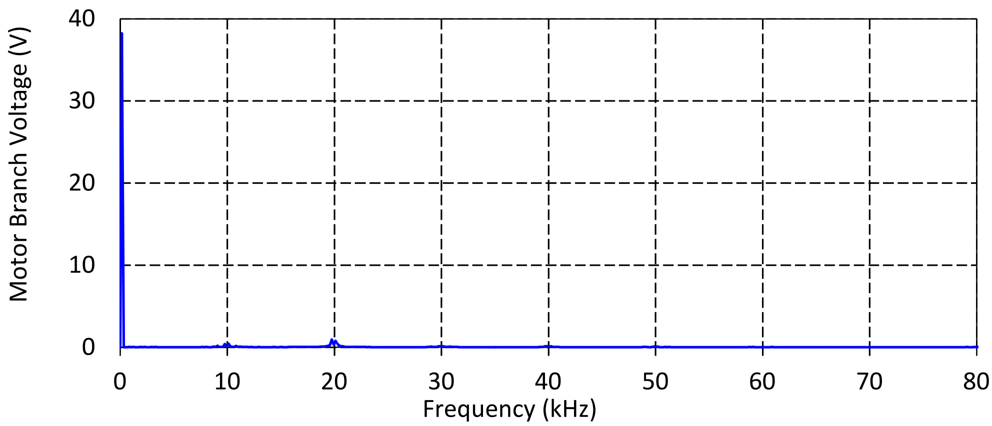

Figure 3.20: FFT of Motor Branch Voltage with Integrated Filter

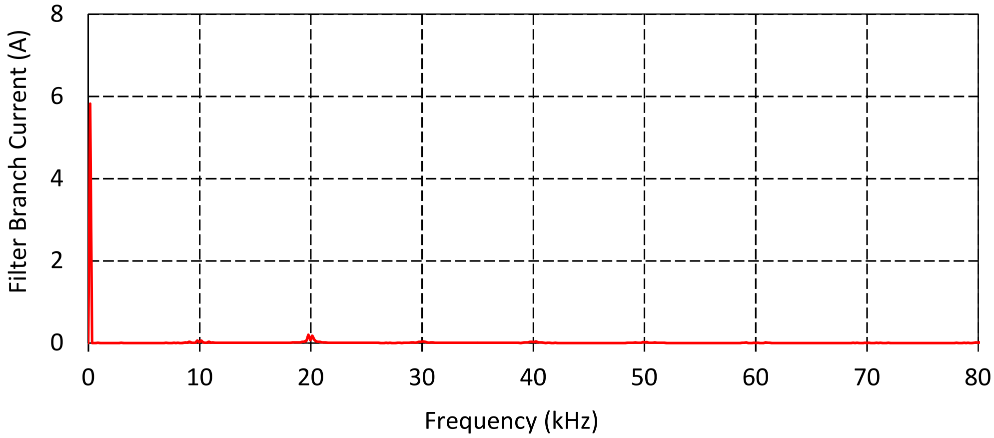

Figure 3.21: FFT of Filter Branch Current with Integrated Filter

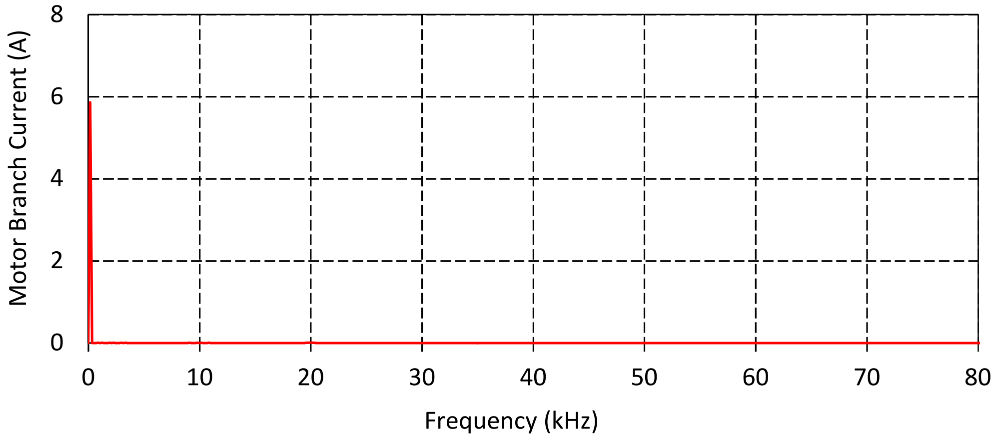

Figure 3.22: FFT of Motor Branch Current with Integrated Filter

From the simulation results, it can be observed that the half part of the motor windings experiences the filtered sine-wave voltages. This reduces the insulation stress from half of the motor windings and the power losses associated with the PWM switching components. Furthermore, the added losses, weight and size due to external filter inductor will also be eliminated. The FFT of the inverter terminals voltage (V_c) and the voltage across motor branch (V_2) are shown in Figure 3.19 and Figure 3.20 respectively, whereas FFT of the filter branch current (i_1) and motor branch current (i_2) are shown in Figure 3.21 and Figure 3.22 respectively. In comparison to the motor operating without filter, the switching component of motor branch voltage is reduced by 98.4% with it's THD reduced to 4.3%. On the other hand, the switching component of motor branch current is reduced by 97.1% with it's THD reduced to 0.25%.

It is important to note that the voltage with high dv/dt is appeared across the filter branch windings. The insulation of the filter branch can be made high to tolerate the high dv/dt voltage. This will allow the motor with integrated filter inductor feasible for the applications where long cables are used between inverter and motor terminals.

To get maximum benefit out of the proposed motor with integrated filter inductor, the filter branch windings has to be a quarter or less of the entire motor winding so that a higher portion of the motor branch windings experience the filtered voltages and currents. This will depend on the design of a RLC output filter i.e. inductance and capacitance required to attenuate the switching component of the inverter. However, the reduction in filter inductance will increase the required capacitance for a given resonance frequency, according to the equation (2.14).

3.5.2.2 Finite Element Results

Results in this section validate the effectiveness of the filter inductor which is integrated into the motor. This can done by injecting the filter branch current obtained from $MATLAB - Simulink$ into the FE model of the motor. The motor branch currents from FE model of the the motor are shown in Figure 3.23. It can be seen that the FE currents of the motor branch are identical to that of $MATLAB - Simulink$ model.

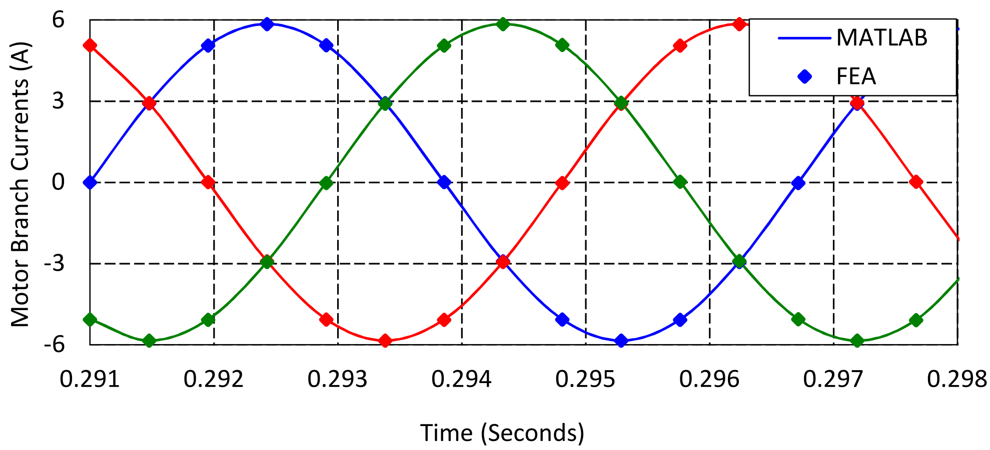

Figure 3.23: MATLAB & FEA Motor Branch Currents

The motor performance in terms of mean electromagnetic torque, current angle (α) percentage torque ripple and total motor losses has been examined. Table V illustrate the performance of the motor with integrated filter inductor. It is worth noting that the effect on the mean torque of the motor is negligible due to lower current angle (α) which is about 1^0. Therefore, only 0.67% of the total mean torque is affected.

The variation in electromagnetic torque developed by the motor can be observed in Figure 3.23. The torque ripple remains the same when compared with the motor operating without output filter (Figure 3.14). This is because the filter branch winding was fixed half of the entire motor windings which in turn doubled the magnitude of switching component as shown in Figure 3.21. This will increase the torque ripple by twice in the filter branch but at the same time, eliminates the torque ripple in the motor branch. Similarly, the total losses dissipation inside the motor are observed very close to the case when the motor is operating without output filter.

Table V: FEA Based Performance of the motor with Integrated Filter Inductor

PARAMETERS	VALUES	UNITS
Torque Ripple Frequency	20	kHz
Mean Torque at loading of 1.5, 3, and 4.5Nm	1.485	Nm
	2.985	Nm
	4.485	Nm
Current Angle (α)	1.02	deg
Torque Ripple at T_{load} = 1.5Nm	9.54	%
Torque Ripple at T_{load} = 3.0Nm	5.33	%
Torque Ripple at T_{load} = 4.5Nm	4.2	%
Total Motor Losses (at 1.5Nm)	36	W

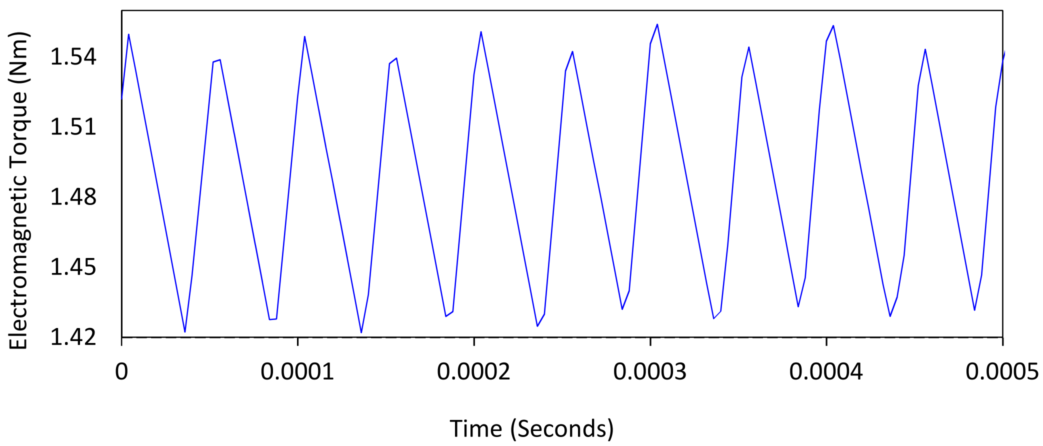

Figure 3.23: Electrometric Torque with Integrated Filter when T_{load} = 1.5Nm

3.5.3 Results for the Motor with External Filter Inductor

3.5.3.1 Simulink Results

The $MATLAB - Simulink$ results of the motor with traditional output filter as shown in Figure 3.1(a) are presented. Figure 3.25 and Figure 3.26 shows the line voltage across the inverter terminals ($V_{c,abc}$) and the line voltage across the motor terminals ($V_{m,abc}$) respectively, whereas the currents ($i_{F,abc}$) through the external filter inductor and motor ($i_{m,abc}$) are illustrated in Figure 3.27 and Figure 3.28.

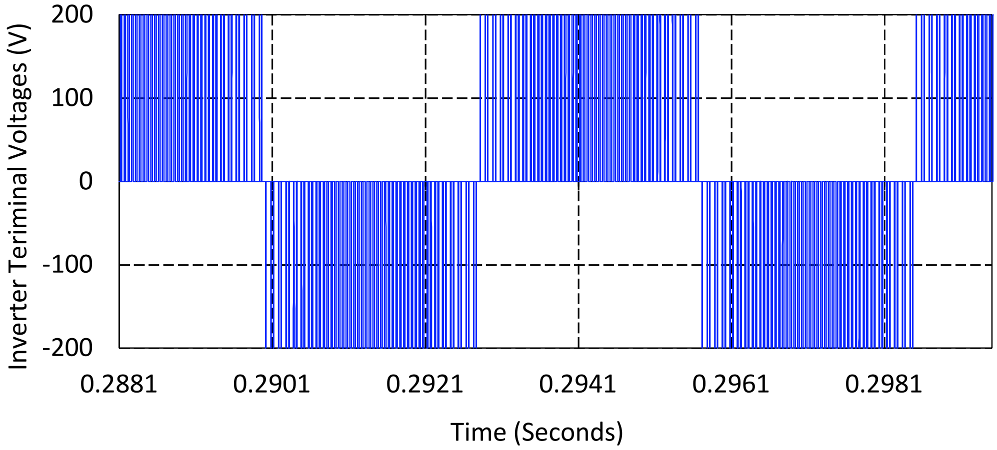

Figure 3.25: Inverter Terminals Voltage with External Filter Inductor (V_{AB})

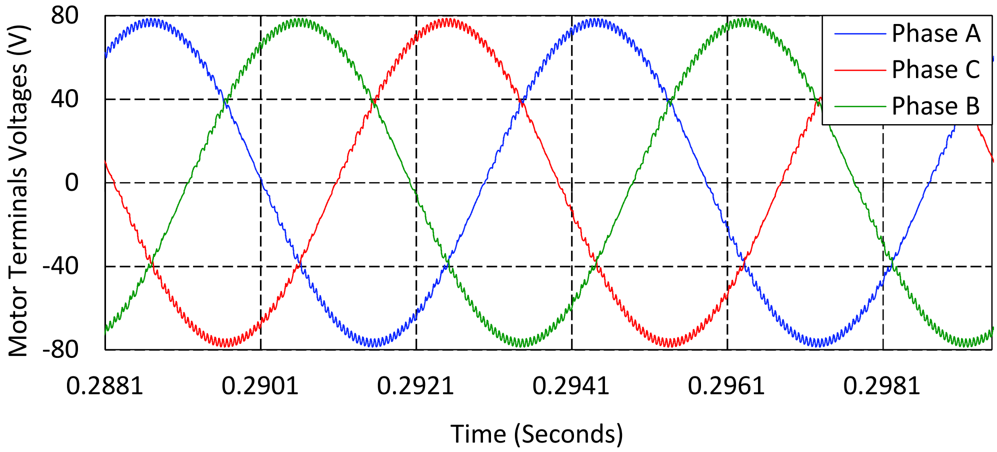

Figure 3.26: Motor Terminals Voltage with External Filter Inductor

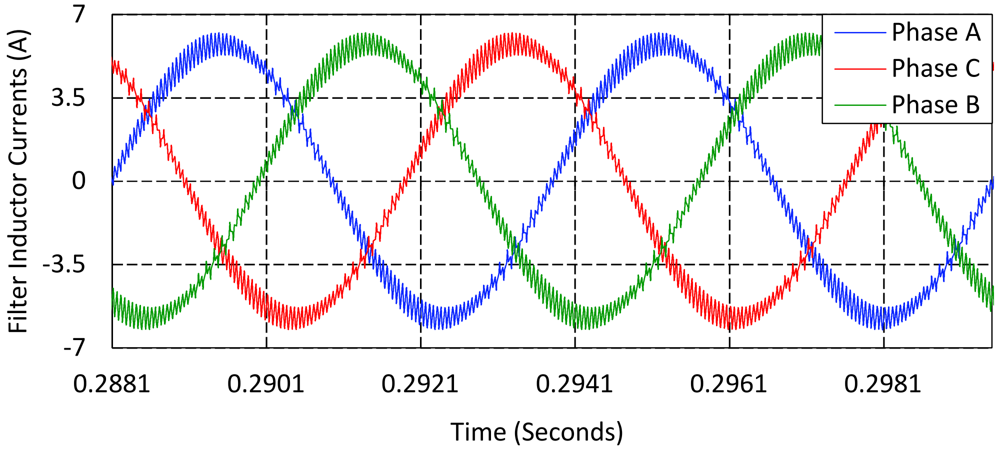

Figure 3.27: Filter Inductor Currents with External Filter Inductor

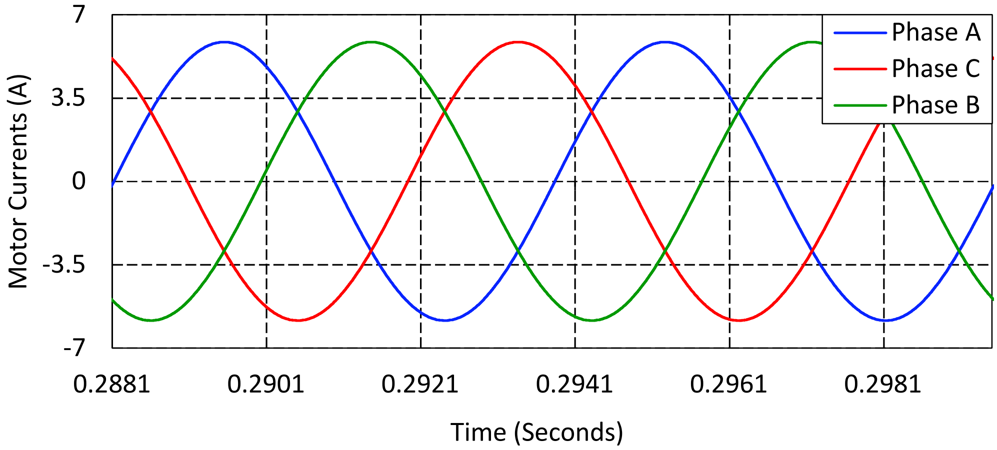

Figure 3.28: Motor Currents with External Filter Inductor

The FFT of the inverter terminals voltage (V_c) and the voltage across motor terminals (V_m) are shown in Figure 3.29 and Figure 3.30 respectively, whereas FFT of the external filter inductor current (i_F) and motor current (i_m) are shown in Figure 3.31 and Figure 3.32 respectively. In comparison with the motor operating without output filter, the switching component of motor terminals voltage is reduced by 98.4% with its THD reduced to 2.22%. On the other hand, the switching component of motor current is reduced by 98.4% with it's THD reduced to 0.1%.

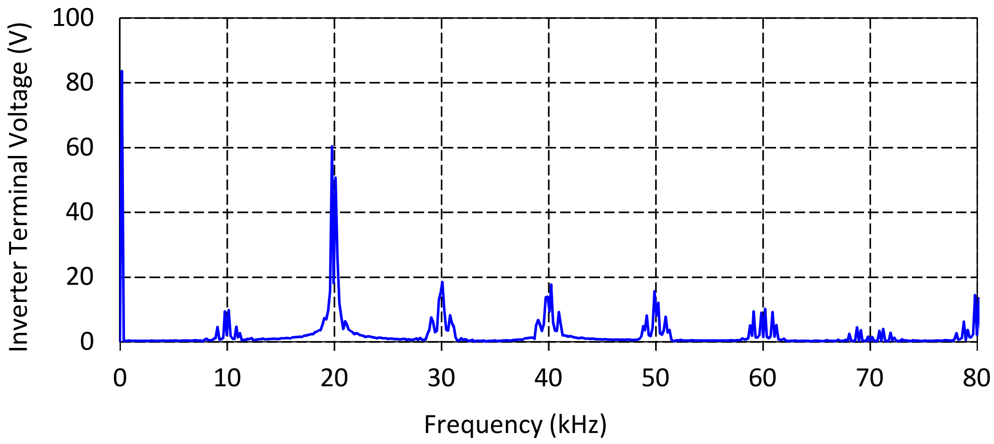

Figure 3.29: FFT of Inverter Terminals Voltage with External Filter Inductor

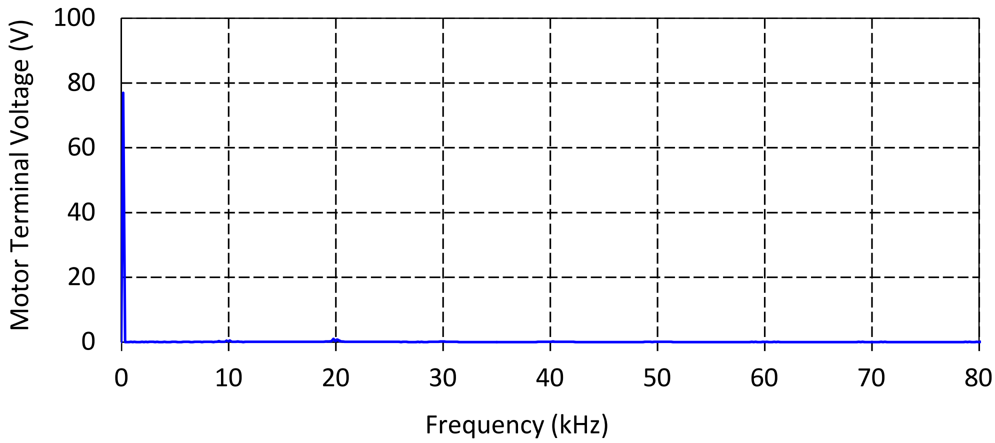

Figure 3.30: FFT of Motor Terminals Voltage with External Filter Inductor

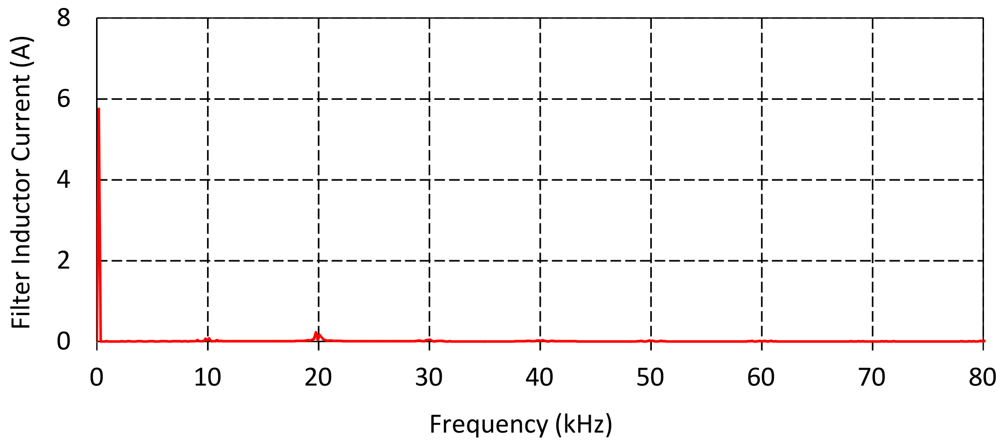

Figure 3.31: FFT of Inverter External filter Inductor Current

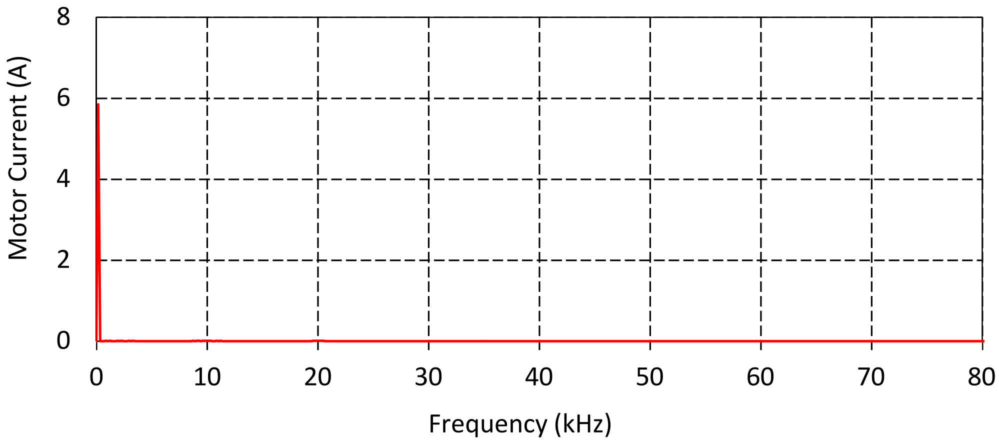

Figure 3.32: FFT of Motor Current with External Filter Inductor

3.5.3.1 Finite Element Results

The simulation results for motor currents as illustrated in Figure 3.28 obtained from $MATLAB - Simulink$ are injected into the FE model of motor (Figure 3.9) in order to evaluate the performance in terms of mean electromagnetic torque, torque ripple and total losses. Similarly, the currents shown in Figure 3.27 are injected into the FE model of external filter inductor (Figure 3.8) to evaluate its performance in terms of total losses and its associated weight and volume.

Table VI: FEA Based Performance of the Motor with External Filter Inductor

PARAMETERS	VALUES	UNITS
Torque Ripple Frequency	Only low order	-
Mean Torque at 1.5, 3 and 4.5 Nm Loading	1.49	Nm
	3.99	Nm
	4.49	Nm
Torque Ripple at T_{load} = 1.5Nm	0.7	%
Torque Ripple at T_{load} = 3.0Nm	0.58	%
Torque Ripple at T_{load} = 4.5Nm	0.54	%
Total Motor Losses (at 1.5Nm)	26.1	W
External Inductor Losses	40.67	W
External Inductor Weight	1.52	Kg
External Inductor Volume	338.7	cm^3

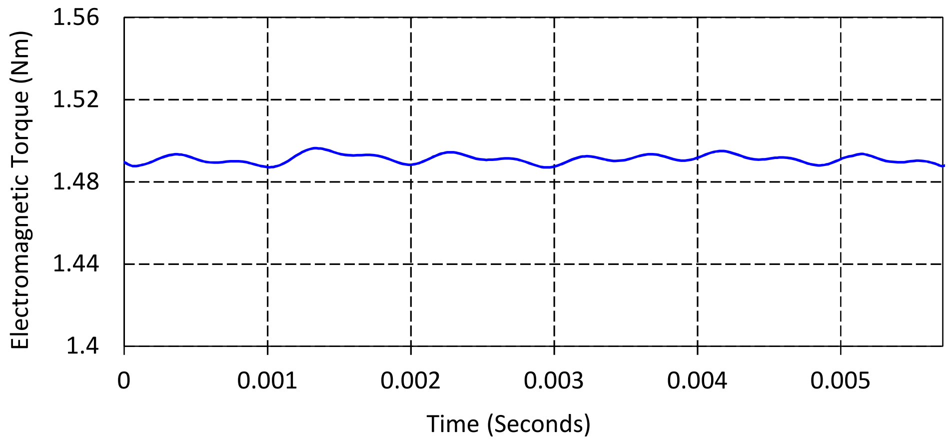

Figure 3.33: Electromagnetic Torque with External Filter Inductor

Table VI shows the performance of the motor with external filter inductor whereas the variation of electromagnetic torque developed by the motor when fed through external filter inductor is shown in Figure 3.33. From Table VI, it can be seen that the torque ripple is reduced significantly when compared to the motor operating without output filter. The total losses remained in the motor are only due to the fundamental component of the motor current, whereas the losses associated with the PWM switching are eliminated. However, the filter inductor losses and its associated weight and volume have been added to the motor drive system.

3.5.4 Comparison of Motor with Integrated and External Filter Inductor

Referring to the Figure 3.22, Figure 3.23, Figure 3.28 and Figure 3.32, it can be observed that the filtering effect of the motor with integrated filter inductor and motor with external filter inductor are alike. Table VII and Table VIII show the FE based performance comparison of the motor with integrated and external filter inductor.

From the results obtained, it can be concluded that the filter inductor losses and its weight and volume have been removed in the motor with integrated filter inductor. It is also worth noting that the effect on the average electromagnetic torque due to the angle (α) is negligible. Nonetheless, torque ripple have been found relatively higher when compared to the motor with external filter inductor and remained same when compared to motor without filter. This is due to the presence of switching current component in the filter branch. This can be observed from

Figure 3.34 which shows the electromagnetic torque without output filter, with traditional filter inductor and with integrated filter inductor, when motor is loaded with 1.5Nm.

Table VII: Loss, Weight & Volume Comparison of Motor with Integrated Filter Inductor and the External Filter Inductor

MOTOR WITH	Motor Losses (W)	External Inductor Losses (W)	Total Losses (W)	External Inductor Weight (Kg)	External Inductor Volume (cm^3)
Integrated Filter Inductor	36	0	36	0	0
External Filter Inductor	26.1	40.67	66.77	1.52	338.7

Table VIII: Mean Torque and Torque Ripple Comparison of Motor with Integrated Filter Inductor and the External Filter Inductor

MOTOR WITH	Mean Torque (Nm)	Torque Ripple (%) at $\boldsymbol{T_{load}}$ = 1.5Nm	Torque Ripple (%) at $\boldsymbol{T_{load}}$ = 3Nm	Torque Ripple (%) at $\boldsymbol{T_{load}}$ = 4.5Nm
Without Filter	1.49	9.54	5.3	4.2
Integrated Filter Inductor (INT)	1.485	9.54	5.33	4.2
External Filter Inductor (EXT)	1.49	0.7	0.57	0.54

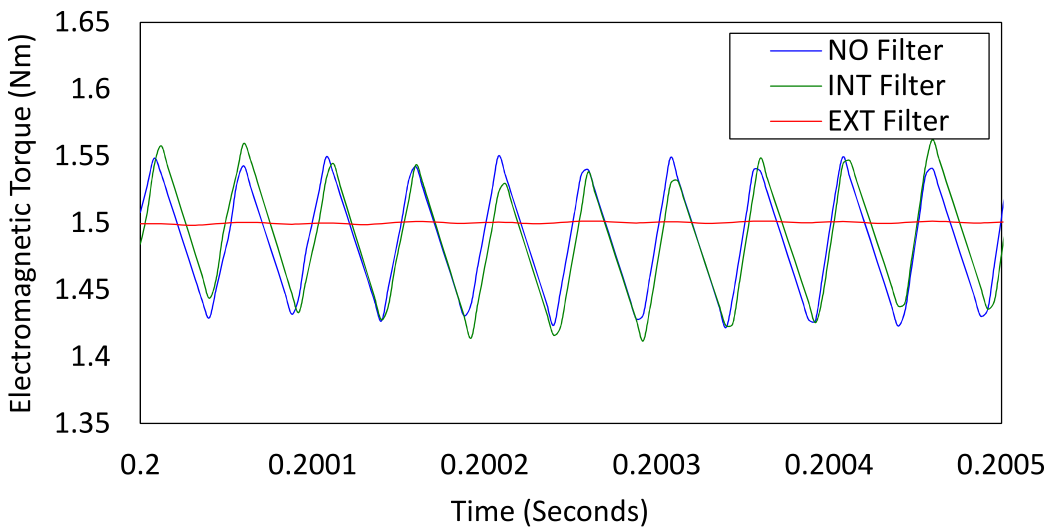

Figure 3.34: Comparison of Electrometric Torque with Integrated and External Filter Inductor when T_{load} = 1.5Nm

3.6 Optimization of Filter Branch Windings

The filter branch of the motor with integrated filter inductor is optimized in order to improve the performance of the motor in terms of reducing total motor losses and output torque ripple. This is done by adjusting the percentage of the filter branch windings from 50% to 10% of the complete motor windings i.e. the filter inductance is varied from 1.3mH to 0.28mH as shown in Figure 3.35. The resonance frequency of the output filter is fixed to 2000Hz and filter capacitance is varied. The variation in filter components due to the change in inductance is shown in Table IX and their respective bode plots are shown in Appendix B. The motor was simulated using FE package with its rotor rotating at 2100 rev/min and mechanical loading varied from 1 Nm to 3 Nm in step of 0.5 Nm. The PWM switching currents were then injected into the motor with an integrated filter inductor and the motor with an external filter inductor.

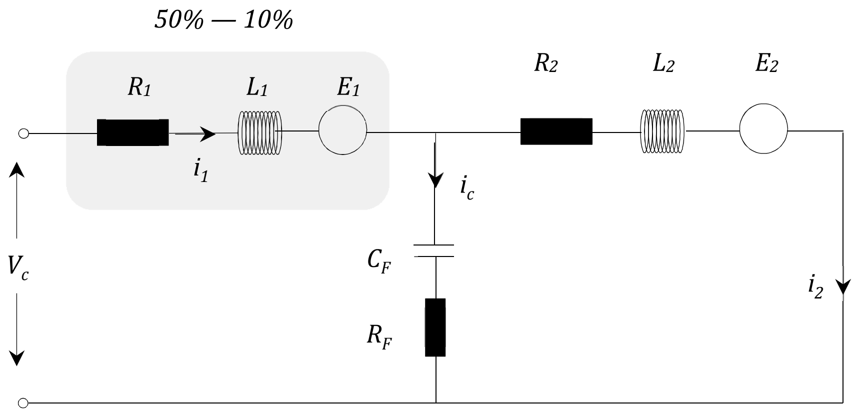

Figure 3.35: Equivalent Circuit of Motor with Integrated filter inductor

Table IX: Values of Filter Components

$L_F = L_1$ (mH)	C_F (μF)	R_F (Ω)
1.3	4.9	2
1.13	5.64	2
0.92	6.63	2
0.79	8	2
0.62	10	2
0.45	14.1	5
0.28	22.5	7

Figure 3.36 shows the motor losses with an integrated inductor with respect to load torque at a different inductance of the filter branch windings. It is important to note that the fundamental copper losses have been neglected as the change in the fundamental copper losses is negligible with the change in the filter branch inductance.

It can be seen that the overall motor losses have been reduced as the inductance of the filter branch is decreased. Since the fundamental current is same for all the inductance values, and hence the fundamental losses, the only loss component which is varying is due to PWM ripple current. As we reduced the filter inductance, the ripple component seen by the filter branch at inverter terminals will increase but at the same time, the motor branch windings will experience more filtered currents.

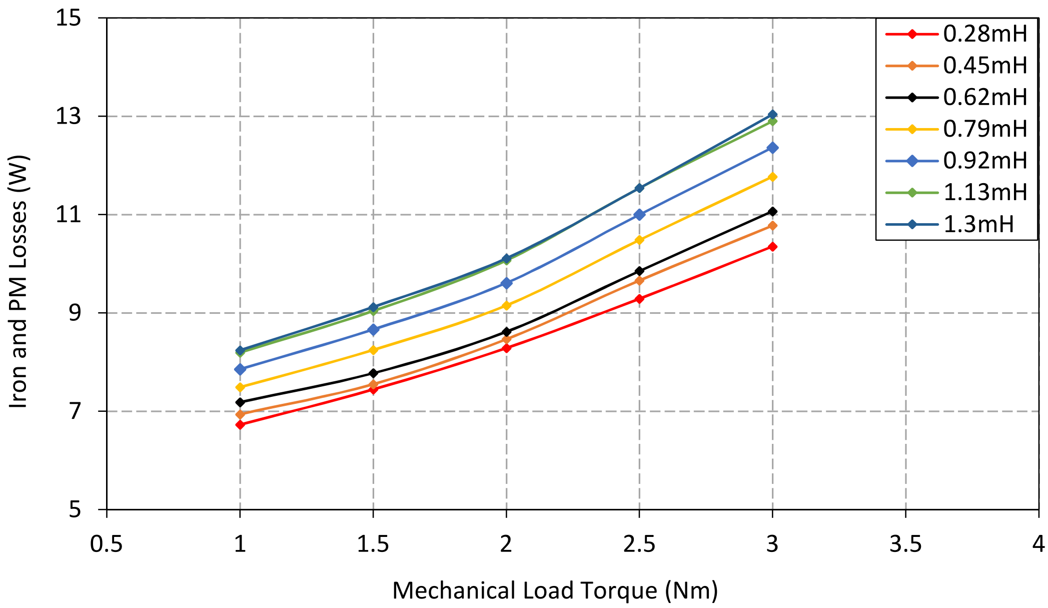

Figure 3.36: Comparison of total motor losses with an integrated inductor at different inductance of the filter branch winding

Furthermore, the transformer action is taking place in the motor branch windings as the filter branch inductance is reduced from 50% of the entire motor windings. Since both filter and motor branch windings are wound on the same slots which leads to switching ripples of both branch to be opposite therefore, the motor branch windings carry switching ripples which is 180 degrees out of phase with respect to ripple current of the filter branch. The effect of the transformer action between filter and motor branch current can be seen from Figure 3.37 and Figure 3.38.

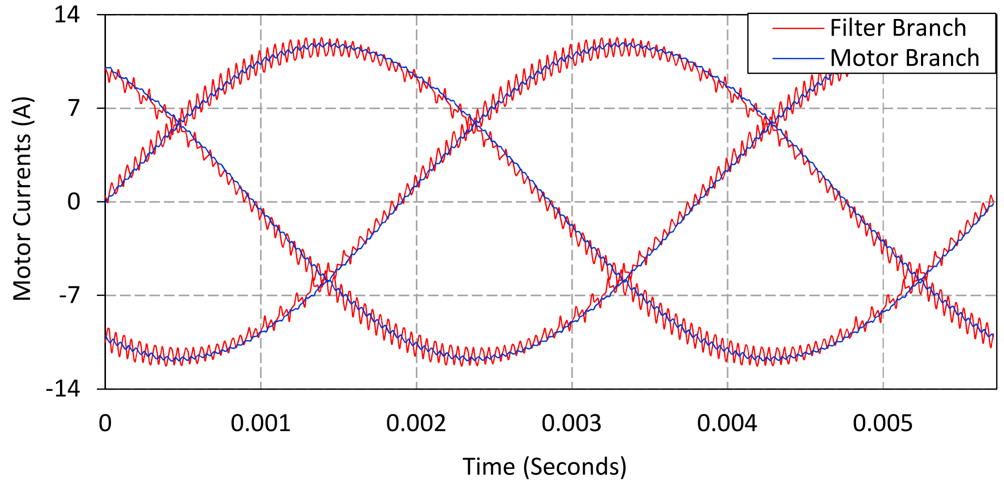

Figure 3.37: Filter and Motor Branch Motor PWM Currents at 0.28mH Filter Inductance and 3Nm Mechanical Load

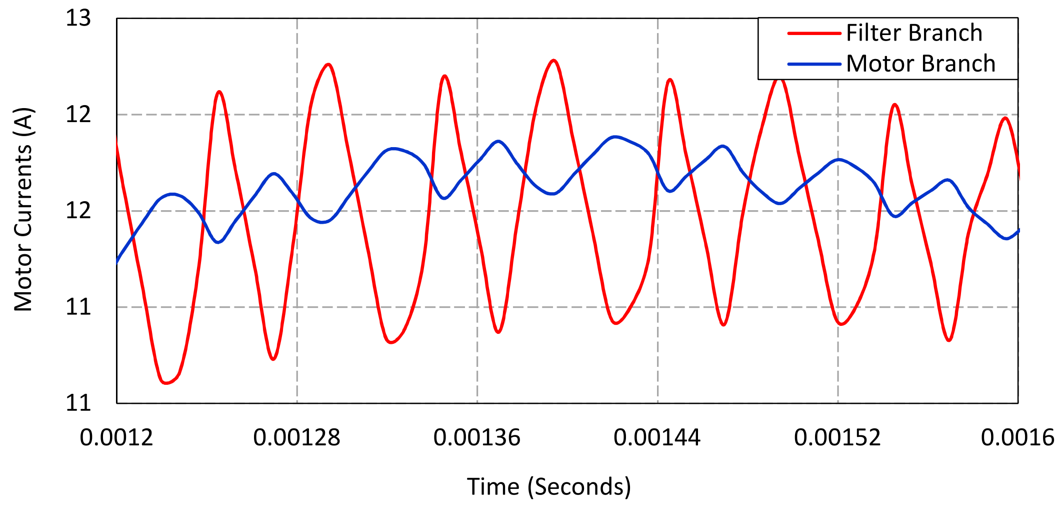

Figure 3.38: Filter and Motor Branch Motor PWM Currents at 0.28mH Filter Inductance and 3Nm Mechanical Load (Zoom View)

3.6.1 Comparative Analysis between Integrated and Traditional System

This section presents the comparative analysis between the motor with an integrated filter inductor and an external filter inductor in terms of total system losses, torque ripple, and power quality.

3.6.1.1 Total Loss Comparison

The loss comparison of the motor with an integrated filter inductor and the motor with an external filter inductor is shown in Figure 3.39 (a)-(g). The total losses of the motor with an integrated filter inductor include: motor iron losses, motor copper losses and the ohmic losses of the permanent magnets, whereas the total losses of the motor with an external filter inductor include: motor iron losses, motor copper loss, PM ohmic loss, inductor iron losses and inductor copper loss. The losses in the RC branch is neglected in this comparative analysis as they are assumed to remain unchanged for both integrated and traditional motor drive systems.

From Figure 3.39(a)-(g), it can be observed that the total losses in the motor with integrated filter inductor are lower than in the motor with an external filter inductor. Moreover, the total losses are increased as the filter branch inductance is decreased. This is due to the fact that lower inductance of an external filter inductor will lead to an increase in switching ripple seen by the motor which has resulted in higher losses in the traditional motor drive system. However, losses in the motor with an integrated filter inductor have been reduced due to the fact that the switching ripple in the motor branch is compensated in the filter branch by transformer's action (cf. Figure 3.38).

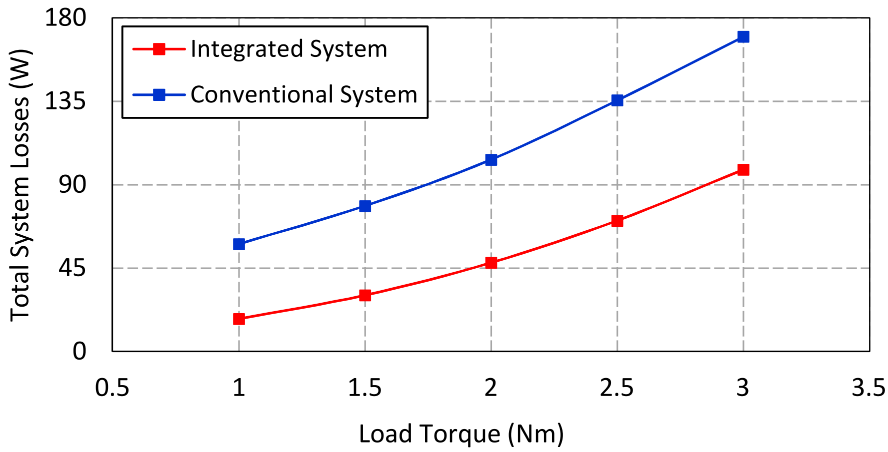

(a) 1.3mH Filter Branch Inductance

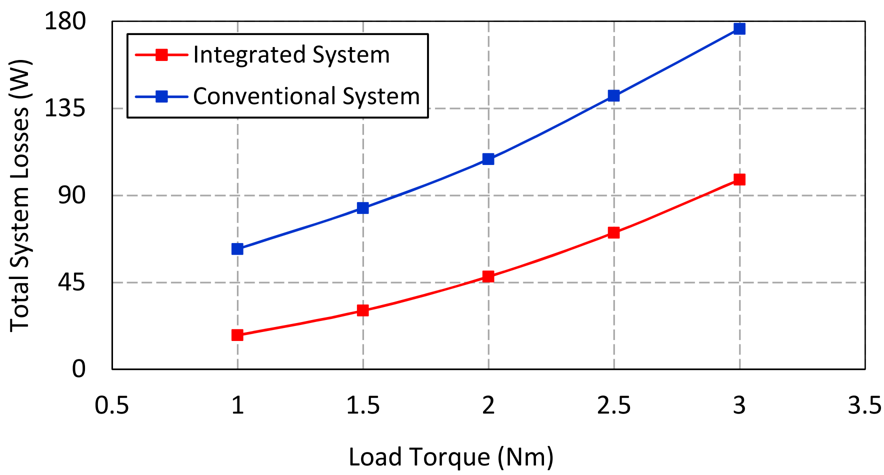

(b) 1.13mH Filter Branch Inductance

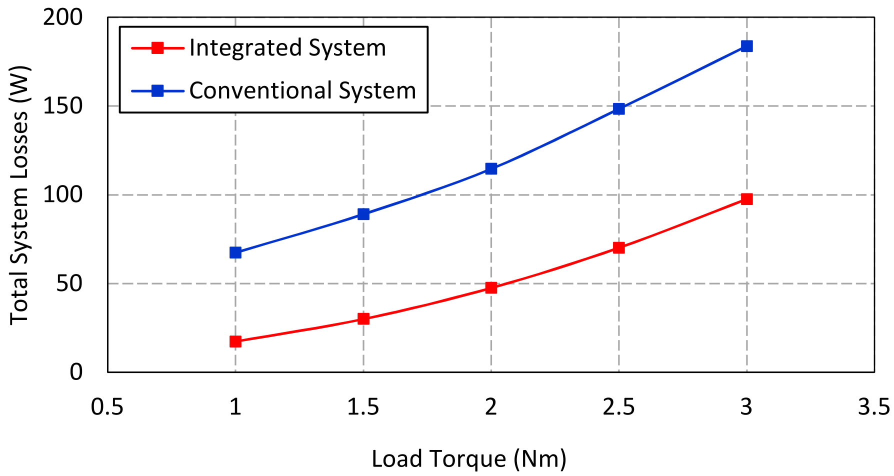

(c) 0.92mH Filter Branch Inductance

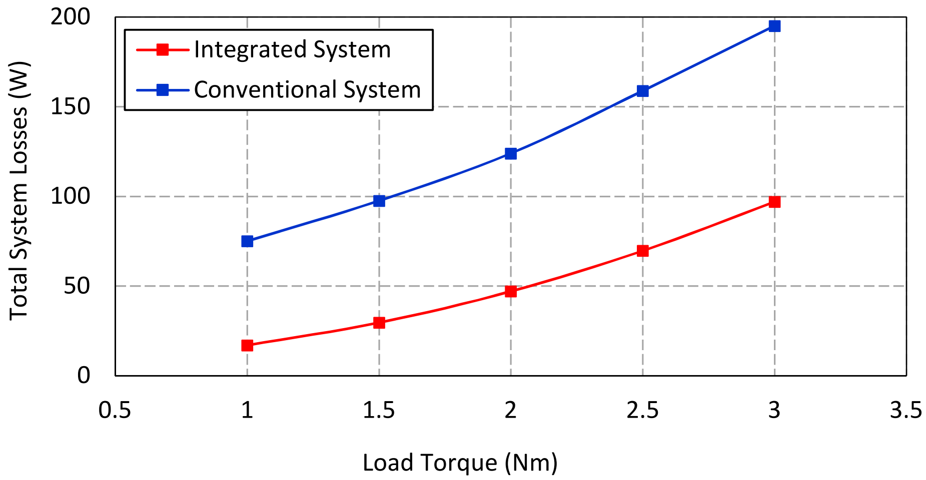

(d) 0.79mH Filter Branch Inductance

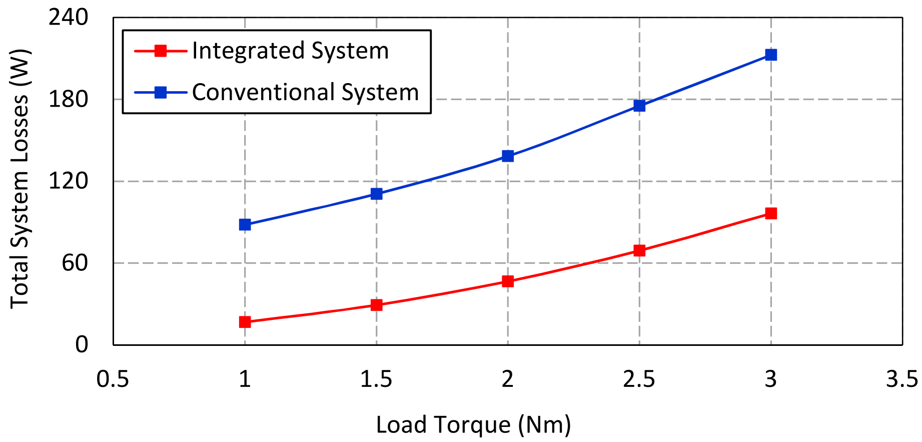

(e) 0.62mH Filter Branch Inductance

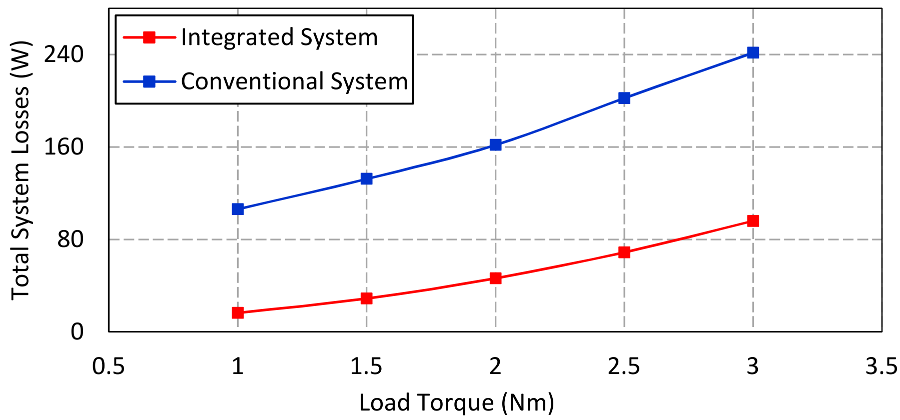

(f) 0.45mH Filter Branch Inductance

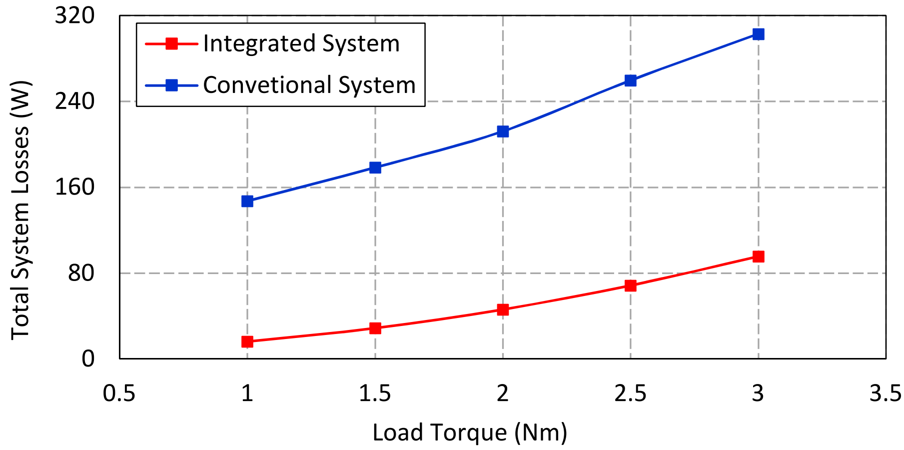

(g) 0.28mH Filter Branch Inductance

Figure 3.39: Comparison of total system losses between Integrated and Traditional PMSM

3.6.1.2 Torque Ripple Comparison

Percentage torque ripple of the motor with and without output filter is compared. Torque ripple of the motor without output filter at different load conditions and the torque ripple of the motor with traditional and integrated filter at 0.28mH inductance is illustrated in Table X.

From Table X, it is shown that the torque ripple for the optimized inductance value is improved in the motor with integrated filter inductor when compared to the motor operating without a filter. This is due to the switching ripples cancellation between filter branch and the motor branch. Moreover, the motor branch experiences increased filtration of 3 phase voltages when the inductance of the filter branch is reduced.

Table X: Motor Torque Ripple with and without Output Filter

MOTOR WITH	Torque Ripple (%) at T_{load} = 1Nm	Torque Ripple (%) at T_{load} = 2Nm	Torque Ripple (%) at T_{load} = 3Nm
No Filter	11.53	6.41	4.84
Integrated Inductor at 0.28mH	5	2.97	2.12
External Inductor at 0.28mH	4.18	2.52	2.10

The performance of the motor with an integrated filter inductor and the external filter inductor at 0.28mH inductance is similar in terms of torque ripple reduction. When compared with the motor operating without output filter, the motor with integrated filter inductor provides the reduction of 56.2%, whereas 57.2% reduction is achieved in the motor with an external filter inductor.

The comparison of torque ripple of the motor with an integrated filter inductor and external filter inductor with respect to the filter inductance is shown in Figure 3.40(a)-(c). It can be observed that the traditional filter performs better for higher filter inductance when compared to the integrated filter.

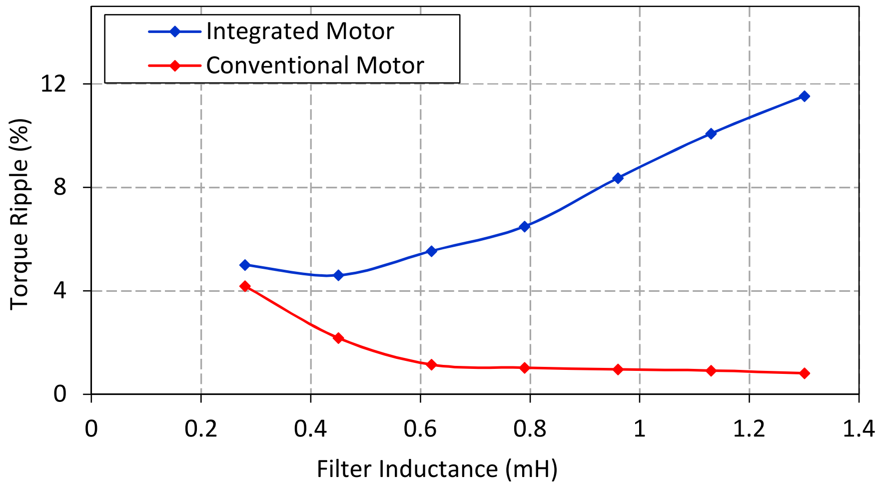

(a) 1 Nm Load Torque

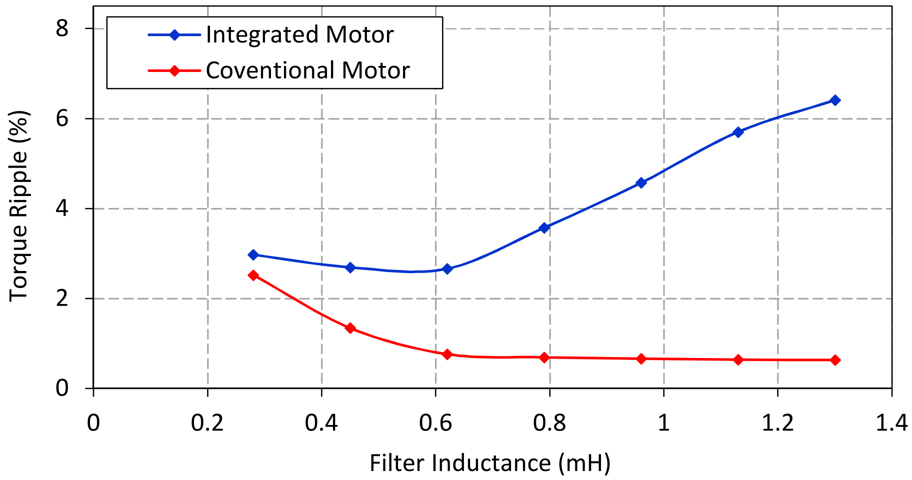

(b) 2 Nm Load Torque

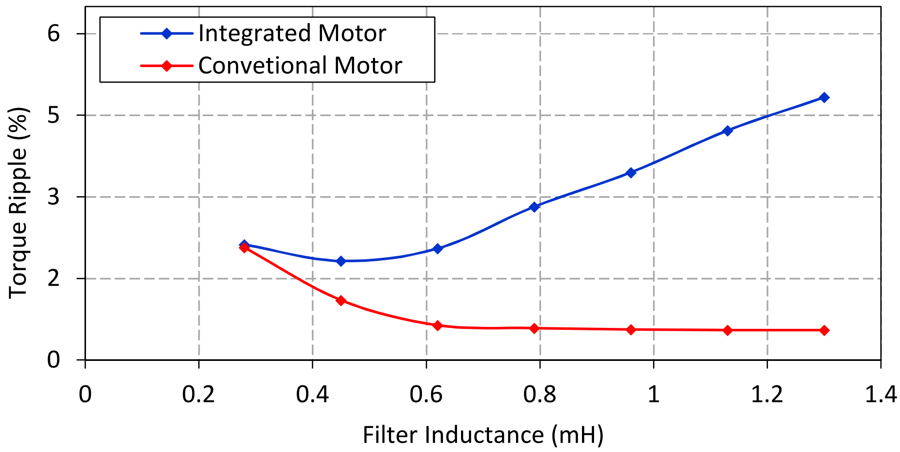

(c) 3 Nm Load Torque

Figure 3.40: Percentage Torque Ripple Comparison between motor with Integrated and traditional filter inductor at Different Loading Conditions

For the lower amount of filter inductance, the torque ripple is increased drastically due to higher switching ripple component which deteriorates the filter performance and increases the requirement of damping resistance than usual and is indicated in Table IX.

It can be argued that the frequency of torque ripple as seen in Figure 3.38 is very high (the same as PWM frequency) and a ripple at this frequency is easily filtered out by the rotor mechanical inertia. However, for high power machines where the switching frequency is limited to 4 kHz (or even less) due to high current required to be controlled, rotor mechanical inertia is not sufficient to filter out the torque ripple and extra arrangements have to be made.

3.6.1.3 Volume and Mass Comparison

The complete volume and mass of the RLC output filter is determined and compared in this section. Figure 3.41(a)-(b) shows the volume and mass comparison of RLC output filter with integrated and external filter inductor. Since the reduction in filter inductance increases the volume and mass of the filter capacitor therefore, it is necessary to choose the output filter with minimum volume and mass. It should be noted here that the volume and mass of the motor is neglected in this comparison of output filter and the volume and mass of the filter inductor does not exist in motor with integrated filter inductor.

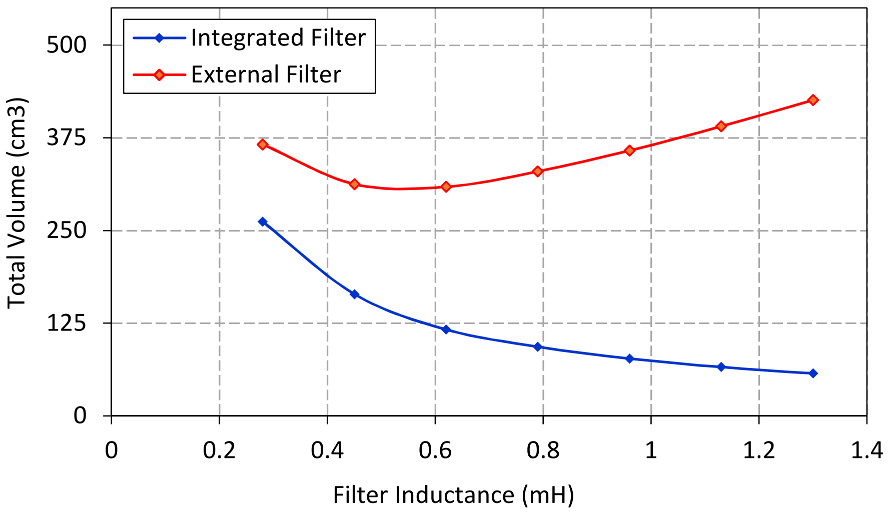

(a) Volume of RLC Output Filter

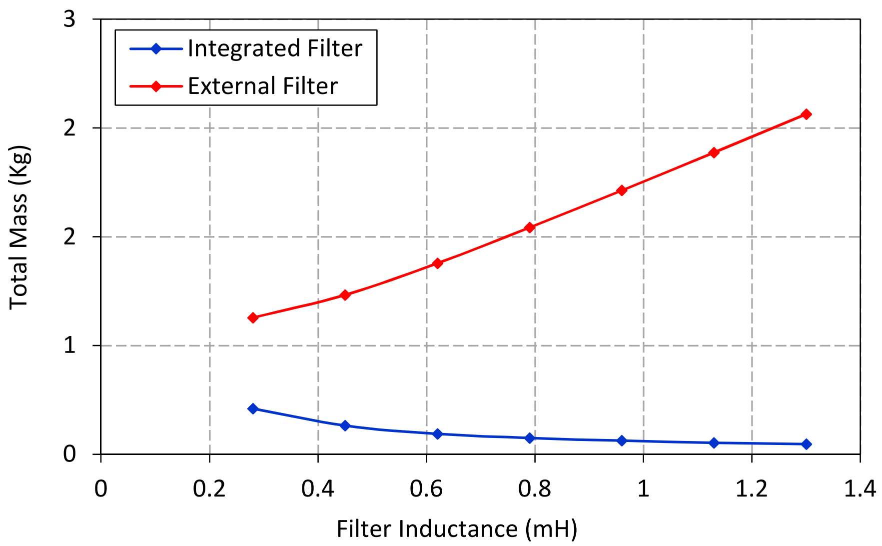

(b) Mass of RLC Output Filter

Figure 3.41: Volume and Mass of RLC output Filter

From Figure 3.41(a), it can be observed that the volume of the output filter with external filter inductor decreases as the filter inductance is reduced until 0.62mH and starts increasing again until 0.28mH. This is because the capacitor volume dominates the inductor volume beyond 0.62mH and vice versa. On the other hand, the filter inductor volume is zero in the motor with integrated filter inductor. The overall volume of the motor with an integrated filter inductor is increasing as the filter capacitance is increased or the filter inductance is decreased.

Figure 3.41(b) shows the overall mass of the RLC output filter. It is observed that overall mass of the external RLC output filter is decreasing proportionally as the filter inductance is reduced. This is because the weight of inductor is dominating throughout and increase in capacitor does not affect the overall weight of the output filter. However, weight of the motor with integrated filter inductor follows the same trend as in the case of volume i.e. weight increases as the filter inductance is reduced due to the absence of inductor volume.

3.7 SUMMARY

This chapter demonstrates a novel approach to integrate the output filter inductor into permanent magnet synchronous machine. The introduction of the integrated output filter inductor along with its practical implementation inside the machine is also presented. A detailed vector control model of the proposed motor with integrated filter inductor, taking into account of modulation and device switching, have been developed using software called "$MATLAB - Simulink$". The equations for the torque and three phase current was derived to model the proposed motor.

Subsequently, the design of an external EE core inductor was briefly described in order to compare its performance with integrated filter inductor. $MATLAB - Simulink$ & FEA results of the proposed motor had been presented with and without output filter. For the motor with integrated filter inductor, the $MATLAB - Simulink$ & FEA results had been compared with the motor with external filter inductor when the filter branch windings were half of the entire motor windings. The results showed that the motor with integrated filter inductor does not require an external inductor which eliminates its losses, weight and volume. However, this comes at the expense of relatively higher torque ripple.

In the end, FEA based optimization of the filter branch was done in terms of the reducing total losses and torque ripple. In the optimization process, filter branch winding was varied from 50% to 10% of the entire motor windings whilst keeping the filter resonance frequency constant. It was noticed that the transformer's action was taken place between the filter and motor branch windings when the filter branch windings were less than half of the entire motor windings. In the optimization process, the torque ripple of the motor with integrated filter inductor was reduced drastically which than becomes comparable to the torque ripple of the motor with external filter inductor.

3.8 REFERENCES:

[1] Y. Sozer, D. A. Torrey, and S. Reva, "New inverter output filter topology for PWM motor drives," *IEEE Transactions on Power Electronics,* vol. 15, pp. 1007-1017, 2000.

[2] C. W. T. Mclyman, *Transformer and Inductor Design Handbook*, Fourth ed.

[3] *AK Steel - Non Oriented Electrical Steels*. Available: http://www.aksteel.com/pdf/markets_products/electrical/non_oriented_bulletin.pdf

[4] *AK Steel - Selection of Electrical Steels for Magnetic Cores*. Available: http://www.aksteel.com/pdf/markets_products/electrical/mag_cores_data_bulletin.pdf

CHAPTER

4

PMSM WITH INTEGRATED FILTER INDUCTOR: EXPERIMENTAL VALIDATION

4.1 INTRODUCTION

This chapter presents the experimental verification of the motor with an integrated inductor that has been proposed in chapter 3. To validate the concept of integrated motor, the *HEMAS* (Helicopter Electromechanical Actuation System) machine is modified which was recently built at The University of Nottingham, UK for *HEMAS* Project.

All test were conducted on an instrumented test-rig which is appropriate for validating and measuring the required performance. The experimental tests were conducted for the motor operating without output filter, motor with an integrated inductor and the motor with an external inductor. The results and discussion have been presented at different rotor speed, mechanical load and inverter switching frequency.

The performance of both integrated and conventional motors have also been compared in terms of its current ripple and FFT followed by a comprehensive experimental loss characterization. The measured experimental losses is also compared with finite element model of the motor with integrated filter inductor.

4.2 EXPERIMENTAL TEST RIG & SETUP

Figure 4.1(a) and Figure 4.1(b) shows the experimental rig and test setup for testing and validating the proposed motor with integrated filter inductor with 50% filter branch windings. For the purpose of validation, the 12 slots 10 poles permanent magnet synchronous machine is modified whose practical implementation is fully described in section 3.2.2 of chapter 3. The prototype of the test machine with filter and motor branch windings is shown in Figure 4.2(a) to Figure 4.2(c).

To test the machine, SpectraQuest's "Drivetrain Diagnostic Simulator" test-rig is used [1] along with 3-phase voltage source inverter. The test-rig and setup are equipped with a DC power supply, 3-phase PWM voltage source inverter, 3 phase integrated motor, torque transducer and the magnetic brake which is acting as a mechanical load on the machine under test.

(a) Voltage Source Inverter and Control Platform

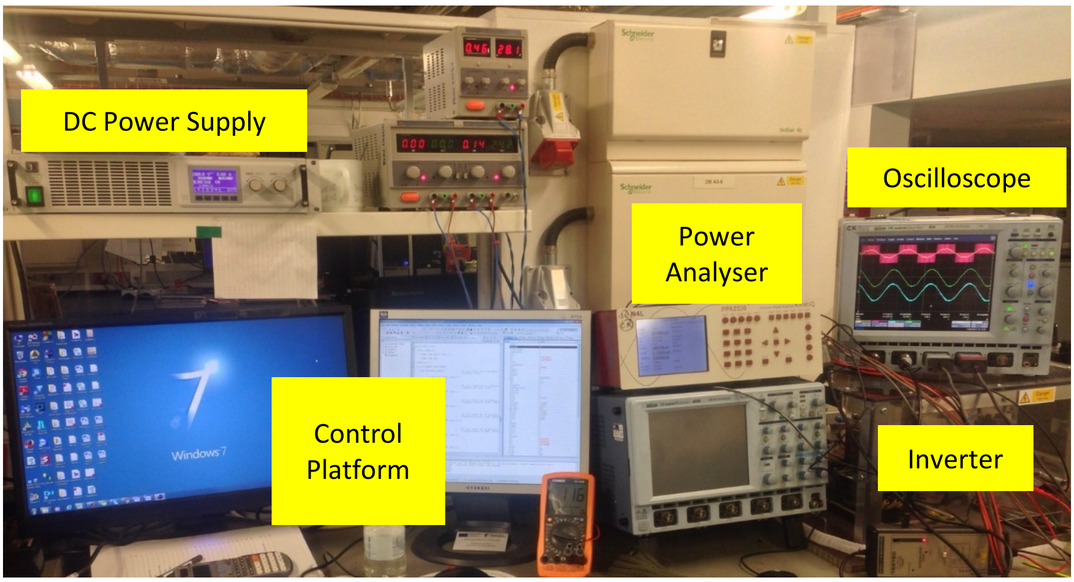

(b) Test-Rig (Drivetrain Diagnostic Simulator)

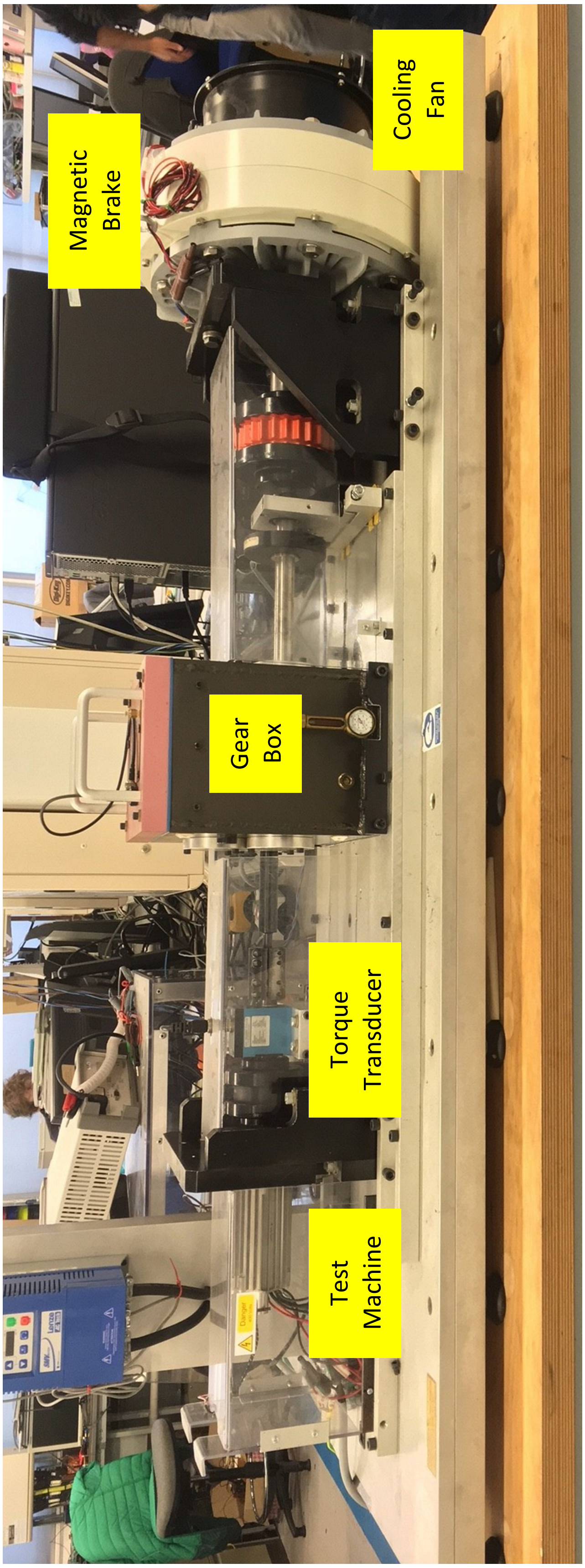

Figure 4.1: Experimental Setup and Test-rig

(a) Prototype Integrated Motor with Housing

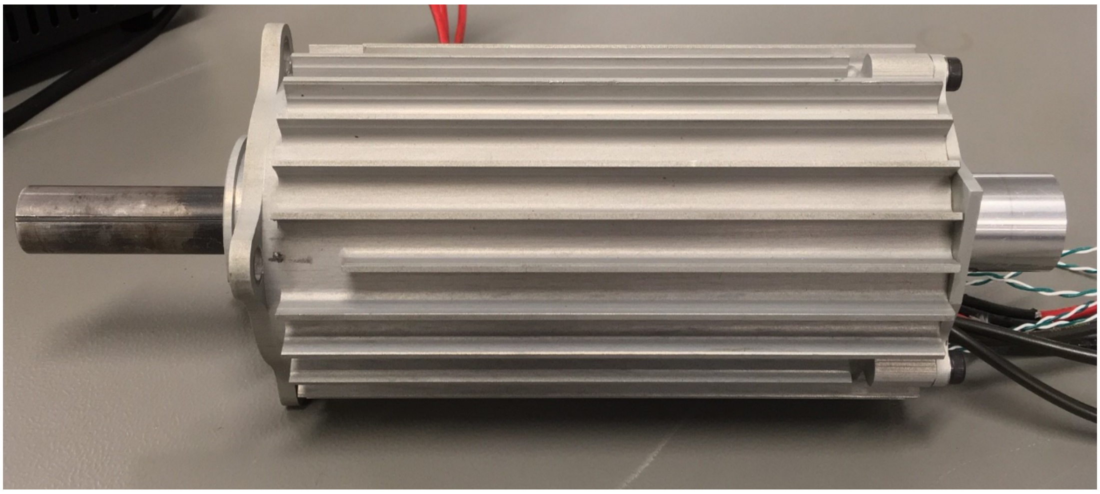

(b) Prototype Integrated Motor without Housing

(c) Filter and Motor Branch Windings Pattern

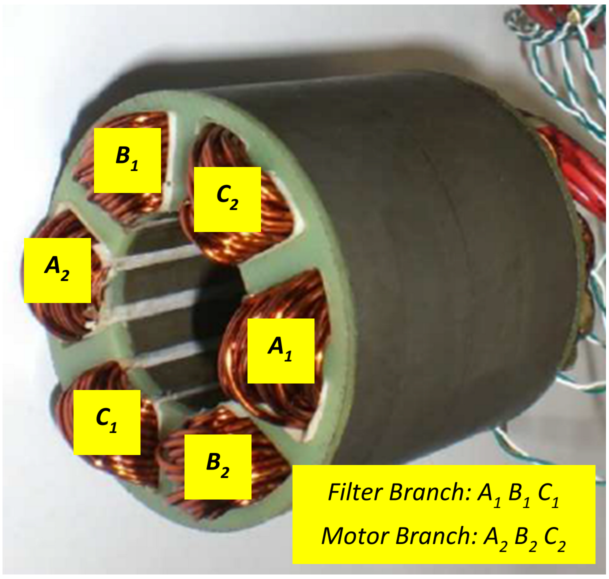

Figure 4.2: Prototype of Integrated Motor and Windings Pattern

4.2.1 Integrated Motor

As discussed in chapter 3, 12 slots 10 poles permanent magnet synchronous machine was selected to validate the concept of integrated output filter inductor. This machine was built at The University of Nottingham, UK for $HEMAS$ (Helicopter Electromechanical Actuation System) project [2-5]. The stator prototype of the machine is shown in Figure 4.2 whereas the rotor structure is shown in Figure 4.3.

(a) PM Rotor of HEMAS Machine

(b) Halback Array Arrangement

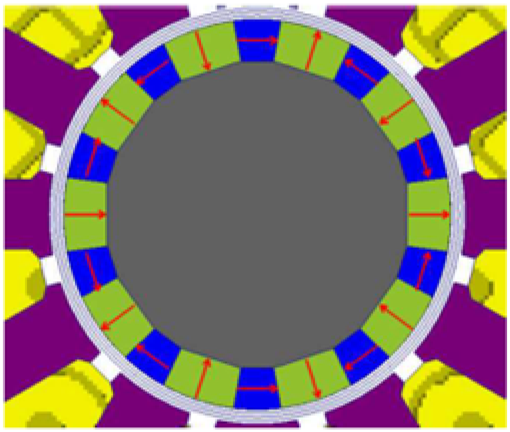

Figure 4.3: PM Rotor of the motor with integrated filter inductor [2-5]

The stator stack is made up of Vacoflux 50 Cobalt-Iron laminations. Each phase consists of 40 turns with 1 mm diameter and class H wire insulation. On the other hand, the rotor is made up of Halback array permanent magnets with non-magnetic stainless sleeves of 0.3mm thickness [5].

The complete motor parameters are shown in Table I and the flight profile [2, 3] for which $HEMAS$ machine was designed is shown in Appendix C1. The maximum operating speed for this experimental validation is chosen 2100 RPM due to the SpectraQuest's "Drivetrain Diagnostic Simulator" speed limitation. Since the $HEMAS$ motor was not designed to produce the maximum torque for continuous operation, the operating torque is not exceeded beyond 3 Nm i.e. it is varied from 1.5 Nm to 3 Nm for the experimental validation.

Table I: Motor Specifications

PARAMETERS	VALUES	UNITS
Motor Connections	2×STAR	-
No. of Turns per phase	2×46	-
Operating Torque	1 Nm – 3 Nm	Nm
Peak Torque	2×4	Nm
Operating Speed	2100	RPM
Maximum Speed	5242	RPM
Phase Resistance	2×0.21	Ω
Phase Inductance	2×1.3	mH
Operating Peak Current	5.85	A
Maximum Peak Current	31	A
No-load Flux Linkage	2×0.017122	Wb.T
Motor Inertia	2×1.65	$Kg.m^2$

4.2.2 RLC Output Filter

A RLC output filter is designed using the procedure as explained in [6] and chapter 2. The filter resistance, inductance and capacitance are chosen as 2Ω, 1.3mH and 4.9μF. The resonance frequency is fixed to 2 kHz, whereas the maximum frequency to avoid the resonance between the filter capacitance and motor inductance is 1.2 kHz. The external filter inductor is shown in Figure 4.4 (a) whereas the filter capacitor and damping resistor are shown in Figure 4.4 (b).

The design procedure of the filter inductor is presented in chapter 3. The filter inductor has 20 turns per phase. The inductance of 1.1mH has been measured which is comparable with its designed value. The method of measuring the inductance is presented in Appendix B. The film type capacitance (KEMET) of 4.7μF is used for the experimental verification with model "R46KR447050M2K Film Capacitor, 4.7μF, X2, 275V, PP (Polypropylene), ± 10%". 5W, 2Ω resistance used is wire-wound resistors having silicon coated axial leads.

(a) Filter Inductor

s

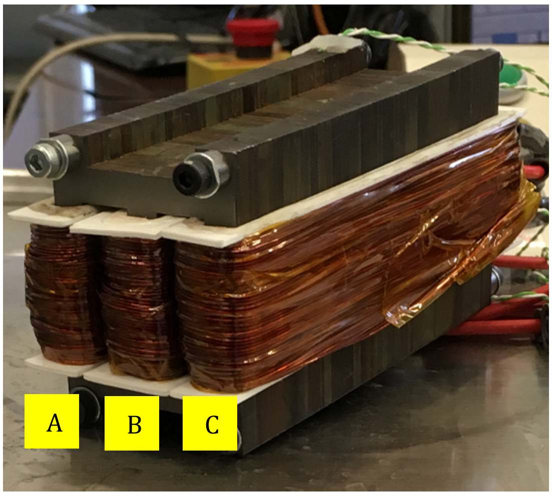

(b) Filter Capacitor and Damping Resistor

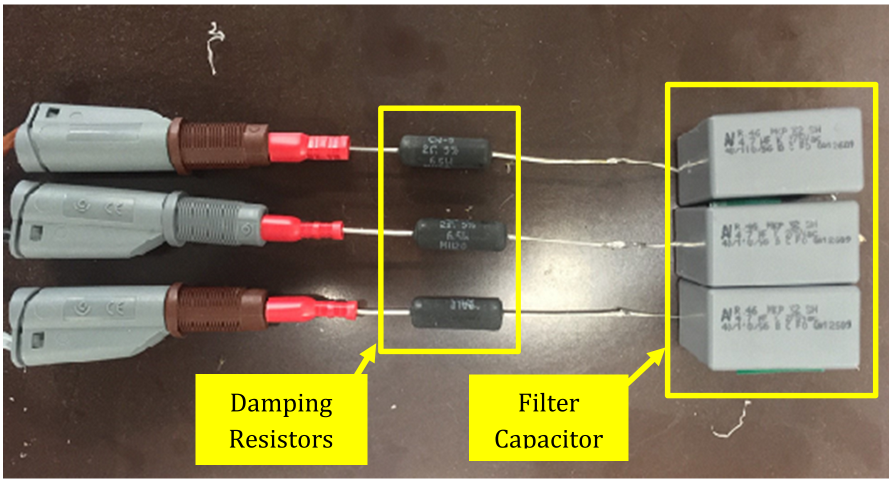

Figure 4.4: Filter Capacitor and Damping Resistor (3-phase)

4.2.3 Power Converter

The motor with integrated filter inductor is supplied by the power converter. The converter used in the experimental test-rig is the same as that used for the $HEMAS$ project as it serve to prove the only the functional concept of integrated output filter inductor. The converter prototype consist of a gate driver board, control board, power switches and input filters board as shown in Figure 4.5 [5]. Three 3-phase $IGBT$ module and the gate-drive circuit are combined with a shared control platform based on $FPGA$, DSP and the power quality input filter.

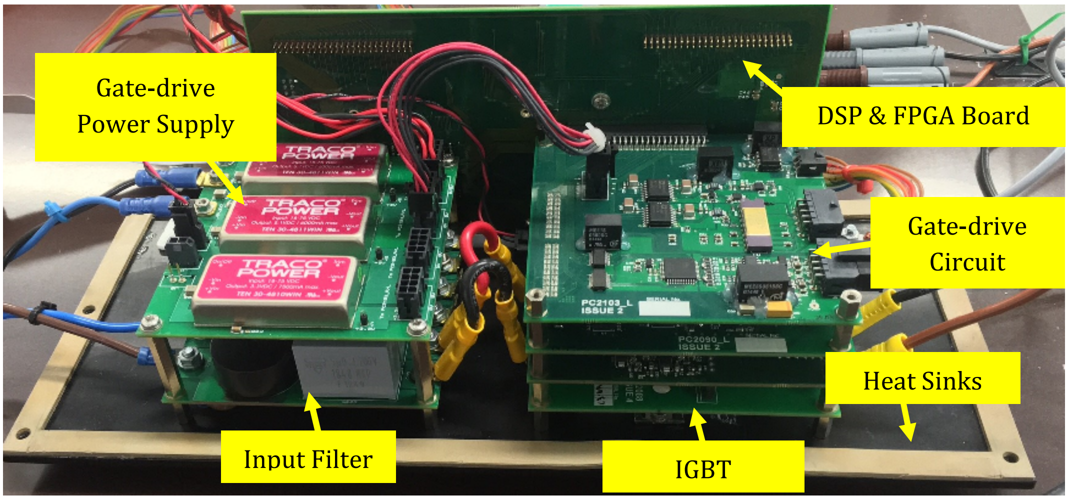

Figure 4.5: Prototype of HEMAS Power Module

4.2.4 Drivetrain Diagnostic Simulator (DDS)

SpectraQuest's Drivetrain Diagnostics Simulator (*DDS*) is specifically designed to simulate industrial drivetrains for experimental and educational purposes. The drivetrain consists of motor, power converter, gearbox system, torque transducer, speed encoder, bearing loader, and magnetic brake as shown in Figure 4.1. It is robust enough to handle heady loads and spacious enough for easy gear placement, setup, and installation of monitoring devices. The features of the *DDS* is shown in Appendix C2, where the motor and converter is replaced with the *HEMAS* motor and converter for validation purpose [1].

4.2.5 Voltage, Current and Power Measurements

The setup to measure the voltage, current, power, and the output torque is shown in Figure 4.6(a) and Figure 4.6(b) and the device details are listed below:

1. LeCroy High Voltage Differential Probe (ADP300, 1000 $V_{RMS\text{-}GROUND}$)
2. LeCroy Current Probe (CP150, 150A, 0.01V/A)
3. Power Analyser (N4L PPA550)
4. KISTLER Torque Transducer (100Nm – 50V. Type: 4502A100RA)

The motor losses were evaluated by measuring the input power to the motor terminals and output power at the shaft. The motor losses is the difference of input electrical power and the output mechanical power which can be expressed as,

$$P_{m,loss} = P_{in} - P_{out} = P_{in} - (T_{out} \,.\, \omega_r) \tag{4.1}$$

where, P_{in} is the input electrical power in watts, P_{out} is the output mechanical power in watts, T_{out} is the measured output torque in Nm and ω_r is rotor speed in rad/s.

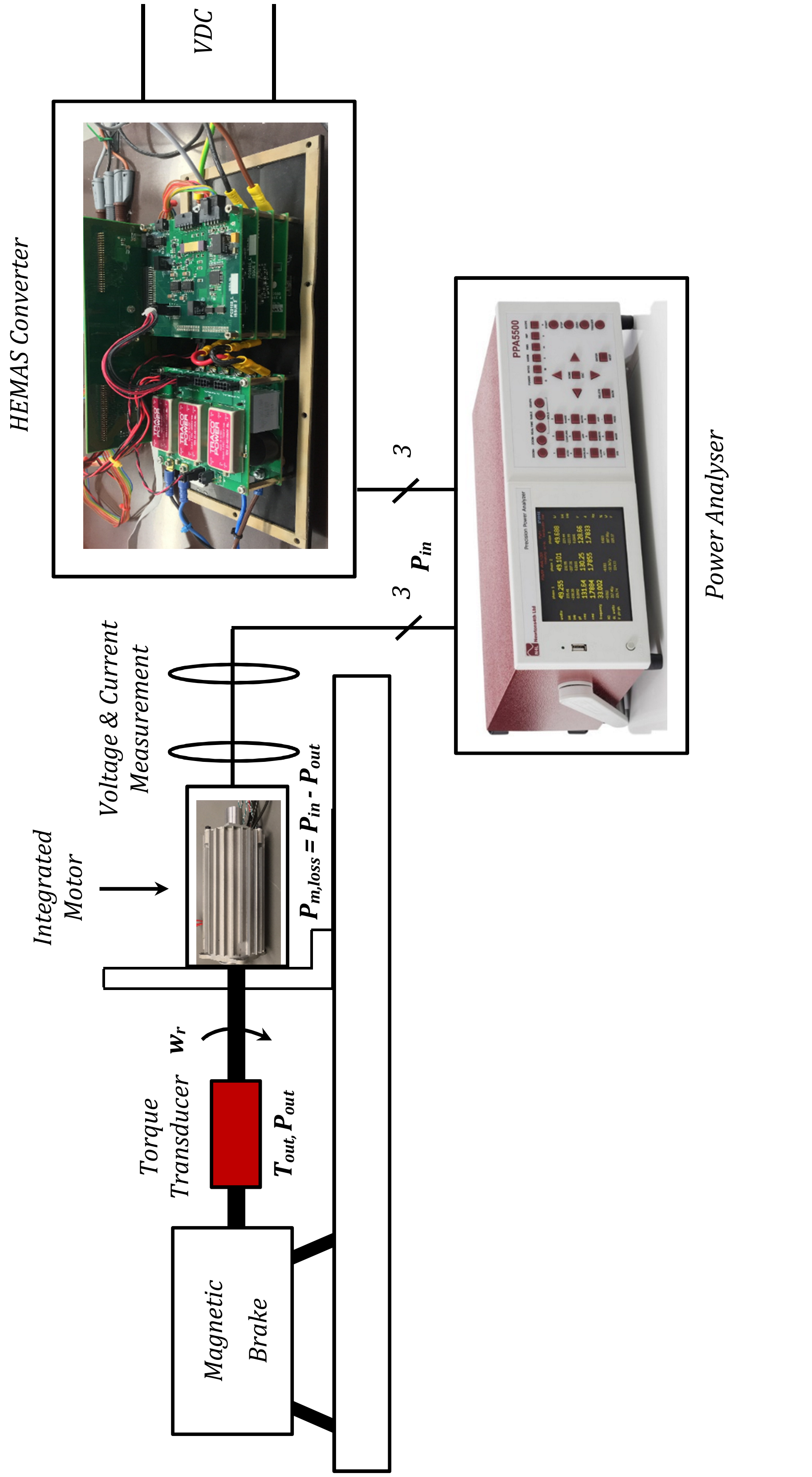

(a) Power, Current and Voltage Measurement of Motor with Integrated Inductor

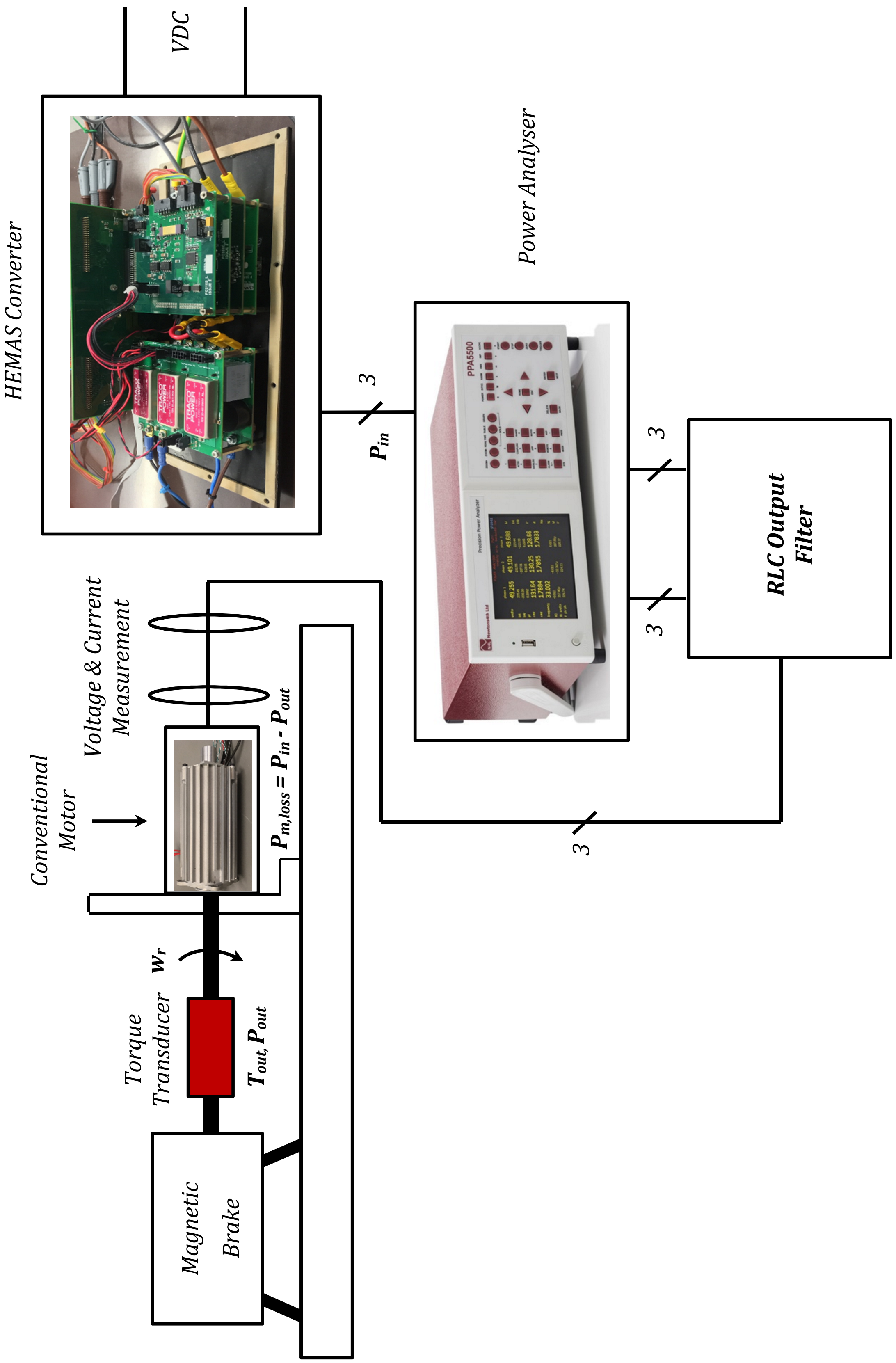

(b) Power, Current and Voltage Measurement of Motor with External Inductor

Figure 4.6: Voltage, Current & Power Measurements

4.3 EXPERIMENTAL RESULTS & DISCUSSIONS:

This section presents the experimental results of the motor with and without output filter. The motor with output filter includes motor with conventional EE core inductor and the motor with integrated inductor. In all cases, motor is driven by voltage source inverter with switching frequency of 10 kHz. The measured filter and motor branch current ripple are presented for switching frequencies of 5, 10 and 15 kHz. Also, the comparison study between motor with conventional inductor and the motor with integrated inductor is presented in terms of motor performance followed by a comprehensive experimental characterization of the motor with integrated inductor. Both motors (with conventional and integrated inductor) were tested at different range of speed and load torque. The motor speed is varied from 1200 RPM to 2100 RPM whereas the load torque is varied in between 1.5 Nm to 3 Nm.

4.3.1 Motor without Output Filter

4.3.1.1 Measured Voltage & Currents

Experimental results were analysed when the motor shown in Figure 4.2 is operated by voltage source inverter drive without any output filter at speed of 2100 RPM and load torque of 1.5 Nm where the inverter is switched with 10 kHz switching frequency. Figure 4.7 and Figure 4.8 shows the motor terminal voltage and motor current respectively. The FFT of the motor terminal voltage and current is shown in Figure 4.9 and Figure 4.10 respectively. The first dominant switching component of motor voltage is at 20 kHz frequency, which is 79.2%, whereas the motor current carries the first dominant switching component at 20 kHz frequency, which is 2.6%. These values are closely comparable with the Simulink results as discussed in chapter 3.

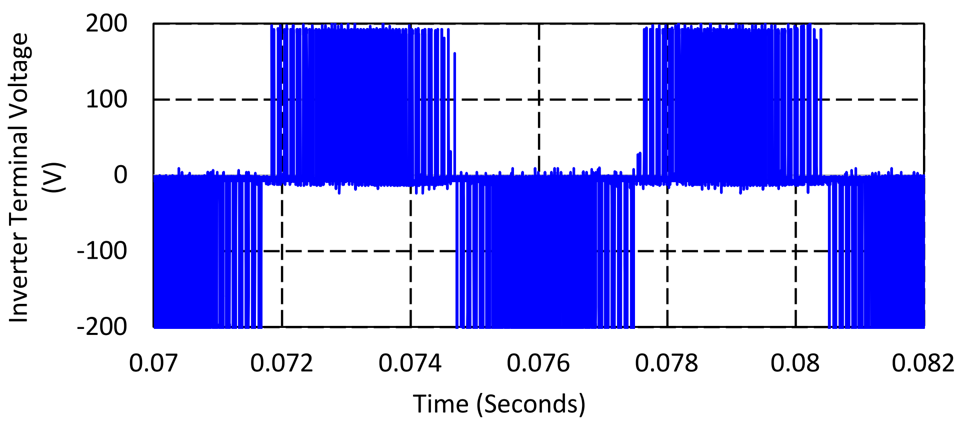

Figure 4.7: Line-to-line Motor Terminals Voltage without Filter (V_{AB})

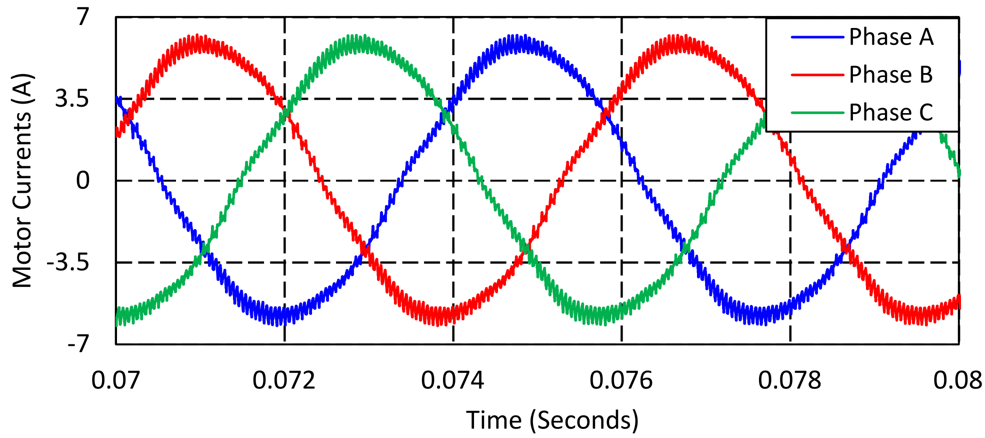

Figure 4.8: Motor Current without Filter

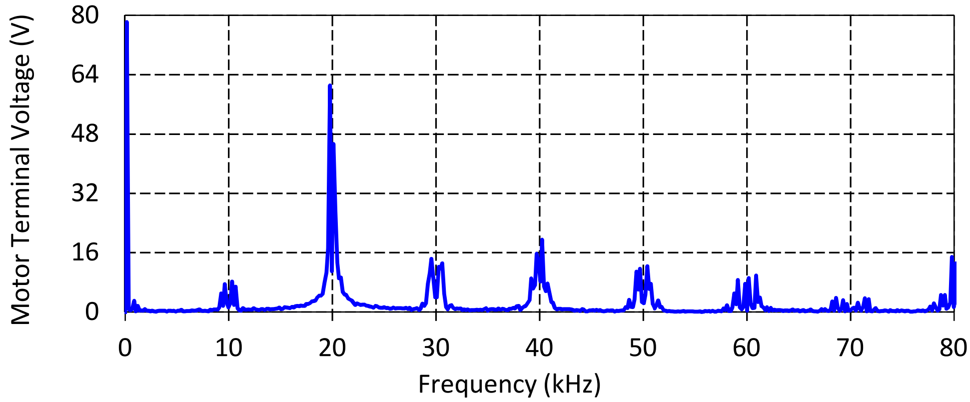

Figure 4.9: FFT of Motor Terminal Voltage without Filter (V_{AB})

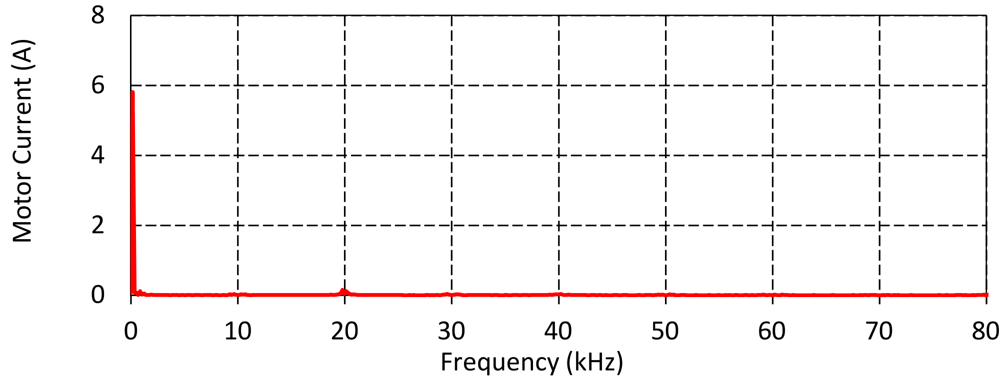

Figure 4.10: FFT of Motor Current without Filter (I_A)

4.3.1.2 Measured Output Torque

The output torque shown in Figure 4.11(a)-(d) is measured using KISTLER torque transducer. The available torque transducer is designed to generate maximum 5V at 100Nm torque. Since the load torque varies from 1.5Nm – 3Nm, it is difficult to precisely measure it using the torque transducer which is rated at 100Nm. In order to see the effect of switching ripple the output torque is estimated through measured motor currents. Since the no-load voltage is sinusoidal it is possible to estimate the output torque by the given relation,

$$T_{out} = \frac{P}{2}\left[\left(\frac{E_{a1}i_{a1}}{\omega_e} + \frac{E_{a1}i_{b1}}{\omega_e} + \frac{E_{a1}i_{c1}}{\omega_e}\right) + \left(\frac{E_{a2}i_{a2}}{\omega_e} + \frac{E_{a2}i_{b2}}{\omega_e} + \frac{E_{a2}i_{c2}}{\omega_e}\right)\right] \quad (4.2)$$

where the T_{out} is the estimated output torque in Nm, P is the number of poles, E_{abc} is the 3 phase no-load voltages in volts, i_{abc} is the measured 3 phase motor currents in ampere and ω_e is the electrical speed in rad/s. Due to the imprecision of torque measurements the output torque is estimated using Eq. 4.2 which corresponds to the measured motor currents.

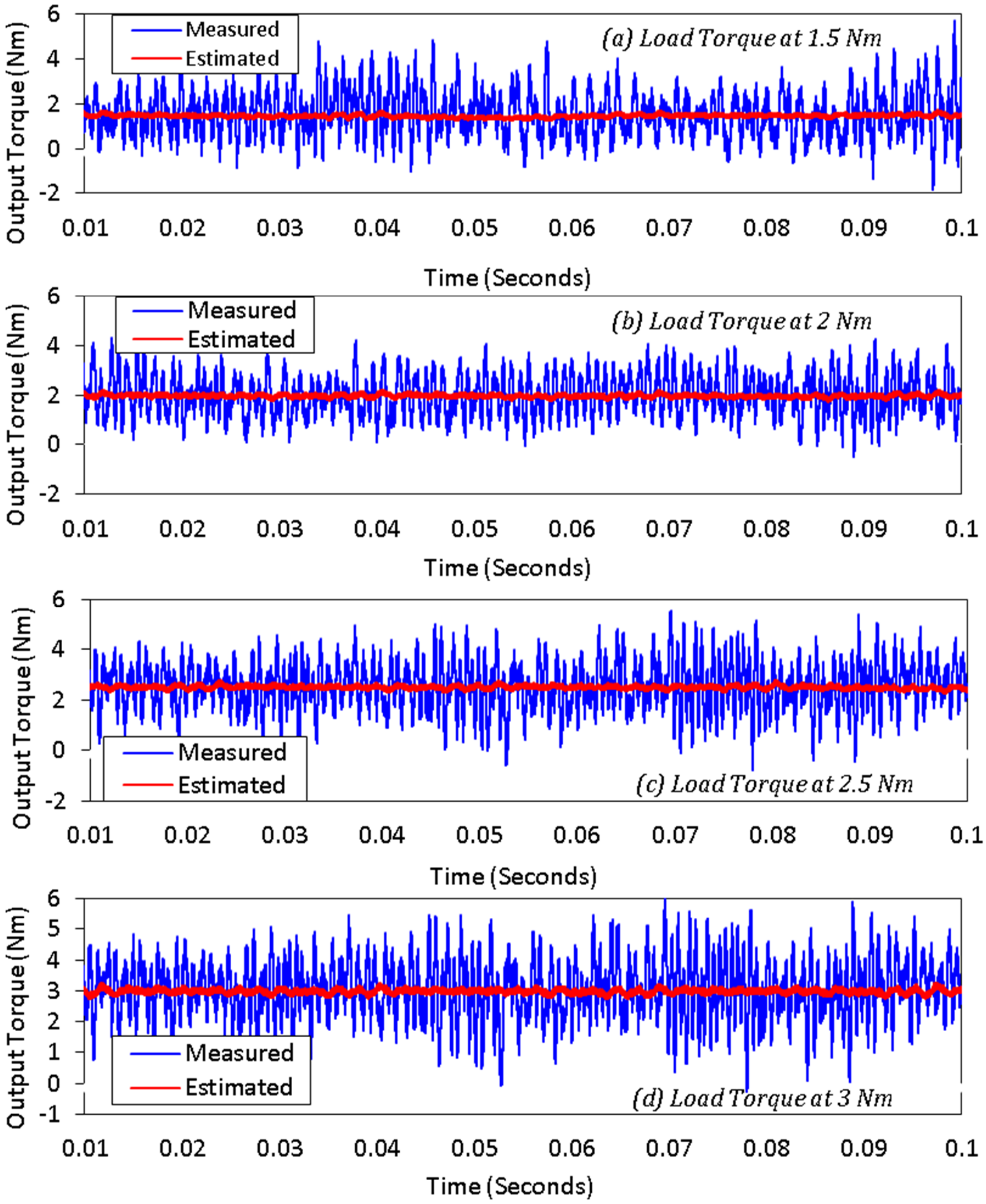

Figure 4.11: Measured & Estimated Output Torque without Filter

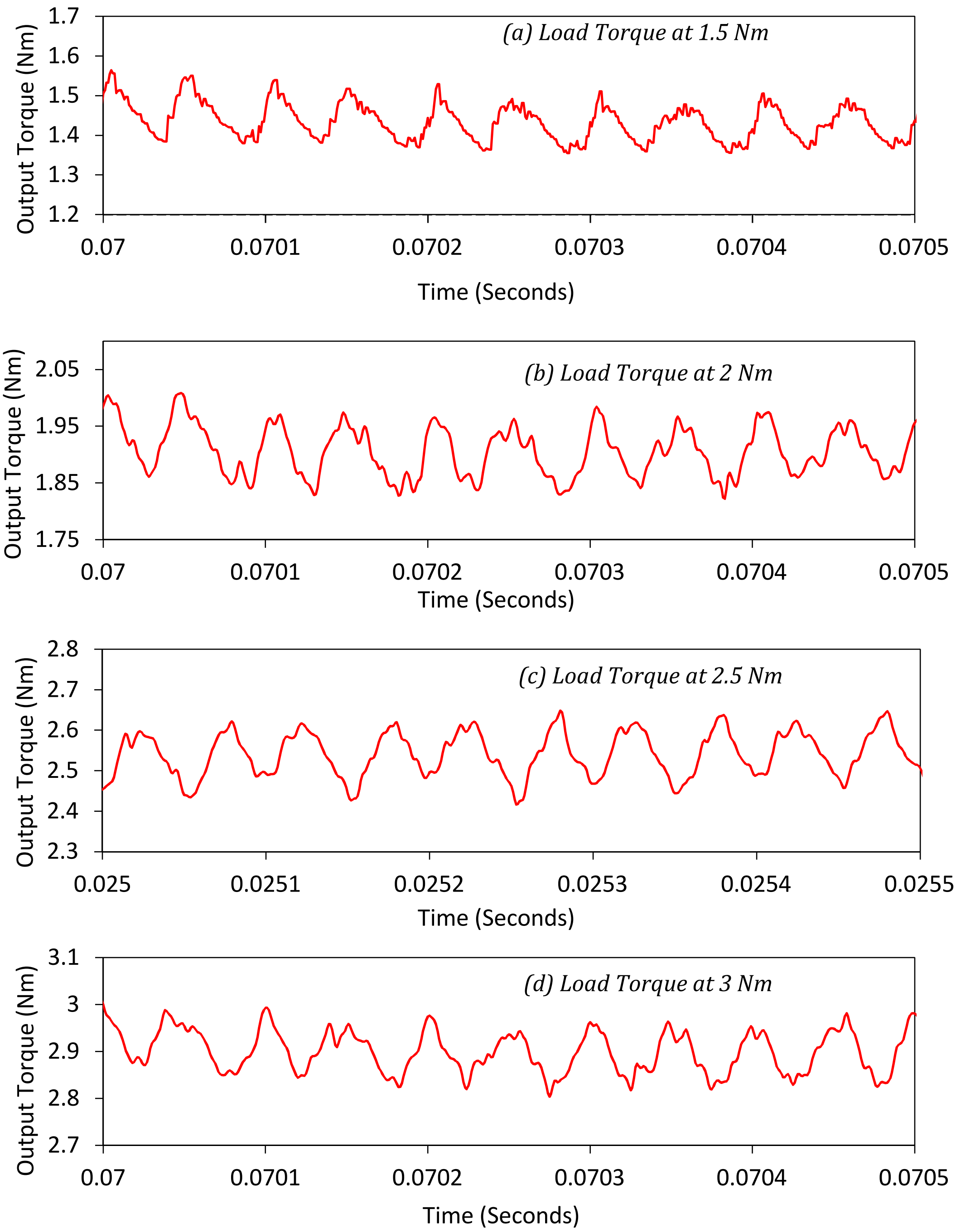

Figure 4.12: Estimated Output Torque without Filter

4.3.2 *Motor with Integrated Filter Inductor*

4.3.2.1 *Measured Voltages, Currents and Output Torque*

In this section, the experimental results are analysed to determine the effectiveness and performance of the motor with integrated filter inductor in steady state condition. The tests were performed at a motor speed of 2100 RPM and load torque of 1.5 Nm. Figure 4.13 and Figure 4.14 shows the line voltage across the inverter terminals ($V_{c,abc}$) and the line voltage across the motor branch winding ($V_{2,abc}$) respectively, whereas the current through the filter branch ($i_{1,abc}$) and the motor branch current ($i_{2,abc}$) are shown in Figure 4.15 and Figure 4.16 respectively.

The output torque is estimated from the measured filter and motor branch currents and is shown in Figure 4.17. The torque ripple at 1.5Nm load is 20% which is identical to torque ripple when the motor is operating without output filter. This is because half of the motor winding is seeing the filtered currents and the half of the motor winding is exposed to PWM currents. When the motor is operating without output filter, full PWM voltages are applied across the motor windings and hence motor windings carry the entire PWM currents.

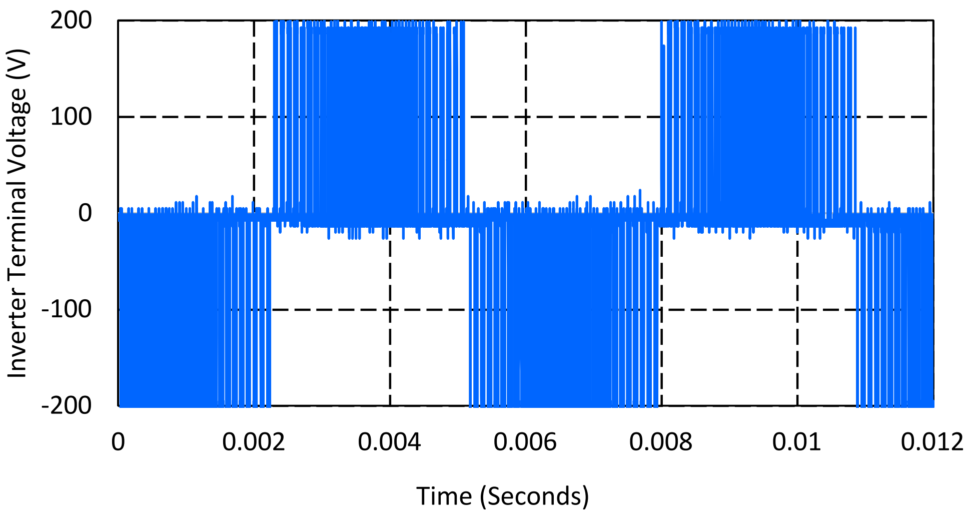

Figure 4.13: Line-to-line Inverter Terminals Voltage with Integrated Filter (V_{AB})

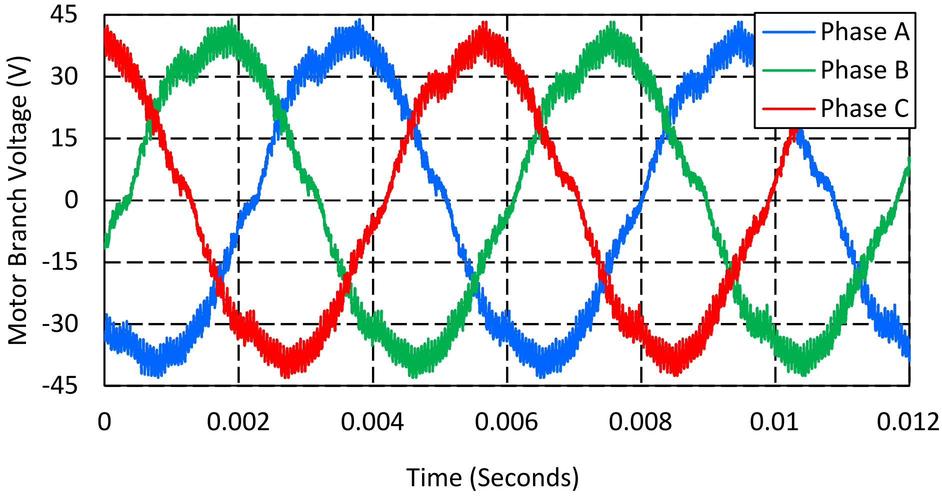

Figure 4.14: Line-to-line Motor Branch Voltage with Integrated Filter

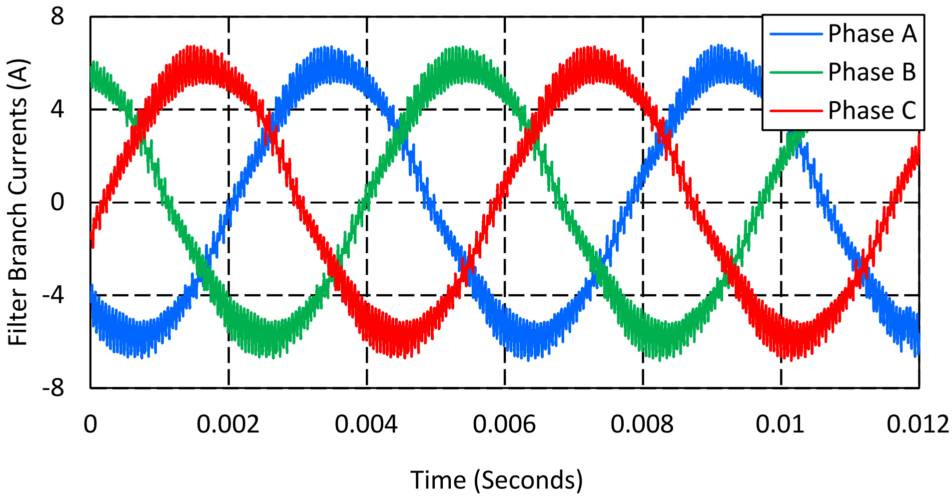

Figure 4.15: Filter Branch Currents with Integrated Filter

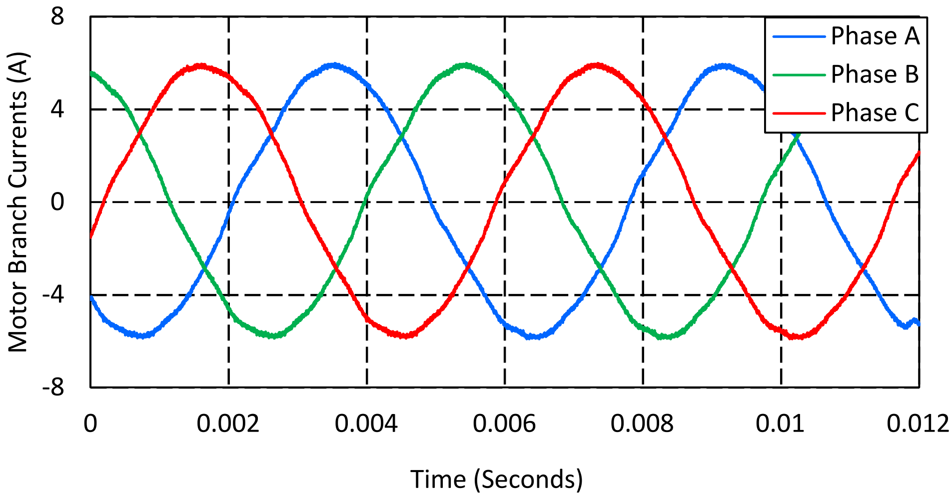

Figure 4.16: Motor Branch Currents with Integrated Filter

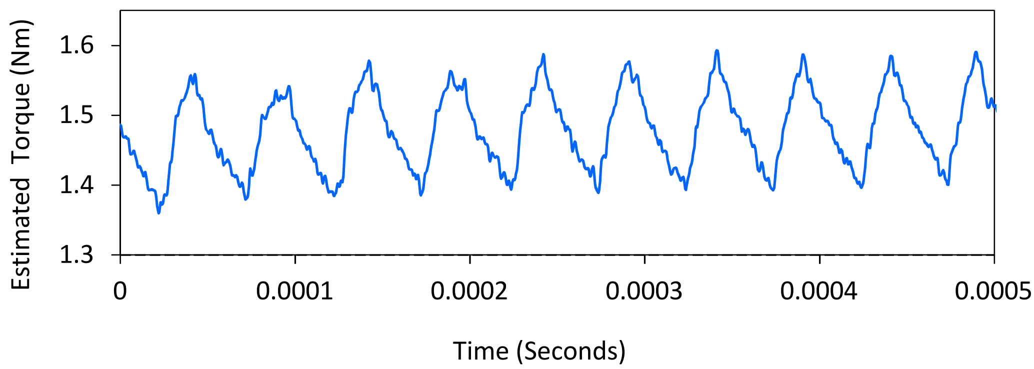

Figure 4.17: Estimated Output Torque with Integrated Filter

From the experimental results, it can be observed that half of the motor windings experience the filtered sine-wave voltages. This reduces the insulation stress from half of the motor windings and the power losses associated with the PWM switching components. Furthermore, the added losses, weight and size due to external filter inductor is also be eliminated.

The FFT of the inverter terminals voltage (V_c) and the voltage across motor branch (V_2) are shown in Figure 4.18 and Figure 4.19 respectively, whereas FFT of the filter branch current (i_1) and motor branch current (i_2) are shown in Figure 4.20 and Figure 4.21 respectively. In comparison with the motor operating without filter, the switching component of motor branch voltage is reduced by 97.9% whereas the switching component of motor branch current is reduced by 95%.

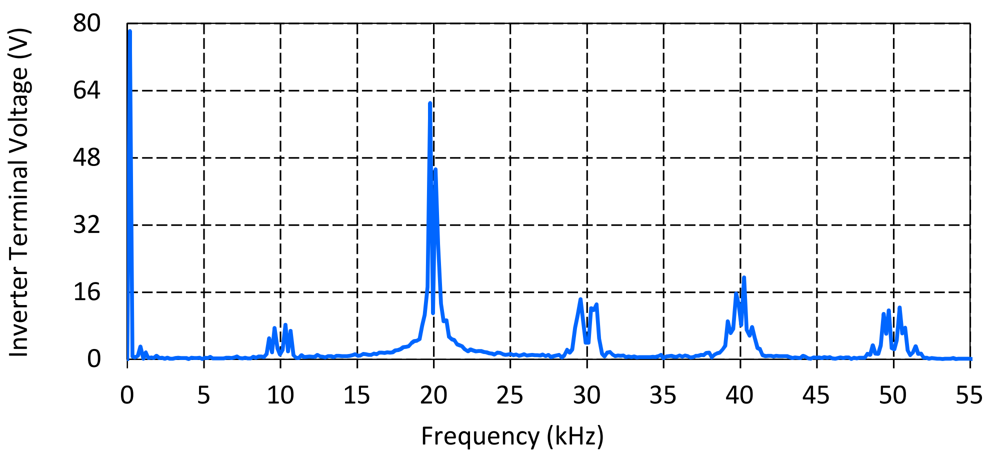

Figure 4.18: FFT of Inverter Terminal Voltage with Integrated Filter

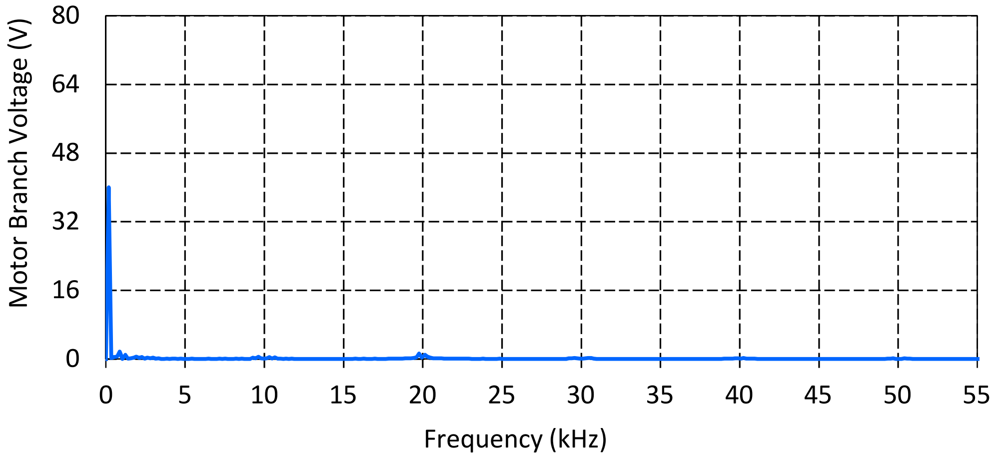

Figure 4.19: FFT of Motor Branch Voltage with Integrated Filter

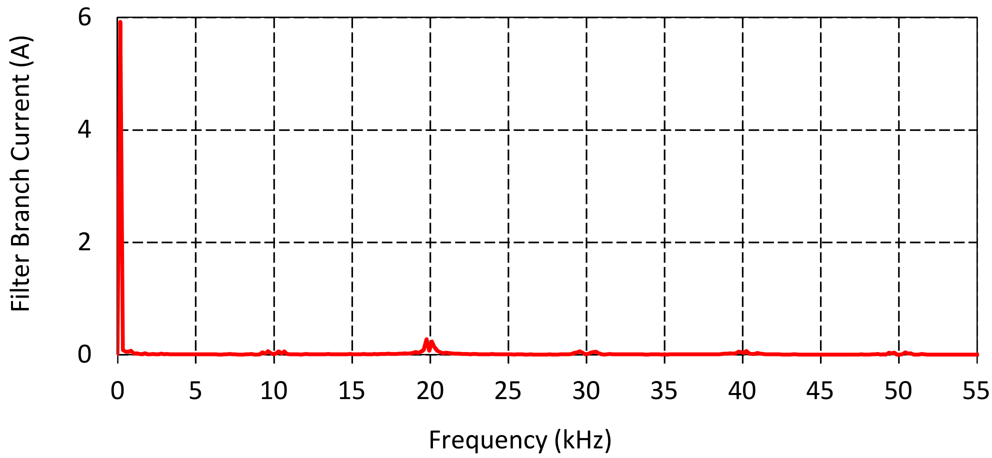

Figure 4.20: FFT of Filter Branch Current with Integrated Filter

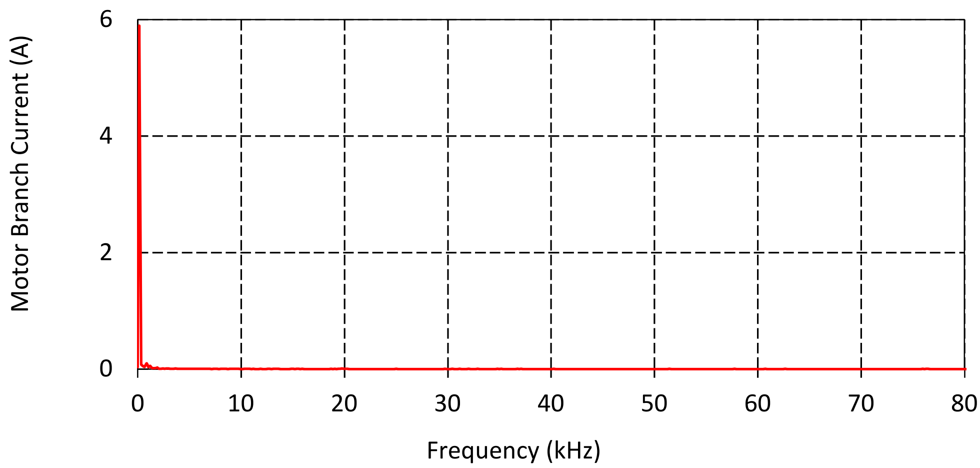

Figure 4.21: FFT of Motor Branch Current with Integrated Filter

A detailed experimental analysis and tests were carried out to validate the motor with integrated filter inductor whilst varying the motor speed, load torque and switching frequency of the inverter. The motor speed is varied from 1200 RPM to 2100 RPM in step of 300 RPM. The load torque is varied between 1.5 Nm to 3 Nm in step of 0.5 Nm. For both variables (motor speed and load torque), the switching frequencies of 10 kHz, 5 kHz, and 15 kHz is considered.

The waveforms of inverter terminal voltage, motor branch voltage, filter branch current, motor branch current and output torque at switching frequency at 10 kHz is shown in Appendix D1 whereas, the filter and motor branch current ripple at switching frequencies of 5, 10 and 15 kHz is shown in section 4.3.2.2.

4.3.2.2 Filter and Motor Branch Current Ripple

Due to the wide measuring range of the torque transducer, it is difficult to measure the torque precisely in the range of 3Nm, so the switching ripple component is evaluated in terms of filter and motor branch currents. Various tests were conducted in order to determine the switching current ripple. The ripple current is expressed in percentage of the fundamental value. The filter and motor branch currents were measured at different speed, mechanical load and switching frequency of the inverter. The motor speed and mechanical load were varied from 1200 RPM to 2100 RPM, 1.5 Nm to 3 Nm respectively at switching frequencies of 5, 10 and 15 KHz. The percentage current ripple of filter branch at different switching frequencies are shown in Figure 4.22 (a)-(c), whereas the motor branch current ripple is shown in Figure 4.23 (a)-(c).

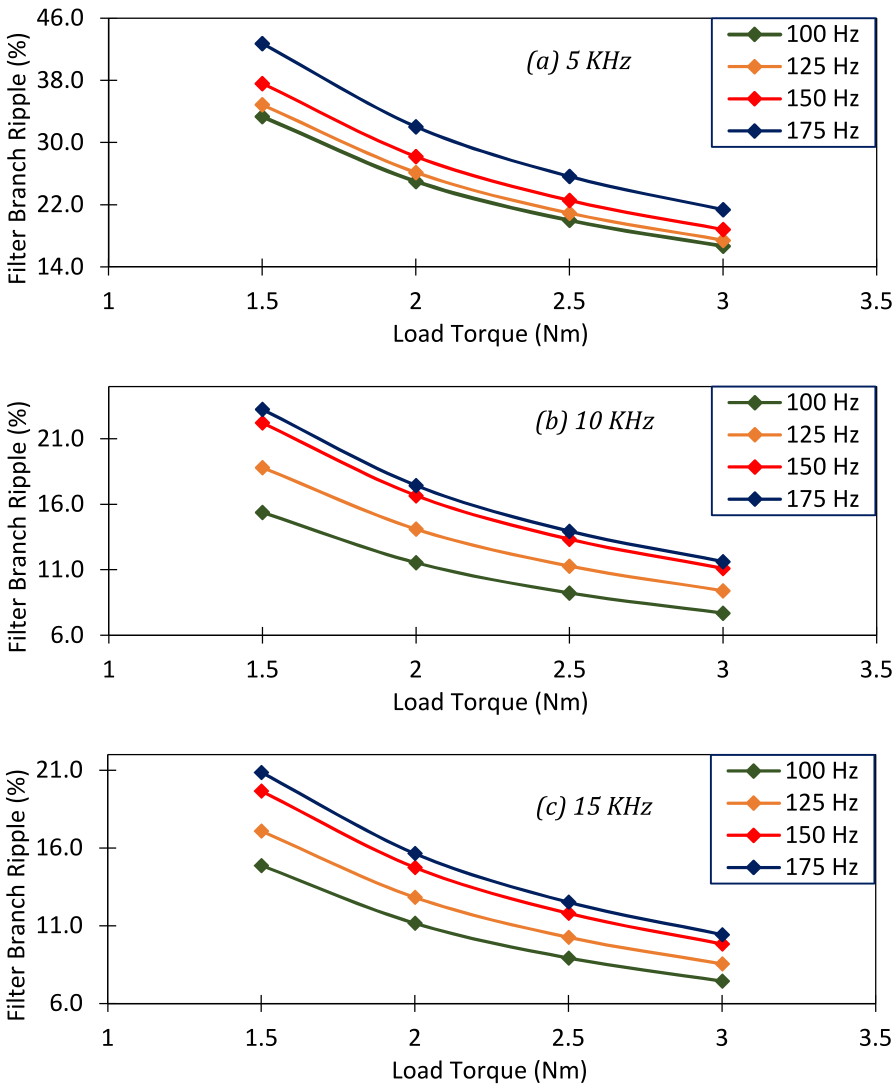

Figure 4.22: Measured Filter Branch Current Ripple (%)

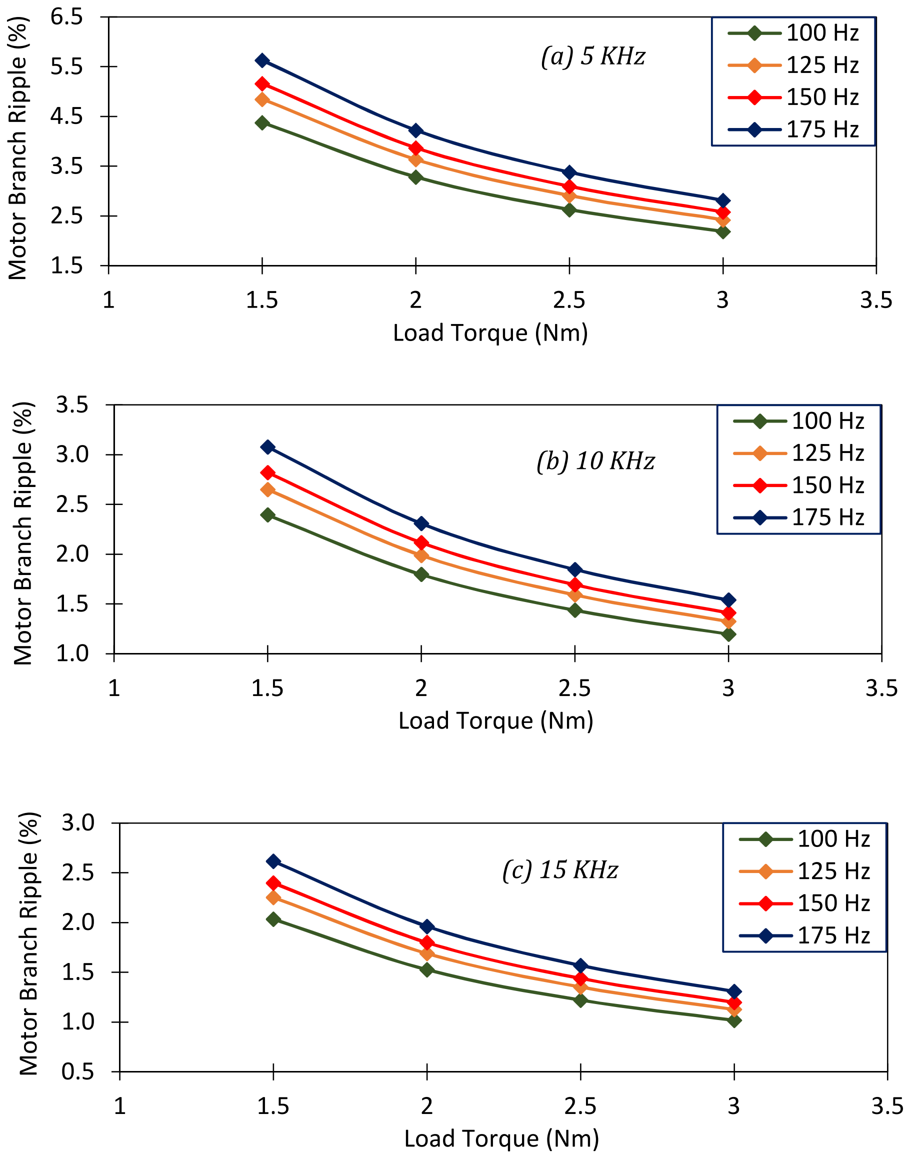

Figure 4.23: Measured Motor Branch Current Ripple (%)

It can be observed that both filter and motor branch currents are reduced as the load torque is increased since the switching ripple component is solely dependent on the filter branch inductance which remains unchanged with the mechanical load on the motor. On the other hand, the ripple current is decreased as the switching frequency of the inverter is increased. This is because the switching period is high for lower switching frequency and hence switching current rises for a longer duration.

4.3.2.3 Phase shift between Filter and Motor Branch Current (α)

The addition of filter capacitance and damping resistance between the motor windings produce a phase shift (α) between filter and the motor branch current. This phase shift affects the electromagnetic torque since only filter branch current is controlled and motor branch current is left uncontrolled. In order to see this effect, the phase shift is estimated using the measured filter and the motor branch current at different rotor speed and load torque and switching frequency held at 10 kHz.

As can be seen from Figure 4.24 that the phase shift due to the filter RC branch is very small. This is because the filter RC branch is designed to act as a high impedance branch at fundamental frequency and act as a low impedance branch above the filter resonance frequency, which will allow the switching component to pass through it.

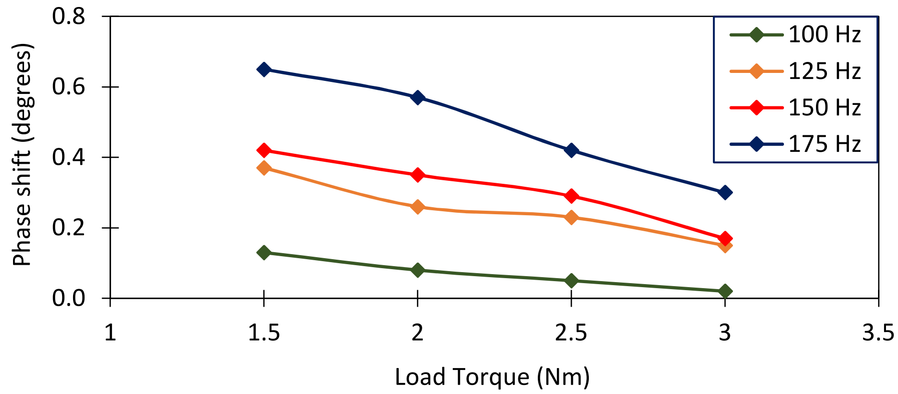

Figure 4.24: Phase shift between Filter and Motor Branch Current at F_{sw}=10 KHz

4.3.3 Motor with External EE Core Filter Inductor

4.3.3.1 Measured Voltages, Currents and Output Torque

Experimental results in this section are examined to determine the performance of the motor with external filter inductor in steady state condition. The tests were performed at a motor speed of 2100 RPM and load torque of 1.5 Nm. Figure 4.25 and Figure 4.26 shows the line voltage across the inverter terminals ($V_{c,abc}$) and the line voltage across the motor windings ($V_{2,abc}$) respectively, whereas the current through the external filter inductor ($i_{1,abc}$) and the motor current ($i_{2,abc}$) are shown in Figure 4.27 and Figure 4.28 respectively.

The output torque is estimated from the measured motor currents and is shown in Figure 4.29. The torque ripple at 1.5Nm load is 7% which is lower than the motor with integrated filter inductor as expected. This is because half of the motor winding in the integrated motor is exposed to PWM currents and the other half seeing the filter currents. On the other hand, entire motor winding sees the filtered currents when the external filter inductor is used which is free from the switching frequency component.

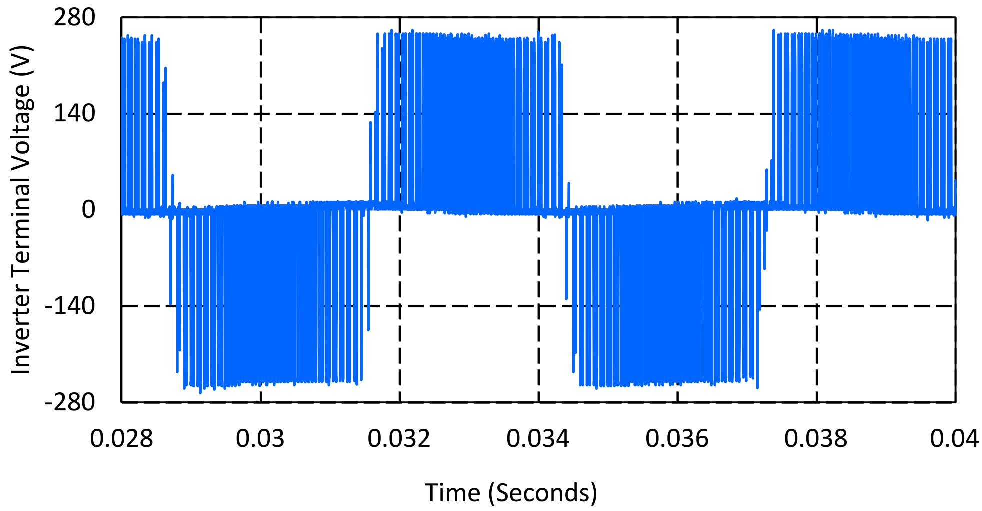

Figure 4.25: Line-to-line Inverter Terminal Voltage with External Filter Inductor (V_{AB})

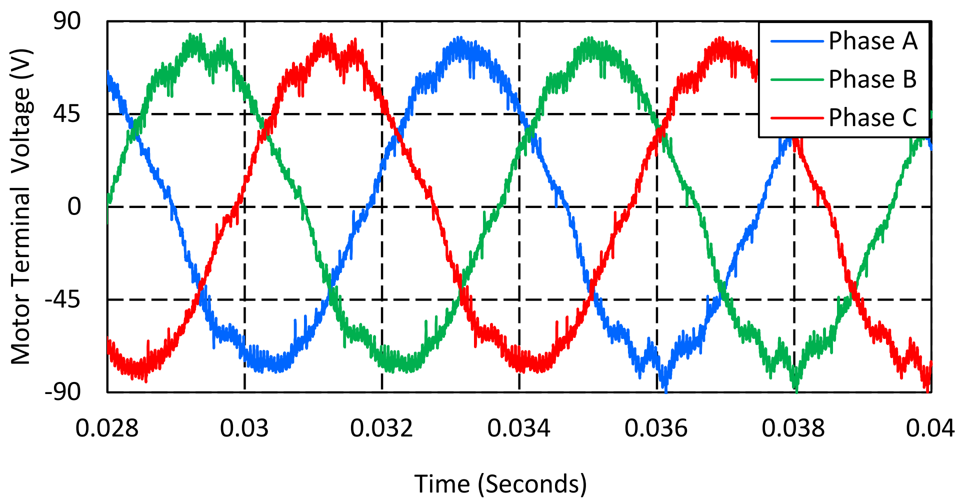

Figure 4.26: Line-to-line Motor Voltage with External Filter Inductor

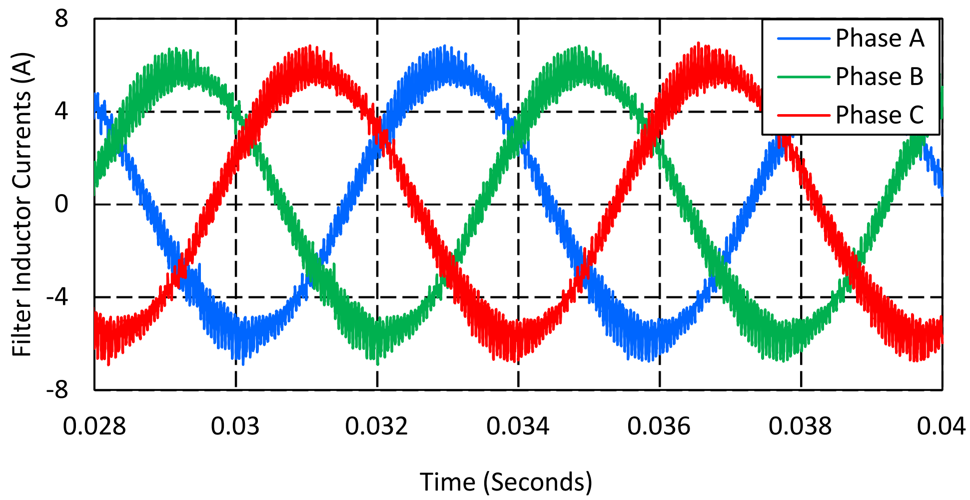

Figure 4.27: Line-to-line Filter Inductor Currents with External Filter Inductor

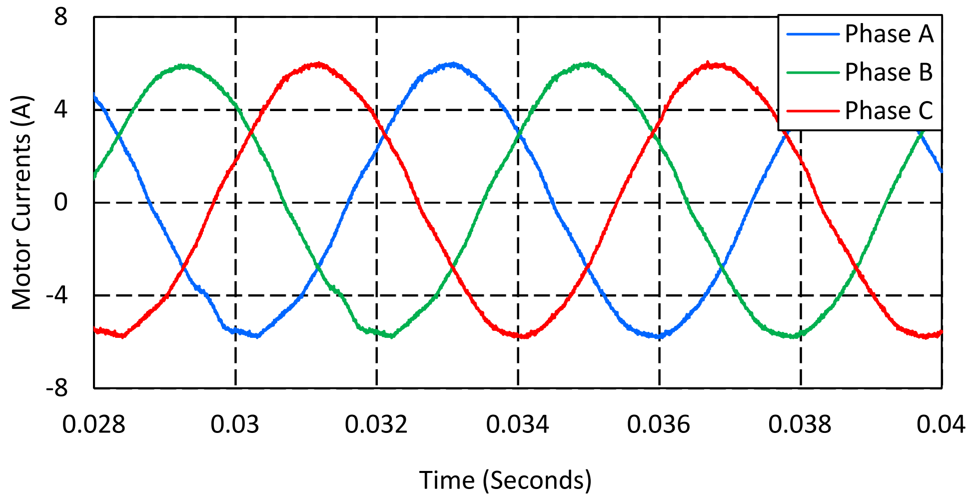

Figure 4.28: Line-to-line Motor Currents with External Filter Inductor

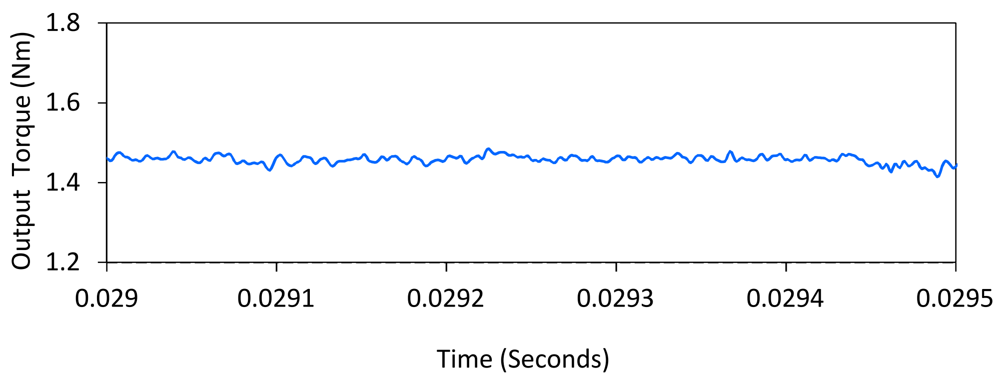

Figure 4.29: Estimated Output Torque with External Filter Inductor

The FFT of the inverter terminals voltage (V_c) and the voltage across motor windings (V_2) are shown in Figure 4.75 and Figure 4.76 respectively, whereas FFT of the filter inductor current (i_1) and motor current (i_2) are shown in Figure 4.77 and Figure 4.78 respectively. In comparison with the motor operating without filter, the switching component of motor terminal voltage is reduced by 97.4% whereas the switching component of motor current is reduced by 95%. The comparison of filter performance in terms of reduction in the switching component is shown in Table II for the motor without output filter, with integrated filter inductor and with external filter inductor.

Table II: % Comparison of Switching Component with and without Filter

Switching Component (20 KHz)	Motor without Output Filter	Motor with Integrated Inductor	Motor with External Inductor	Units
Motor Voltage	62	1.31	1.62	V
Motor Current	0.15	0.008	0.008	A

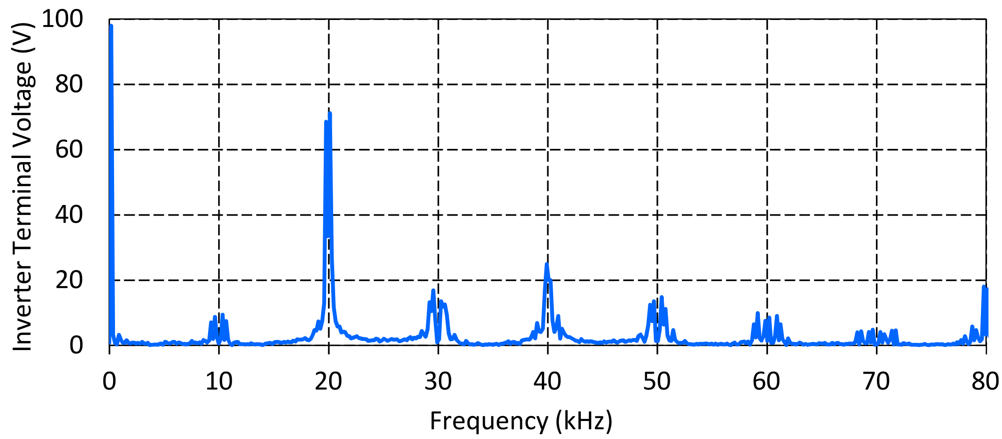

Figure 4.30: FFT of Inverter Terminal Voltage with External Filter Inductor

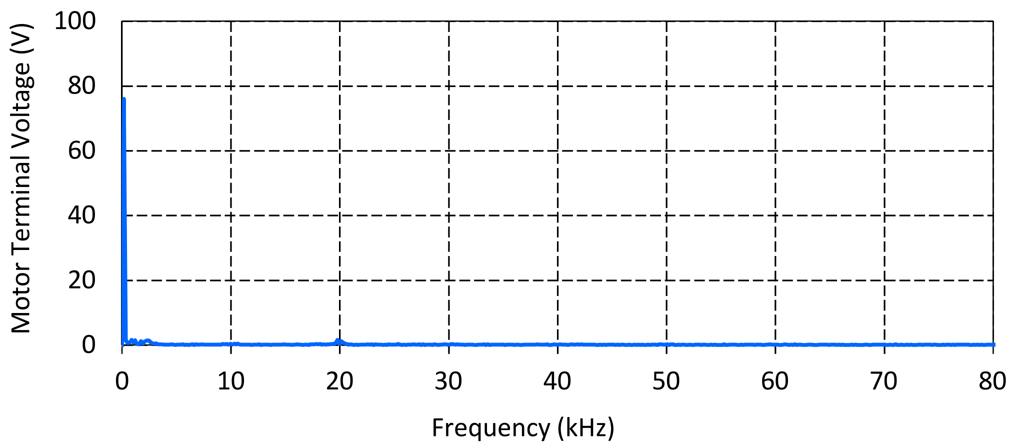

Figure 4.31: FFT of Motor Branch Voltage with External Filter Inductor

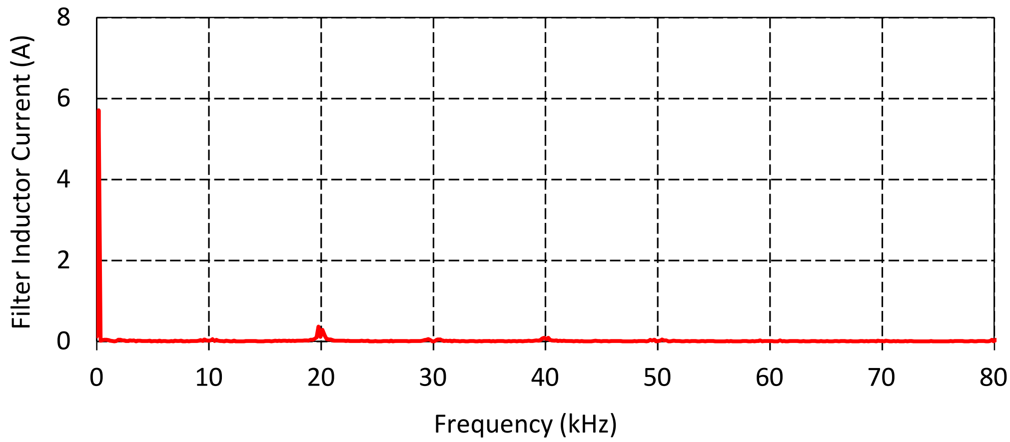

Figure 4.32: FFT of Filter Branch Current with External Filter Inductor

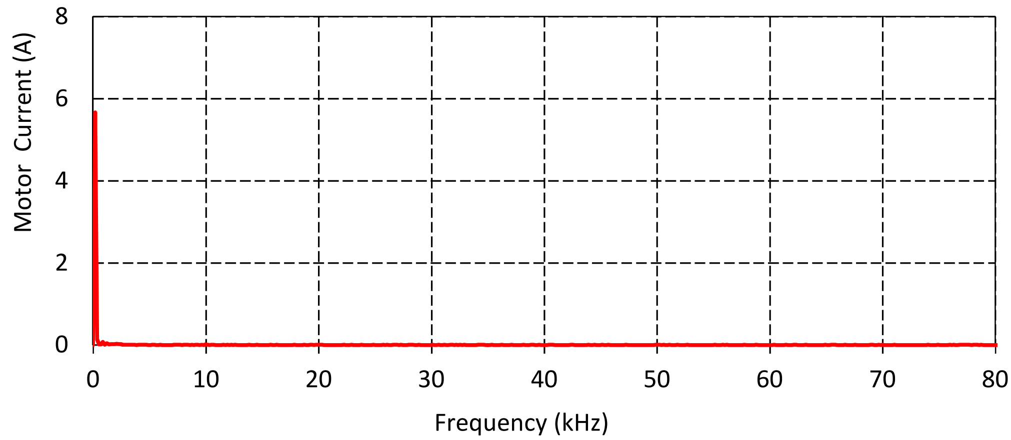

Figure 4.33: FFT of Motor Branch Current with External Filter Inductor

The waveforms of inverter terminal voltage, motor branch voltage, filter inductor current, motor current and output torque at switching frequency at 10 kHz is shown in Appendix D2 whereas, the motor current ripple at switching frequencies of 5, 10 and 15 kHz is shown in section 4.3.3.3.

4.3.3.3 Motor Current Ripple

Various tests were conducted in order to determine the switching ripple of motor current. The ripple current is expressed in percentage with respect to the fundamental value. The motor currents were measured at different speed, mechanical load and switching frequency of the inverter. The motor speed and mechanical load were varied from 1200 RPM to 2100 RPM, 1.5 Nm to 3 Nm respectively at switching frequencies of 5, 10 and 15 kHz. The percentage current ripple of the motor current is shown in Figure 4.34 (a)-(c).

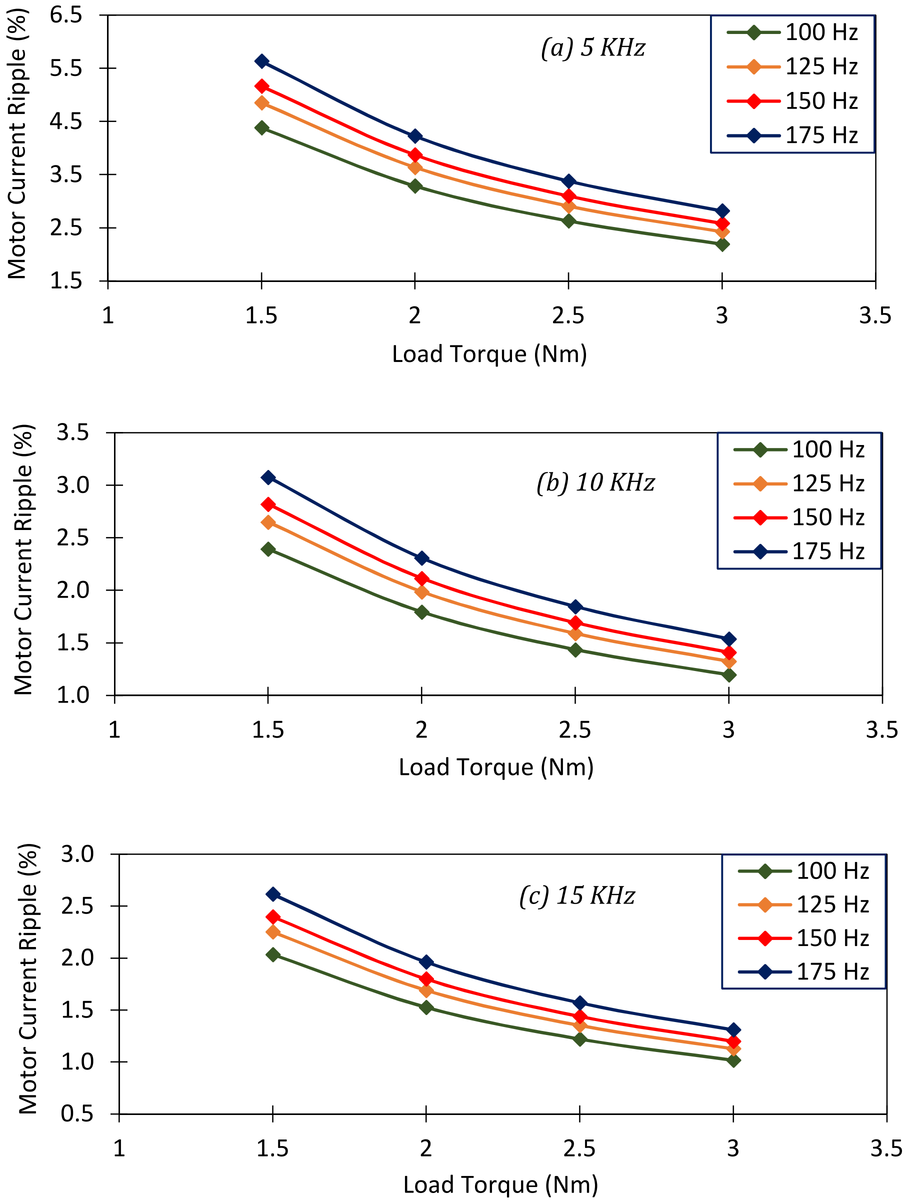

Figure 4.34: Measured Motor Current Switching Ripple (%)

4.4 Comprehensive Experimental Loss Characterization

4.4.1 Total Loss Comparison

The motor losses were evaluated by measuring the input electrical power to the motor terminals and output mechanical power delivered at the shaft as illustrated in Figure 4.6 (a)-(b). The motor losses is the difference of input electrical power and the output mechanical power which can be expressed as,

$$P_{m,loss} = P_{in} - P_{out} = P_{in} - (T_{out} \,.\, \omega_r) \tag{4.2}$$

where, P_{in} is the input electrical power in watts, P_{out} is the output mechanical power in watts, T_{out} is the measured output torque in Nm and ω_r is rotor speed in rad/s.

The motor losses were measured at different rotor speed and mechanical load while keeping the inverter switching frequency at 10 kHz. The motor speed is varied from 1200 RPM to 2100 RPM in step of 300 RPM whereas the load torque is applied from 1.5 Nm to 3 Nm in step of 0.5 Nm.

Figure 4.35 (a)-(d) shows the total loss comparison of the motor with an integrated inductor and the motor with an external inductor at the frequency of 100 Hz, 125 Hz, 150 Hz and 175 Hz respectively. It can be observed that the total losses in the motor with external filter inductor are higher than the integrated motor due the added losses associated with the external inductor. The added losses of the external inductor and its associated weight and volume are removed since the integrated motor does not require the external inductor to filter out the switching component.

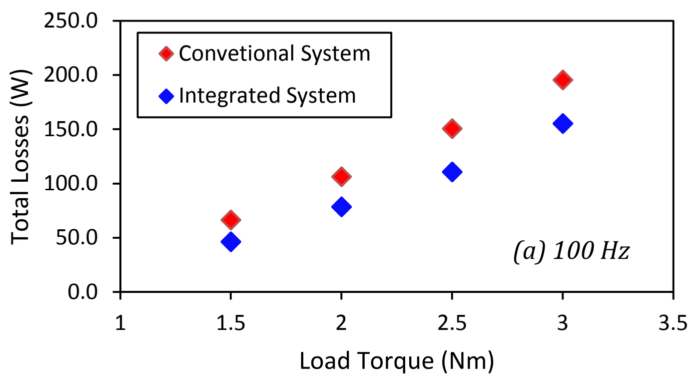

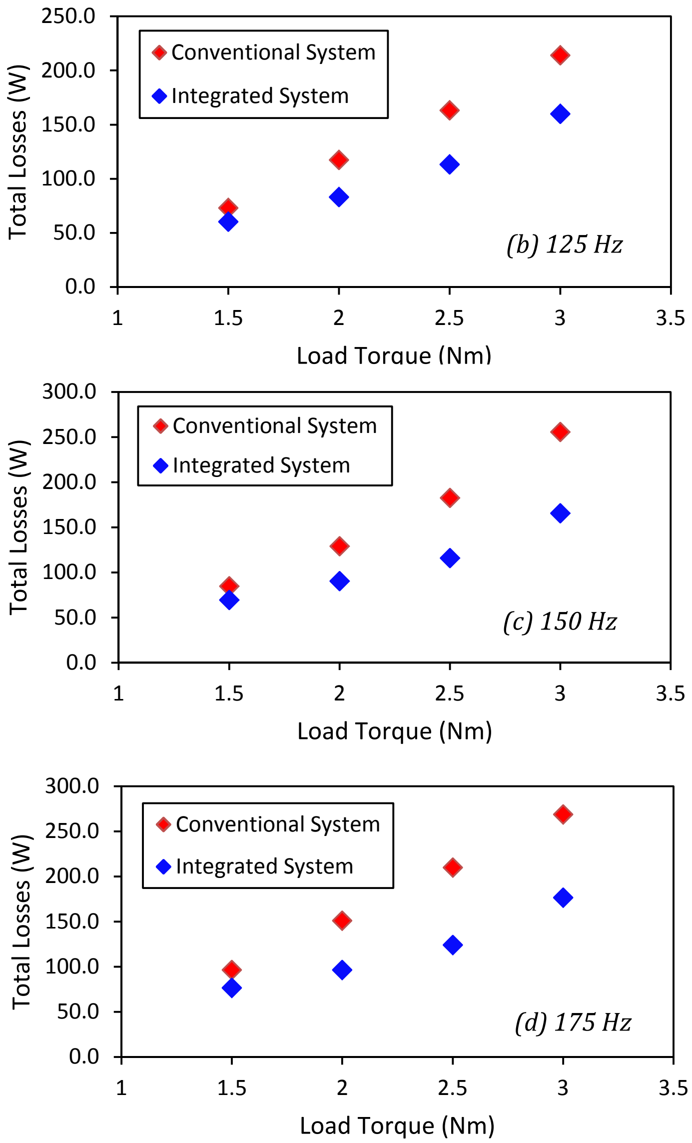

Figure 4.35: Total Loss Comparison of motor with integrated and external inductor

4.4.2 Comparison with Finite Element

In order to compare the finite element results with experimentation, the integrated motor was current driven at 1.5 Nm, 2 Nm 2.5 Nm and 3 Nm. The simulations were carried out at different rotor speeds (electrical) which was varied from 100 to 175 Hz in step of 25 Hz as shown in Figure 4.36 (a)-(d). The total losses include: iron loss, copper loss and eddy current ohmic loss in the permanent magnets whereas the windage and bearing friction losses have been neglected.

It can be observed that the measured motor losses are in a good agreement with the finite element. The difference between the finite element and measured losses might come from the contact resistances, windage and bearing friction losses which have not been considered in the finite element model.

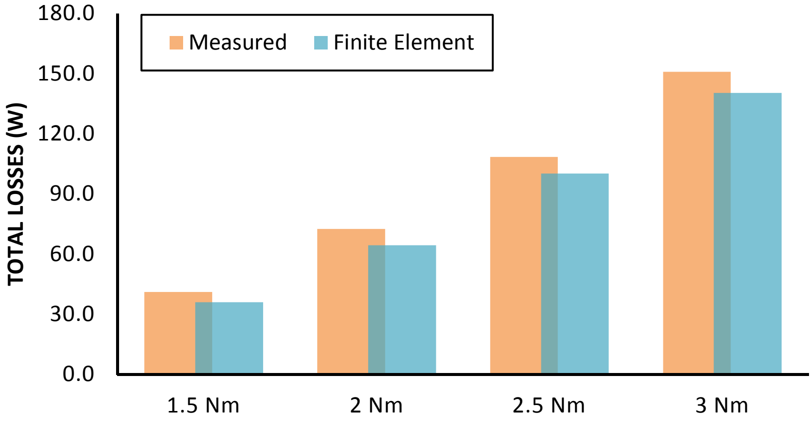

(a) Load Torque at 100 Hz

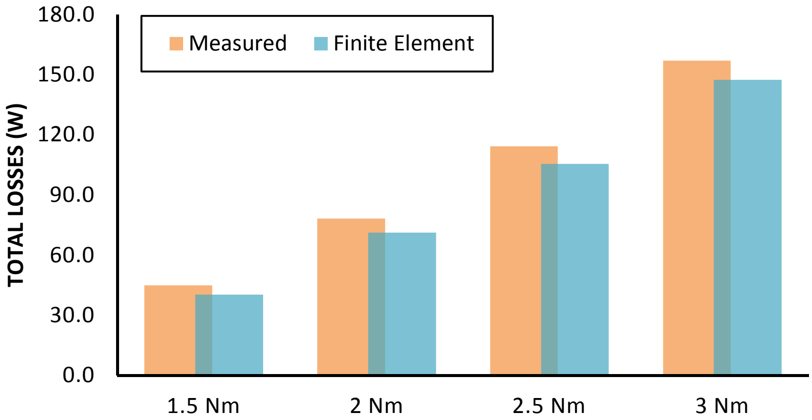

(b) Load Torque at 125 Hz

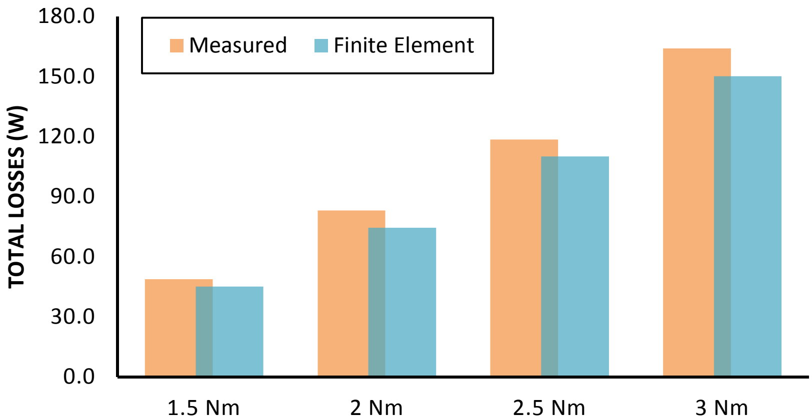

(c) Load Torque at 150 Hz

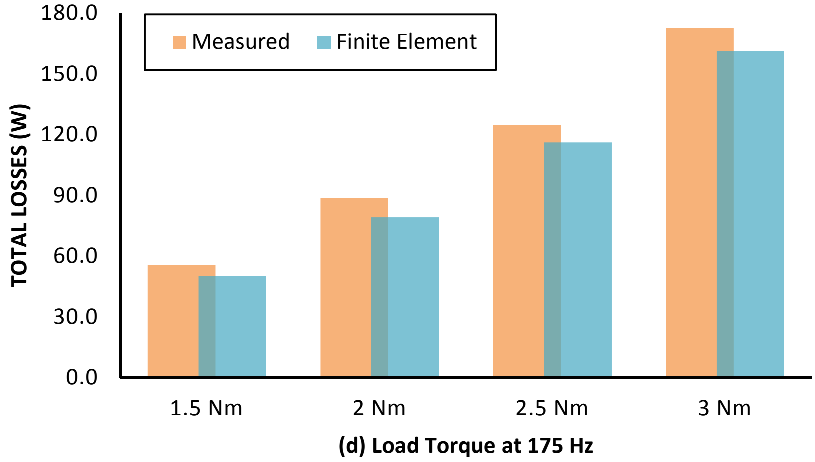

Figure 4.36: FE and Measured Losses of motor with integrated Inductor

4.5 SUMMARY

This chapter described briefly the experimental setup and test-rig to validate the proposed motor with integrated filter inductor with 50% filter branch windings. The experimental results were presented for the motor operating without output filter, motor with integrated inductor and the motor with external EE core inductor. The experimental tests were conducted at different rotor speeds, mechanical load on the shaft and inverter switching frequency. The results were presented in terms of inverter terminal voltage, motor voltage, filter current, motor current output torque and torque ripple. The FFT of inverter voltage, motor voltage, and filter current, motor current had been compared.

The experimental results showed that the proposed integrated motor with 50% filter branch windings effectively eliminates the need of an external filter inductor which reduces the overall losses and associated weight and volume however, the torque ripple is alike when compared to motor operating without filter. From the experimental results, it can be observed that the voltage stress and losses due to PWM current are eliminated in half of the motor windings. Furthermore, the voltage drop due to the external filter inductor is eliminated as well when the integrated motor topology is adopted which reduces the need for extra voltage required by the motor drives from the DC link.

The effectiveness of the motor with integrated and motor with external inductor was determined by comparing the switching ripple current of the motor. The results show identical reduction for both integrated and conventional motors. A comprehensive loss characterization was presented in terms of total losses of the motor with integrated filter inductor followed by the comparison of losses estimated through the finite element with the experimental ones. The finite element losses showed a good agreement with the measured losses of the integrated motor.

4.6 REFRENCES:

[1] *Drivetrain Diagnostics Simulator*. Available: http://spectraquest.com/drivetrains/details/dds/

[2] M. Rottach, C. Gerada, T. Hamiti, and P. W. Wheeler, "Fault-tolerant electrical machine design within a Rotorcraft Actuation Drive System optimisation," in *6th IET International Conference on Power Electronics, Machines and Drives (PEMD 2012)*, 2012, pp. 1-6.

[3] M. Rottach, C. Gerada, T. Hamiti, and P. W. Wheeler, "A computationally efficient design procedure for actuator motors using magnetic reluctance-and thermal resistance network models," in *2012 XXth International Conference on Electrical Machines*, 2012, pp. 2526-2532.

[4] M. Rottach, C. Gerada, and P. W. Wheeler, "Evaluation of motor-drive segmentation strategies for fault-tolerance," in *2013 IEEE ECCE Asia Downunder*, 2013, pp. 530-536.

[5] M. Rottach, C. Gerada, and P. W. Wheeler, "Design optimisation of a fault-tolerant PM motor drive for an aerospace actuation application," in *7th IET International Conference on Power Electronics, Machines and Drives (PEMD 2014)*, 2014, pp. 1-6.

[6] Y. Sozer, D. A. Torrey, and S. Reva, "New inverter output filter topology for PWM motor drives," *IEEE Transactions on Power Electronics,* vol. 15, pp. 1007-1017, 2000.

CHAPTER

5

INTEGRATED MOTOR-SHAPED FILTER INDUCTORS

5.1 INTRODUCTION

This chapter demonstrates novel integrated motor-shaped inductors for motor drive applications. Motor-shaped inductors can be of two types: integrated rotational inductor and integrated rotor-less inductor. The chapter presents the idea of motor-shaped inductors. The integrated rotational inductor is then validated through the finite element to demonstrate the effectiveness of the proposed novel approach followed by its importance and applications. Subsequently, the design procedure of motor-shaped inductors is then presented. At the end, design optimization of motor-shaped inductors is carried out in terms of total losses, weight and AC copper resistance for different slot-pole combinations and winding configuration.

5.2 MOTOR-SHAPED INDUCTORS

The inductor shown in Figure 5.1 is completely different from the traditional inductors that are commonly being employed in the power electronics & drives industry. The motor-shaped integrated inductors are categorized into the following class,

1. Motor-shaped Rotational Inductor and,
2. Motor-shaped Rotor-less Inductor

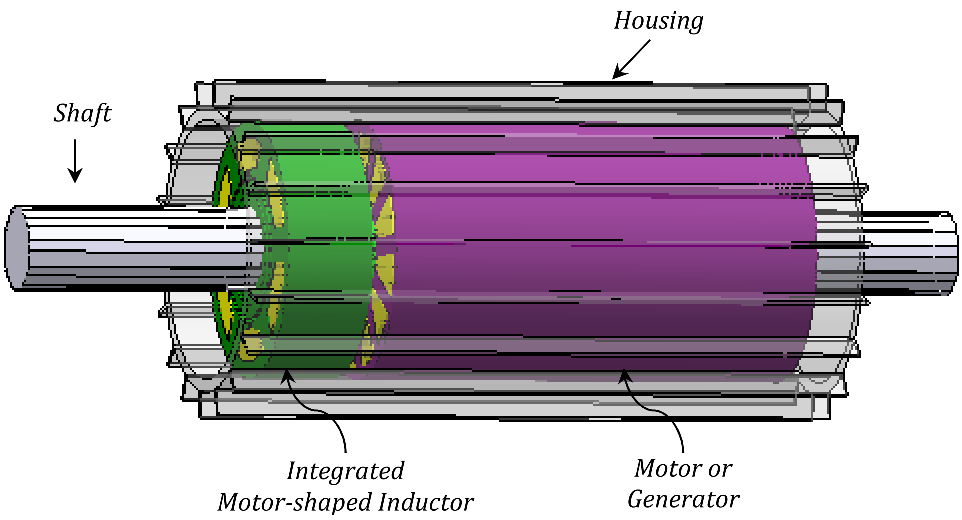

Figure 5.1: Axial View of Integrated Motor-shaped Inductor

5.21 Rotational Inductor

The motor-shaped rotational inductor shown in Figure 5.2 has a stator and a rotor just like electric motor or generator but without any magnets, windings or saliency on the rotor. This motor like shape makes it feasible for the inductor to integrate within the motor or generator by keeping the inductor's rotor on the common rotating shaft. Moreover, the stator of the motor-shaped inductor can use the same motor housing, which completely eliminates the need for a separate cooling system. Since the motor-shaped inductor utilizes the shared cooling system as that of the motor, it can be sized with higher current densities. This would allow a design engineer to design a more compact inductor which leads to a reduction in overall weight and volume.

On the other hand, iron losses through the rotor of the motor-shaped rotational inductor can be minimized if its rotor is rotating synchronously with the motor shaft. Since the magnetic field in the stator of the motor and inductor is rotating at synchronous speed, the magnetic field through the rotor of the inductor will remain induction free. Furthermore, there is a possibility of optimizing its inductance by varying its physical layout such as slot opening, slot opening height, teeth width, teeth height etc. In terms of applications, the motor-shaped rotational inductor is more appropriate for output filter applications, where rotor can be placed easily on the motor shaft and iron losses can be minimized at synchronous speed.

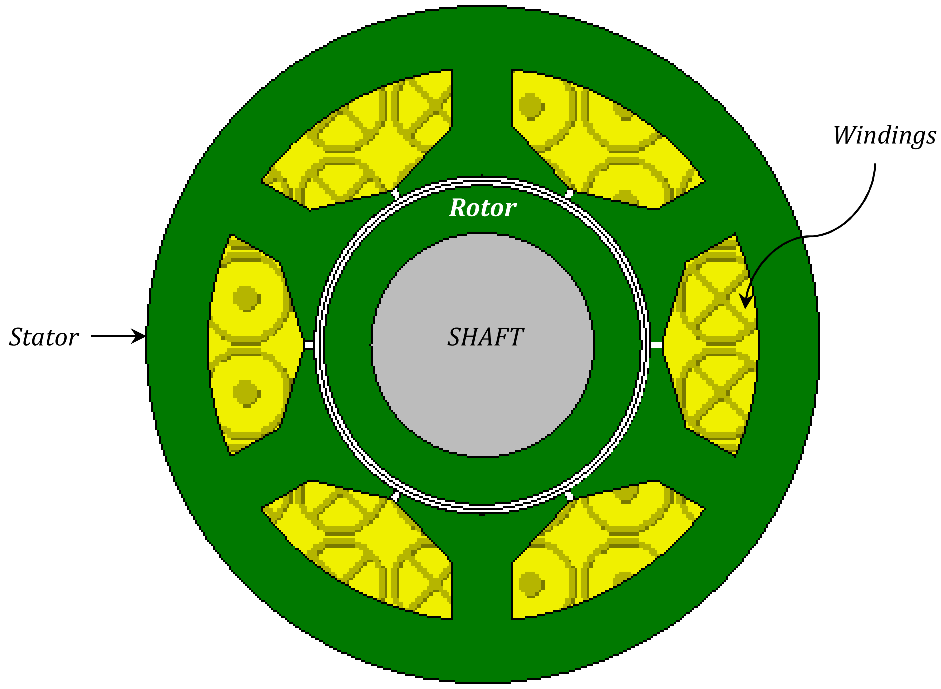

Figure 5.2: 2D View of Motor-shaped Rotational Inductor

5.2.1.1 FE Validation of Rotational Inductor

A FE model was developed as shown in Figure 5.3 in $MagNet - Infolytica$ to verify the concept of motor-shaped rotational inductor. The rotational inductor was driven at the peak current of 18A and the supply frequency of 1000Hz with the rotor rotating and with rotor at standstill. The X and Y components of magnetic flux density in the rotor at one fixed point were assessed for both standstill and rotating rotor. The X and Y components of magnetic flux density were then converted into the $d - q$ reference frame. As the q component of the rotor flux density is zero, only the d component of the rotor flux density is shown in Figure 5.3.

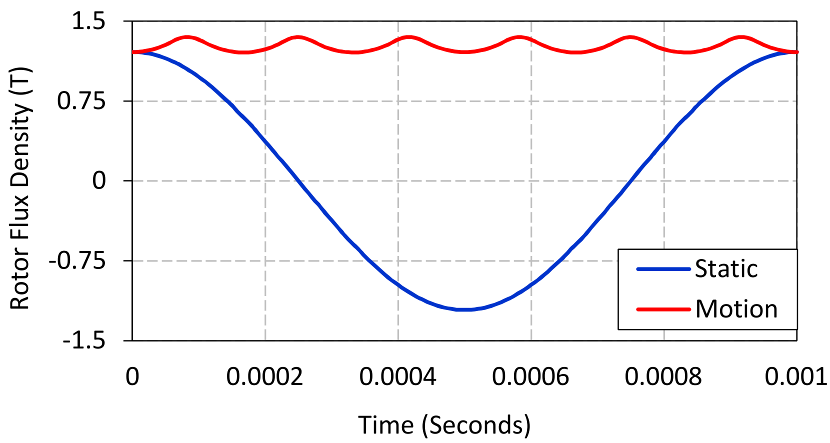

Figure 5.3: 2D View of Motor-shaped Rotational Inductor

From the results obtained, it can be observed that the magnetic field in the rotor is stationary when the rotor rotates at synchronous speed therefore, minimizes the iron losses through the rotor. However, it does contain harmonics due to slotting effect of the stator core. On the other hand, the magnetic field is varying sinusoidally with time when the rotor is at standstill. The iron losses of rotational inductor associated with hysteresis and eddy currents are shown in Table I. The core material used for the motor shaped rotational inductor is silicon steel ($M - 15$) [1, 2]. From Table I, it is important to note that both hysteresis and eddy currents losses have been reduced considerably in the rotor when rotor is rotating synchronously with the speed of magnetic field in the stator, which is produced by the stator currents. 78.2% loss reduction is obtained for the rotational inductor when the rotor is rotating as compared to the stationary rotor. However, a small amount of iron loss is still present due to the slotting effect of the stator windings and the non-uniform distribution of magnetic field in the rotor.

Table I: Rotor Iron Loss for Rotational Inductor

PARAMETERS	STATIC	MOTION	UNITS
Hysteresis Loss	17.4	1.33	W
Eddy Current Loss	33.6	9.77	W
Total Losses	51	11.1	W
Loss Reduction	-	78.2	%

5.22 Rotor-less Inductor

As its name suggests, the motor-shaped rotor-less inductor as shown in Figure 5.4 has the same structure as the motor-shaped rotational inductor without rotor and with larger slot opening height to avoid the magnetic saturation. The rotor-less inductor can also be integrated with the motor or generator by placing it axially inside the same housing. In terms of applications, this design is a suitable solution for high power line inductors or isolation transformers where supply frequency is fixed and cooling requirements are high. It can also be employed for power transformer applications, where there is a need of integrating power transformers within the same housing as that of the generator.

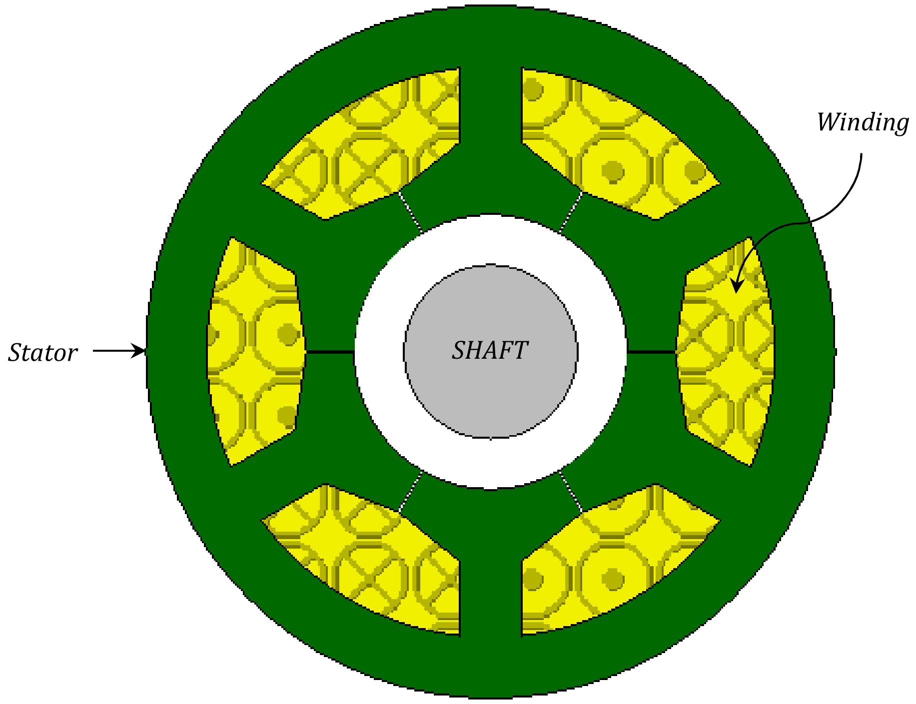

Figure 5.4: 2D View of Motor-shaped Rotor-less Inductor

5.3 DESIGN PROCEDURE FOR MOTOR-SHAPED INDUCTORS

This section presents the design procedure of motor-shaped integrated inductor i.e. rotational inductor and rotor-less inductor. The design procedure of motor-shaped inductors are linked to the design of EE core inductor as explained in section 1.3. Once the area product ($W_a.A_c$) is calculated for the design of EE core inductor, the motor-shaped inductors can be sized up by the following procedure.

5.3.1 Sizing of Motor-shaped Inductors

The structural layout of the motor-shaped rotational and rotor-less is shown in Figure 5.5(a) and Figure 5.5(b) respectively, whereas the flowchart algorithm of converting EE core inductor into motor-shaped inductors is shown in Figure 5.6. For both motor-shaped inductors, windows area (W_a) is kept same for each slot in order to have a common reference point for comparison between EE core and motor-shaped inductors, hence the cooling system is kept the same for EE core and motor-shaped inductor. For 6 slots inductor, the tooth width (T_w) is selected close to the limb length (L_{limb}) of EE core inductor as the core area (A_c) is variable near the tooth. For higher slots inductor tooth width needs to be adjusted in proportion to the total number of slots. The back iron width (B_w) is adjusted to keep the identical flux density in the core. The airgap length (L_g) and the slot opening (S_o) are varied until the required flux density (B_{max}) is reached in the stator teeth and back iron. Subsequently, the rotor width (R_w) is varied until the same flux density is achieved as that of teeth and back iron. In the end, rotor is removed for the rotor-less inductor and slot opening height (S_{oh}) is increased to keep the uniform flux density throughout the stator slots. Since the airgap between rotor and stator is absent in case of rotor-less inductor, the inductance is only controlled by the width of stator slot openings.

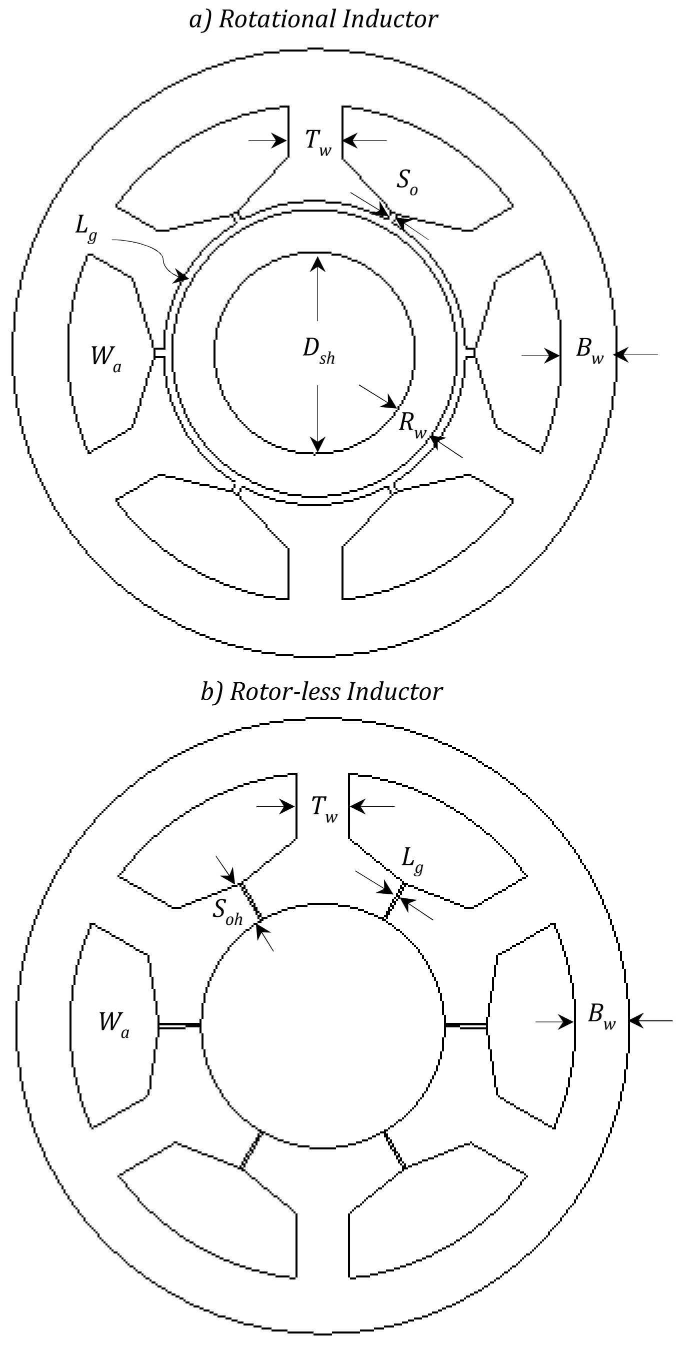

Figure 5.5: Structural Layout of Motor-shaped Inductors

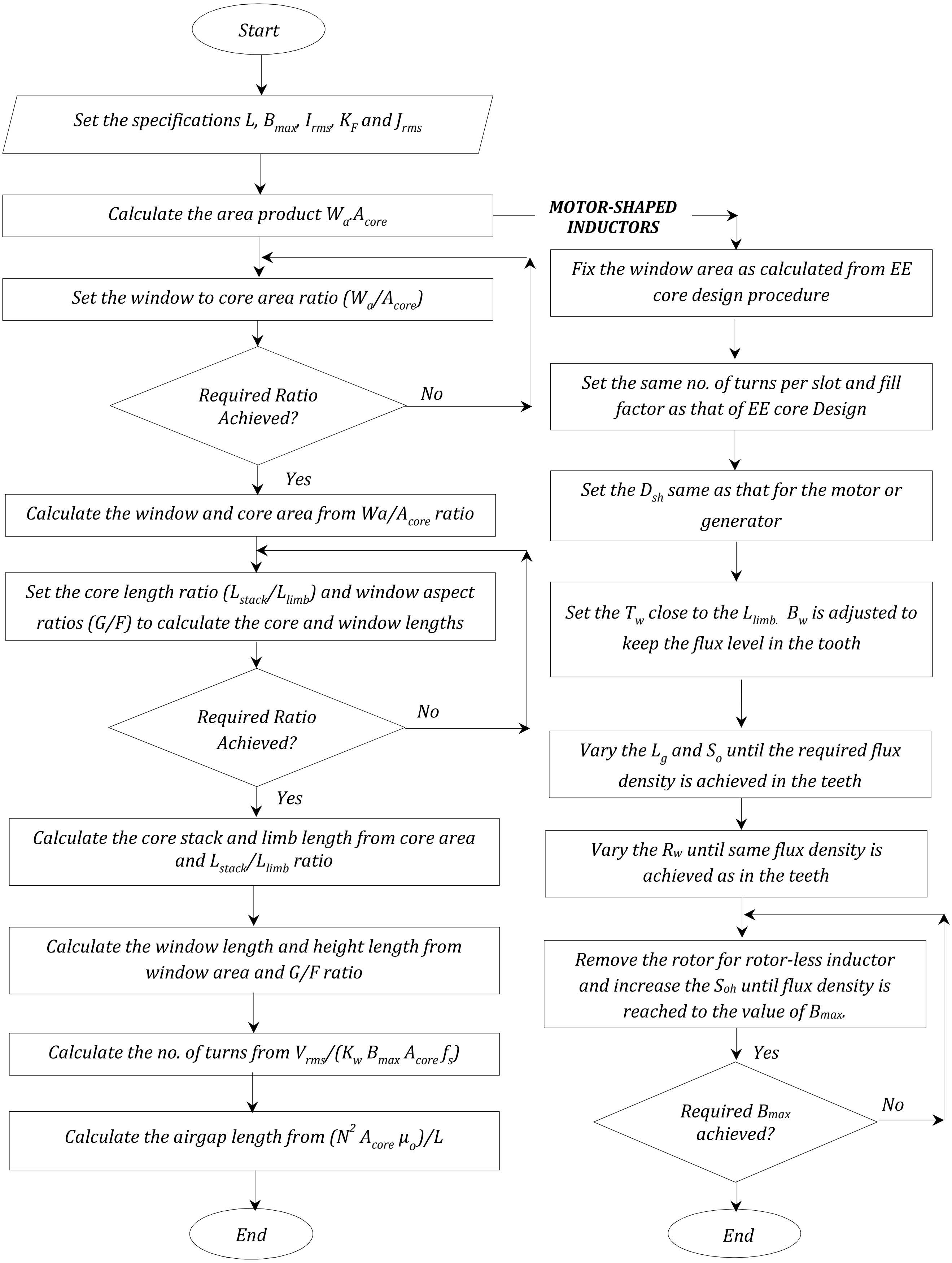

Figure 5.6: Method to Converter EE Core Inductor to Motor-shaped Inductor

5.4 DESIGN OPTIMIZATION OF ROTATIONAL INDUCTOR

A number of motor-shaped inductors were designed, with various slot-pole combinations for integrated rotational inductors. The rotational inductors were optimized and then compare with conventional EE core inductor in terms of total losses, weight and AC resistance of the stator windings. 2, 4 and 6 poles with 6, 12 and 18 slots have been considered. On the other hand, concentrated winding (CNW) and distributed winding (DW) with single layer (SL) and double layer (DL) were considered. All inductor designs were modelled and analyzed through two dimensional finite element analyses (FEA). EE core inductor, which is designed in chapter 3 is compared with motor-shaped rotational inductors. For the purpose of fair comparison, the type of core material, synchronous inductance, operating flux density, fundamental frequency, switching frequency, number of turns per slot, slot fill factor, slot area, conductor diameter and cooling considerations were kept same, the details of which are provided in Table II.

Table II: Specifications of Rotational Inductor Design

SPECIFICATIONS	VALUES	UNITS
Core Material	Non-oriented Steel M – 15	-
Required Inductance	1.3	mH
Operating Current	18	A
Operating Frequency	1000	Hz
Switching Frequency	10, 15 & 20	kHz
Turns per slot	20	-
Slot Fill Factor	0.5	-
Slot Area	212	mm-sq
Conductor Diameter	2.6	mm
RMS Current Density	2.36	A/mm^2
Shaft Diameter	27	mm
Cooling Considerations	Natural Convection	-

In the inductor design procedure, the DC copper loss (without end windings) and axial length of the inductor were initially kept same for both EE core and rotational inductors. Since the DW gives higher inductance than CNW, the axial length of rotational inductor was altered to keep the synchronous inductance constant for all rotational inductor designs.

The effect of the end winding power loss is also considered in the comparative analysis between the EE core and rotational inductors. The calculation of end winding length is approximated through an arc of a semi-circle as shown in Figure 5.7. The total mean length per turn of a conductor is twice the sum of axial length and end winding which is an arc of semi-circle around the corner. The side cross-section of end winding lengths for different winding configurations is shown in Figure 5.8.

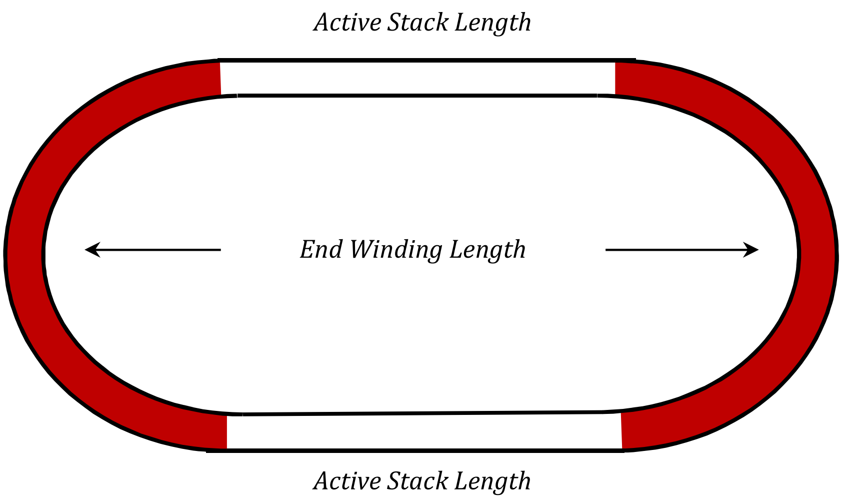

Figure 5.7: Single Conductor with End Winding Length

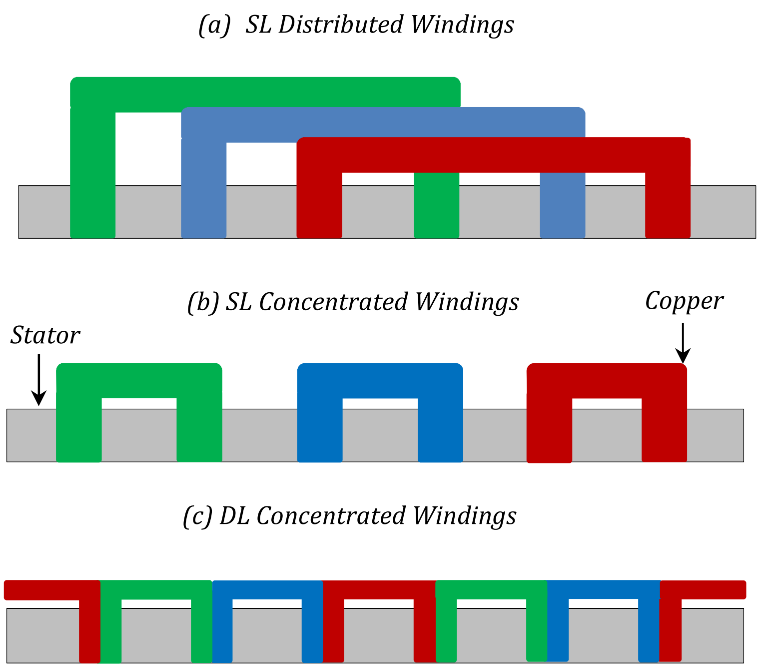

Figure 5.8: Side-cross-section of End Winding Length

The motor-shaped rotational inductors are optimized, analyzed and compared with EE core inductor (shown in Figure 3.7) in terms of total losses and weight. The design optimization and the comparative analysis of EE core and rotational inductor with different slot-pole combination are presented below. DW and CNW with SL and DL for each slot-pole combination are considered. The slot-pole combinations which are feasible for SL and DL windings respectively are shown in Table III and Table IV.

Table III: Possible Combinations for Single Layer Windings

Pole-Slot	6	12	18
2	√	√	√
4	×	√	×
6	×	×	√

Table IV: Possible Combinations for Double Layer Windings

Pole-Slot	6	12	18
2	√	√	√
4	√	√	√
6	×	×	√

5.4.1 2 Poles with 6, 12 and 18 slots Combination

The design optimization and performance comparison of 2 poles rotational inductor with 6, 12 and 18 slots combination is presented in Table V. The flux distribution and winding configuration of 2 poles rotational inductor designs with 6, 12 and 18 slots combination are shown in Figure 5.9(a) to Figure 5.9(l). The flux distribution is plotted at an instant when phase A is reached at its peak value. The total inductor losses include iron and copper losses at fundamental supply current whereas, the total weight includes the weight of the stator, rotor, and copper winding including the end windings.

It can be observed from the Table V, the DW gives the higher inductance as compared to CNW. This is because; the full pitch arrangement of the DW induces higher voltage across it. The short pitch arrangement of the CNW resulted in a lower synchronous inductance. The comparison of the axial length of the rotational inductor is also shown which is varied in proportion to keep the required synchronous inductance of 1.3mH. The synchronous inductance is the same for SL and DL design since changing from SL to DL affects only the end winding length.

With respect to the EE inductor, most efficient motor-shaped rotational inductor design is 2 poles combination with 18 slots DW with both SL and DL arrangements. The total losses reduction in 18 slots rotational inductor with DW is 45.3% when compared with EE core inductor. In general, 12 slots rotational inductor contributes better performance in terms of total inductor losses. For 12 slots rotational inductor, the total losses are reduced from 151.4W to 92.6W, which is 38.8% reduction. However, there is a slight increase in the weight of about 5.2% with respect to the EE core inductor. Moreover, the CNW requires higher axial length to meet the inductance requirement of 1.3mH which in turn increases the total inductor losses and its associated weight. The comparison of the total losses and weight; between EE and rotational inductor with 6, 12 and 18 slots combination is presented in Figure 5.10 and Figure 5.11 respectively.

Table V: Comparison of 2 Poles with 6, 12 and 18 Slots Rotational Inductor

SLOTS	EE Core	RT CNW SL	RT DW SL	RT CNW DL	RT DW DL
Total Losses [W]					
6	151.4	166	119.9	215.4	154.1
12	151.4	146.6	92.6	320.8	92.6
18	151.4	156.2	82.7	362.7	82.7
Total Weight [Kg]					
6	2.28	2.74	2.39	3.5	2.35
12	2.28	3.53	2.4	4.92	2.44
18	2.28	3.7	3.17	5.9	3.17
Synchronous Inductance [mH]					
6	1.3	1.2	2.3	1.2	2.3
12	1.3	1.4	5.1	1.4	5.1
18	1.3	1.8	8.4	1.8	8.4
Stack Length for Required Synchronous Inductance of 1.3mH [mm]					
6	114.5	124	64.7	124	64.7
12	114.5	106.3	29.2	106.3	29.2
18	114.5	84.6	17.71	84.6	17.71

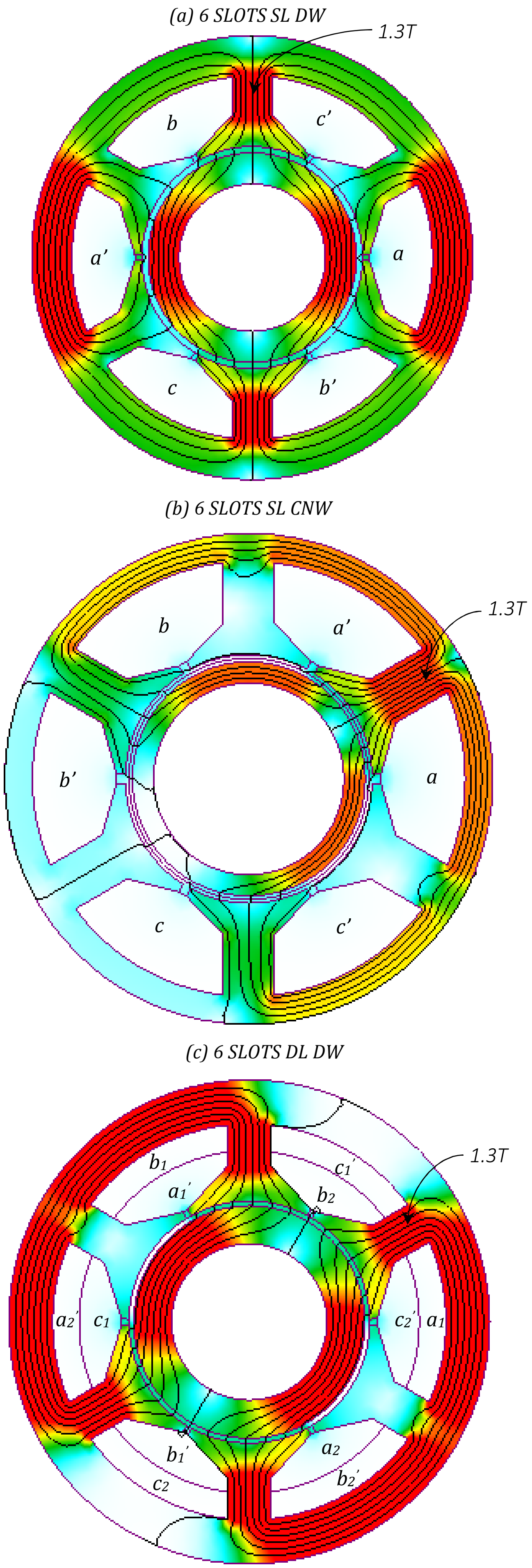
(a) 6 SLOTS SL DW
1.3T
b
c’
a’
a
c
b’
(b) 6 SLOTS SL CNW
1.3T
b
a’
b’
a
c
c’
(c) 6 SLOTS DL DW
1.3T
b_1
c_1'
a_1'
b_2
a_2'
c_1
c_2'
a_1
b_1'
a_2
c_2
b_2'

(d) 6 SLOTS DL CNW

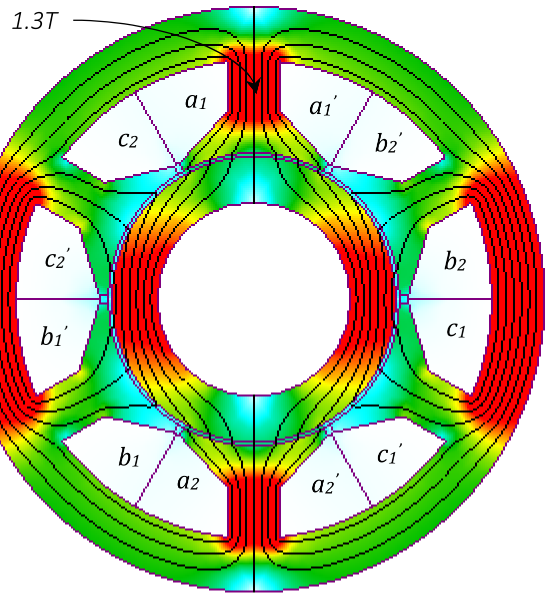

(e) 12 SLOTS SL DW

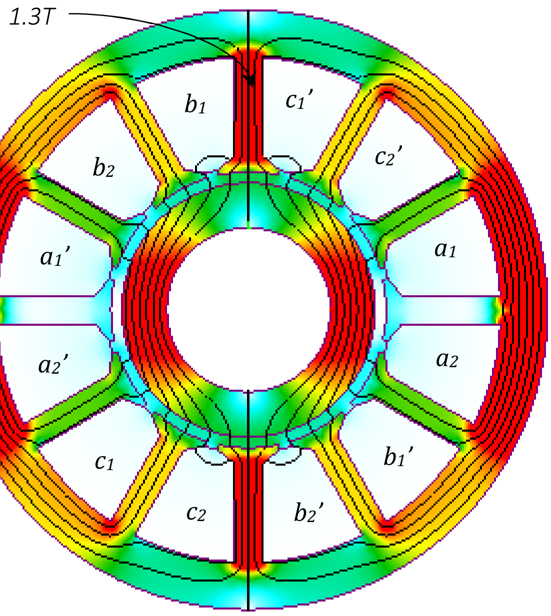

(f) 12 SLOTS SL CNW

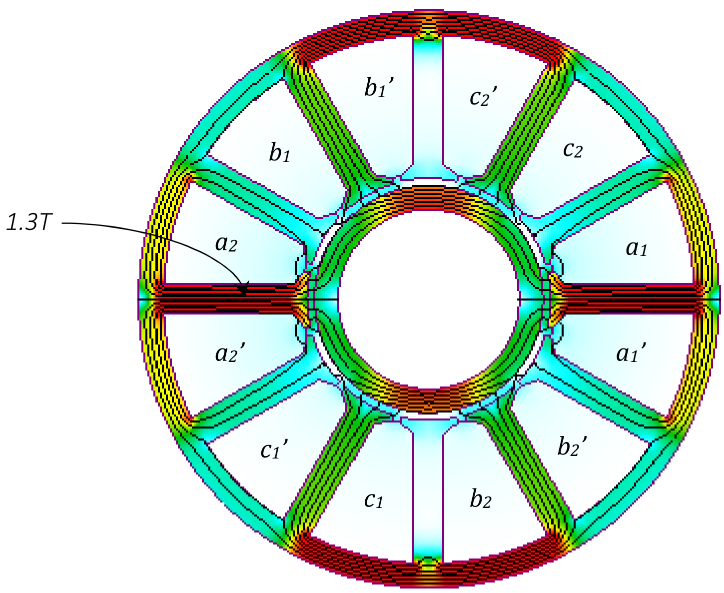

(g) 12 SLOTS DL DW

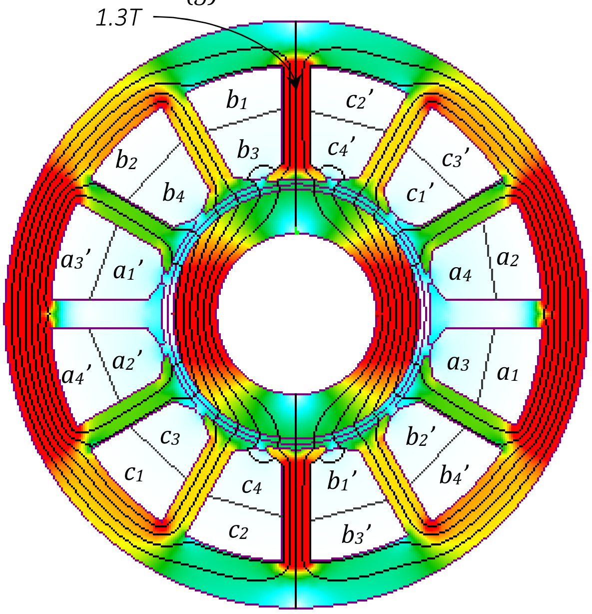

(h) 12 SLOTS DL CNW

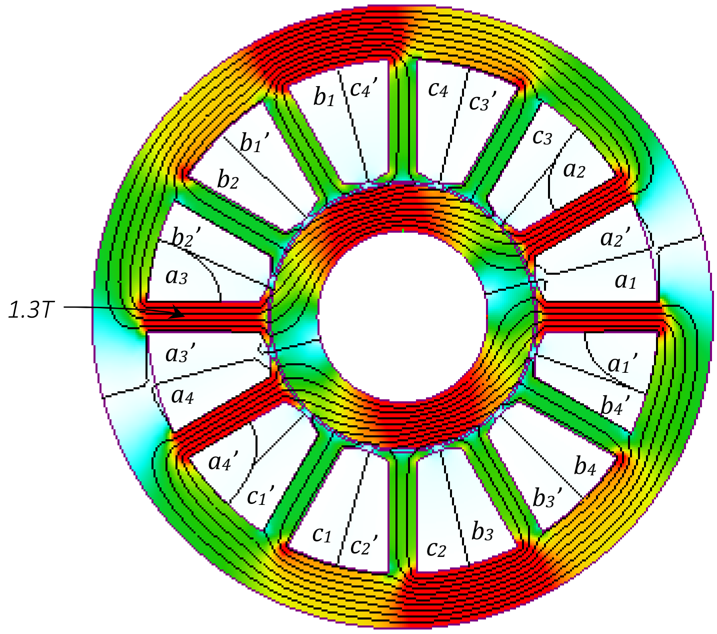

(i) 18 SLOTS SL DW

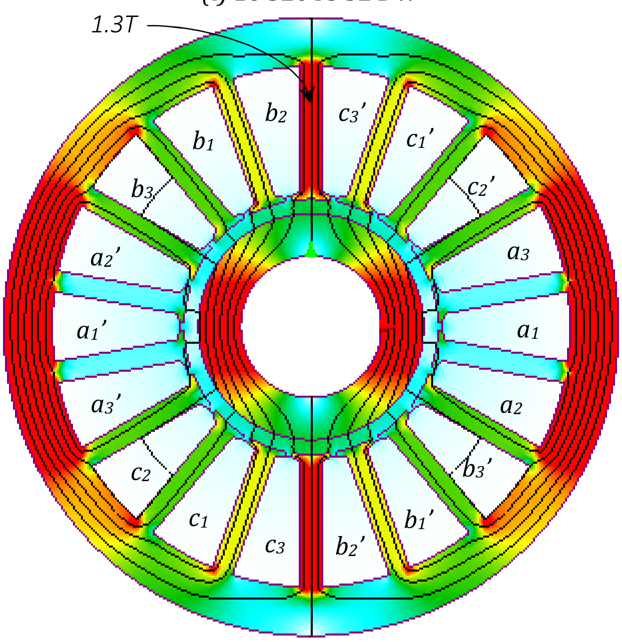

(j) 18 SLOTS SL CNW

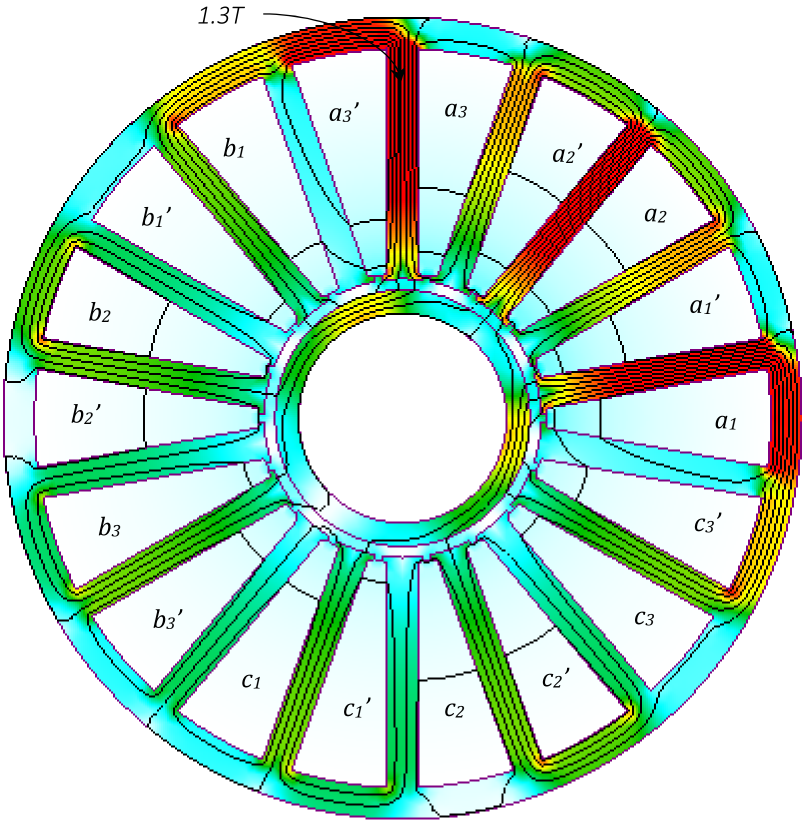

(k) 18 SLOTS DL DW

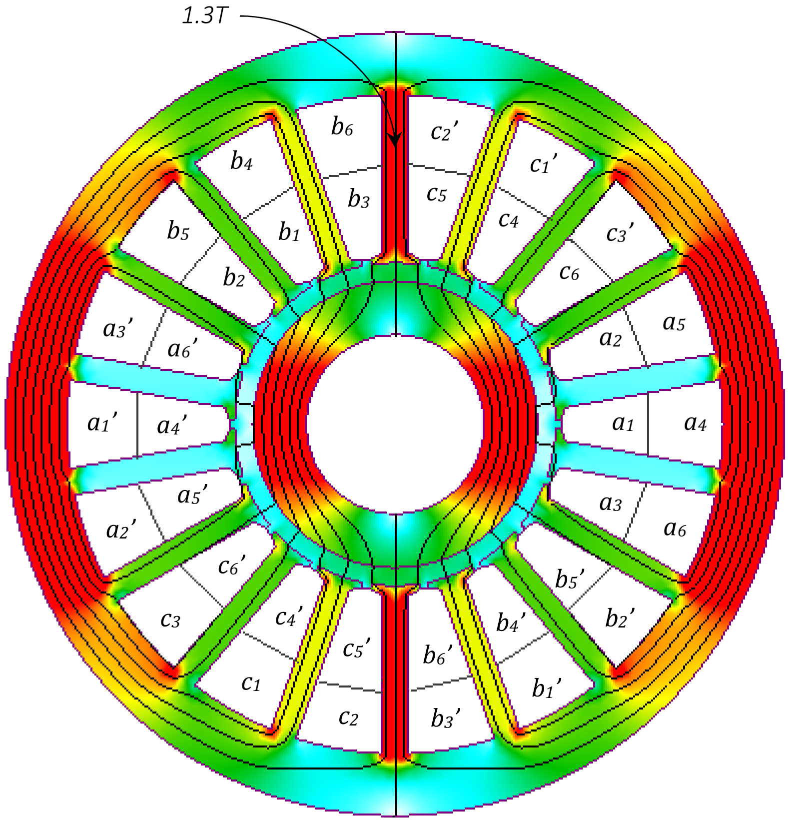

(l) 18 SLOTS DL CNW

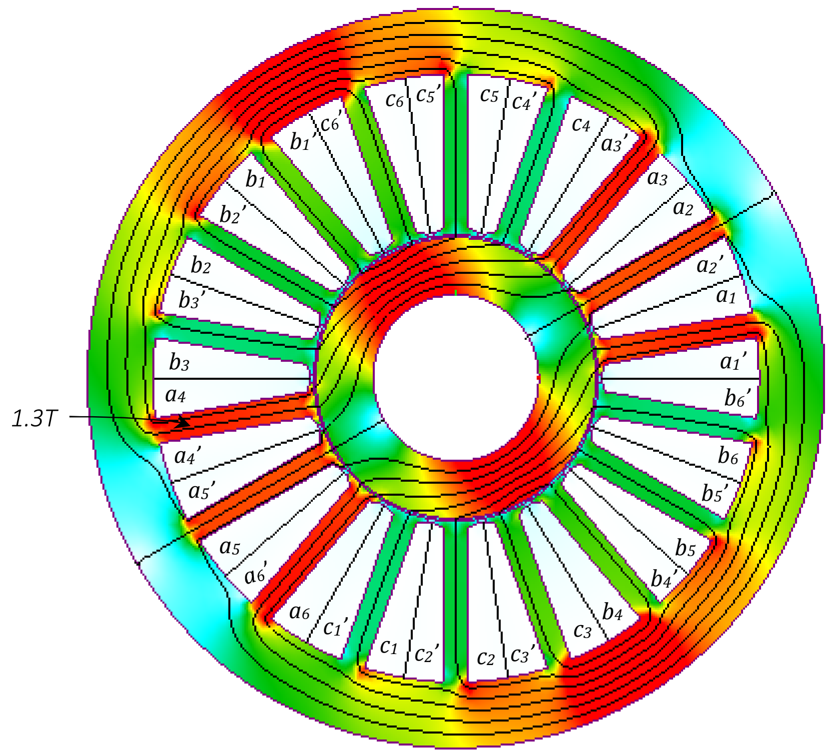

Figure 5.9: Flux Distribution and Winding Configuration of 2 Poles Rotational Inductor

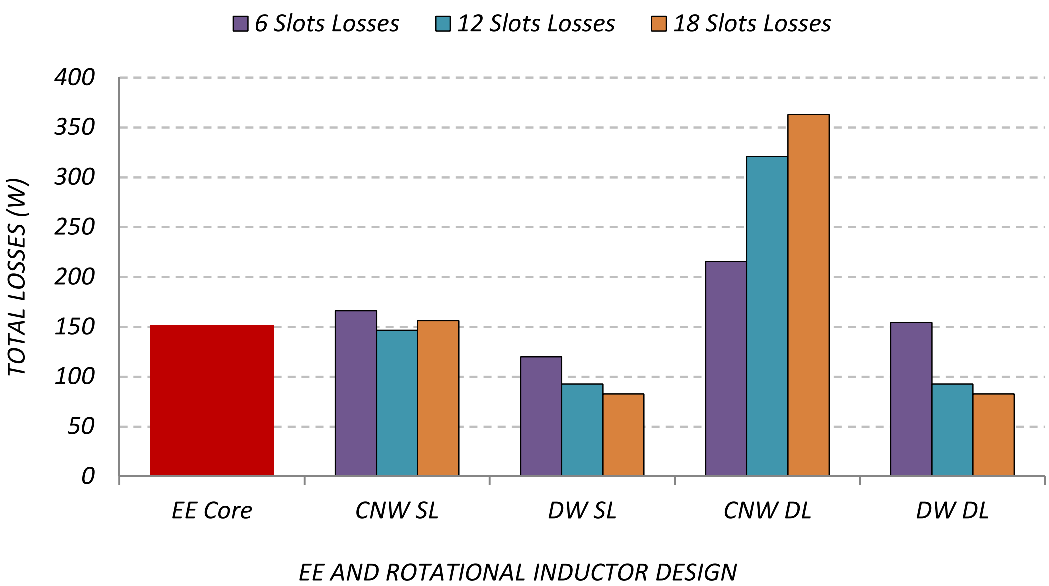

Figure 5.10: Loss Comparison of 2 Poles Rotational Inductor

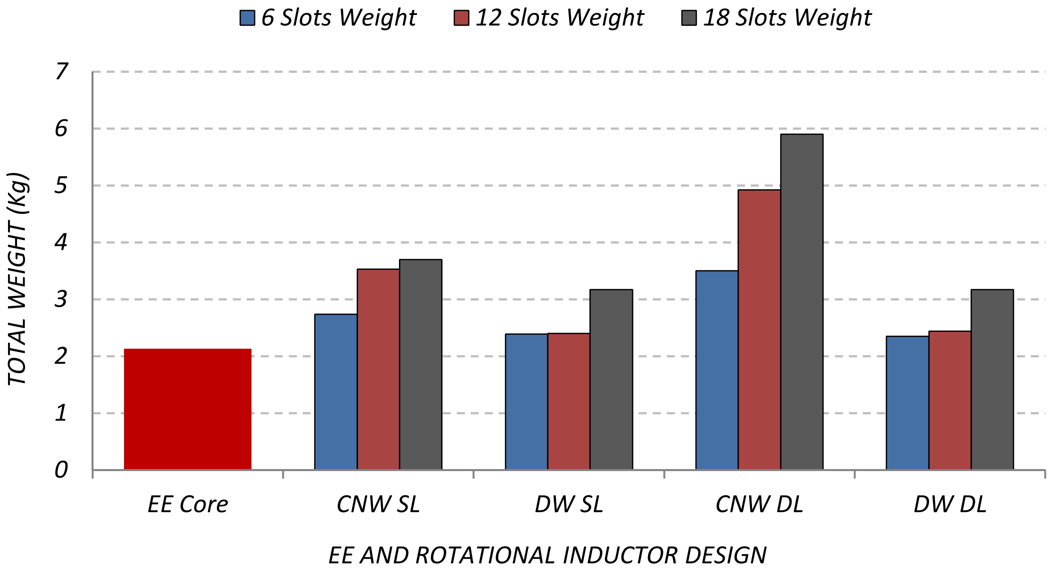

Figure 5.11: Weight Comparison of 2 Poles Rotational Inductor

5.4.2 4 Poles with 6, 12 and 18 slots Combination

The design optimization and performance comparison of 4 poles rotational inductor with 6, 12 and 18 slots combination are presented in Table VI. The flux distribution (when phase A is reached at its peak value) and winding configuration of 4 poles rotational inductor designs with 6, 12 and 18 slots combination are shown in Appendix E1. From the Table VI, it can be observed that the $SL\ DW$ gives the higher inductance as compared to $SL\ CNW$ due to different windings arrangement. The $DL\ DW$ also gives the higher inductance than $DL\ CNW$ in 12 and 18 slots inductors, whereas the inductance remain unchanged in $DL\ DW$ and $DL\ CNW$ for 6 slots inductor.

Table VI: Comparison of 4 Poles with 6, 12 and 18 Slots Rotational Inductor

SLOTS	EE Core	RT CNW SL	RT DW SL	RT CNW DL	RT DW DL
Total Losses [W]					
6	151.4	-	-	178	185.9
12	151.4	102.7	107.5	105.4	114.5
18	151.4	-	-	257.1	98.4
Total Weight [Kg]					
6	2.28	-	-	2.63	2.63
12	2.28	3.39	2.5	3.5	2.5
18	2.28	-	-	4.25	2.76
Synchronous Inductance [mH]					
6	1.3	-	-	1.16	1.16

12	1.3	1.53	2.56	1.5	2.56
18	1.3	-	-	1.9	4.7
Stack Length for Required Synchronous Inductance of 1.3mH [mm]					
6	114.5	-	-	128.2	128.2
12	114.5	97.23	57.7	99.2	58.1
18	114.5	-	-	78.3	31.7

As stated earlier, the axial length is varied in proportion to keep the synchronous inductance of 1.3mH whereas, the new inductor axial length is shown in Table VI. The synchronous inductance and hence axial length is remain unchanged (negligible change) for SL and DL inductor designs. With respect to the EE core inductor, the most efficient motor-shaped rotational inductor design is a 4 poles combination with 18 slots $DL\ DW$. For 18 slots rotational inductor with $DL\ DW$, the total losses are reduced from 151.4W to 98.6W, which is 35% reduction. For 12 slots inductor with SL DW, the total losses are reduced by 29%. The weight of the 12 slots rotational inductor with $SL\ DW$ is increased by 9.6% with respect to the EE core inductor. The comparison of the total losses and weight between EE and rotational inductor with 6, 12 and 18 slots combination is shown in Figure 5.12 and Figure 5.13 respectively.

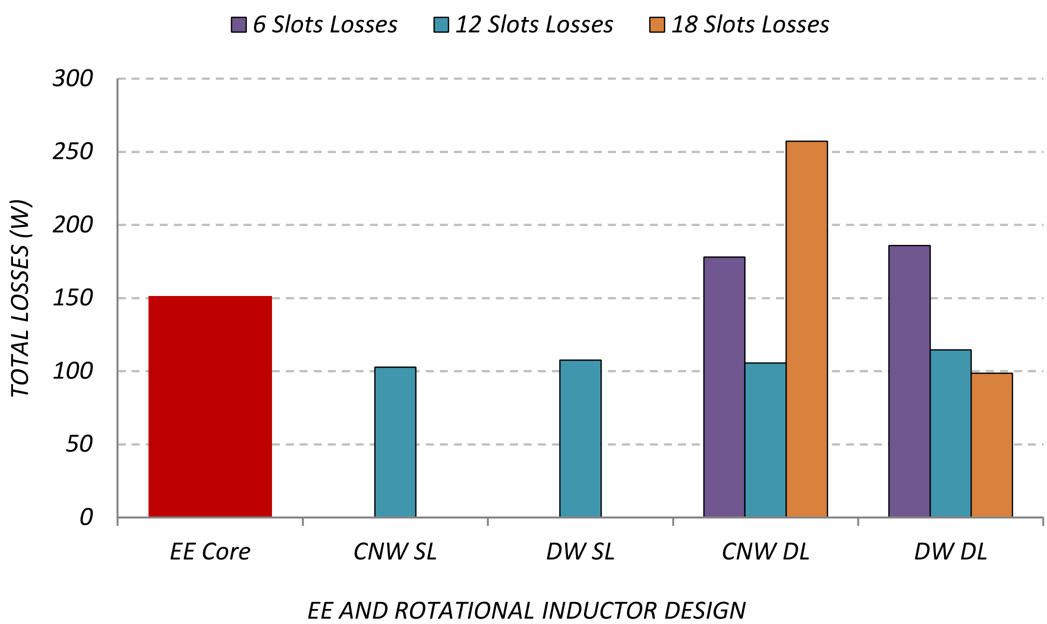

Figure 5.12: Loss Comparison of 4 Poles Rotational Inductor

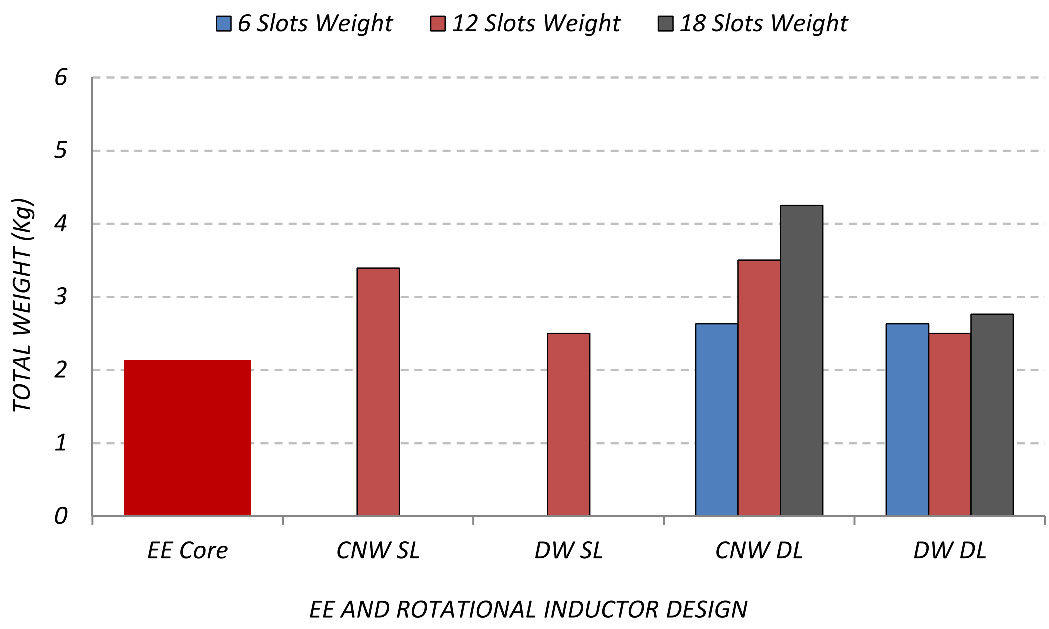

Figure 5.13: Weight Comparison of 4 Poles Rotational Inductor

5.4.3 6 Poles with 18 slots Combination

The performance comparison of 6 poles rotational inductor with 18 slots is presented in Table VII as the combination of 6 poles with 6 and 12 slots is not possible. The flux distribution (when phase A is reached at its peak value) and winding configuration of 6 poles rotational inductor designs with 18 slots combination are shown in Appendix E2. It can be observed from the Table VII that the SL and DL DW gives the higher inductance as compared to CNW. The new axial length is changed in accordance to keep the synchronous inductance of 1.3mH. The most efficient design in 6 poles combination is 18 slots rotational inductor with SL DW which comes at the cost of relatively higher weight. For 18 slots rotational inductor with DW, the total losses are reduced from 151.4W to 113.7W for SL and 114.8W for DL inductor design, which is a reduction of 24.9% and 24.1% respectively. The comparison of the total losses and weight between EE and rotational inductor with 18 slots combination is shown in Figure 5.14.

Table VII: Comparison of 4 Poles with 6, 12 and 18 Slots Rotational Inductor

SLOTS	EE Core	RT CNW SL	RT DW SL	RT CNW DL	RT DW DL
Total Losses [W]					
6	151.4	-	-	-	-
12	151.4	-	-	-	-
18	151.4	139.1	113.7	218.4	114.8
Total Weight [Kg]					
6	2.28	-	-	-	-
12	2.28	-	-	-	-
18	2.28	3.71	2.78	3.91	2.87
Synchronous Inductance [mH]					
6	1.3	-	-	-	-
12	1.3	-	-	-	-
18	1.3	1.5	2.97	1.48	2.88
Stack Length for Required Synchronous Inductance of 1.3mH [mm]					
6	114.5	-	-	-	-
12	114.5	-	-	-	-
18	114.5	99.2	50.2	100.6	51.7

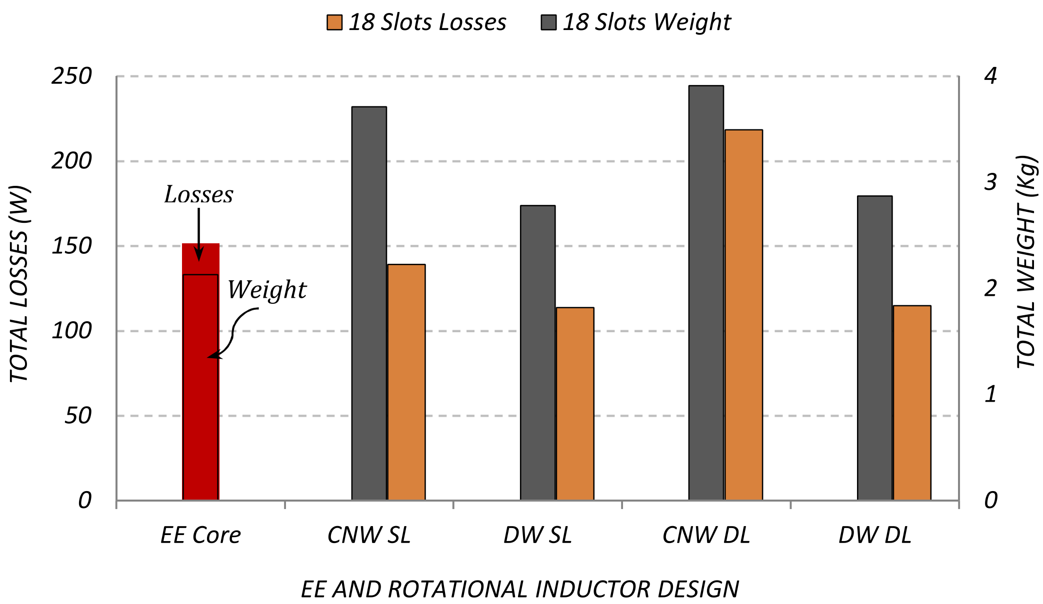

Figure 5.14: Weight and Loss Comparison of 6 Poles Rotational Inductor

5.5 DESIGN OPTIMIZATION OF ROTOR-LESS INDUCTOR

Same winding configurations as that of the motor-shaped rotational inductor discussed in the previous section are employed for motor-shaped rotor-less inductors. The design optimization with different slot-pole combinations are discussed below.

5.5.1 2 Poles with 6, 12 and 18 slots Combination

The design optimization and performance comparison of 2 poles rotor-less inductor with 6, 12 and 18 slots combination are presented in Table VIII. The flux distribution and winding configuration of 2 poles rotational inductor designs with 6, 12 and 18 slots combination are shown in Appendix E3. As described in the previous section for the rotational inductor, the total inductor losses for rotor-less inductor include iron and copper losses at fundamental supply current whereas, the total weight include the weight of the stator, rotor, and copper winding including the end windings.

It can be observed from Table VIII that the DW gives the higher inductance for rotor-less inductors as compared to CNW. This is because; the full pitch arrangement of the DW induces higher voltage induction. The short pitch arrangement of the CNW resulted in a lower synchronous inductance. The axial length of the rotor-less inductor is varied in order to keep the required synchronous inductance with respect to EE inductor. The synchronous inductance remain same in DW for SL and DL design for 6, 12 and 18 slots inductor designs.

With respect to the EE inductor, the most efficient inductor design for a 2 poles combination is 18 slots DW with both SL and DL arrangements. The total losses in 18 slots rotor-less inductor with DW is reduced by 44.5% when compared to EE core inductor. In general, 12 slots rotor-less inductor contributes better performance in terms of total inductor losses and weight at the same time. For 12 slots rotor-less inductor, the total losses are reduced to 92.8W, which is 39% reduction and its associated weight is slightly increased by 7%. Moreover, the CNW requires higher axial length to meet the inductance requirement which in turn increases the total inductor losses and its associated weight. The comparison of the total losses and weight between EE and rotational inductor for 2 poles with 6, 12 and 18 slots combination is presented Figure 5.15 and Figure 5.16 respectively.

Table VIII: Comparison of 2 Poles with 6, 12 and 18 Slots Rotor-less Inductor

SLOTS	EE Core	RT CNW SL	RL DW SL	RL CNW DL	RL DW DL
Total Losses [W]					
6	151.4	128.8	146.4	244.9	179.1
12	151.4	143.7	92.8	303.4	96.3
18	151.4	144.5	84	433.1	84
Total Weight [Kg]					
6	2.28	2.63	2.27	3.6	2.21
12	2.28	3.05	2.44	6.32	2.77
18	2.28	3.8	3.51	9.77	3.51
Synchronous Inductance [mH]					
6	1.3	1.3	2.3	1.3	2.3
12	1.3	1.39	2.81	0.81	2.79
18	1.3	1.43	3.41	0.66	3.41
Stack Length [mm]					
6	114.5	114.5	64.7	114.5	64.7
12	114.5	107.1	52.94	183.8	53.4
18	114.5	104	43.6	225.5	43.6

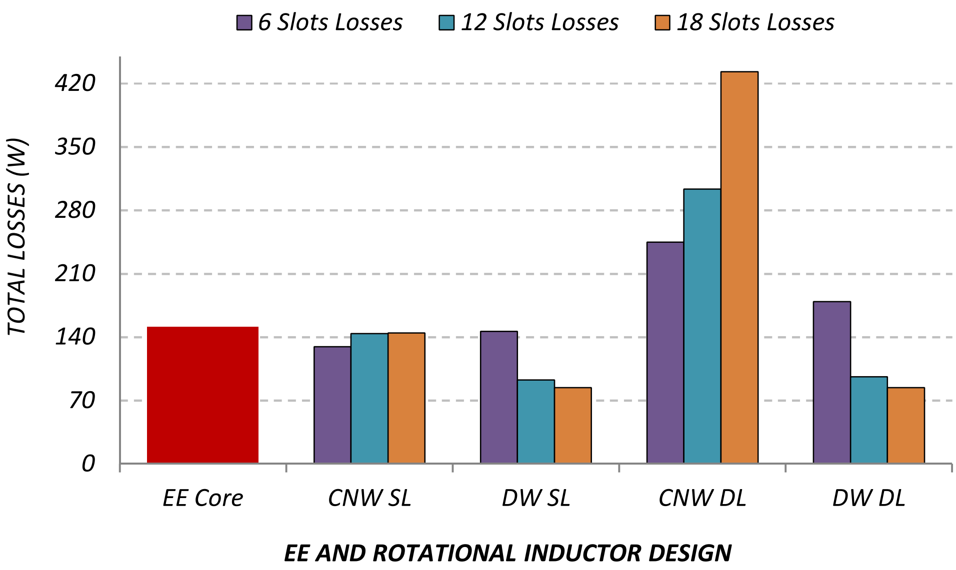

Figure 5.15: Loss Comparison of 2 Poles Rotor-less Inductor

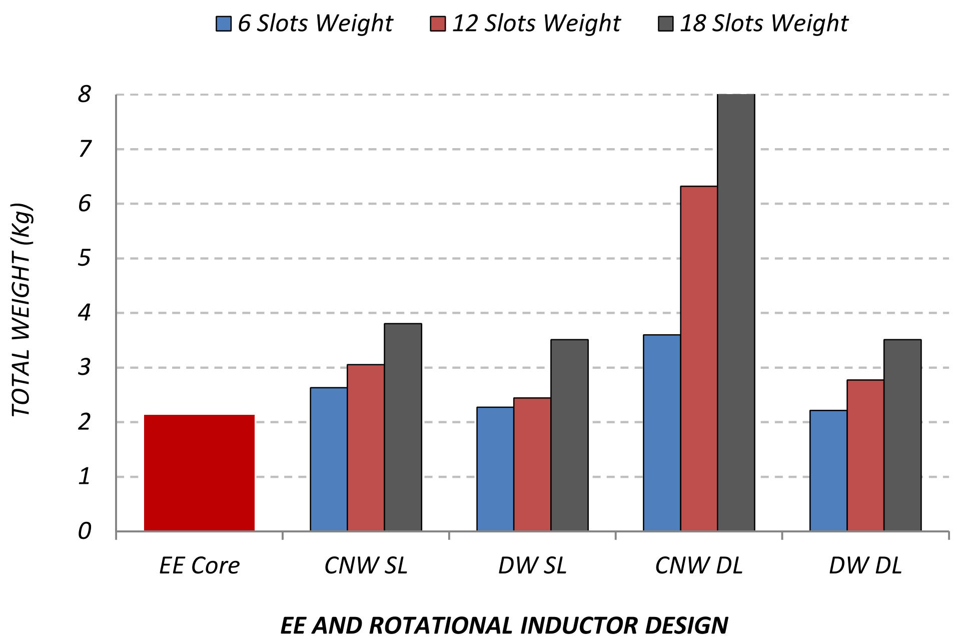

Figure 5.16: Weight Comparison of 2 Poles Rotor-less Inductor

5.5.2 4 Poles with 6, 12 and 18 slots Combination

The design optimization and performance comparison of 4 poles rotor-less inductor with 6, 12 and 18 slots combination are presented in Table IX. The flux distribution (when phase A is reached at its peak value) and winding configuration of 4 poles rotational inductor designs with 6, 12 and 18 slots combination are shown in Appendix E4. From the Table IX, it can be observed that the DW gives the higher inductance as compared to CNW due to different winding arrangements, whereas the inductance remain unchanged in $DL\ DW$ and $DL\ CNW$ for 6 slots inductor. The axial length is varied in order to keep the required synchronous inductance (with respect to EE inductor) and the new inductor axial length is shown in Table VI. With respect to the EE core inductor, the most efficient inductor design is 4 poles combination with 18 slots $DL\ DW$.

For 18 slots rotor-less inductor with $DL\ DW$, the total losses are reduced to 98.1W, which is a reduction of 35.1% with respect to the EE core inductor. The weight of the 12 slots rotor-less inductor with SL and $DL\ DW$ is lower than 18 slots inductor. The total loss reduction of 25.6% is achieved for 12 slots rotor-less inductor with $DL\ DW$ but the weight is increased by 13.1% with respect to EE core inductor. The comparison of the total losses and weight between EE and rotational inductor with 6, 12 and 18 slots combination is shown in Figure 5.17 and Figure 5.18 respectively.

Table IX: Comparison of 4 Poles with 6, 12 and 18 Slots Rotor-less Inductor

SLOTS	EE Core	RT CNW SL	RT DW SL	RT CNW DL	RT DW DL
Total Losses [W]					
6	151.4	-	-	196.1	197.5
12	151.4	117.3	114.5	192.4	112.6
18	151.4	-	-	225.1	98.1
Total Weight [Kg]					
6	2.28	-	-	2.31	2.39
12	2.28	3.22	2.61	3.78	2.58
18	2.28	-	-	5.34	3.14
Synchronous Inductance [mH]					
6	1.3	-	-	1.16	1.16
12	1.3	1.3	2.56	1.3	2.59
18	1.3	-	-	1.3	3.52
Stack Length [mm]					
6	114.5	-	-	128.2	128.2
12	114.5	114.5	58.1	114.5	57.4
18	114.5	-	-	114.5	42.3

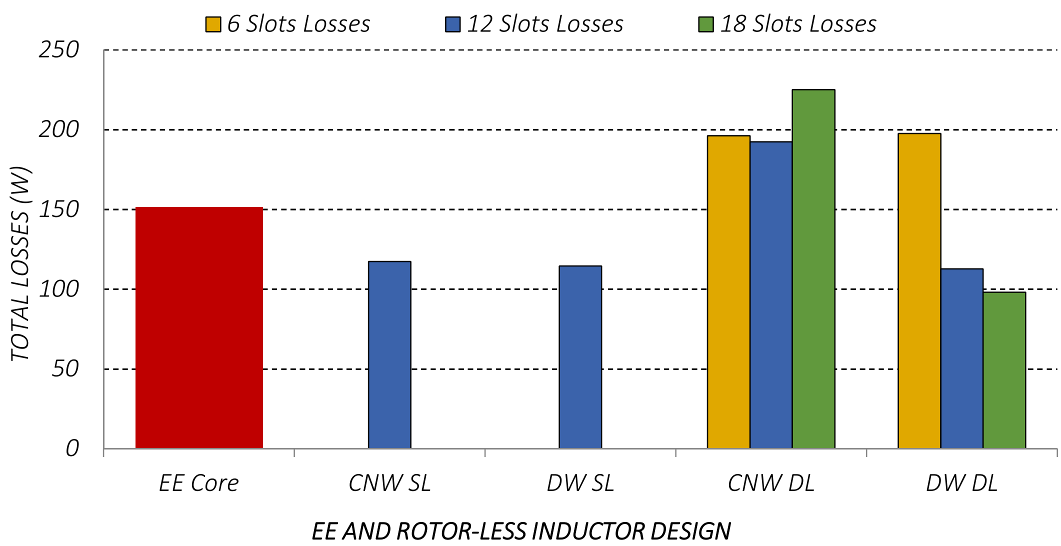

Figure 5.17: Loss Comparison of 4 Poles Rotor-less Inductor

Figure 5.18: Weight Comparison of 4 Poles Rotor-less Inductor

5.5.3 6 Poles with 18 slots Combination

The performance comparison of 6 poles rotor-less inductor with 18 slots is presented in Table X. The combination of 6 poles with 6 and 12 slots is not possible. The flux distribution and winding configuration of 6 poles rotor-less inductor designs with 18 slots combination are shown in Appendix E5.

Table X: Comparison of 6 Poles with 6, 12 and 18 Slots Rotor-less Inductor

SLOTS	EE Core	RT CNW SL	RL DW SL	RL CNW DL	RL DW DL
Total Losses [W]					
6	151.4	-	-	-	-
12	151.4	-	-	-	-
18	151.4	124.7	128.7	201.2	122.1
Total Weight [Kg]					
6	2.28	-	-	-	-
12	2.28	-	-	-	-
18	2.28	3.81	2.73	3.96	2.81
Synchronous Inductance [mH]					
6	1.3	-	-	-	-
12	1.3	-	-	-	-
18	1.3	1.45	2.95	1.45	2.95
Stack Length [mm]					
6	114.5	-	-	-	-
12	114.5	-	-	-	-
18	114.5	102.7	50.5	103.4	50.5

It can be observed from Table VII that the DW gives the higher inductance as compared to CNW in both SL and DL case. The axial length is changed in order to keep the required synchronous inductance (with respect to the EE core inductor). The most efficient design is a 6 poles combination with 18 slots with both SL DW and DL DW. For 18 slots rotor-less inductor with DW, the total losses are reduced to 128.7W for SL and 122.1W for DL, which is a reduction of 15% and 19.3% respectively. But the weight of 18 slot with DL DW is increased to 2.81Kg which an increase of 23.2%. The comparison of the total losses and weight between EE core and rotational inductor with 18 slots combination is shown in Figure 5.19.

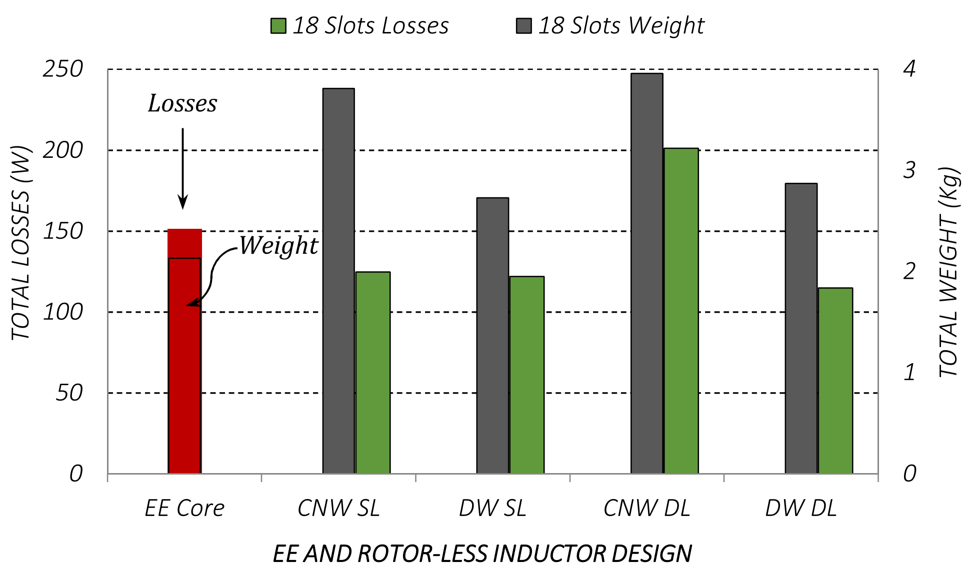

Figure 5.19: Weight and Loss Comparison of 6 Poles Rotor-less Inductor

5.6 COMPARISON OF AC COPPER LOSS

The most efficient designs were chosen from the design optimization of motor-shaped inductors to analyze its AC copper loss. The AC copper loss due to skin and proximity effects are compared with traditional EE core inductor. For the rotational inductors single inductor design has been chosen from each of the pole and slot column. The selected rotational inductor designs are: 6 slots (6S) 2P DW SL, 12 slots (12S) $2P\ DW\ SL$, 18 slots (18S) $2P\ DW\ SL$, 12S $4P\ DW\ SL$ and 18S $6P\ DW\ SL$. All the chosen designs of rotational inductor are lowest in total losses.

For the rotor-less inductors one inductor has been chosen from each of the slot combination with 2 poles. This is because 2 poles stator windings contributes the lowest leakage flux. The designated rotor-less inductor designs are: 6 slots (6S) $2P\ CW\ SL$, 12 slots (12S) $2P\ DW\ SL$, 18 slots (18S) $2P\ DW\ SL$. The flux distribution (when phase A is reached at its peak value) and the induced current density of each of the selected inductor design is shown in Figure 5.20(a) to Figure 5.20(i).

The solid conductors were modelled in order to evaluate the AC copper loss at both fundamental and switching frequencies. The magnitude of the switching harmonic component is assumed to be 5% of the fundamental current. The switching harmonic current superimposed on the fundamental current was injected into the FE model. The FE model is modeled considering a controlled current source. The injected current waveforms are shown in Figure 5.21. The relation between the DC and AC copper loss is defined by the given expression,

$$P_{copper} = P_{dc} + P_{ac}$$

Where, P_{copper} is the total copper losses, P_{dc} is the DC copper loss considering the end winding effect and P_{ac} is the AC copper loss due to skin and proximity effect where end winding AC copper loss effect is neglected.

(a) EE Core Inductor

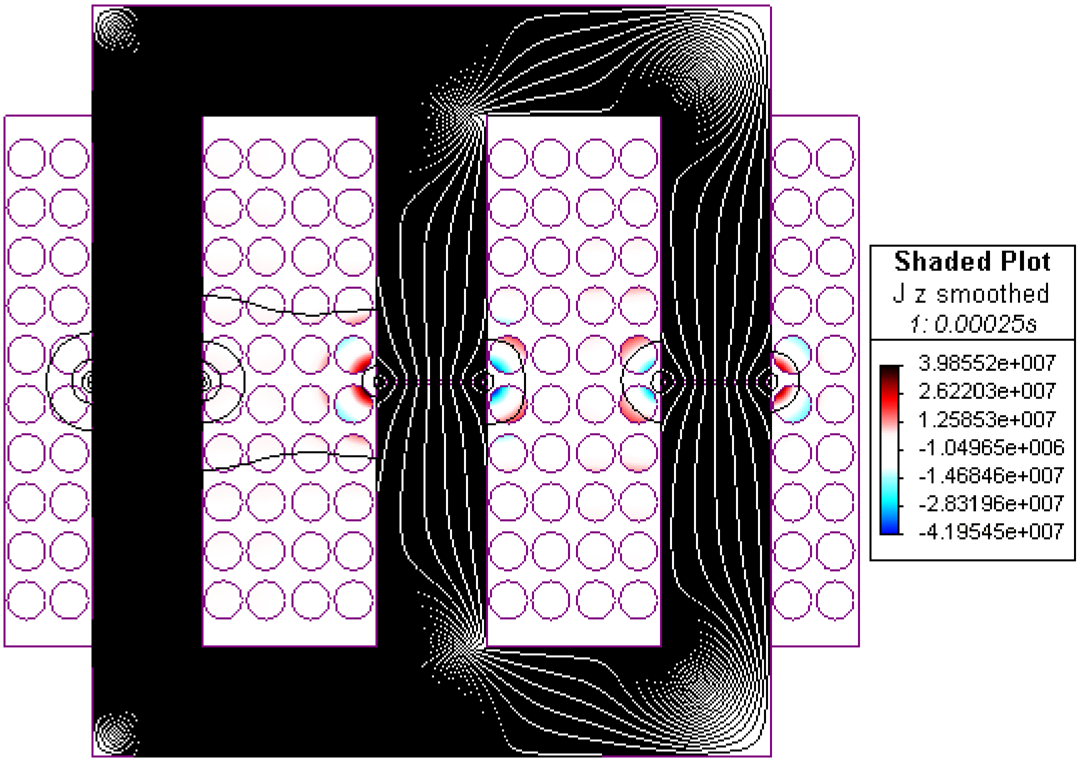

(b) RT 6S 2P SL DW

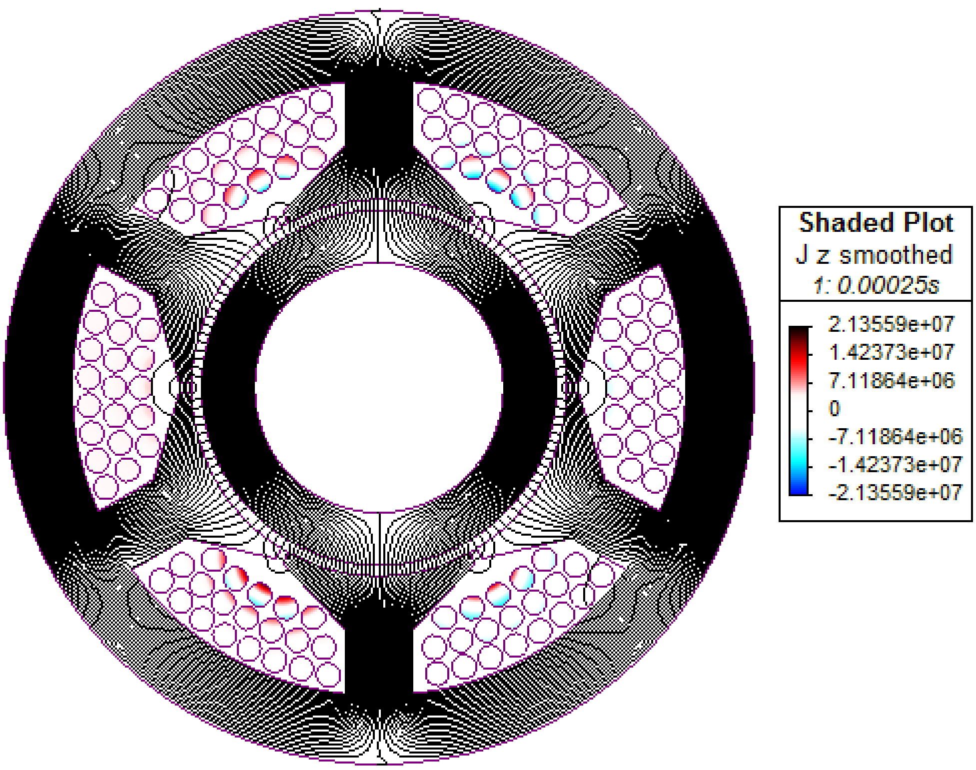

(c) RT 2P 12S DW SL

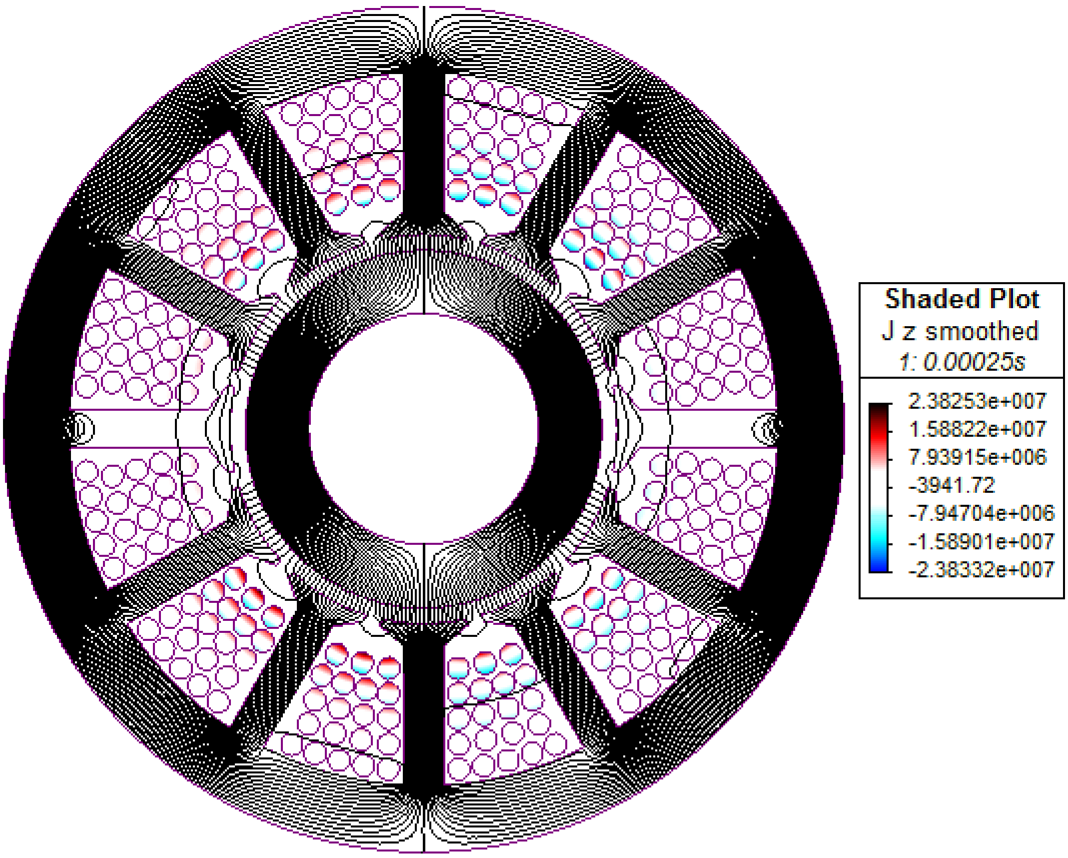

(d) RT 18S 2P SL DW

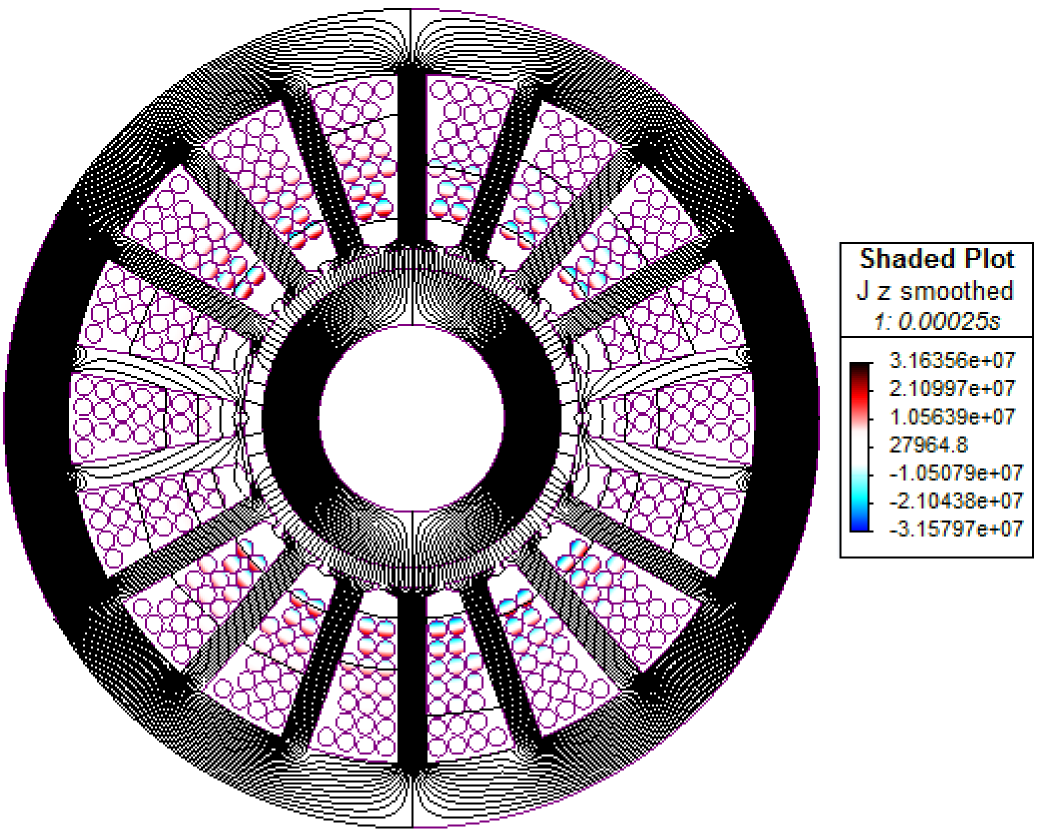

(e) RT 4P 12 DW SL

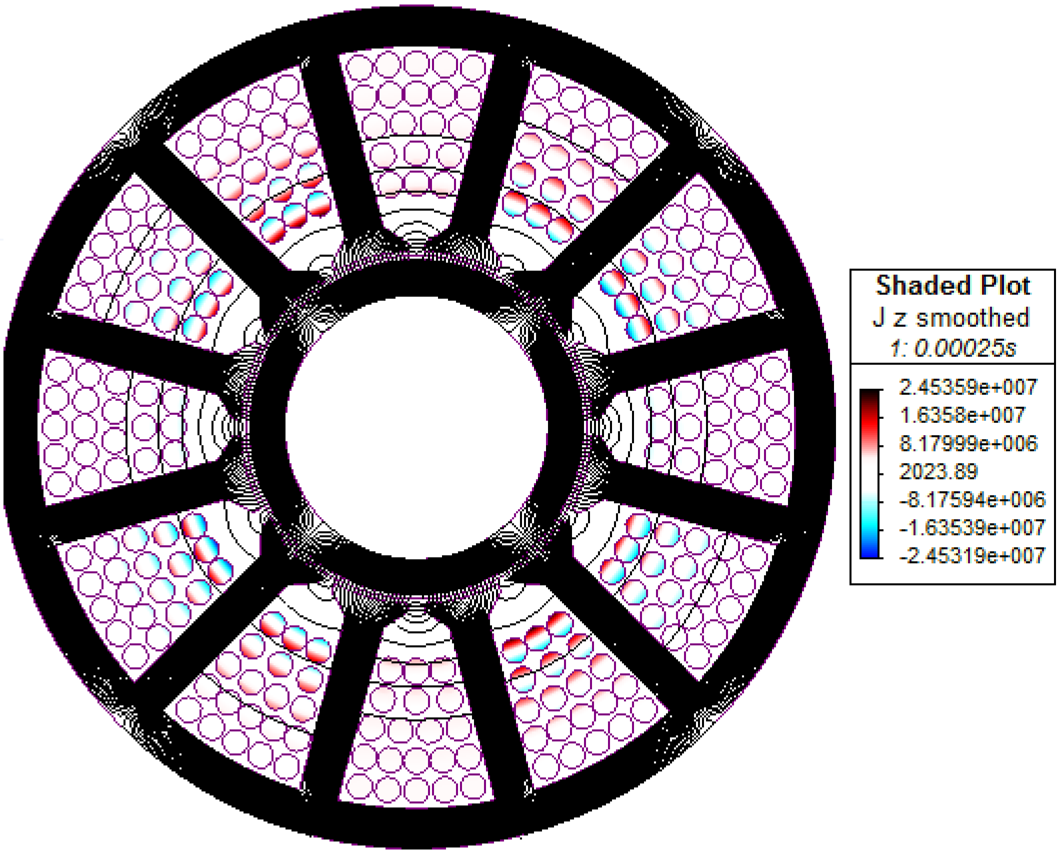

(f) RT 6P 18 DW SL

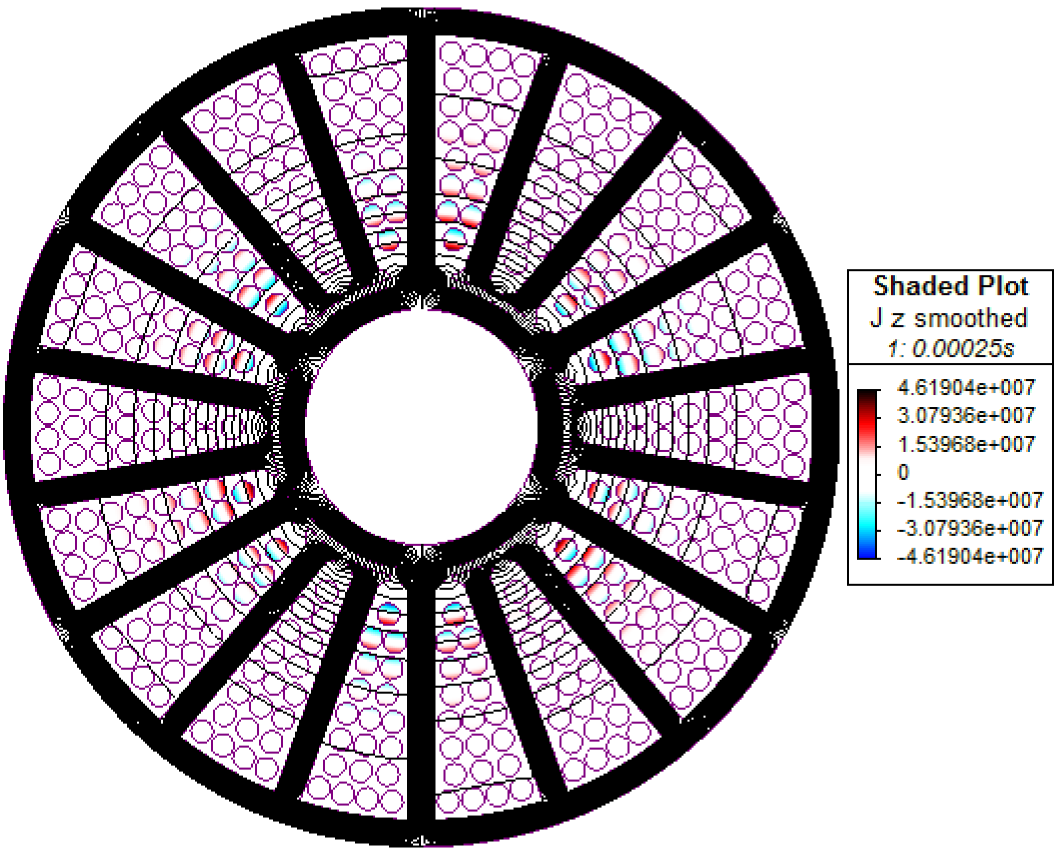

(g) RL 6S 2P SL CNW

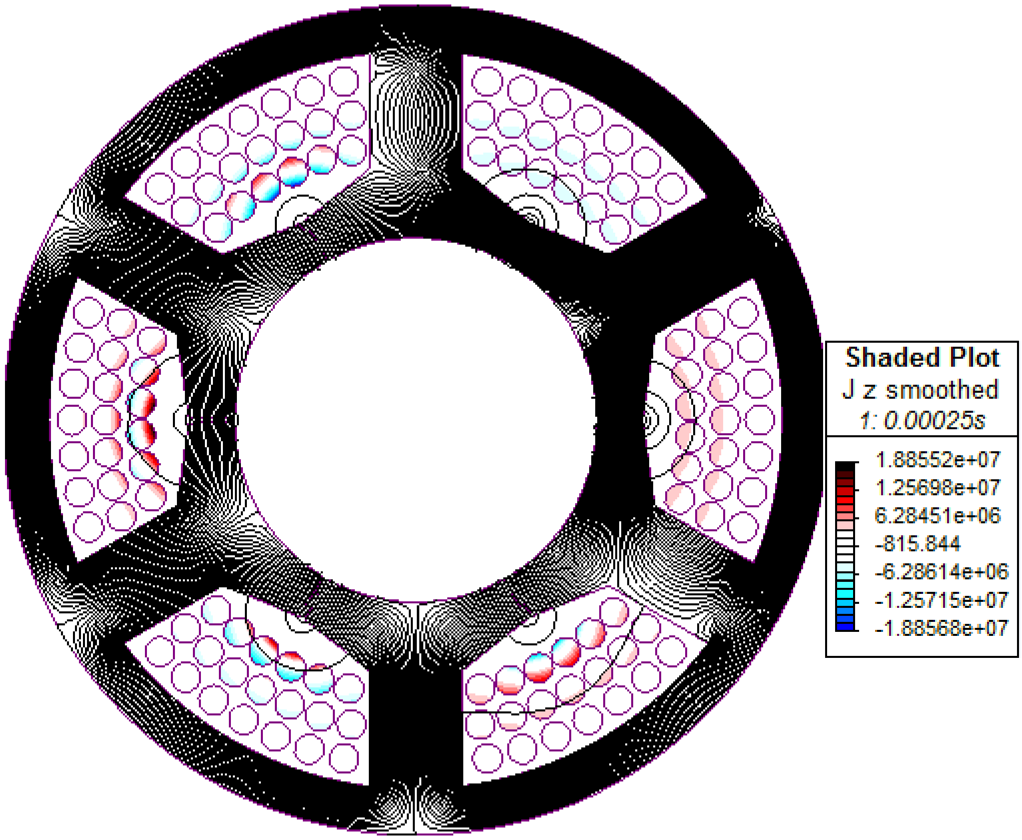

(h) RL 12S 2P SL DW

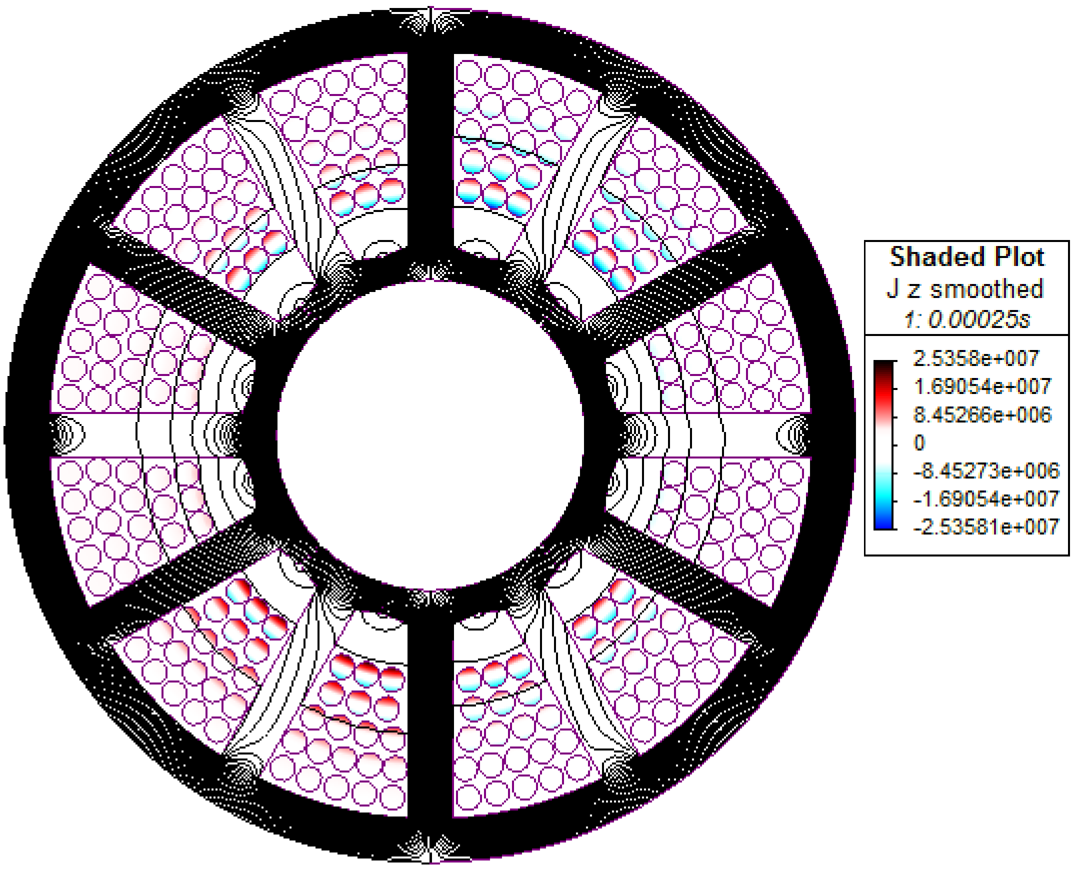

(i) RL 2P 12S DL DW

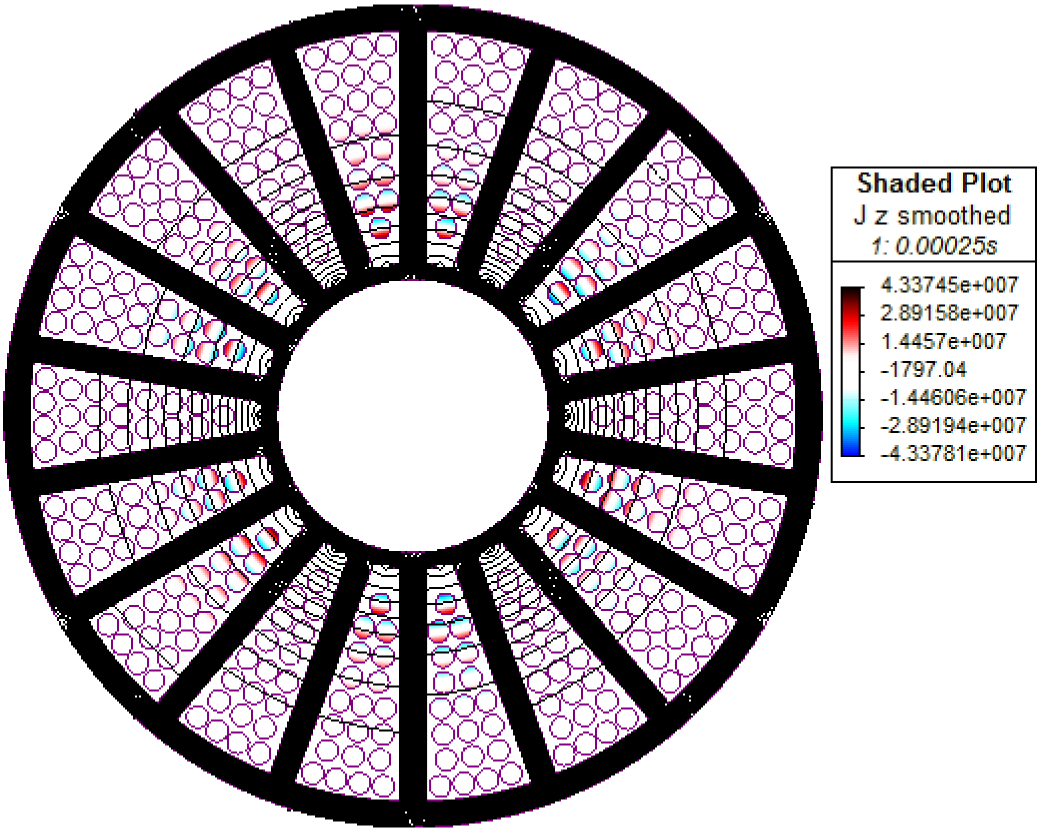

Figure 5.20: Flux Distribution and Current Density of Motor-shaped Inductors

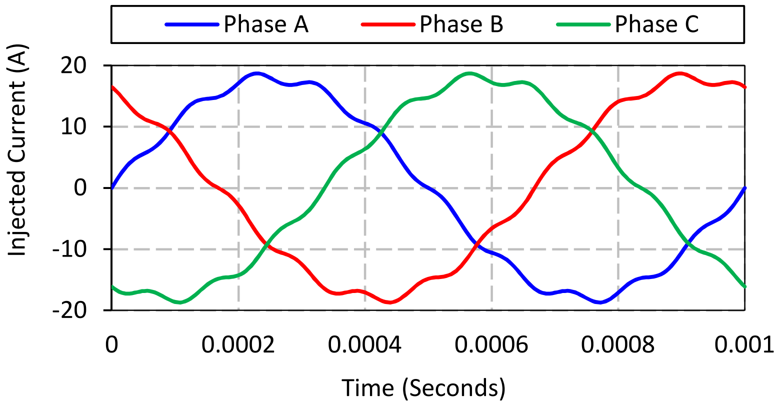

(a) Injected current with 10 kHz switching

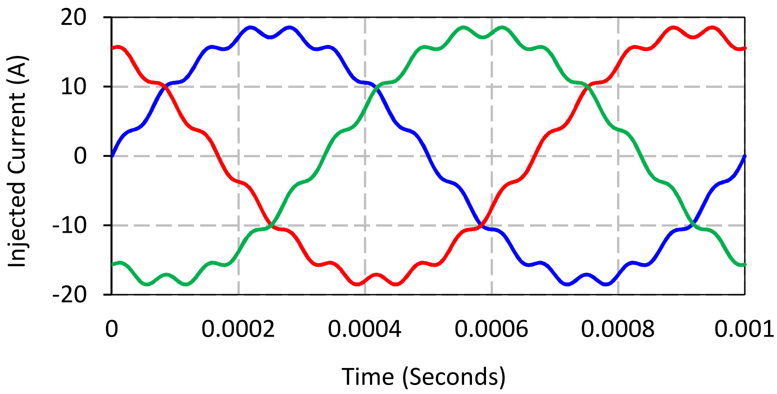

(b) Injected current with 15 kHz switching

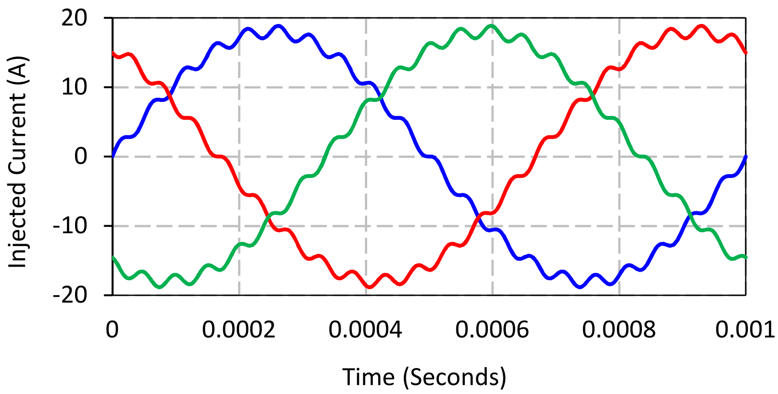

(c) Injected current with 20 kHz switching

Figure 5.21: FEA Injected Currents at different Switching Frequencies

The AC copper loss in the EE core inductor is determined to be higher than that of motor-shaped inductors at fundamental and all considered switching frequencies (10, 15 and 20 kHz), the details of which are illustrated in Table XI, Table XII, Figure 5.22 and Figure 5.23. The current density plot of EE core inductor can be seen from Figure 5.20 (a). The peak point of current density due to proximity effect is occurring near the airgap which is 41.9 A/mm^2.

6 slots 2 poles rotational inductor with single layer distributed windings ($RT\ 6S\ 2P\ SL\ DW$) contributes the lowest AC copper resistance at both fundamental and all considered switching frequencies among all selected inductor designs. The AC copper loss reduction of 72% is achieved at fundamental the frequency, while the AC copper loss reduction of 74% is achieved at all considered switching frequencies respectively, when compared to the EE core inductor. The current density plot of 6 slots 2 poles rotational inductor can be seen from Figure 5.20 (b). The peak point of current density due to proximity effect is occurring near the slot opening airgap which is 21.3 A/mm^2.

12 Slots 2 poles rotational inductor with single layer distributed winding ($RT\ 12S\ 2P\ DW\ SL$) offers the reduction of 53.43% at fundamental frequency, whereas the reduction of 58.26%, 59.25% and 59.93% is achieved at all switching frequencies respectively. The current density plot of 12 slots 2 poles rotational inductor can be seen from Figure 5.20 (c). The peak point of current density due to proximity effect is occurring near the slot opening airgap which is 23.8 A/mm^2.

On the other hand, 18 Slots 2 poles rotational inductor with single layer distributed winding ($RT\ 18S\ 2P\ DW\ SL$) is unable to offer AC loss reduction due to higher leakage and fringing fluxes around the stator slots opening. Since the number of the conductors per slot are kept constant, the number of turns per phase is increased with increase in number of slots. This leads to increase in overall AC copper resistance. The current density plot of 18 slots 2 poles rotational inductor can be seen from Figure 5.20 (d). The peak point of current density due to proximity effect is occurring near the slot opening airgap which is 31.5 A/mm^2.

It is important to note that most of the conductors are placed close to the airgap in EE core inductor which results in to more fringing effect. In contrast, conductors of motor-shaped inductors are placed far from the slot opening and airgap therefore, the fringing flux cutting through the conductors is reduced. The effect of leakage flux is likewise reduced in rotational inductor due to the distributed configuration of the stator windings which leads to the lower leakage flux [3, 4]. The fringing and leakage fluxes crossing the conductors is the main reason for the increased AC resistance, and hence, increases AC copper loss at both fundamental and all switching frequencies.

For the 12 slots 4 poles rotational inductor with single layer distributed windings ($RT\ 12S\ 4P\ SL\ DW$), the AC copper loss at fundamental frequency is reduced by 2.78% and reduction of 5.83%, 8.5% and 10.33 is obtained at all considered switching frequencies respectively. The current density plot of 12 slots 4 poles rotational inductor can be seen from Figure 5.20 (e). The peak point of current density due to proximity effect is occurring near the slot opening airgap which is 24.5 A/mm^2.

The AC copper loss are increased more than twice for 18 slots 6P rotational inductors, when compared to the conventional EE core inductor. This is because the flux path for $4P$ and $6P$ inductors is smaller than the $2P$ inductor and has increased the effect of leakage flux crossing through the stator slots and conductors. The current density plot of 18 slots 6 poles rotational inductor can be seen from Figure 5.20 (f). The peak point of current density due to proximity effect is occurring near the slot opening airgap which is 46.1 A/mm^2.

For the rotor-less inductor ($RL\ 6S\ 2P\ SL\ CNW$), the AC loss reduction of 53.7% is obtained at fundamental frequency, whereas the reduction of 59.5%, 59.8 and 60.1% is obtained at all switching frequencies respectively with respect to the EE core inductor. The current density plot of 6 slots 2 poles rotor-less inductor can be seen from Figure 5.20 (g). The peak point of current density due to proximity effect is occurring near the slot opening airgap which is 18.8 A/mm^2.

12 slots 2 poles rotor-less inductor with single layer distributed windings ($RL\ 12S\ 2P\ SL\ DW$) does not contribute AC loss reduction at fundamental frequency, the whereas a reduction of 12.3%, 15.8 and 16.4% is achieved at all considered switching frequencies respectively. The current density plot of 12 slots 2 poles rotor-less inductor can be seen from Figure 5.20 (h). The peak point of current density due

to proximity effect is occurring near the slot opening airgap which is 25.3 A/mm^2.

On the other hand, 18 slots 2 poles rotor-less inductor with single layer distributed windings (RL $18S$ $2P$ SL DW) is also incapable to give AC copper loss reduction due to increased leakage and fringing fluxes around the stator slots opening and also due to increased number of turns per phase. The current density plot of 12 slots 2 poles rotor-less inductor can be seen from Figure 5.20 (i). The peak point of current density due to proximity effect is occurring near the slot opening airgap which is 43.3 A/mm^2.

Table XI: AC Copper Loss Comparison of Rotational Inductors with EE Core Inductor

FSW (kHz)	EE Core	RT 6S 2P SL DW	RT 12S 2P SL DW	RT 18S 2P SL DW	RT 12S 4P SL DW	RT 18S 6P SL DW	UNIT
1	17.49	4.89	8.15	15.39	17.00	53.23	W
10	1.42	0.37	0.59	1.12	1.33	3.77	W
15	1.98	0.51	0.81	1.53	1.81	5.45	W
20	2.47	0.64	0.99	1.89	2.21	6.87	W

Table XII: AC Copper Loss Comparison of Rotor-less Inductors with EE Core Inductor

FSW (kHz)	EE Core	RL 6S 2P SL CNW	RL 12S 2P SL DW	RL 18S 2P SL DW	UNIT
1	17.49	8.10	17.49	53	W
10	1.42	0.57	1.24	4.07	W
15	1.98	0.80	1.67	5.90	W
20	2.47	0.99	2.06	7.43	W

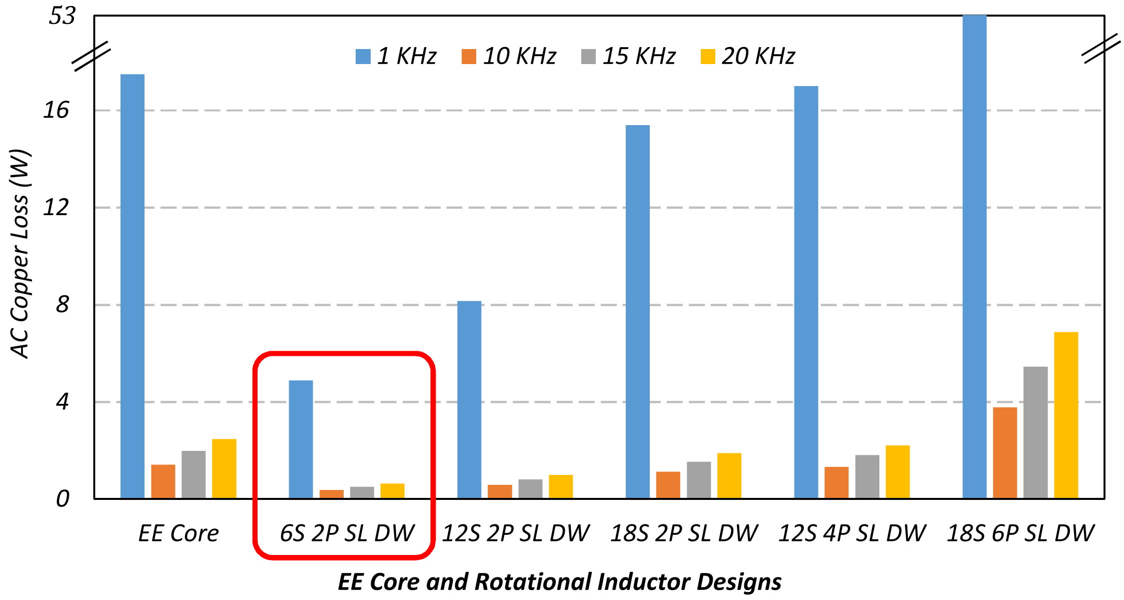

Figure 5.22: AC Copper Loss Comparison of Rotational Inductor with EE Core Inductor

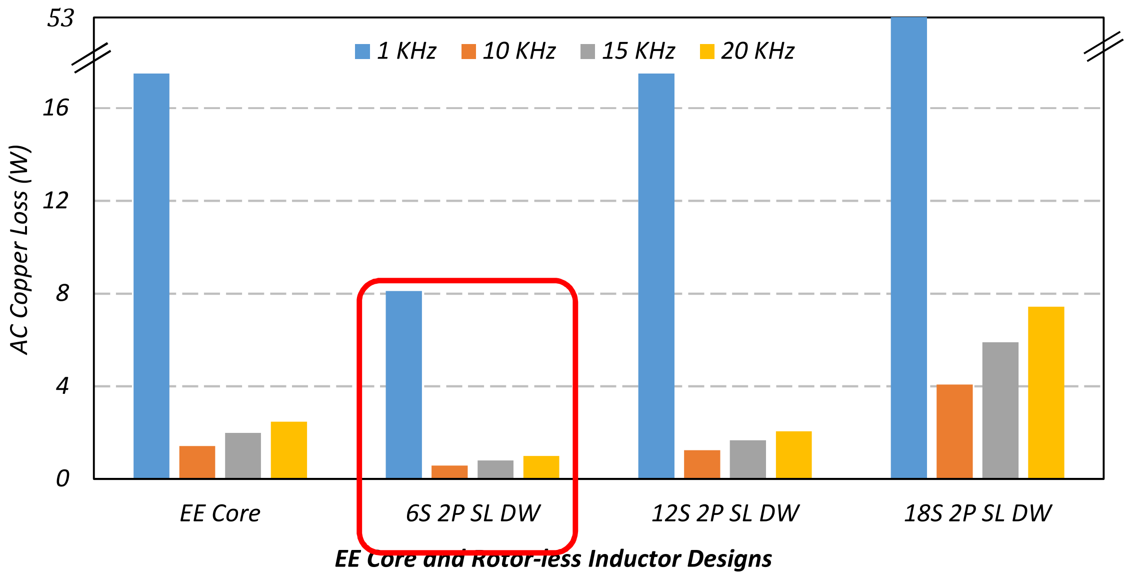

Figure 5.23: AC Copper Loss Comparison of Rotor-less Inductor with EE Core Inductor

5.7 INTEGRATED INDUCTOR DESIGN FOR 45KW STARTER-GENERATOR

A case study of the motor-shaped integrated inductor has been presented by designing a high current density output choke used to smooth the current of 45kW starter-generator as shown in Figure 5.24. The design details of the 45 kW starter-generator are shown in Table XIII. The aim of this study is to investigate the effect of high current density on the inductor design and to compare its design with conventional EE core air-cooled inductor in terms of weight and volume.

Since the inherent inductance (99 μH) of the starter-generator is very low, an additional inductance is needed to increase the overall inductance by twice as seen by the converter module. This increase in inductance will not only reduce the switching ripple from the current waveform but also aid the control system of the starter-generator.

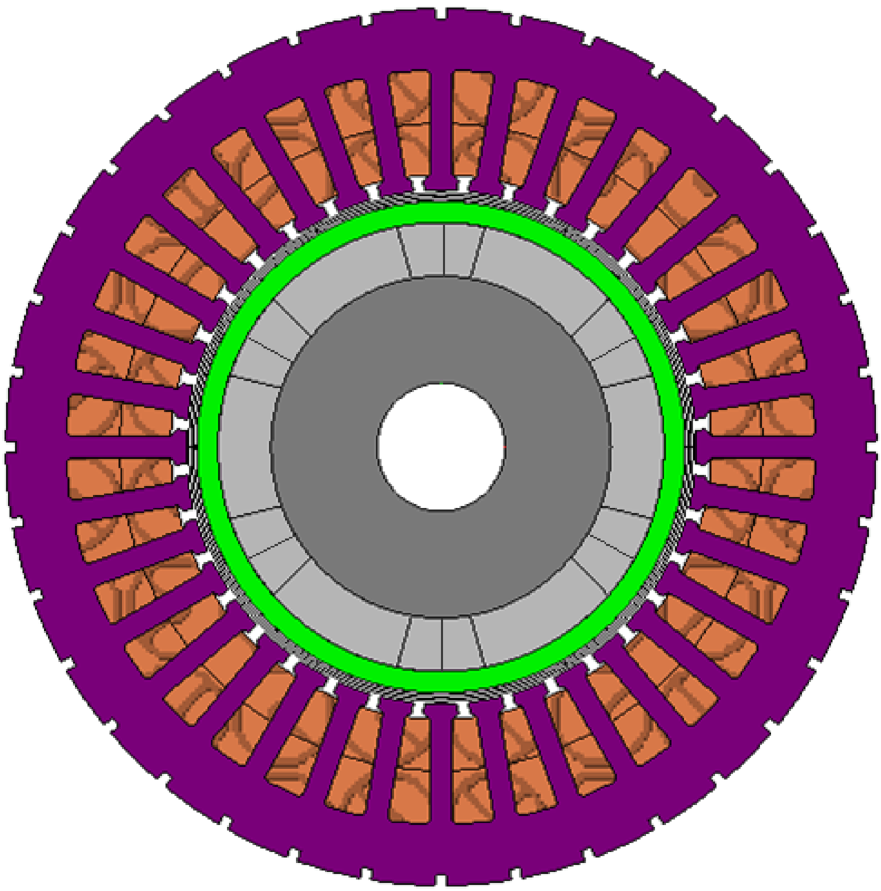

Figure 5.24: 36 Slots 6 Poles 45KW Starter-Generator

Table XIII: Parameters of Starter-generator

PARAMETERS	VALUE	UNIT
No. of Slots	36	-
No. of Poles	6	-
Base Speed / Rated Speed	8	KRPM
RMS Current at 8 kRPM	236.7	A
RMS Current Density	18	A/mm^2
Active Stack Length	80.2	mm
Outer Diameter	164	mm
Inner Diameter	96	mm
Shaft Diameter	4	mm
Phase Resistance	13.2	mΩ
d-axis Inductance	99	μH
q-axis Inductance	99	μH

5.7.1 Inductor Sizing

6 slot integrated rotor-less inductor with $DL\ CNW$ is chosen to design it at RMS current density of 18 A/mm^2 whereas the EE core inductor is designed for natural convection cooling system. The $DL\ CNW$ is chosen in order to limit the overall volume of the end-windings. Both conventional and integrated inductor are sized up using the design process as explained in section 3.4.1 and section 5.3.1 respectively. The cross-section and flux distribution (when phase A is reached at its peak value) of conventional and integrated inductor is shown in Figure 5.25(a)-(d). The specifications of the convectional and integrated inductor are presented in Table XIV and Table XV respectively.

The following assumptions have been made while sizing the both integrated and conventional EE core inductor. They are:

1. Window to Core Area Ratio, $W_a/A_c = 0.7$
2. Core Stack to Limb Length Ratio, $L_{stack}/L_{limb} = 0.77$
3. Window Height to Length Ratio, $G/F = 3$

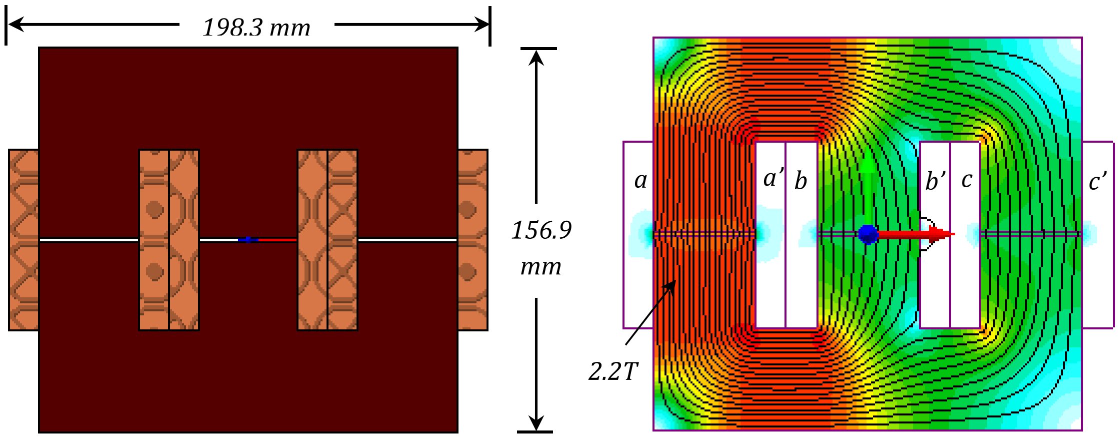

(a) Cross-section of Integrated Inductor

(b) Flux distribution of Integrated Inductor

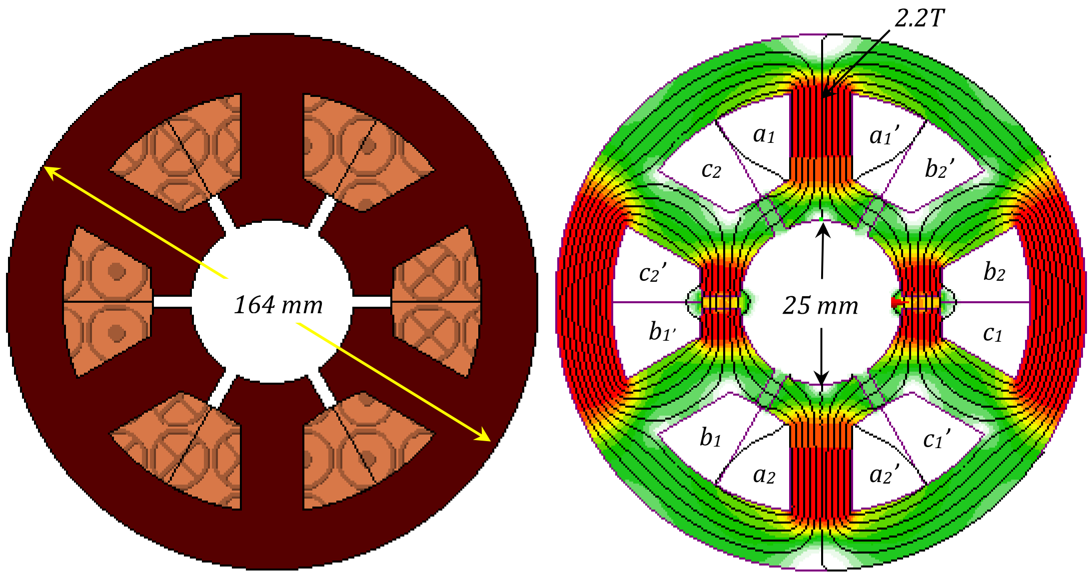

(c) Cross-section of Integrated Inductor

(d) Flux distribution of Integrated Inductor

Figure 5.25: Cross-section and Flux Distribution of Conventional & Integrated Inductor

Table XIV: Specifications of EE core Inductor

SPECIFICATIONS	VALUE	UNIT
Core Material	Hiperco 50A 0.014	-
Required Inductance	100	μH
RMS Operating Current	236.9	A
Peak Flux Density	2.3	T
Slot Fill Factor	0.5	-
RMS Current Density	4.8	A/mm^2
Waveform Factor (K_w)	4.44	-

Table XV: Specifications of Integrated Inductor

SPECIFICATIONS	VALUES	UNIT
Core Material	Hiperco 50A 0.014	-
Required Inductance	100	μH
RMS Operating Current	236.9	A
Peak Flux Density	2.3	T
Slot Fill Factor	0.5	-
RMS Current Density	18	A/mm^2
Waveform Factor (K_w)	4.44	-
Hole for the motor shaft	> 4	mm
Outer Diameter	164	mm

5.7.2 Comparison of EE core and Integrated Inductor

Both conventional and integrated inductors are compared in terms of their weight and volume. The total weight and volume include iron core and copper including the end-windings. The end-windings length is calculated using the method described in section 5.4. The comparison of sizing parameters between conventional and integrated inductor is shown in Table XVI whereas its design parameters are shown Table XVII.

Table XVI: Sizing Comparison of EE core and Integrated Inductor

SIZING PARAMETERS	EE Core Inductor	Integrated Inductor	UNIT
Iron Weight	6.84	2.44	Kg
Copper Weight (With End Windings)	3.10	1.99	Kg
Total Weight (Iron + Copper)	9.94	4.43	Kg
Total Volume (Iron + Copper)	2078	981.8	cm^3

Table XVII: Design Parameters of EE core and Integrated Inductor

DESIGN PARAMETERS	EE Core Inductor	Integrated Inductor	UNIT
Area Product	181.6	45.7	cm^4
Synchronous Inductance	90	90	μH
Peak Flux Density	2.2	2.2	T

Phase Resistance	1.0	8.2	mΩ
Turns per Phase	10	36	-
Slot Fill Factor	0.5	0.5	-
Slot Area	1840	925	mm^2
Conductor Diameter	8.0	4.0	mm
Active Stack Length	32	20	mm
Active Stack Length for 100μH	36	22.5	mm
Total Stack Length (With End Windings)	66.8	46.5	mm

Significant reduction in weight and volume is achieved by designing the integrated inductor at the same current density of starter-generator. The weight of the integrated inductor is reduced by 55.4% whereas its associated volume is reduced by 52.7% when compared to conventional EE core inductor.

The phase resistance of the integrated inductor is 8.2 times higher than EE core inductor due to different current density specifications whereas the associated thermal losses are assumed to manage by the existing cooling system of the starter-generator. The synchronous inductance of 90μH is obtained for both conventional and integrated inductors which can be increased to required value of 100μH by adjusting the active stack length of the stator. The inductance values are validated using the FE simulations.

5.8 SUMMARY

Novel integrated options for passive filter inductors were presented in this chapter that can potentially be implemented for input grid filters, DC link filters and inverter output filters. The novel integrated options include: motor-shaped rotational and motor-shaped rotor-less inductor. The study that has been carried out in this chapter suggests the rotor-less inductor is more appropriate where the operating frequency is fixed and hence can be employed for input grid and DC link filter inductors whereas the rotational inductor is a suitable solution for inverter output filters where the operating frequency is variable and the rotor losses can be minimized through the rotor magnetic path. The potential advantage of employing the motor-shaped inductor is that it shares the existing cooling system of the motor or generator which allow us to design it with higher current densities. This leads to enormous reduction of inductor weight and volume.

A number of motor-shaped inductors were designed and optimized in terms of total loss and weight while considering the degrees of freedom of slot-pole combinations and winding configuration. All the design were compared with conventional EE core inductor in terms of total loss and weight.

12 slots 2 poles rotational inductor with $SL\ DW$ seems to be a best candidate in terms of total losses. The total losses at fundamental frequency was reduced by 39% with only 5.2% increase in weight. On the other hand, 6 slots rotational inductor with S$L\ DW$ has contributed the lowest AC copper resistance at both fundamental and switching frequencies of 10, 15 and 20 kHz. The reduction of 72.04% was achieved at fundamental frequency, whereas the reduction of 74.14%, 74.13 and 74.12% is achieved at all switching frequencies respectively with respect to the EE core inductor.

12 slots 2 poles rotor-less inductor with $SL\ DW$ looked to be a best candidate in terms of total losses. The total losses at fundamental frequency was reduced by 39% with only 7% increase in weight. On the other hand, 6 slots rotor-less inductor with $SL\ DW$ has contributed the lowest AC copper resistance at both fundamental and switching frequencies of 10, 15 and 20 kHz. The reduction of 72.04% was achieved at fundamental frequency, whereas the reduction of 59.5%, 59.8 and 60.1% is achieved at all switching frequencies respectively with respect to the EE core inductor.

A case study of motor-shaped integrated inductor was also presented in this chapter. The application of aerospace starter-generator was considered to smooth out the switching ripple from the current waveforms by introducing the inductance of 99 μH. The integrated inductor was designed at RMS current density of 18 A/mm^2. The integrated inductor was compared with conventional EE core inductor which had provided the reduction of 55.4% and 52.7% in weight and volume of the inductor respectively.

5.9 REFERENCES:

[1] *AK Steel - Non Oriented Electrical Steels*. Available: http://www.aksteel.com/pdf/markets_products/electrical/non_oriented_bulletin.pdf

[2] *AK Steel - Selection of Electrical Steels for Magnetic Cores*. Available: http://www.aksteel.com/pdf/markets_products/electrical/mag_cores_data_bulletin.pdf

[3] L. Chong, R. Dutta, and M. F. Rahman, "Performance comparison between concentrated and distributed wound IPM machines used for field weakening applications," in *International Aegean Conference on Electrical Machines and Power Electronics and Electromotion, Joint Conference*, 2011, pp. 616-619.

[4] A. Walker, M. Galea, C. Gerada, A. Mebarki, and D. Gerada, "Design considerations for high performance traction machines: Aiming for the FreedomCar 2020 targets," in *2015 International Conference on Electrical Systems for Aircraft, Railway, Ship Propulsion and Road Vehicles (ESARS)*, 2015, pp. 1-6.

CHAPTER

6

INTEGRATED MOTOR-SHAPED ROTATIONAL INDUCTOR: EXPERIMENTAL VALIDATION

6.1 INTRODUCTION

This chapter describes an experimental validation of the integrated motor-shaped rotational inductor proposed in chapter 5. For concept validation, 12 slots 2 poles rotational inductor is chosen from the design optimization which is presented in section 5.4. The tests were conducted on 3-phase induction motor drive rated at 49 kW, 20,000rpm which is suitable for validating and measuring the required performance of the rotational inductor whilst spinning the induction motor at no-load. The shaft of the induction motor is coupled with the rotor of rotational inductor whereas its stator is supplied by programmable AC power source.

The results and discussion have been presented at different rotor speeds and supply frequencies. Subsequently, the performance of both the rotational inductor and conventional EE core inductor have been compared in terms of synchronous inductance, power losses, DC and AC resistance, power quality, weight and volume.

6.2 DESCRIPTION OF THE EXPERIMENTAL SETUP

Figure 6.1(a)-(c) shows the experimental rig, test inductor, and setup for testing and validating the concept of the rotational inductor. For the purpose of validation, 12 slots 2 poles rotational inductor is chosen from the design optimization of motor-shaped integrated inductors as presented in section 5.4. The construction of the test inductor is shown in Figure 6.2(a)-(b). The inductor's rotor is mounted on the external shaft which is coupled to the shaft of the induction motor. The ball bearing with an inner and outer diameter of 20mm and 32mm is chosen as shown in Figure 6.1(b) which is rated at 20,000 rpm and suitable for testing the required performance. The stator of the inductor is fitted inside the casing with the endcaps at each end. The specification of induction motor drive, the technical drawings and construction of EE the core and rotational inductor are shown in Appendix G.

To test the inductor, the induction motor is driven at no-load whereas the stator of the rotational inductor is supplied by the programmable power supply ($Chroma$ Programmable AC Source 61511). The power loss measurements have been taken using power analyser (N4L PPA550) which is interfaced with the Desktop PC as shown Figure 6.1(c).

To compare the performance of rotational inductor, the EE core inductor is also tested which is supplied by the same $Chroma$ AC source whose design procedure is presented in chapter 3. The filter inductor has 20 turns per phase and the inductance of 1.1mH has been measured which is comparable with its designed value. The method of estimating the inductance is presented in Appendix F.

(a) Experimental Test Rig

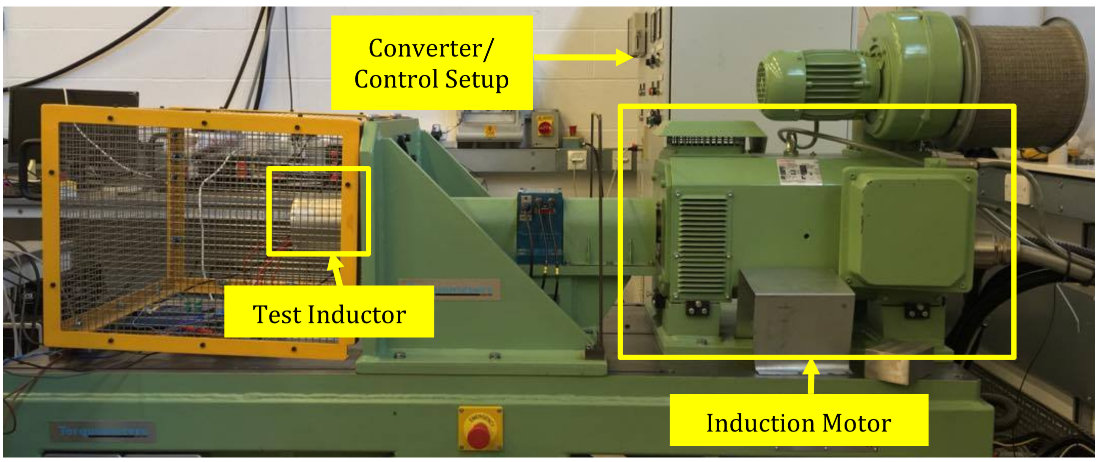

(b) Test Inductor

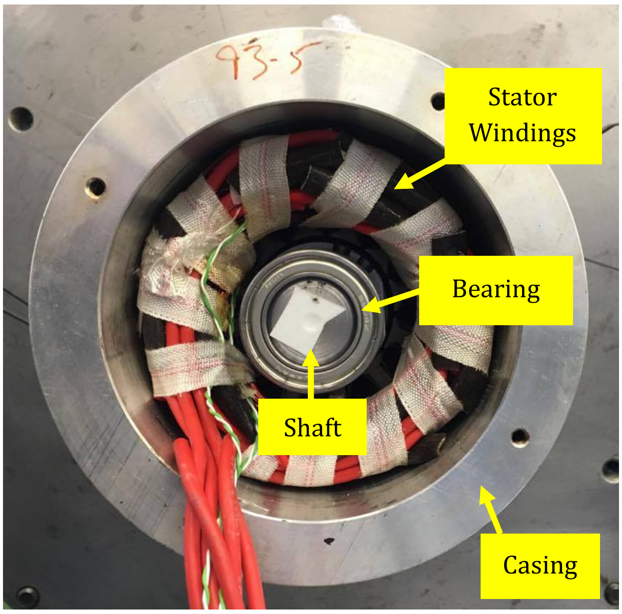

(c) Experimental Test Setup

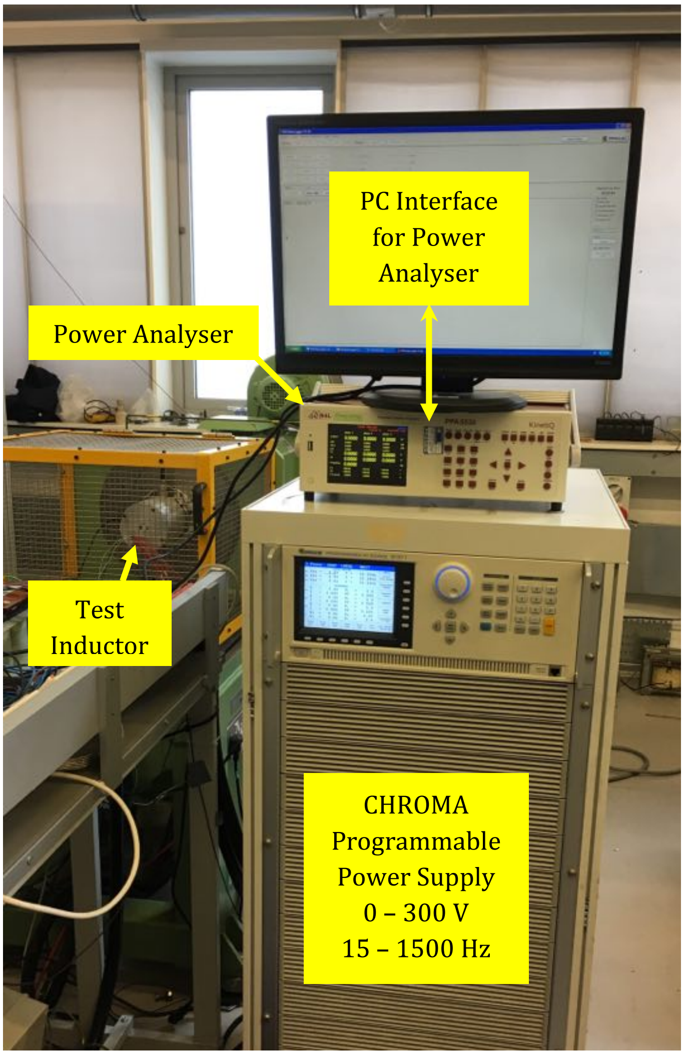

Figure 6.1: Experimental Rig and Test Setup for Rotational Inductor

(a) Stator Construction

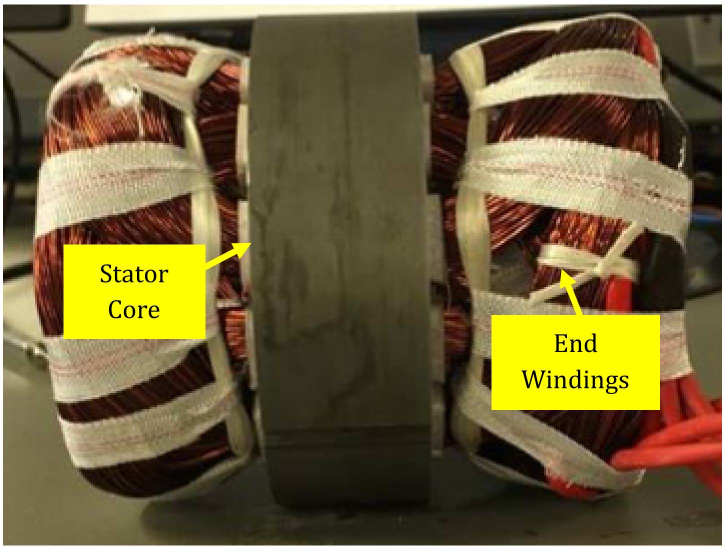

(b) Casing, Rotor shaft, Casing and Endcaps

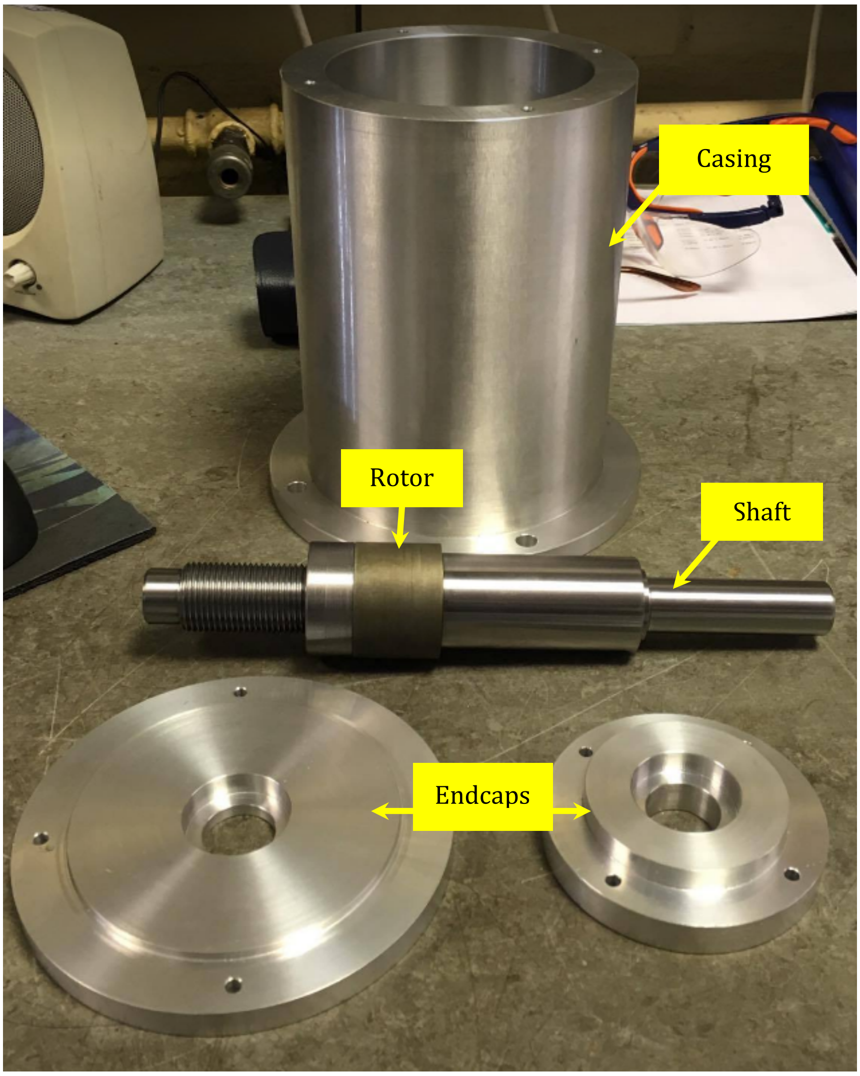

Figure 6.2: Construction of Rotational Inductor

6.3 EXPERIMENTAL MEASUREMENT

The setup to measure the power losses of the rotational inductor is shown in Figure 6.3 and the devices used for the experimental measurements are listed below:

1. Chroma *AC* Source 61511 (0 – 300V, 0 – 1500 Hz)
2. Power Analyser (N4L PPA550)
3. PC for Interfacing the Power Analyser

The inductor losses were evaluated by measuring the input power at the terminals of the inductor at different supply frequencies and controlling the peak current of 18A by adjusting the voltage of *AC* power supply. For measuring the power losses of *EE* core inductor, same procedure is applied as that of rotational inductor.

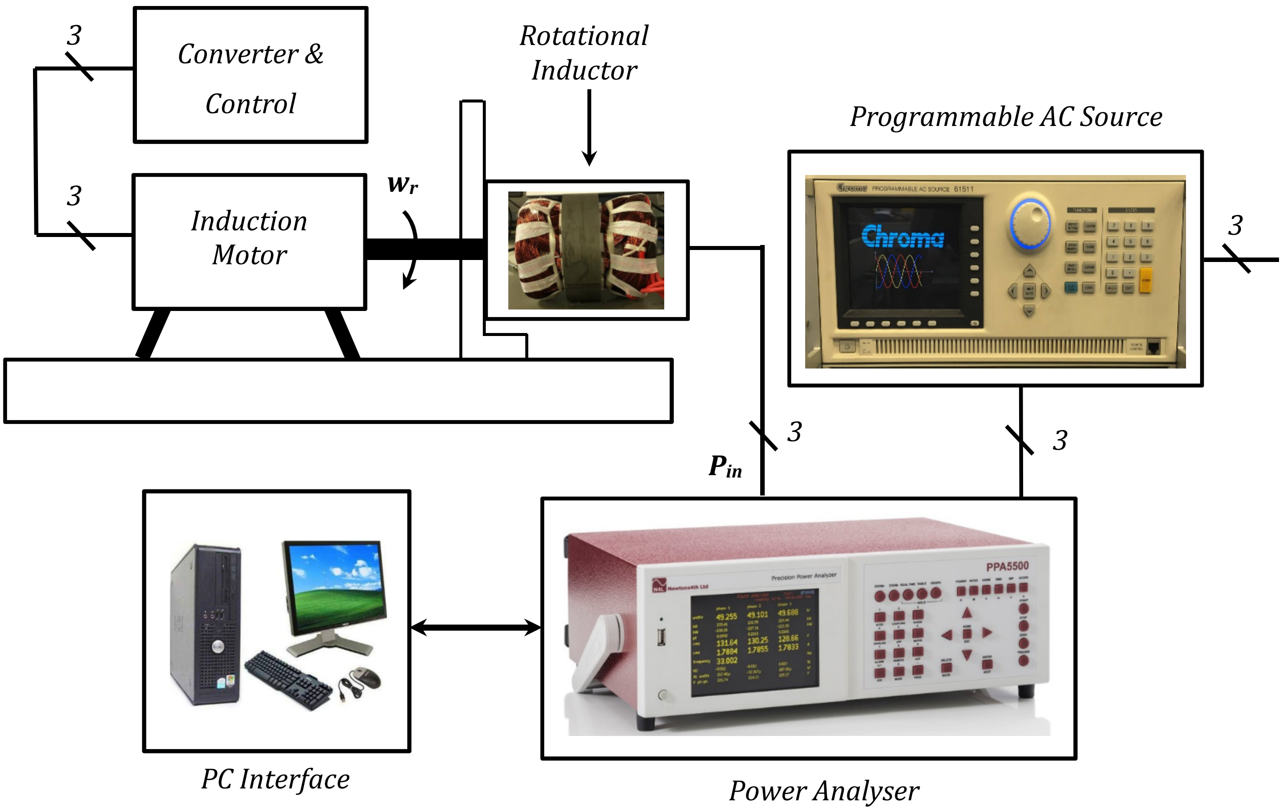

Figure 6.3: Experimental Measurements of Rotational and EE core Inductor

6.4 PARAMETERS MEASUREMENT

In this section, the DC resistance, synchronous inductance, active weight and volume of the rotational and EE core inductors are measured. The parameters comparison of rotational and EE core inductors are illustrated in Table I. For measuring the DC resistance $FLUKE$ (8846A 6-1/2 DIGIT) multimeter is used as shown in Appendix H. The synchronous inductance is estimated using the measured current and power factor by adjusting the voltage supplied of programmable power supply. The method to estimate the synchronous inductance is shown in Appendix F. Furthermore, the PC is interfaced with the power analyser in order to measure inductor losses in real time.

Table I: Parameter Comparison of Rotational and EE core Inductor

PARAMETERS	EE CORE INDUCTOR	ROTATIONAL INDUCTOR	UNIT
Synchronous Inductance	1.09	1.52	mH
DC Resistance	43	80	mΩ
	39.4	52.6	mΩ/mH
Active Weight	2.2	2.20	Kg
	2.02	1.45	Kg/mH
Active Volume	529.9	754.3	cm^3
	493.2	496.2	cm^3/mH

Both rotational and EE core inductors were designed for 1.3mH in chapter 3 and 5 respectively. The EE core inductor gives the inductance of 1.09mH which is very close to the designed value. However, the inductance of rotational inductor is more than the designed value. This is due the inductance of end windings added to the synchronous inductance of 1.09mH.

For the purpose of fair comparison, the parameters shown in Table I are normalized to the ratio of synchronous inductance since the inductance is different in both inductors. The active weight and volume of both inductors (Iron, Copper, and Bobbins) have also been compared whose weight scaling is presented in Appendix H. It can be seen that weight-to-inductance ratio of the rotational inductor is reduced by 28.2% and the volume-to-inductance ratio is alike. On the other hand, the DC resistance-to-inductance ratio of rotational inductor is more than EE core inductor due to the higher end windings length.

It is worth noting here that the comparison of weight-to-inductance and volume-to-inductance ratios are based on the air convection cooling system. Nonetheless, when the rotational inductor is designed at higher current density the enormous weight and volume reduction is predictable due to the lower area product.

6.5 EXPERIMENTAL RESULTS & DISCUSSION

This section presents the concept validation, experimental results and discussion of the rotational inductor and its performance comparison with conventional EE core inductor in terms of total loss-to-inductance ratio, AC resistance-to-inductance ratio, synchronous inductance, voltage and current $\%THD$.

6.5.1 Experimental Results of the Rotational Inductor

The rotational inductor is tested under different supply frequency both when the rotor is rotating and standstill in order to validate the concept. The peak inductor current of 18A is imposed by adjusting the voltage of programmable AC power supply. Figure 6.4 (a)-(c) shows the measured total inductor losses with respect to real time at supply frequency of 100 Hz, 200 Hz and 300 Hz respectively with standstill rotor and rotor rotating at synchronous speed of 6 kRPM, 12 kRPM and 18 kRPM respectively. It is clearly seen that the inductor losses are reduced as the rotor speeds up to its synchronous speed at different operating supply frequencies. The percentage of loss reduction increases as the rotor speed is raised. This is due to the fact that the magnetic field through the rotor of the inductor is induction free when rotating synchronously with the magnetic field of the stator windings.

Figure 6.5 (a)-(c) shows the variation in the iron losses with respect to different supply frequencies and rotor speed both in positive and negative directions. The iron losses were separated by subtracting the 3-phase copper losses and plotted against the rotor speed. As expected, the iron losses are minimum at synchronous speed whereas it increases as the slip is increased in the counter-clockwise direction. The maximum point of losses arises when the rotor is rotating at synchronous speed in the counter-clockwise direction where the slip is doubled.

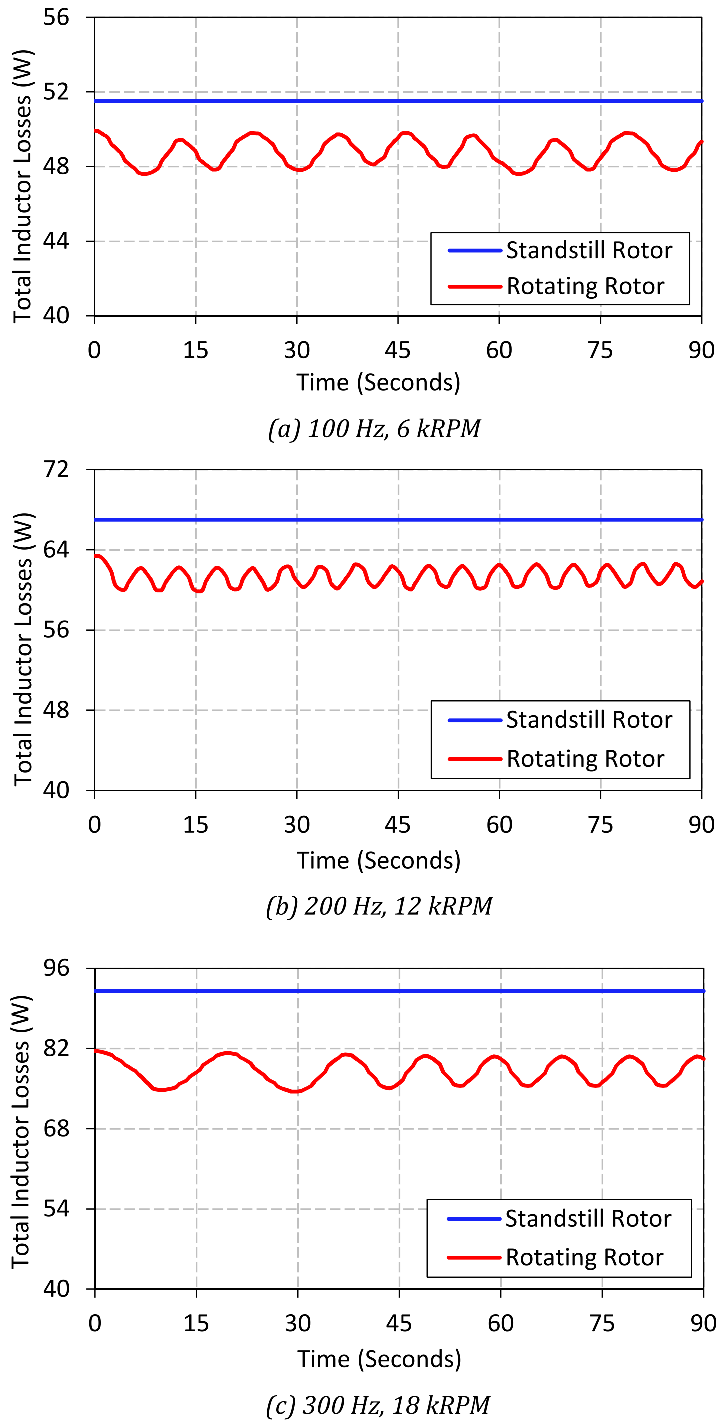

Figure 6.4: Measured Inductor Losses at 6, 12 and 18 kRPM Rotor Speeds

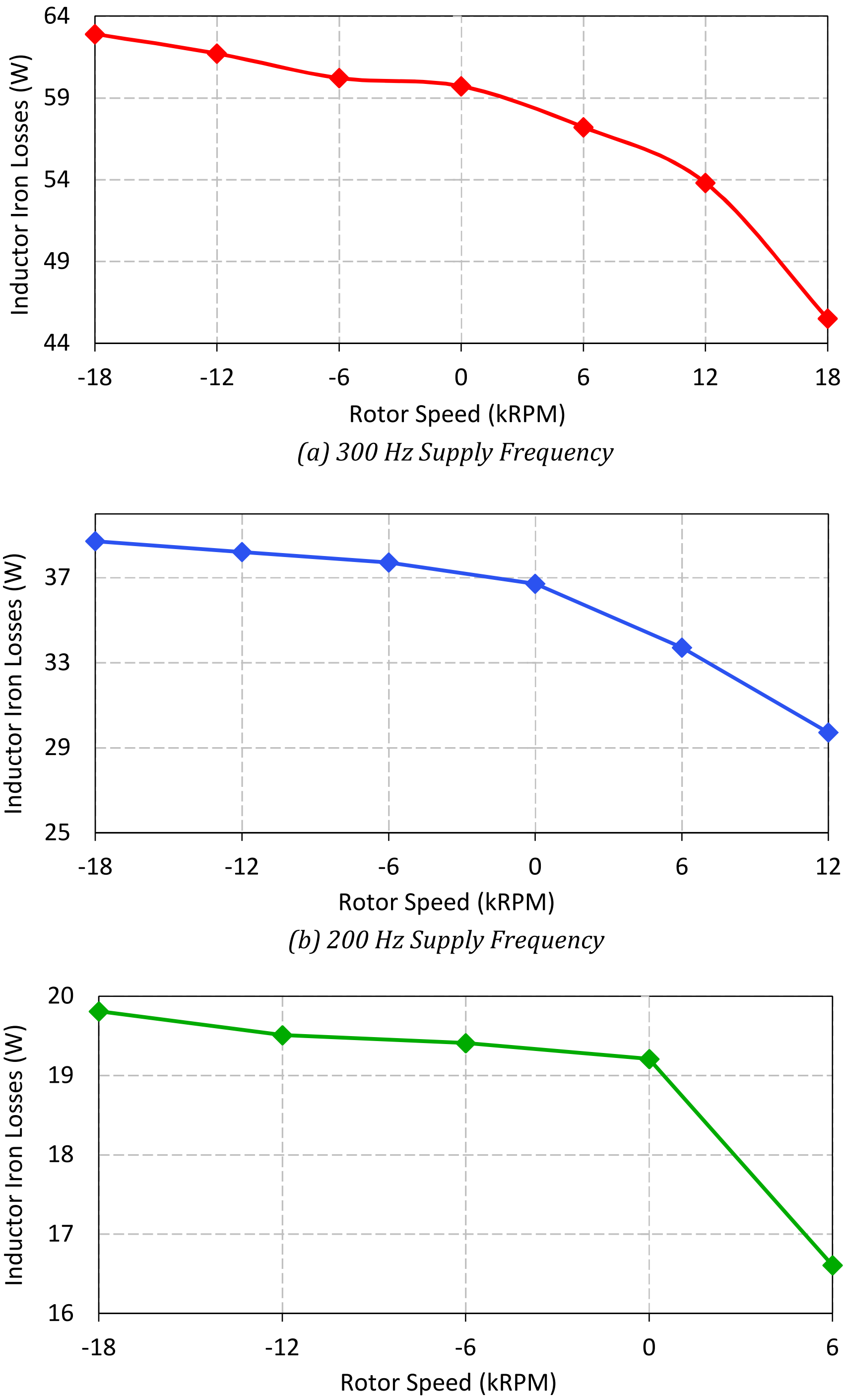

(a) 300 Hz Supply Frequency

(b) 200 Hz Supply Frequency

(c) 100 Hz Supply Frequency

Figure 6.5: Measured Iron Losses at 100, 200 and 300 Hz

6.5.2 Comparison with EE Core Inductor

This section presents the comparative analysis between the rotational inductor and conventional EE core inductor in terms of total loss-to-inductance ratio, AC resistance-to-inductance ratio, synchronous inductance and their respective voltage and current $\%THD$.

6.5.2.1 Total Loss-to-Inductance Comparison

Table II shows the total loss-to-inductance ratio comparison of rotational and EE core inductor when peak current of 18A is imposed. As can be observed that the total loss-to-inductance ratio is reduced and hence total loss reduction is increased for the rotational inductor as the motor speeds up to 18 kRPM. Since the inductance of EE core inductor is less compared to rotational inductor along with reduced iron losses the loss-to-inductance ratio is higher. The reduction of 9.6% and 22.5% is achieved at the rotor speed of 12 kRPM and 18 kRPM respectively whereas the EE core gives lower loss-to-inductance ratio at 6 kRPM due to low rotor speed.

Table II: Total Loss Comparison of Rotational and EE core Inductor at 18A Current

Supply Frequency (Hz)	Rotor Speed (kRPM)	EE Core Inductor (W/mH)	Rotational Inductor (W/mH)	Total Loss Reduction (%)
100	6	29.5	32.12	-8.8
200	12	45.1	40.78	9.6
300	18	66.1	51.19	22.5

6.5.2.2 AC Resistance-to-Inductance Ratio Comparison

To look at the effect of resistance versus supply frequency the phase resistance was measured using the $N4L - PSM1735$ Impedance Analyser/LCR meter. The phase resistance of both EE core and rotational inductor was measured up to 20 kHz in step of 1.1 kHz which is normalised to resistance-to-inductance ratio. Figure 6.6(a)-(b) shows the variation of resistance-to-inductance ratio with respect to the supply frequency. The difference of resistance-to-inductance ratio indicates the leakage and fringing effect of the particular device. As expected, the leakage and fringing effect in EE core inductor is higher than the rotational inductor.

As discussed in chapter 5, most of the conductors are placed close to the airgap in EE core inductor which results in to more fringing effect. In contrast, conductors of motor-shaped inductors are placed far from the slot opening and airgap therefore, the fringing flux cutting through the conductors is reduced. The effect of leakage flux is likewise reduced in rotational inductor due to the distributed configuration of the stator windings which leads to the lower leakage flux [1, 2]. The fringing and leakage fluxes crossing the conductors is the main reason for increased the AC resistance.

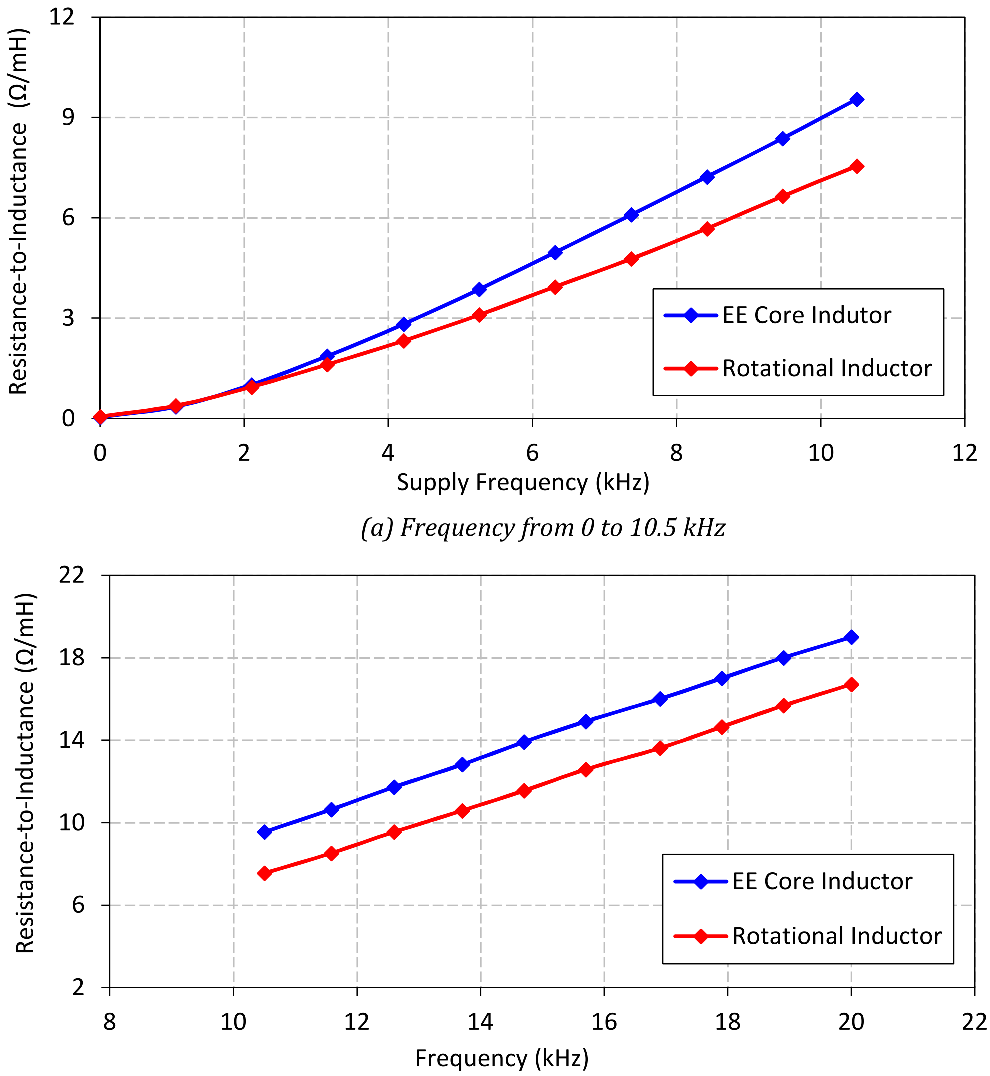

(a) Frequency from 0 to 10.5 kHz

(b) Frequency from 10.5 to 20 kHz

Figure 6.6: Comparison of Phase Resistance-to-Inductance Ratio

6.5.2.3 Synchronous Inductance and THD Comparison

To determine the point of magnetic saturation in the core the synchronous inductance, voltage and current $\%THD$ of both EE core and rotational inductor are plotted against RMS current as shown in Figure 6.7 (a)-(c). The inductor current is controlled from 7.2A to 15.8A by adjusting the voltage of programmable AC power supply. As expected, the point of magnetic saturation is nearby RMS current of 12.5A for both EE core and rotational inductor. However, the voltage and current $\%THD$ of rotational inductor appears to be superior when compared to the EE core inductor.

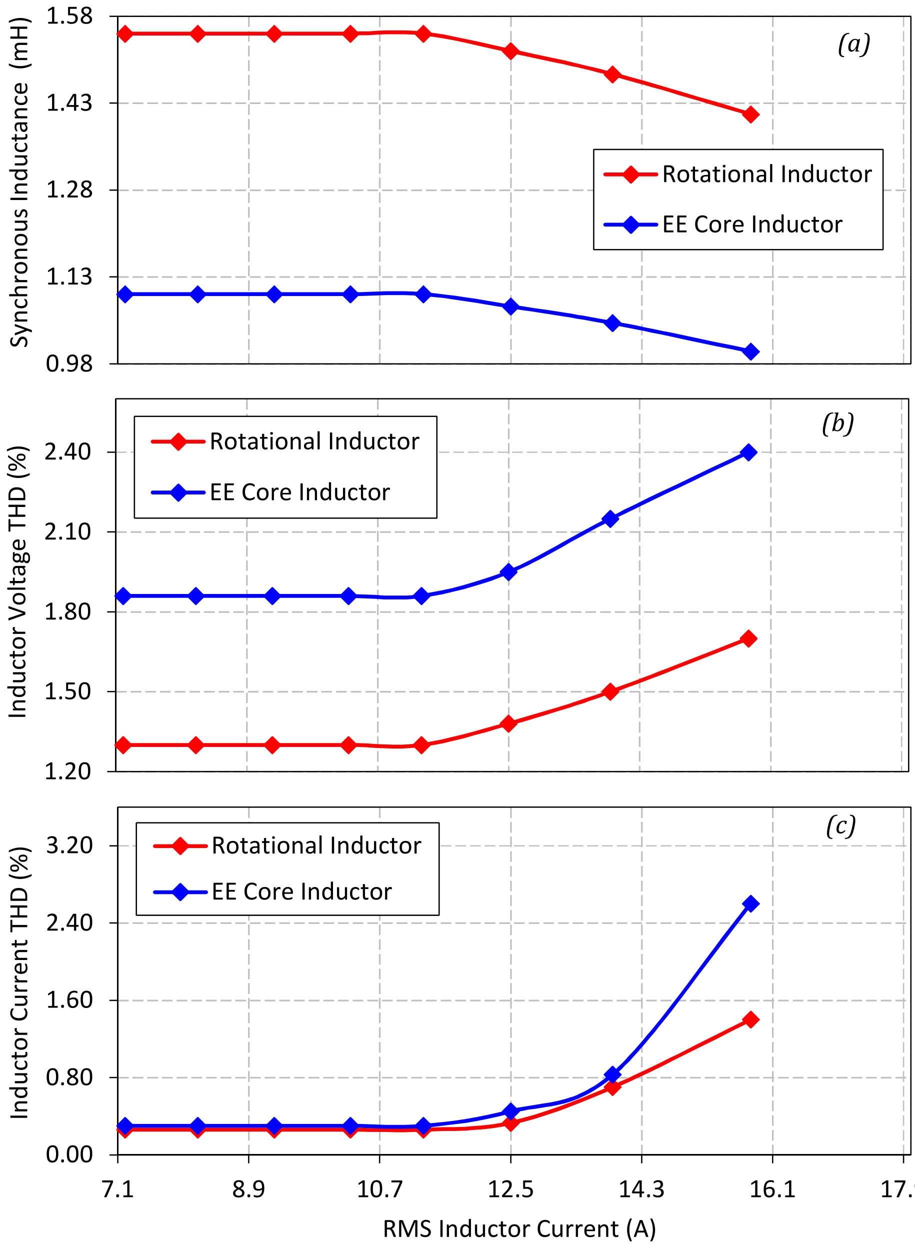

Figure 6.7: Comparison of Synchronous Inductance, Voltage and Current %THD

6.6 SUMMARY

Experimental validation of motor-shaped rotational inductor was presented in this chapter. For concept validation, 12 slots 2 poles rotational inductor was chosen from the design optimization as presented in section 5.4. The experimental tests for rotational inductor were conducted on 3-phase induction motor drive rated at 49 kW, 20,000rpm. The results and discussion of power losses for rotational inductor was presented at different rotor speeds and supply frequencies. Subsequently, the performance of both rotational inductor and conventional EE core inductor was compared in terms of total loss-to-inductance ratio, DC and AC resistance-to-inductance ratio, weight-to-inductance ratio, volume-to-inductance ratio, synchronous inductance, voltage and current $\%THD$.

From the experimental study, it was shown that the iron losses in rotational inductor were minimum when its rotor is rotating at synchronous speed where the slip is zero and the iron losses were increased as the slip is increased. The maximum iron losses occurred when the rotor is rotating at synchronous speed in the counter-clockwise direction where the slip is doubled.

In comparison with EE core inductor, total loss-to-inductance ratio was reduced by 22.5% at synchronous speed whereas the weight-to-inductance ratio was reduced by 28.2%. The AC resistance-to-inductance ratio, voltage and current $\%THD$ of rotational inductor was also looked to be superior to EE core inductor. However, DC resistance-to-inductance ratio was higher for EE core inductor and the volume-to-inductance ratio was alike for both rotational and EE core inductors.

6.7 REFERENCES

[1] L. Chong, R. Dutta, and M. F. Rahman, "Performance comparison between concentrated and distributed wound IPM machines used for field weakening applications," in *International Aegean Conference on Electrical Machines and Power Electronics and Electromotion, Joint Conference*, 2011, pp. 616-619.

[2] A. Walker, M. Galea, C. Gerada, A. Mebarki, and D. Gerada, "Design considerations for high performance traction machines: Aiming for the FreedomCar 2020 targets," in *2015 International Conference on Electrical Systems for Aircraft, Railway, Ship Propulsion and Road Vehicles (ESARS)*, 2015, pp. 1-6.

CHAPTER

7

CONCLUSION

&

FURTHER WORK

7.1 CONCLUSION:

This chapter draws together the findings of the research that have been carried out in this thesis. Two novel integrative approaches were proposed, investigated and compared with the conventional system. The main objective was to develop and design a solution to integrate the passive filter inductors within the envelope of the electrical machine both from the functional and physical point of view.

The problems of traditional motor drives and the necessity of integration were discussed in chapter 1. Importance was subsequently given to the review of passive filters being used at present which was reported in chapter 2. It covered the grid-side, DC link and output passive filter followed by the integrated passive filters which is being used in motor drives.

In chapter 3, a functional integration of passive filter inductor has proposed that uses the motor's inherent magnetics which eventually acts as a filter inductance by introducing the filter capacitance and resistance between the motor windings. A mathematical and FE model of the integrated motor was developed using the $MATLAB^{®}$ and $MagNet - Infolytica$ in order to predict the performance of motor drive with integrated inductor and compare it with the traditional motor drives system.

For the purpose of comparing traditional and integrated motor drive systems, a separate EE core filter inductor was designed and sized using "Area Product" approach. It was demonstrated that the filtering effect of the motor with integrated inductor and the motor with external inductor were alike. Moreover, the losses, weight and volume of the external has been eliminated when the integrated motor was chosen. Subsequently, the optimization of the integrated motor was presented by adjusting the filter branch windings from 1.3mH to 0.28mH. The torque ripple, total losses, weight and volume was compared with the conventional motor drive system. The results have shown that the total losses and torque ripple in the integrated motor reduces as the filter branch inductance is decreased due to the transformer action between the filter branch and motor branch windings.

In comparison with the conventional motor drive system the integrated motor drives is superior in terms of total losses, weight, and volume. However, the torque ripple of the integrated motor was improved for the filter branch inductance of 0.28mH with respect to the motor without output filter and was comparable with the motor drive system with conventional EE core inductor.

Chapter 4 present the experimental validation of the motor with an integrated inductor at 50% filter branch windings. The windings of an existing $HEMAS$ motor was modified to validate the concept of motor with integrated inductor. In order to compare it with the conventional motor drive, an external EE core inductor was manufactured. The experimental tests were conducted at different rotor speeds, mechanical load on the shaft and the inverter switching frequency. The inverter terminal voltage, motor voltage, filter current, motor current output torque and torque ripple were compared.

A comprehensive experimental loss characterization of the integrated and conventional motor was presented which was also compared with the FE analysis. The

FE losses showed a good agreement with the experiments in the integrated. The experimental results have ultimately shown that the integrated motor completely eliminates the need of an external inductor which makes it an appropriate solution for the motor drives which carries a bulky and lossy inductor due to its high current rating. In comparison with EE core inductor, the weight and volume was completely eliminated for the motor with integrated inductor whereas the total loss reduction of 20.4%, 25.3%, 35.2% and 34.3% is achieved at the load torque of 3 Nm and supply frequency of 100, 125, 150 and 175 Hz respectively.

In chapter 5, physical integration of passive filter inductors was introduced which include: motor-shaped rotational and motor-shaped rotor-less inductor. Both inductors share the existing motor or generator housing which have resulted in an effective physical integration. The motor-shaped inductors can potentially be implemented for applications of input grid filter, DC link filter and inverter output filter.

A number of motor-shaped inductors were designed and optimized in terms of total loss and weight while considering the slot-pole combinations and winding configuration as the degrees of freedom. In comparison with conventional EE core inductor, 12 slots 2 poles rotational inductor with SL DW seemed to be a best configuration in terms of total losses. On the other hand, 6 slots rotational inductor with $SL\,DW$ has the lowest AC copper resistance at both fundamental and all considered switching frequencies. Finally, a case study of high current density motor-shaped inductor for the application of aerospace starter-generator have shown the enormous reduction of inductor's weight and volume despite of its power losses which was assumed to be managed by the existing cooling system of motor or generator.

Experimental validation of the 12 slots 2 poles rotational inductor and its performance comparison with conventional EE core inductor was presented in Chapter 6. It was shown that the iron losses in rotational inductor were minimum when its rotor is rotating at synchronous speed. In comparison with EE core inductor, total loss-to-inductance ratio was reduced by 22.5% at synchronous speed whereas the weight-to-inductance ratio was reduced by 28.2%.

The AC resistance-to-inductance ratio, voltage and current $\%THD$ of rotational inductor was also looked to be superior to EE core inductor. However, DC resistance-to-inductance ratio was higher for EE core inductor and the volume-to-inductance ratio was alike for both rotational and EE core inductors.

7.2 ADVANTAGES AND LIMITATIONS

The novel outcomes of this research, as detailed in the previous section, summarise its main advantages. The most significant of these are listed below along with its limitations:

7.2.1 Motor (PMSM) with Integrated Inductor

- The integrated motor that uses the inherent motor magnetics completely eliminates the need of an external inductor which makes it a suitable solution for the motor drives with high current ratings.
- Since the external filter inductor is completely removed, the power losses and its associated weight and volume are also eliminated.
- The need of extra voltage drop for the external inductor is also eliminated which has to supply by the DC link in the case of motor drive with external filter inductor.
- However, only a part of the motor windings will experience the PWM voltages. The insulation of that part of the motor windings can be made with high grade insulating material. Since the part of the motor windings that is exposed to PWM voltages is just a fraction of the entire motor windings, therefore, the quantity and hence the cost of high grade insulating material will be minimum.

7.2.2 Integrated Motor-shaped Inductors

- The motor-shaped rotor-less inductor is more appropriate for applications where the operating frequency is fixed and hence can be employed for input grid and DC link filter inductors and isolation transformers.
- The motor-shaped rotational inductor is a suitable solution for the inverter output filters where the operating frequency is variable and the rotor losses can be minimized through the rotor magnetic path.

- The potential advantage of adopting the motor-shaped inductors is: sharing the existing cooling system of the motor or generator which allows to size it at high current density that leads to a significant reduction of inductor weight and volume.

- The shared cooling system will eliminate the need of an external cooling system for the inductor which reduces the effort for a thermal engineer to consider the two separate cooling system for the inductor and the motor or generator.

- Since the cooling system is shared the rotor-less inductor can also be employed for power transformer applications, where there is a need of integrating power transformers within the same housing as that of the generator.

- However, above all advantages, the only limitation comes from the power losses. The power losses of the inductor or transformer have to be managed by the cooling system of the existing motor or generator. Additionally, the axial length of the housing would need to be increased to place the inductor or transformer.

7.3 FURTHER WORK

Although much has been realized in terms of integrating passive filter inductors and their related tasks, there is scope to extend this study:

- The concept of the motor with integrated filter presented in chapter 3 can also be implemented on the other topologies of the electrical machines such as induction motors and switch reluctance motors etc.

- In chapter 4, the experimental study was only conducted with 50% filter branch windings. The experimental validation of less than 1.3 mH filter branch inductance should be experimented to see the ripple cancellation effect between the filter and motor branch due to the transformer's action.

- In chapter 5, the analysis has only be done for passive filter inductors. It is worth to look at the analysis of transformers used in motor drives system where the integration is needed. Similarly, the study of motor-shaped inductors is required for the grid-side input and DC link smoothing inductors.

- Although the work presented in chapter 5 is only based on the electromagnetic models, there is a need of combined electromagnetic-thermal modeling with the existing motor or generator when the motor-shaped inductor is considered for integrated technology motor drives application.

APPENDIX A: BASICS OF MAGNETIC CIRCUIT DESIGN

A. MAGNETIC COMPONENTS DESIGN:

Magnetic components such as inductor and transformer are basic need in almost all the power electronics and motor drives system. They are used as a filter to reduce unwanted signals noises and also used to limit the rate of change of current in snubber circuit etc. Transformers, on the other hand are energy transfer devices which transfers the energy from one level to another. They can also be used to provide electrical isolation in a circuit.

A1. MAGNETIC CORE:

Non-magnetic materials such as air, paper, copper etc. have low magnetic permeability that do not to pass magnetic flux easily whereas magnetic materials like iron, nickel, cobalt and their alloys that have high magnetic permeability (ranging from hundreds to thousands). The advantages of using magnetic core over air core are that the magnetic path length is well defined and flux is essentially confined to the core except in the vicinity of the winding. The permeance and non-linear nature of magnetic material set the limit that how much magnetic flux can be established in the magnetic core before getting it into saturation.

A2. MAGNETIC CIRCUIT:

According to the Ampere's law,

$$Ni = Hc\,lc = \Phi\frac{l_c}{\mu_r\,\mu_o\,A_c} = \Phi Rcore = MMF \qquad (A1)$$

Where, Ni is the ampere turns of the coil that drives the magnetic field around the core also called the magneto-motive force (MMF), H_c is the magnetic field intensity of the core, l_c is the mean magnetic path length, μ_r and μ_o is the relative and free space permeability respectively, A_c is the cross sectional core area, ϕ is the magnetic flux and R_c is the reluctance of the core. From Eq. A1,

$$Rcore = \frac{l_c}{\mu_r\,\mu_o\,A_c} \qquad (A2)$$

The Eq. A1 is the analogous to the ohm's law in which EMF and MMF drives the circuit, magnetic flux and electric current flows in the circuit depending on the material resistance and reluctance respectively.

So far, the discussion has been made for only core material magnetic circuit. Airgap plays an important role when there is the need of storing the linear energy in the magnetic circuit.

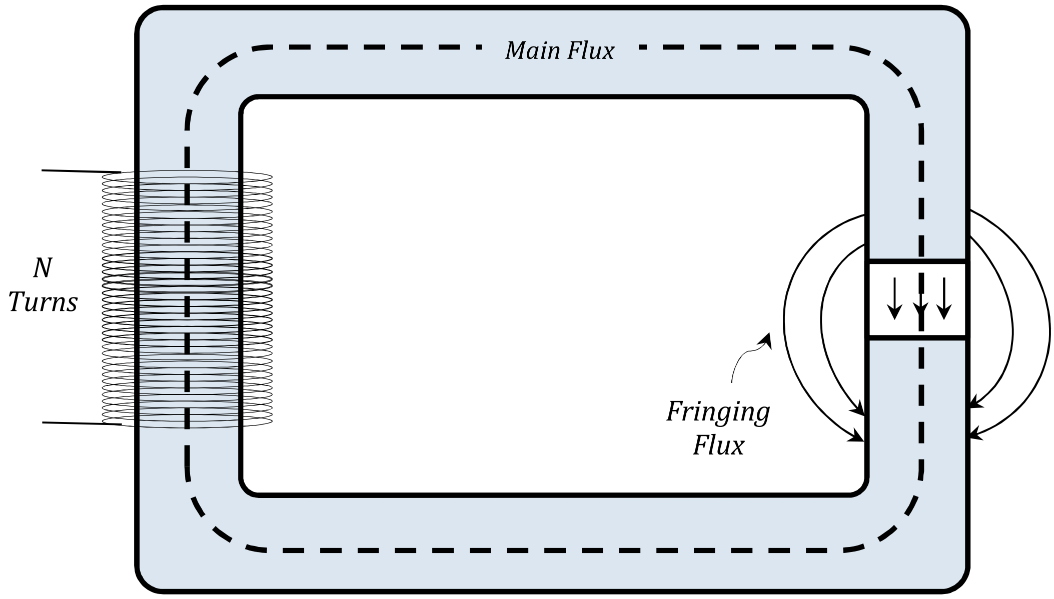

Figure A1: Magnetic air-gapped core

Figure A1 shows the air-gapped magnetic core which gives rise to energy storage. This arrangement is basic of inductor which is used in the field of power electronics and motor drives. With gapped core the MMF is given by,

$$MMF = \Phi\left(R_c + R_g\right) = \Phi\left(\frac{l_c}{\mu_r\, \mu_o\, A_c} + \frac{l_g}{\mu_o\, A_c}\right) = \Phi\left(\frac{l_g}{\mu_o\, A_c}\right) \qquad (A3)$$

$$\therefore R_g \gg R_c$$

Where $R_g$is the reluctance of airgap is, l_g is the airgap length, l_c is the core magnetic path length, μ_e is the effective relative permeability of gapped core. In Eq. A3 it is assumed that cross-sectional area of the core and the airgap are same by neglecting the fringing effect.

A3. NECESSITY OF USING GAPPED CORE

Figure A2 shows the B-H characteristic curves of ferrite magnetic material, air and ferrite material with airgap (gapped core). It can be seen that, saturation of gapped core occurs at a much higher value of field. This implies that when gapped core is used there is more room to store the magnetic energy before getting the core into saturation.

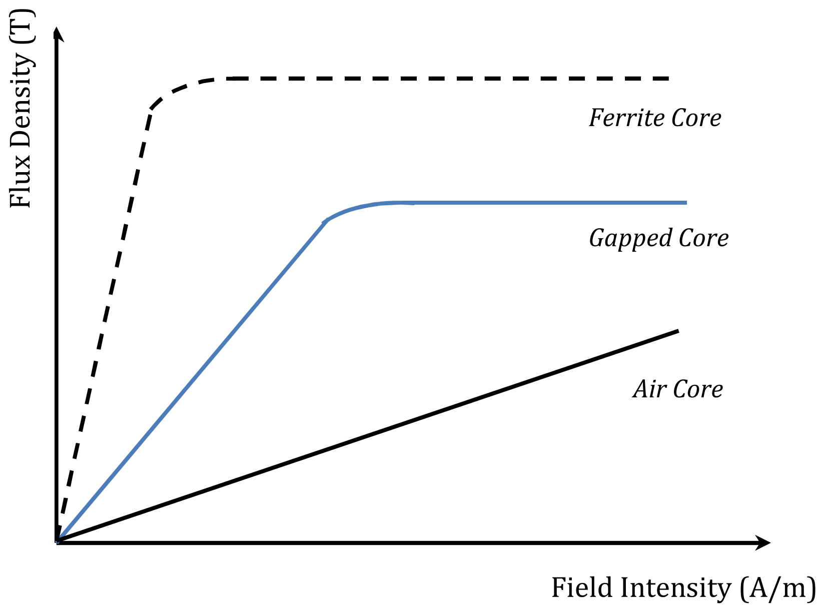

Figure A2: BH curve of iron and air

A4. SELF AND MUTUAL INDUCTANCE:

According to the faraday's law, whenever conductor cuts the magnetic field or cut by the magnetic field an EMF is induced as long as the coil flux is changing. The magnitude of induced EMF is equal to the rate of change of flux linkage in the coil and its direction is defined by the Lenz's law. Mutual inductance is the ability of one coil to induce the voltage in neighbouring coil when current is changing in first coil. This ability of voltage induction in nearby coil is known as mutual induction whereas the self-induction is a current carrying coil has flux linkage due to its own current apart from the outside source of flux.

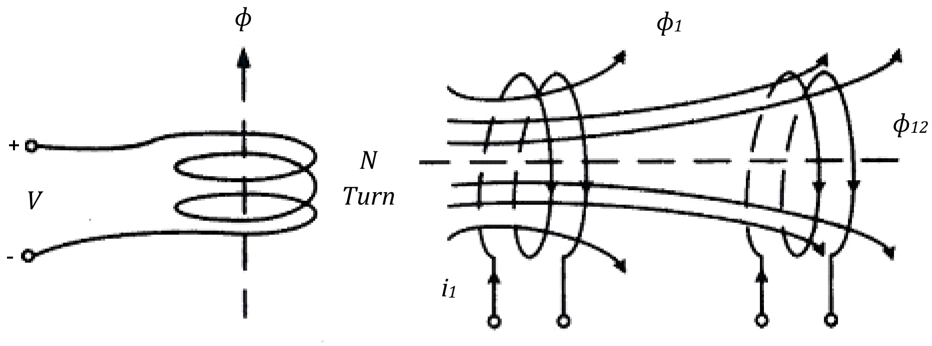

Figure A3: Self and mutual inductance

To understand the inductance principle, let's take two coils as shown in Figure A3, where current through coil 1 is i_1 and ψ_{12} is the flux linking to the coil 2 due to coil 1. This flux linking to the coil 2 gives rise to an induced EMF in coil 2 by mutual induction.

The flux linkages with coil 1 and 2 when coil 1 carries a current i1 are given by,

$$\Psi_1 = N_1\, \Phi_1 = L_1\, i_1 \; and \; \Psi_{12} = N_1\, \Phi_{12} = M_{12}\, i_1 \qquad (A5)$$

And the flux linkages with coil 1 and 2 when coil 2 carries a current i_2 are given by,

$$\Psi_2 = N_2\, \Phi_2 = L_2\, i_2 \; and \; \Psi_{21} = N_2\, \Phi_{21} = M_{21}\, i_2 \qquad (A6)$$

Where, L_1 and L_2 are self-inductance of coil 1 and 2 itself and M_{12} and M_{21} are mutual inductances. If iron saturation is neglected, all four coefficients (L_1, L_2, M_{12} and M_{21}) are independent of current and $M_{12} = M_{21} = M$

A5. INDUCTANCE CALCULATION FOR 3 PHASE SYSTEM:

The equivalent circuit of 3 phase inductor is shown in Figure A4, when the inductor is energised from a 3 phase supply, the electrical dynamic equations per phase is as under,

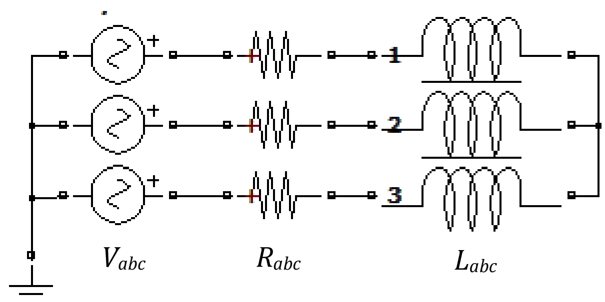

Figure A4: Equivalent circuit of a 3 phase Inductor

$$V_a = R_c I_a + \frac{d}{dt}\Psi_a \tag{A7}$$

$$V_b = R_a I_b + \frac{d}{dt}\Psi_b \tag{A8}$$

$$V_c = R_a I_c + \frac{d}{dt}\Psi_c \tag{A9}$$

Where the flux linkages are,

$$\Psi_a = L_{aa}I_a + L_{ab}I_b + L_{ac}I_c = L_s I_a + M\,I_B + M\,I_c \tag{A10}$$

$$\Psi_b = L_{ab}I_a + L_{bb}I_b + L_{bc}I_c = MI_a + L_s\,I_B + M\,I_c \tag{A11}$$

$$\Psi_c = L_{ac}I_a + L_{bc}I_b + L_{cc}I_c = MI_a + M\,I_B + L_s\,I_c \tag{A12}$$

Where, L_s and M is the self and mutual inductance respectively. The synchronous or equivalent inductance is $L = L_s \pm M$ where sign ± is the polarity of windings which shows the addition or subtraction of flux. In order to find out the inductances, inductor is energised by only one phase with rated current. When $I_a = I_{rated}$ and $I_b = I_c = 0$, Eq. (A10) and (A11) will give the self and mutual inductance respectively.

A6. FRINGING FLUX:

Whenever an air gap is inserted between magnetic paths, fringing flux is induced at the gap as shown in Figure A1. Fringing flux decreases the total reluctance of magnetic path, and, therefore increases the inductance by some amount to a value greater than the designed inductance. The effect of fringing flux is a function of gap dimension, shape of pole faces and the shape, size and location of the winding. The fringing factor can be calculate as:

$$FF = \left(1 + \frac{L_g}{\sqrt{A_{core}}} ln\left(\frac{2G}{L_g}\right)\right) \tag{A13}$$

Where G is the window height as defined in chapter 1. Since the fringing factor can affect the inductance of an inductor therefore it is necessary to recalculate the number of turns. The new number of turns using fringing factor is given as:

$$N_{new} = \sqrt{\frac{L_s L_g}{0.4\pi A_{core} FF (10^{-8})}} \qquad (A14)$$

It is unlikely to affect the inductance if the fringing factor is close to unity and hence the fringing effect of the device is minimum. However if the fringing factor is high the new number turns must recalculate for the final design using the Eq. A13.

APPENDIX B: BODE PLOT OF RLC OUTPUT FILTER

B1. Bode Diagram when L=1.13mH, C=5.64μF and R=2Ω

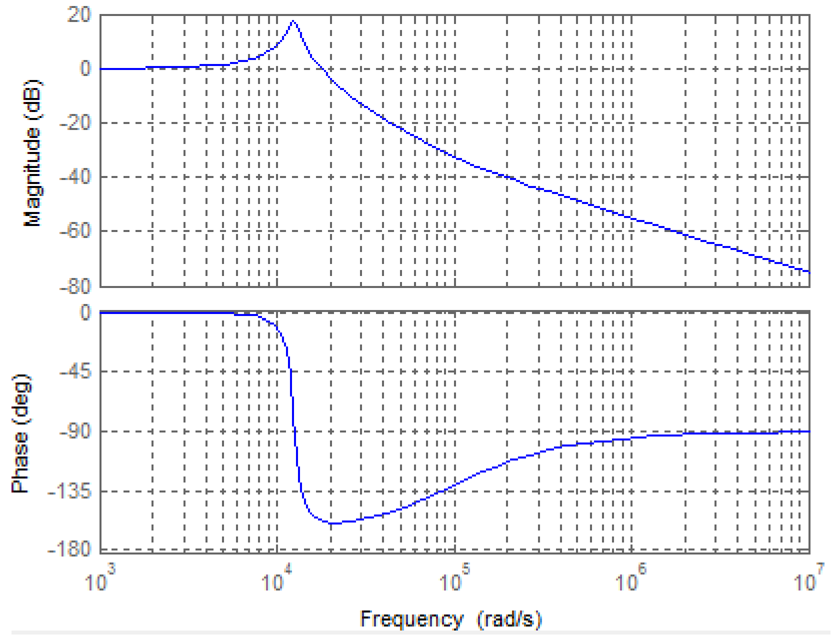

Figure B1: Bode Diagram when L=1.13mH, C=5.64μF and R=2Ω

B2. Bode Diagram when L=0.92mH, C=6.63μF and R=2Ω

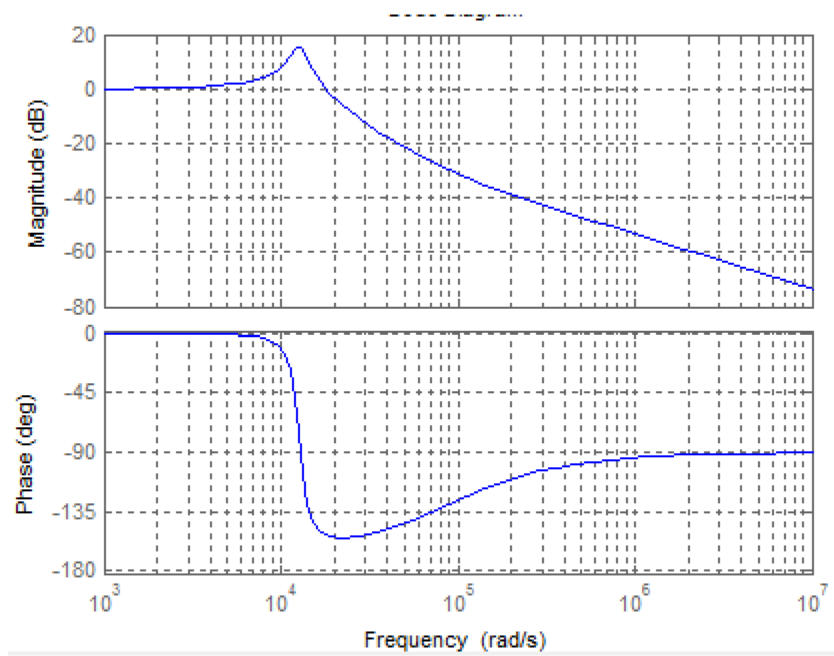

Figure B2: Bode Diagram when L=0.92mH, C=6.63μF and R=2Ω

B3. Bode Diagram when L=0.79mH, C=8μF and R=2Ω

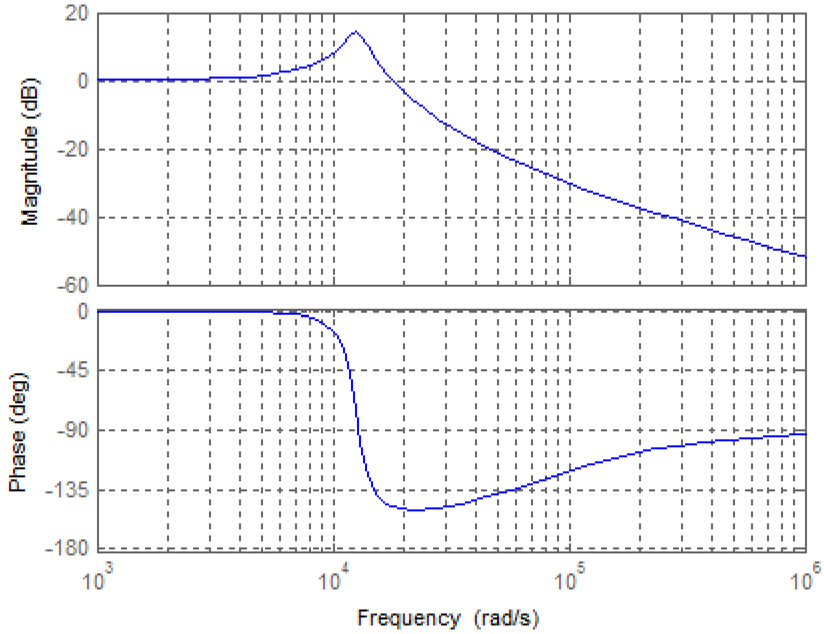

Figure B3: Bode Diagram when when L=0.79mH, C=8μF and R=2Ω

B4. Bode Diagram when L=0.62mH, C=10μF and R=2Ω

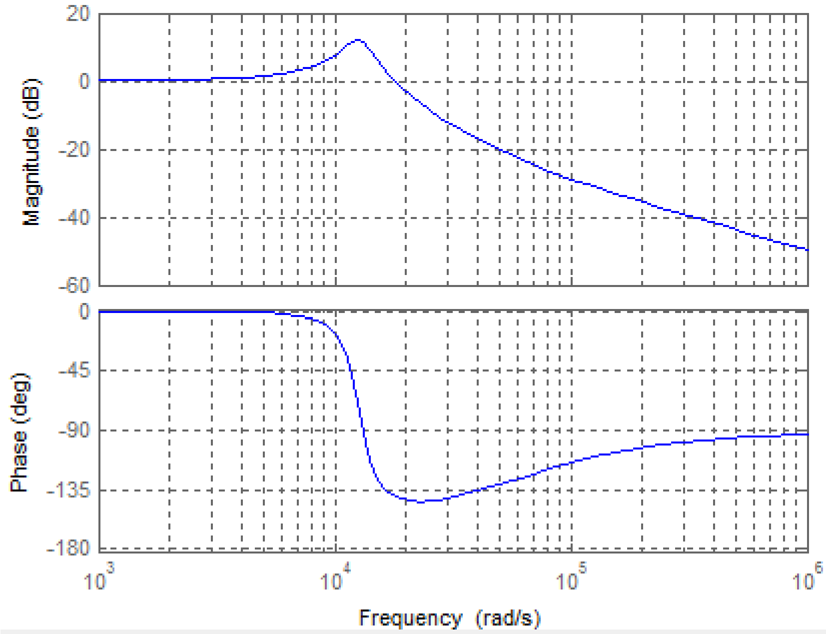

Figure B4: Bode Diagram when L=0.62mH, C=10μF and R=2Ω

B5. Bode Diagram when L=0.45mH, C=14.1μF and R=5Ω

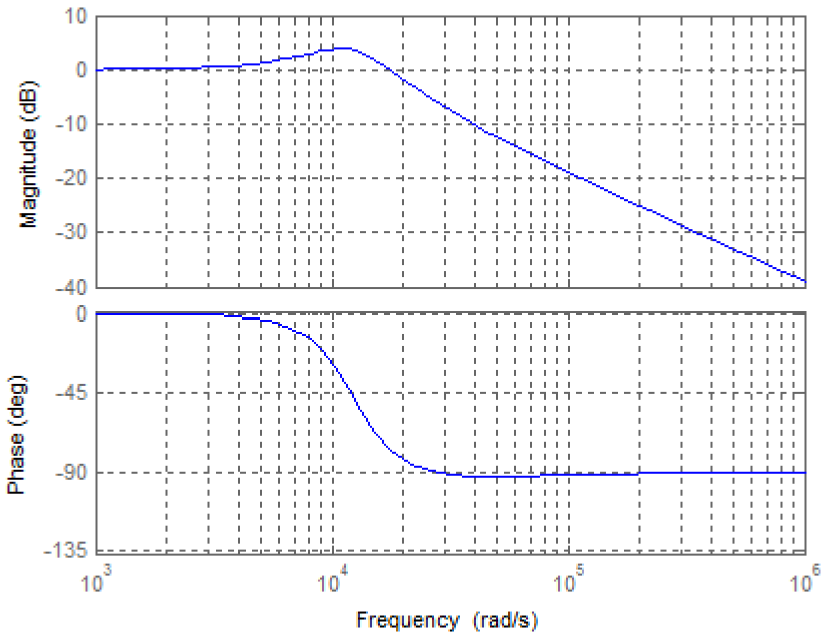

Figure B5: Bode Diagram when L=0.45mH, C=14.1μF and R=5Ω

B6. Bode Diagram when L=0.28mH, C=22.5μF and R=7Ω

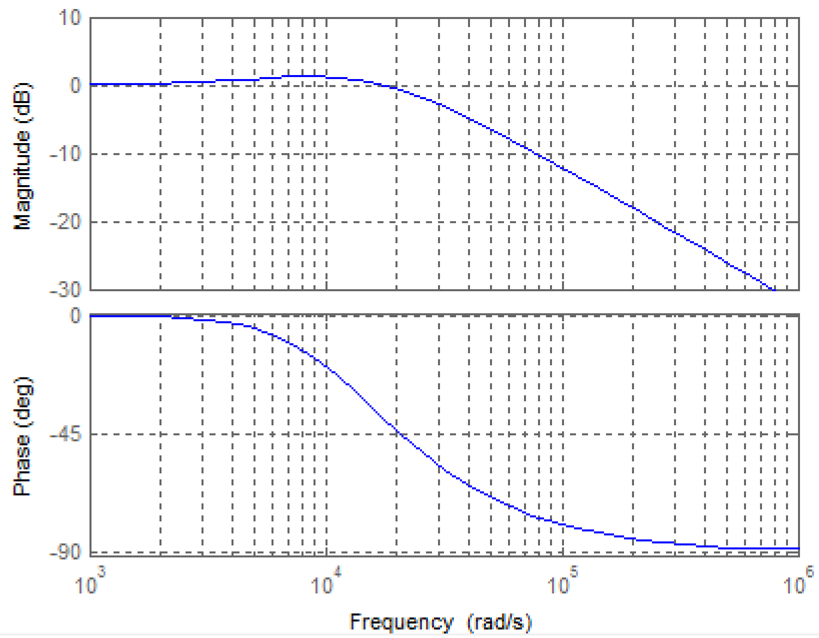

Figure B6: Bode Diagram when L=0.28mH, C=22.5μF and R=7Ω

APPENDIX C: HEMAS FLIGHT PROFILE & DDS FEATURES

C1: HEMAS Profile

Table I: HEMAS Flight Profile

Flight Profile	Duration (sec)	Speed (rad/s)	RMS Current (A)
1	600	50	2.2
Transient	1	550	24
11	8	50	5
Transient	1	550	24
13	34	50	3.2
Transient	1	550	24
2	60	50	2.2
Transient	1	550	24
15	10	50	7.2
Transient	1	550	24
2	60	50	2.2
Transient	1	550	24
5	40	50	3
Transient	1	550	24
1	600	50	2.9

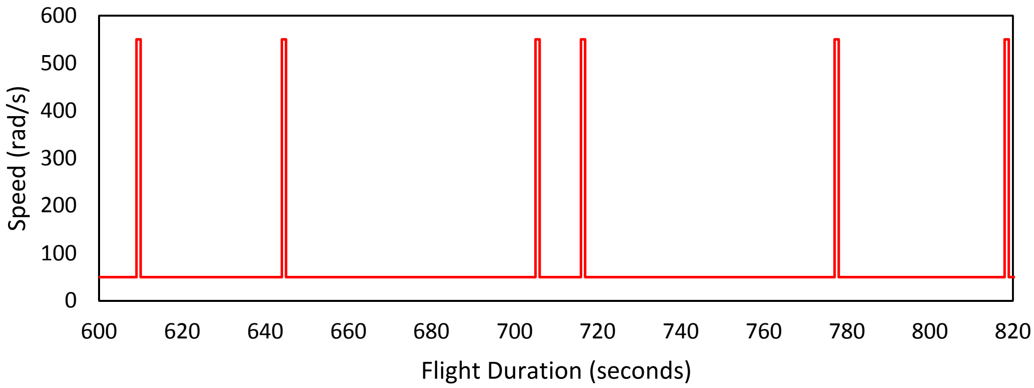

Figure C1: HEMAS Speed Profile

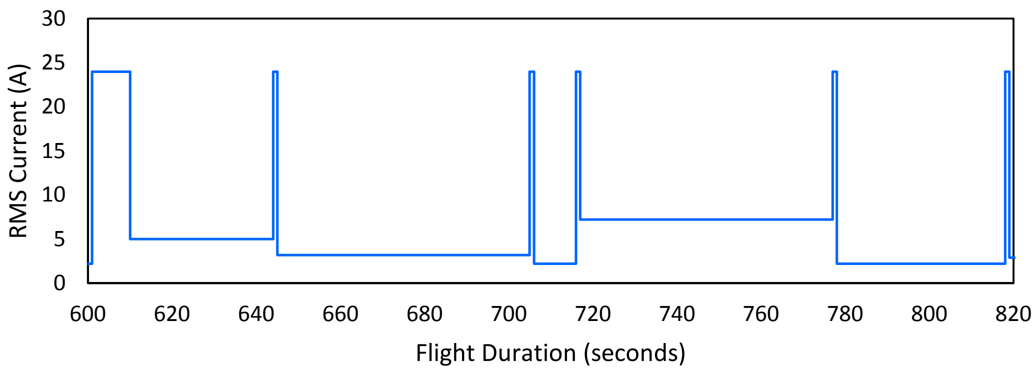

Figure C2: HEMAS Load Profile

The HEMAS flight profile including speed and load characteristics with time is shown in Table I, Figure C1 and Figure C2 respectively. The transient period of the profile is 1 seconds at which speed and RMS load current are 550 rad/s and 24A. The speed of the rotor is 50 rad/s for steady state time interval whereas the load current varies from 2.2A to 7.2A.

C1: DDS Specifications

Table II: SpectraQuest's DDS Specifications

ELECTRICAL	
Motor	3 Phase, 3 HP motor, pre-wired self-aligning mounting system for easy installation/removal.
Drive	3 HP variable frequency AC drive with multi-featured front panel programmable controller
RPM range	0 to 5000 rpm variable speed
Voltage	230 VAC, Three phase, 60/50 Hz
MECHANICAL	
Shaft Diameter	1″ diameter; Turned, Ground, & Polished (TGP) steel
Torque meter	Up to 100N.m with built-in 360 pulse encoder
Parallel Gearbox	2 stage, 2.5 maximum ratio per stage, spur or helical gears
Magnetic Brake	1.5 to 32 lb.ft capacity heavy duty magnetic particle brake
PHYSICAL	
Weight	Approximately 200 lb
Dimensions	L=45″ (114cm), W=20″(50cm), H=24″ (60cm)

APPENDIX D: EXPERIMENTAL RESULTS AT 10 kHz SWICTHING FREQUENCY

Appendix D1: Experimental Results of the motor with integrated Inductor

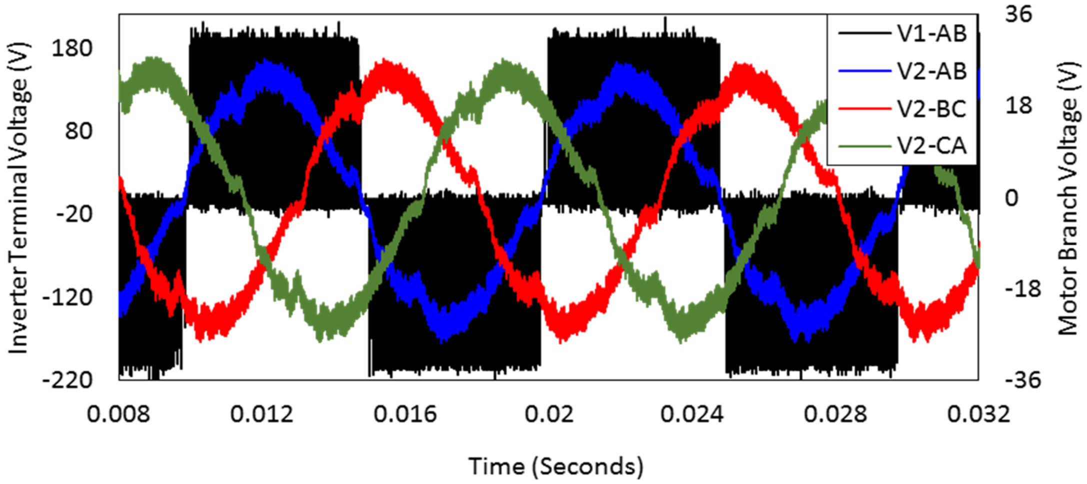

Figure D1.1: Line-to-line Inverter Terminals Voltage & Motor Branch Voltage at 100 Hz and 1.5Nm

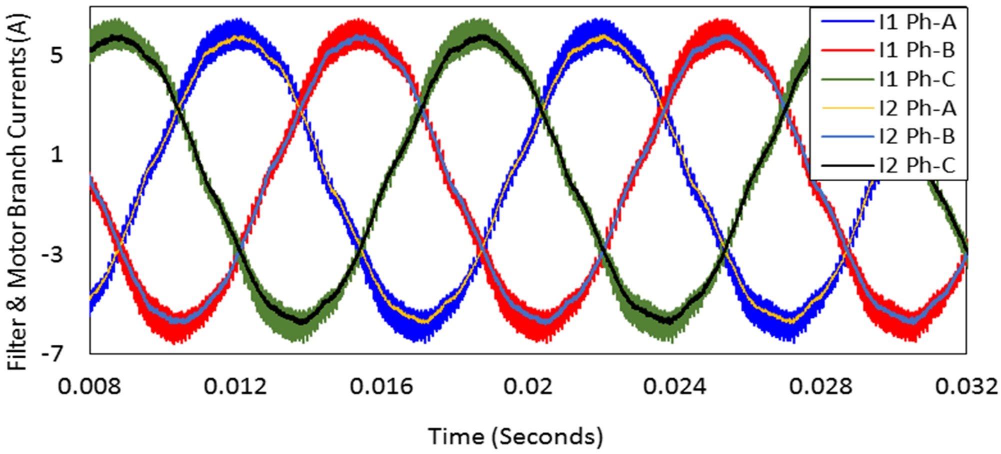

Figure D1.2: Line-to-line Filter & Motor Branch Currents at 100 Hz and 1.5 Nm

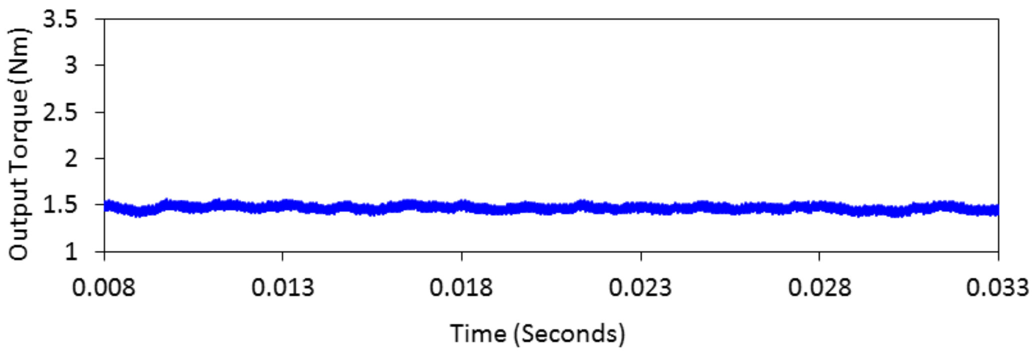

Figure D1.3: Estimated Output torque at 100 Hz and 1.5 Nm

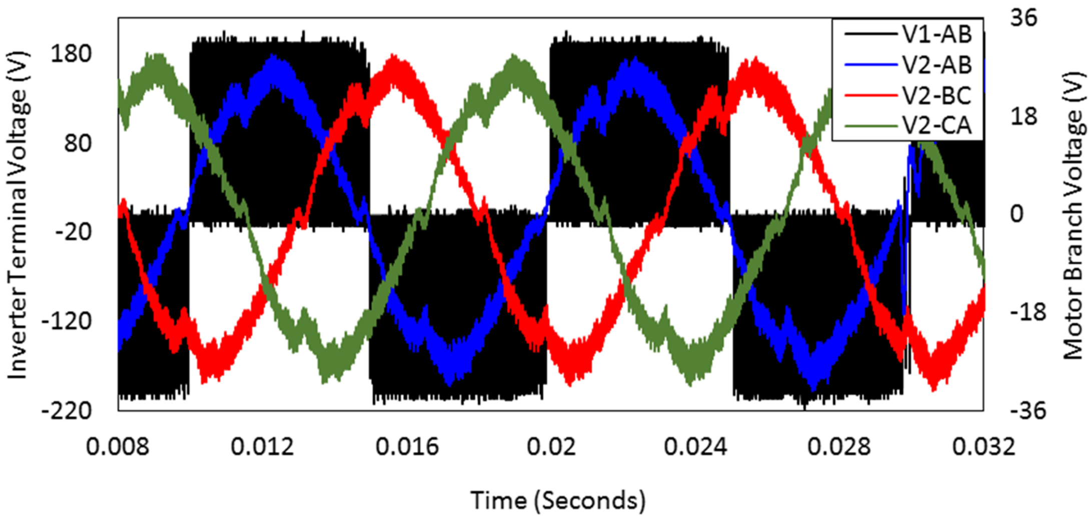

Figure D1.4: Line-to-line Inverter Terminals Voltage & Motor Branch Voltage at 100 Hz and 2Nm

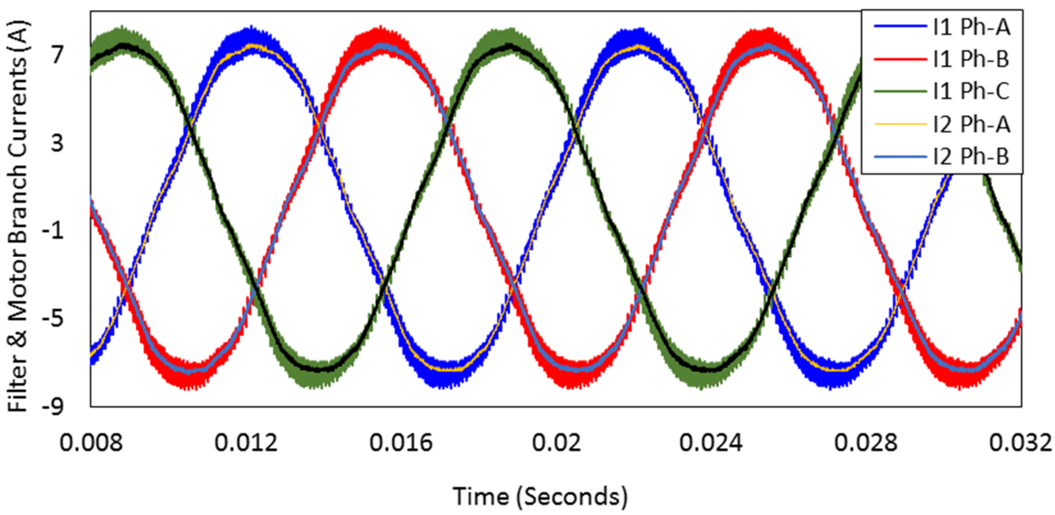

Figure D1.5: Line-to-line Filter & Motor Branch Currents at 100 Hz and 2 Nm

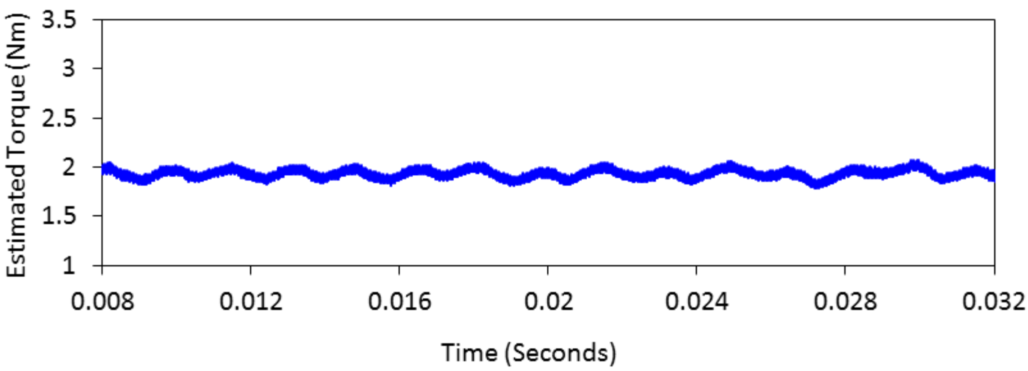

Figure D1.6: Estimated Output torque at 100 Hz and 2 Nm

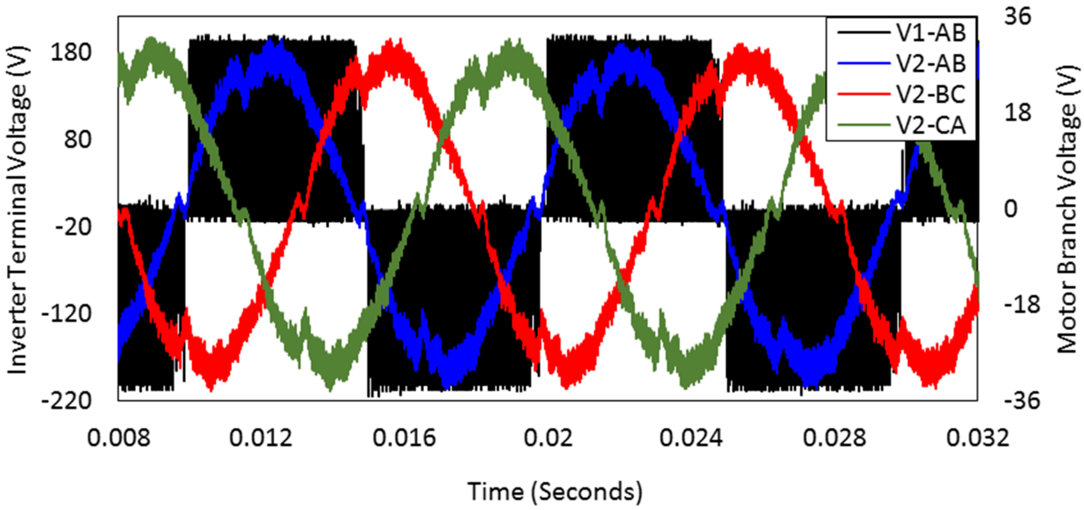

Figure D1.7: Line-to-line Inverter Terminals Voltage & Motor Branch Voltage at 100 Hz and 2.5Nm

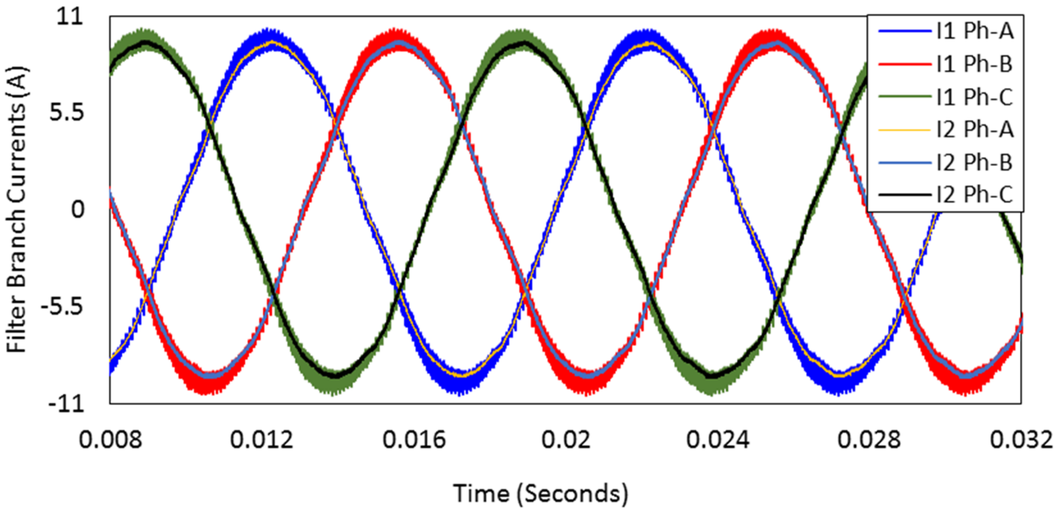

Figure D1.8: Line-to-line Filter & Motor Branch Currents at 100 Hz and 2.5 Nm

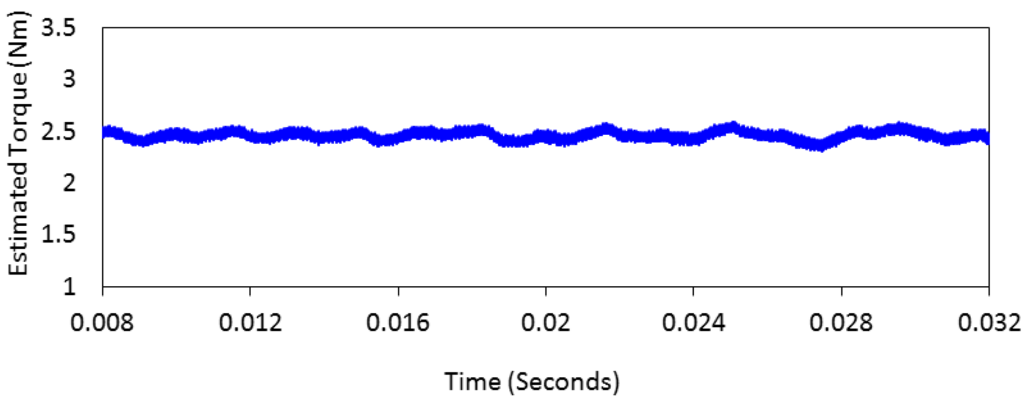

Figure D1.9: Estimated Output torque at 100 Hz and 2.5 Nm

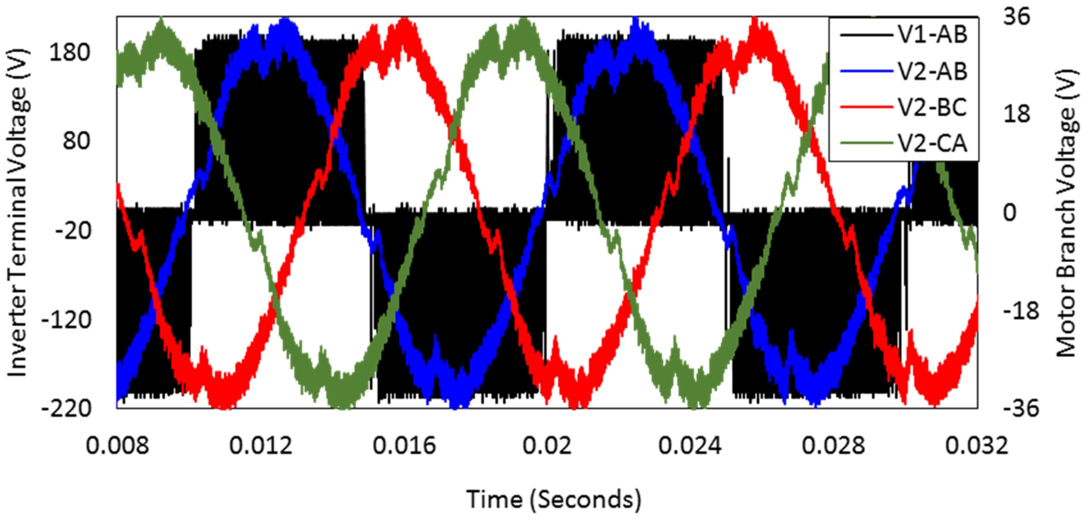

Figure D1.10: Line-to-line Inverter Terminals Voltage & Motor Branch Voltage at 100 Hz and 3Nm

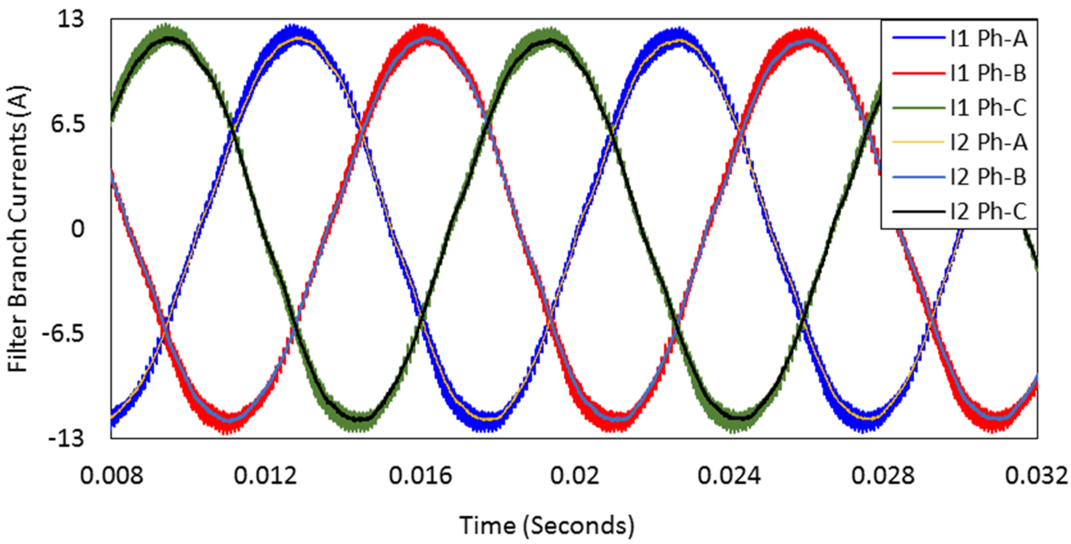

Figure D1.11: Line-to-line Filter & Motor Branch Currents at 100 Hz and 3 Nm

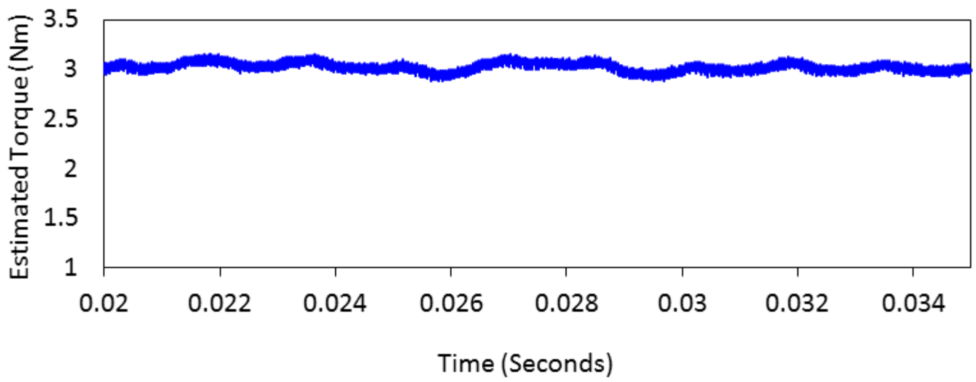

Figure D1.12: Estimated Output torque at 100 Hz and 3 Nm

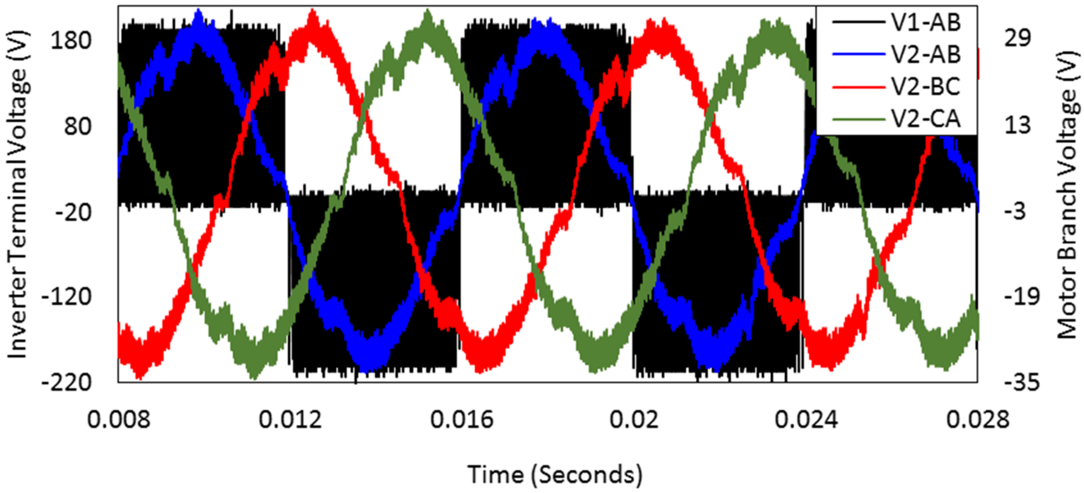

Figure D1.13: Line-to-line Inverter Terminals Voltage & Motor Branch Voltage at 125 Hz and 1.5Nm

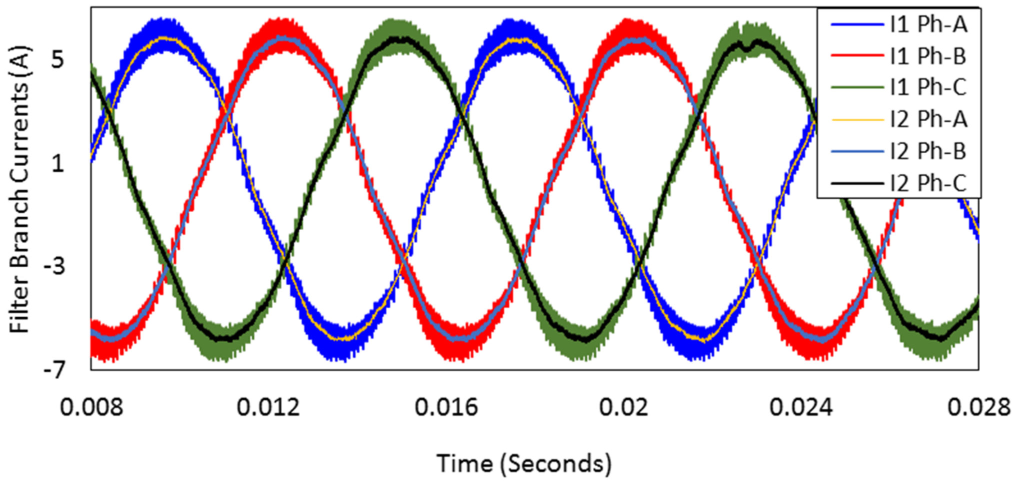

Figure D1.14: Line-to-line Filter & Motor Branch Currents at 125 Hz and 1.5 Nm

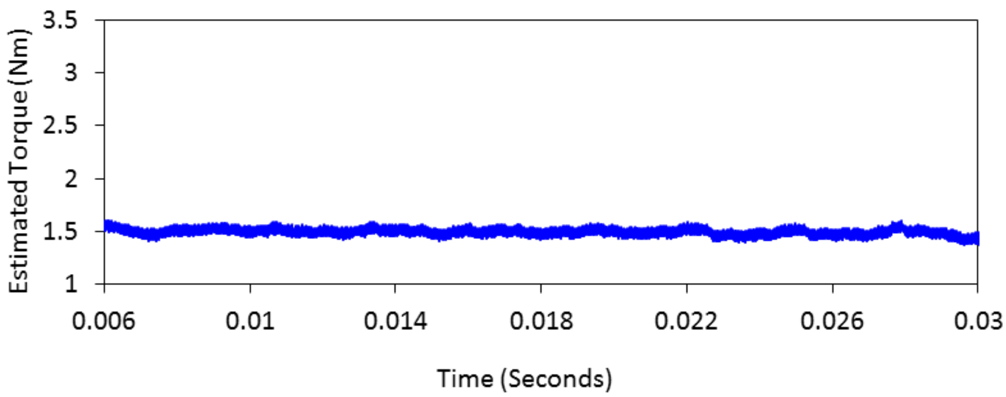

Figure D1.15: Estimated Output torque at 125 Hz and 1.5 Nm

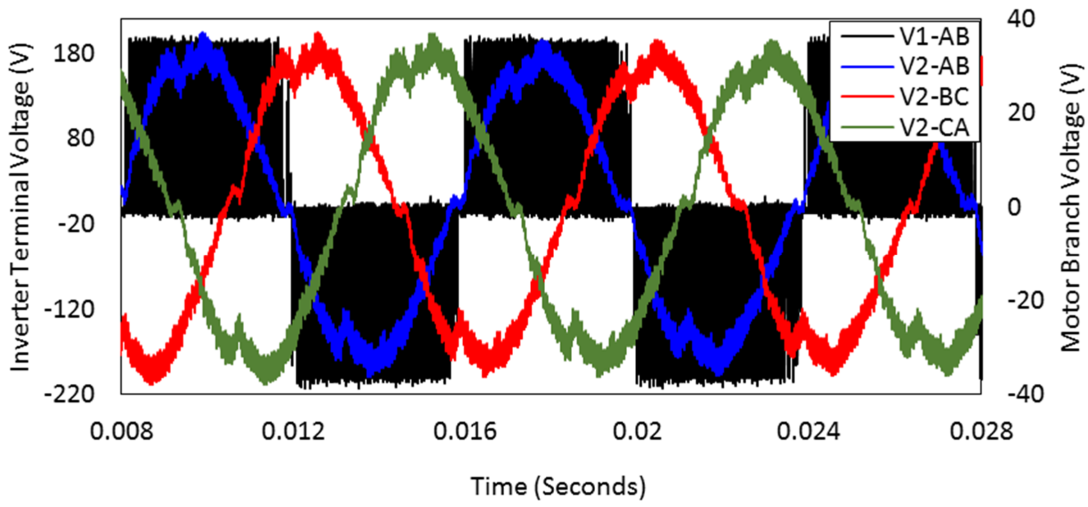

Figure D1.16: Line-to-line Inverter Terminals Voltage & Motor Branch Voltage at 125 Hz and 2Nm

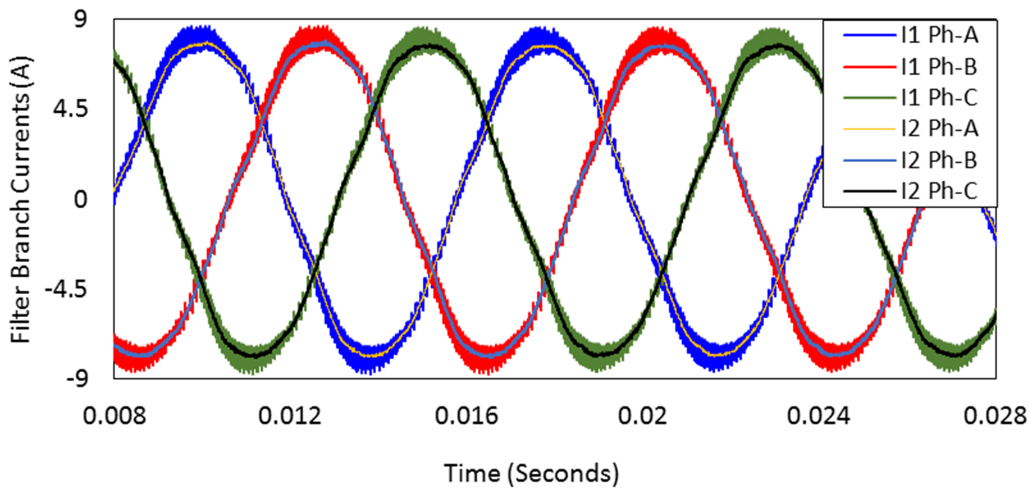

Figure D1.17: Line-to-line Filter & Motor Branch Currents at 125 Hz and 2 Nm

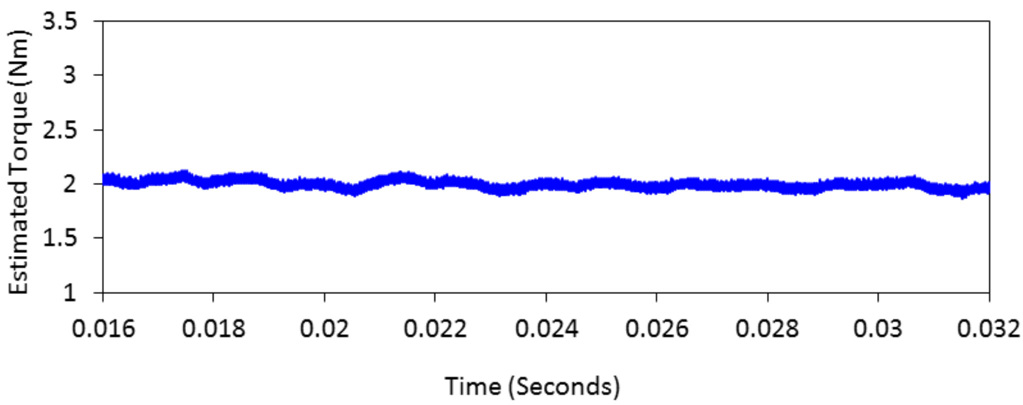

Figure D1.18: Estimated Output torque at 125 Hz and 2 Nm

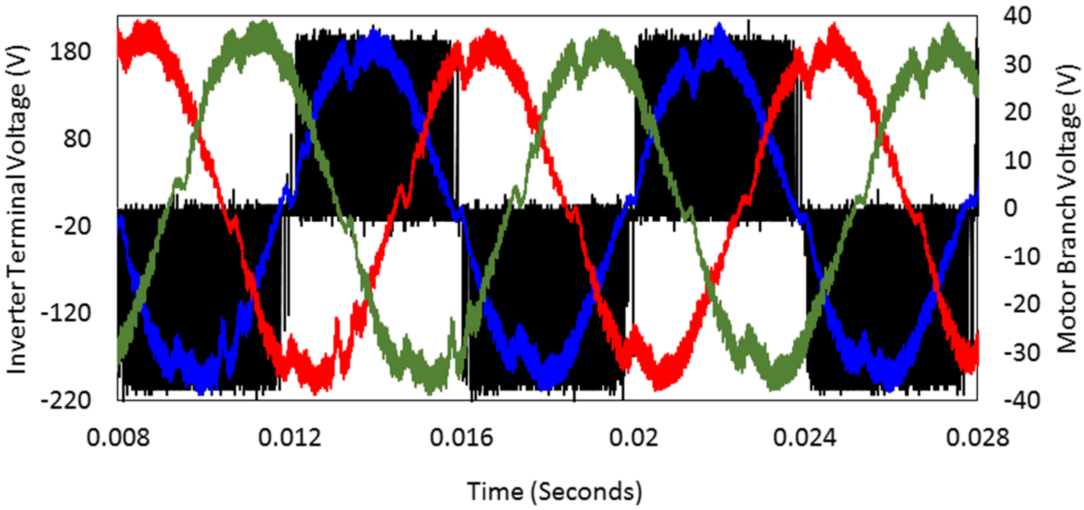

Figure D1.19: Line-to-line Inverter Terminals Voltage & Motor Branch Voltage at 125 Hz and 2.5Nm

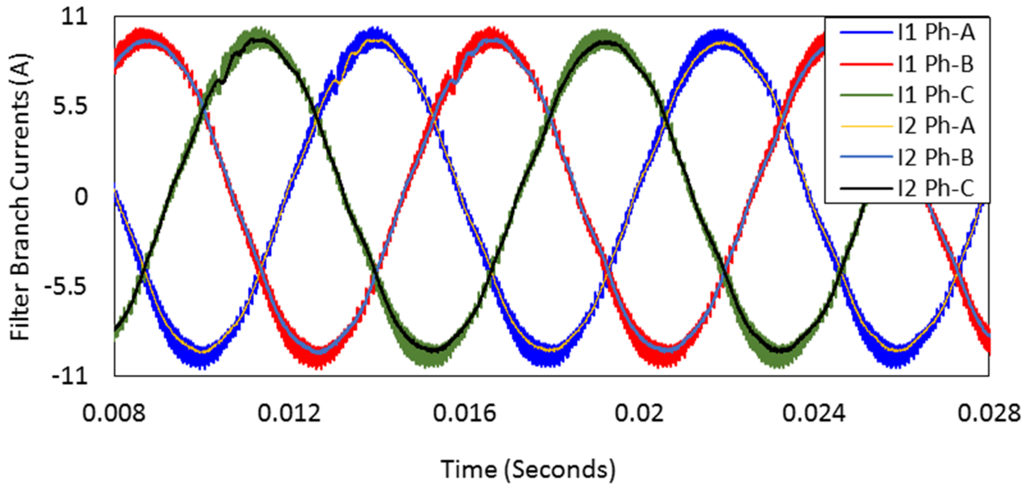

Figure D1.20: Line-to-line Filter & Motor Branch Currents at 125 Hz and 2.5 Nm

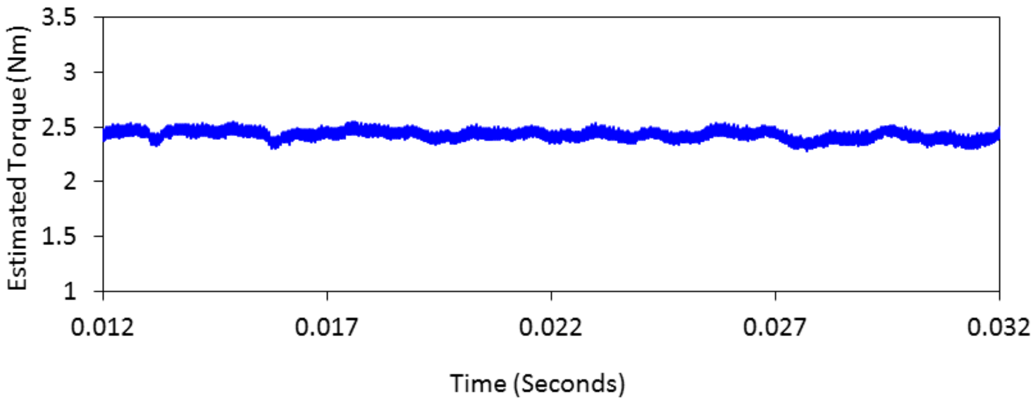

Figure D1.21: Estimated Output torque at 125 Hz and 2.5 Nm

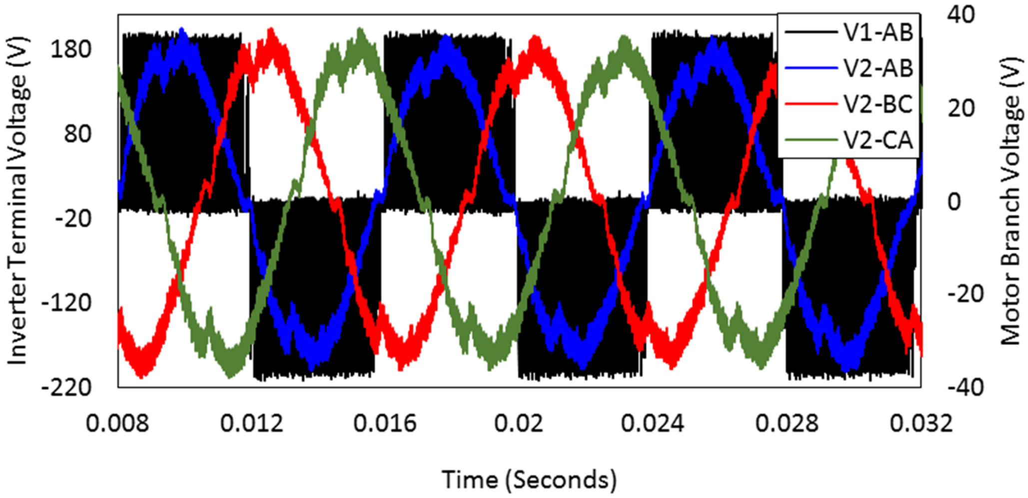

Figure D1.22: Line-to-line Inverter Terminals Voltage & Motor Branch Voltage at 125 Hz and 3Nm

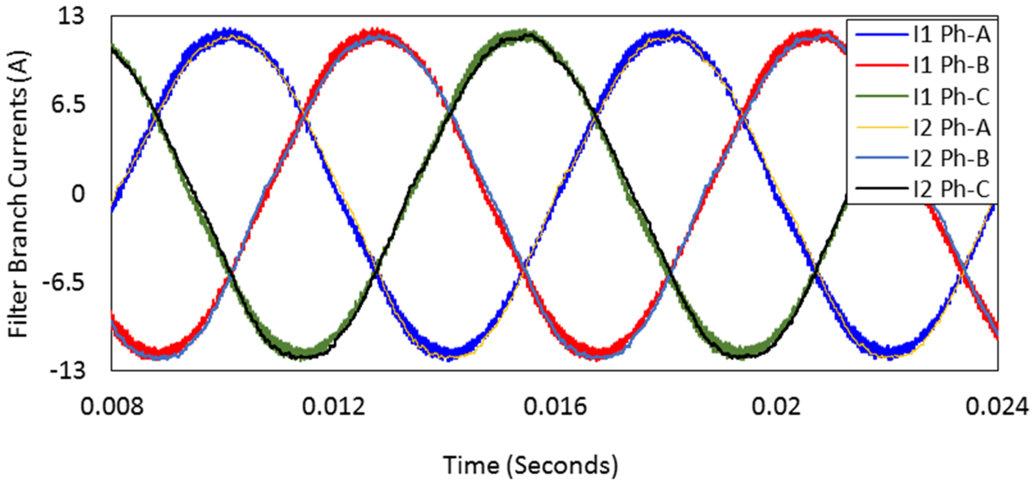

Figure D1.23: Line-to-line Filter & Motor Branch Currents at 125 Hz and 3 Nm

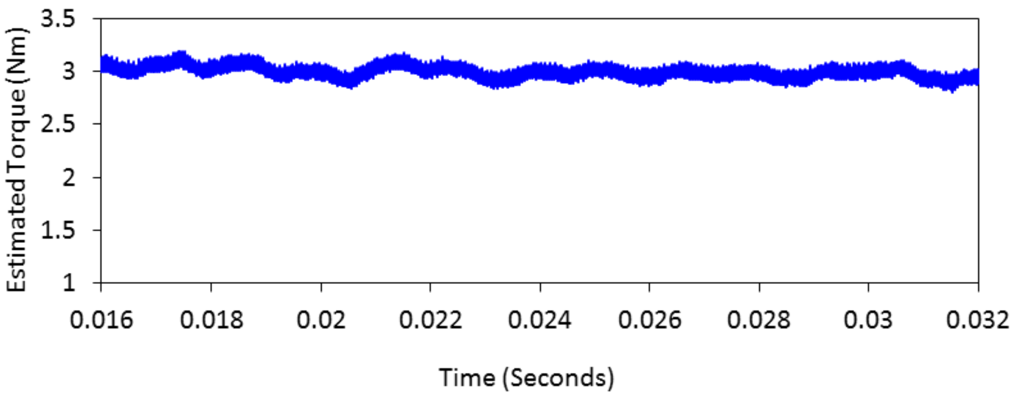

Figure D1.24: Estimated Output torque at 125 Hz and 3 Nm

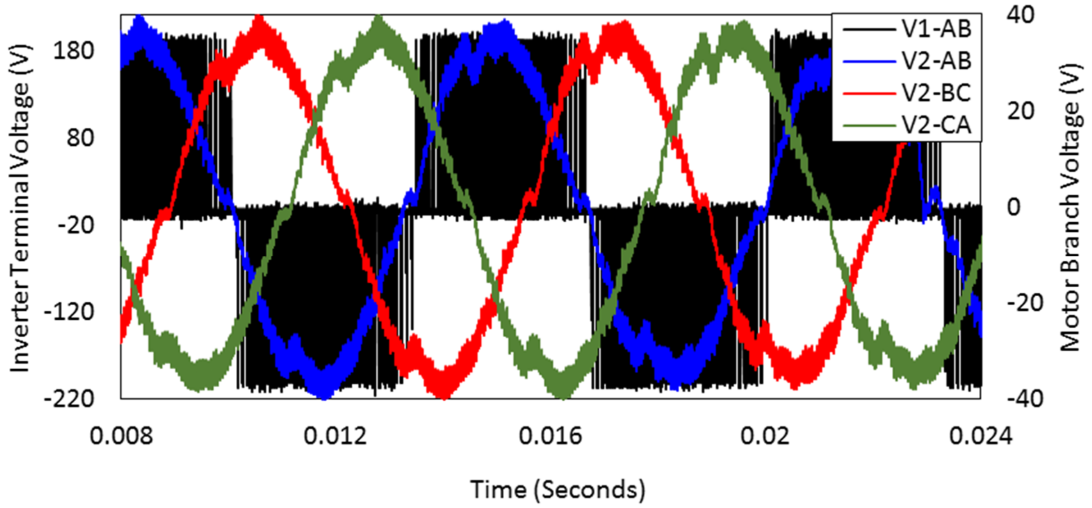

Figure D1.25: Line-to-line Inverter Terminals Voltage & Motor Branch Voltage at 150 Hz and 1.5Nm

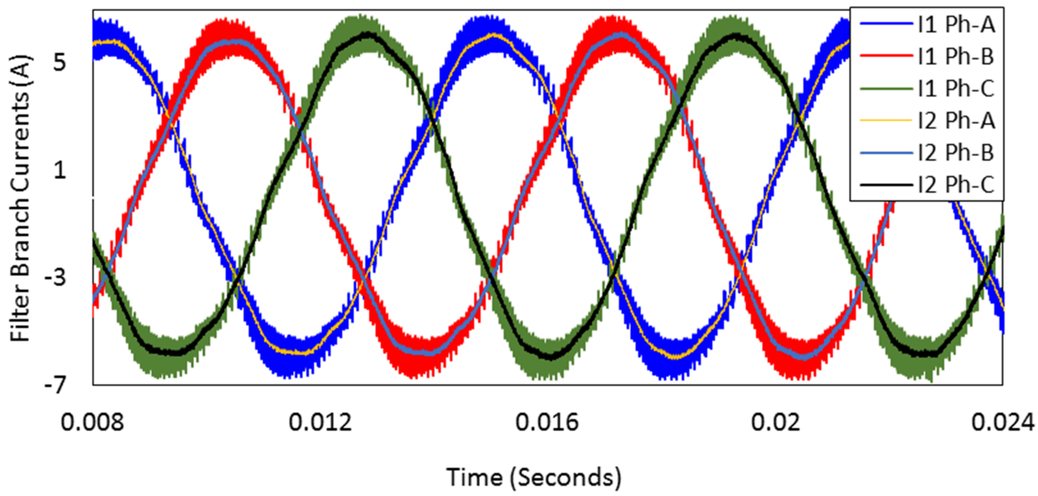

Figure D1.26: Line-to-line Filter & Motor Branch Currents at 150 Hz and 1.5 Nm

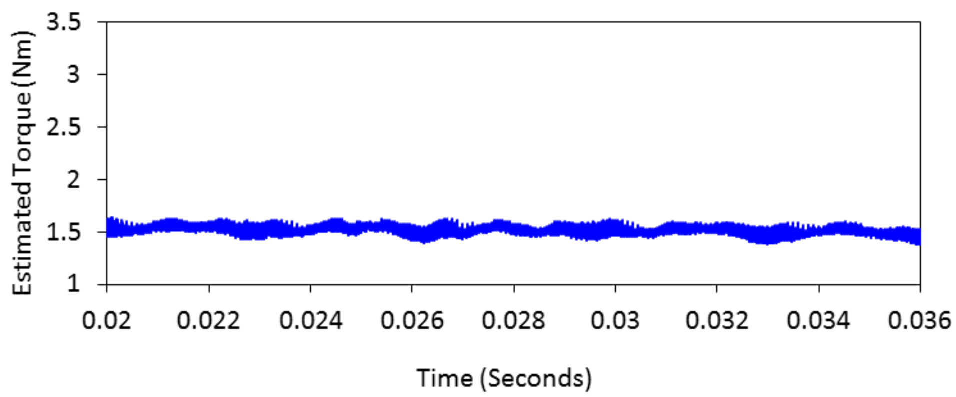

Figure D1.27: Estimated Output torque at 150 Hz and 1.5 Nm

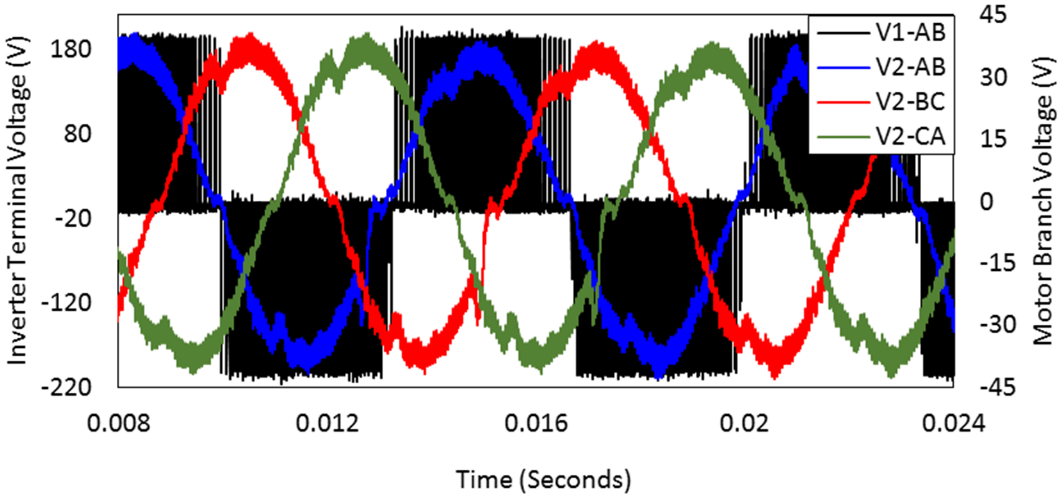

Figure D1.28: Line-to-line Inverter Terminals Voltage & Motor Branch Voltage at 150 Hz and 2Nm

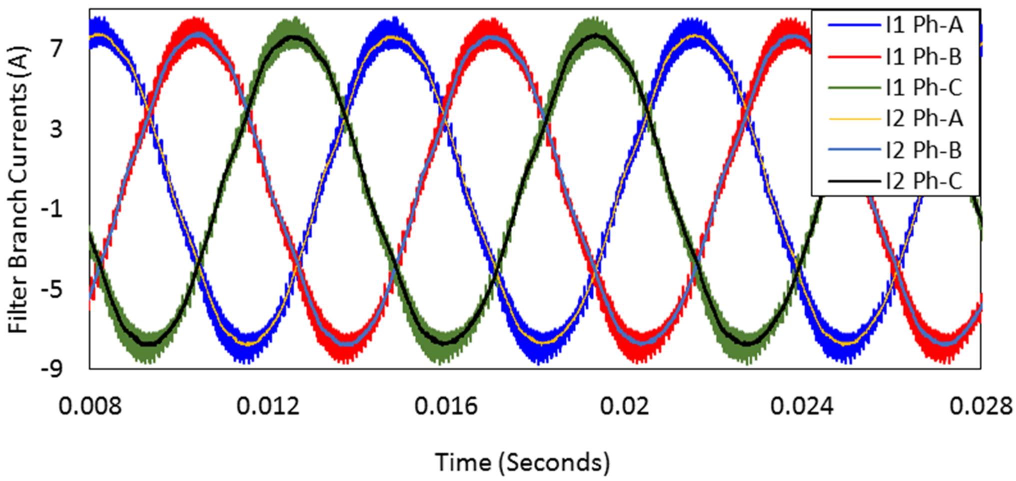

Figure D1.29: Line-to-line Filter & Motor Branch Currents at 150 Hz and 2 Nm

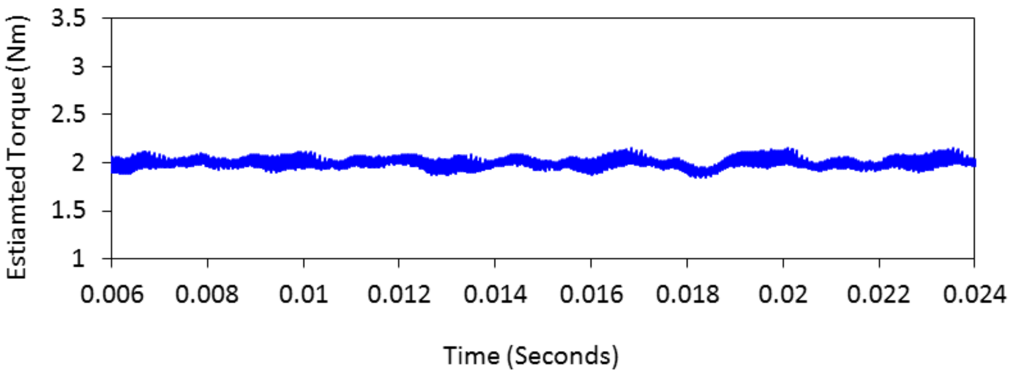

Figure D1.30: Estimated Output torque at 150 Hz and 2 Nm

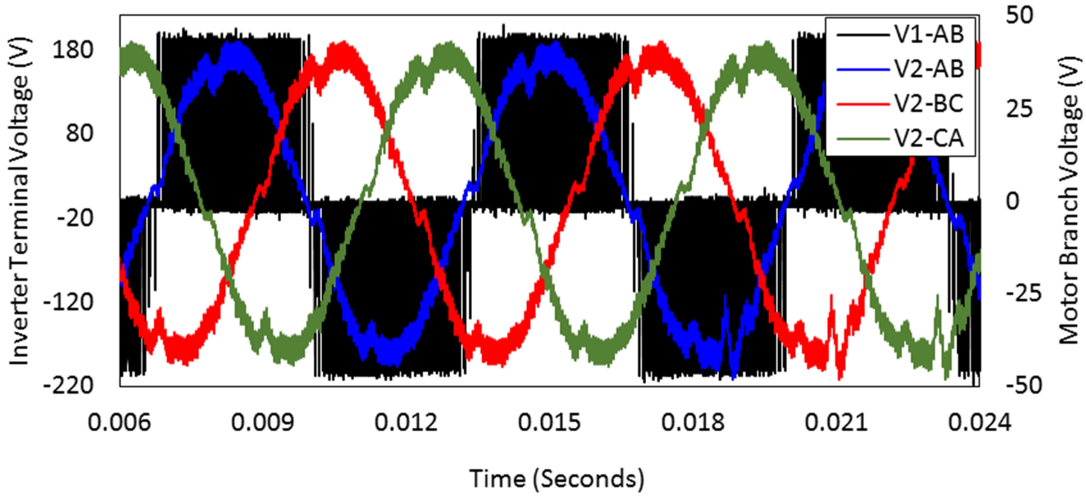

Figure D1.31: Line-to-line Inverter Terminals Voltage & Motor Branch Voltage at 150 Hz and 2.5Nm

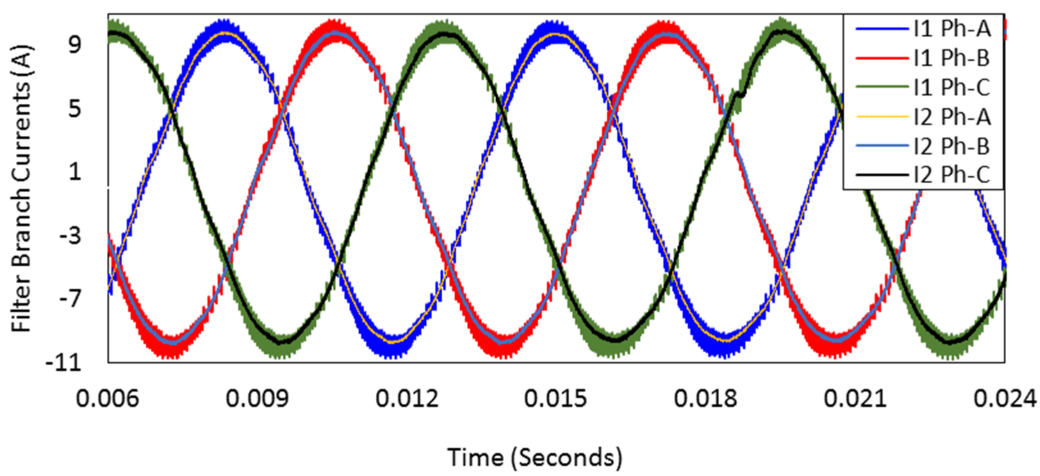

Figure D1.32: Line-to-line Filter & Motor Branch Currents at 150 Hz and 2.5 Nm

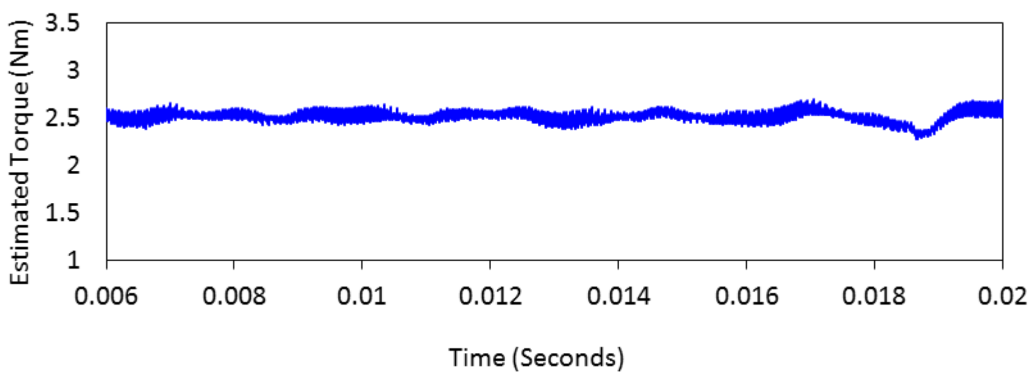

Figure D1.33: Estimated Output torque at 150 Hz and 2.5 Nm

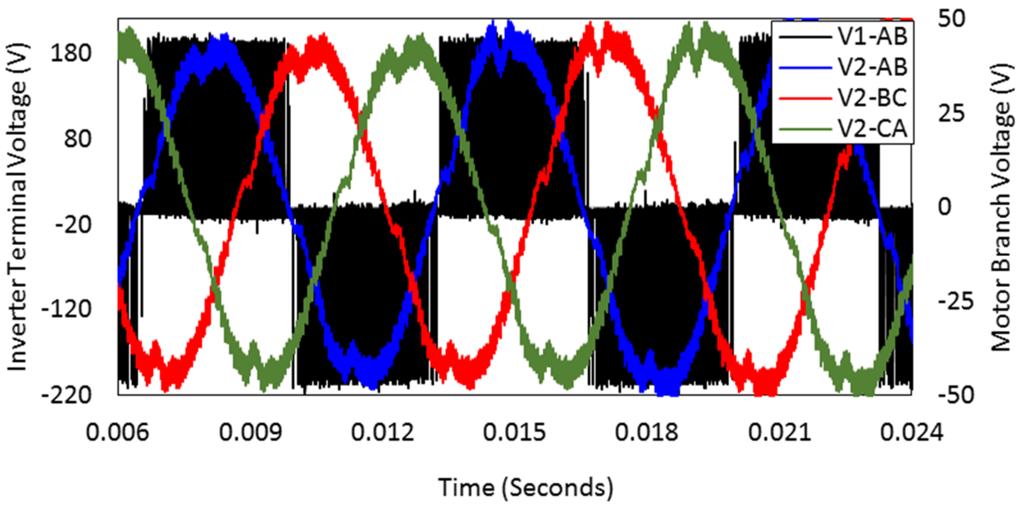

Figure D1.34: Line-to-line Inverter Terminals Voltage & Motor Branch Voltage at 150 Hz and 3Nm

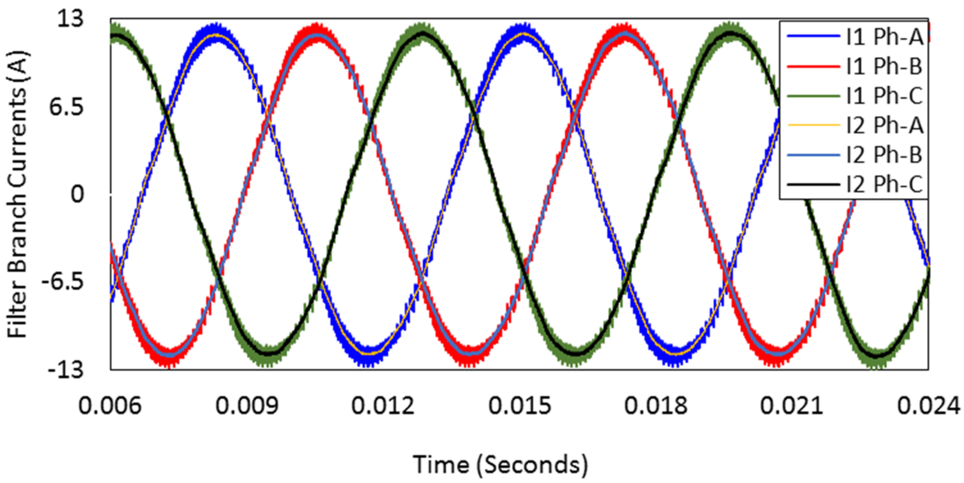

Figure D1.35: Line-to-line Filter & Motor Branch Currents at 150 Hz and 3 Nm

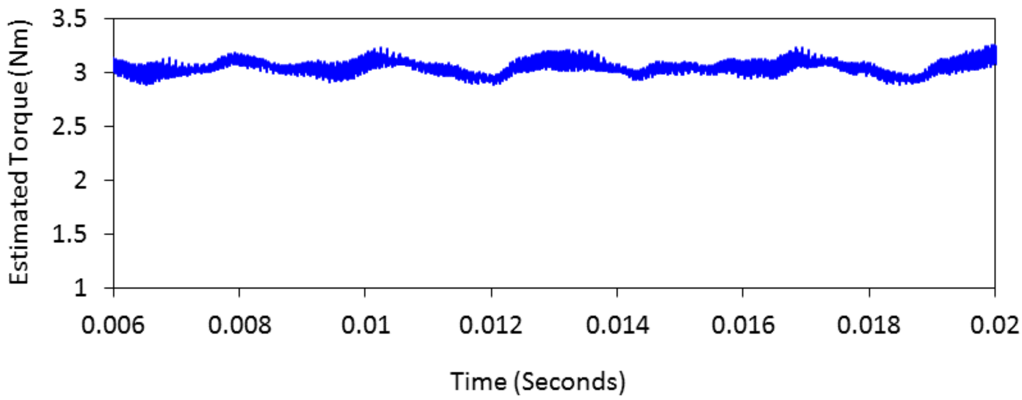

Figure D1.36: Estimated Output torque at 150 Hz and 3 Nm

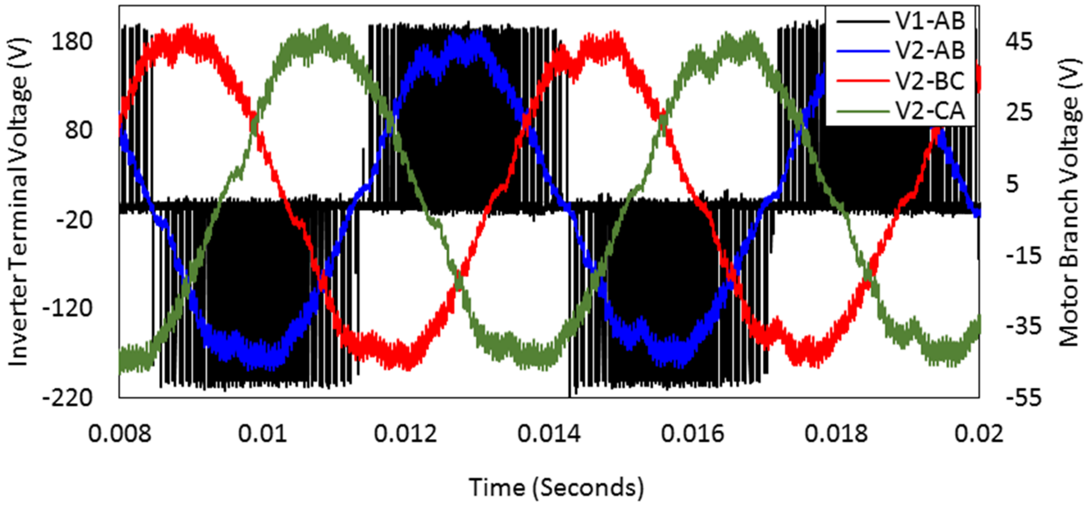

Figure D1.37: Line-to-line Inverter Terminals Voltage & Motor Branch Voltage at 175 Hz and 2Nm

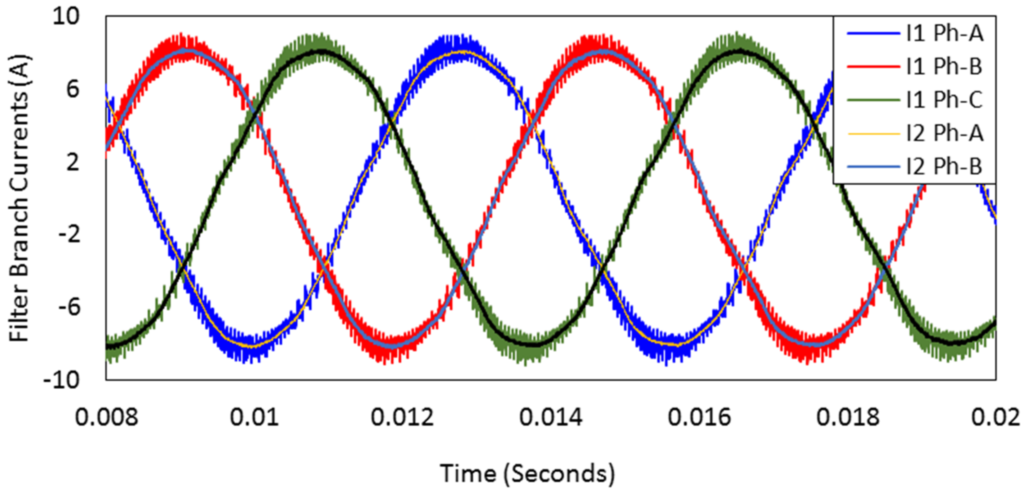

Figure D1.38: Line-to-line Filter & Motor Branch Currents at 175 Hz and 2 Nm

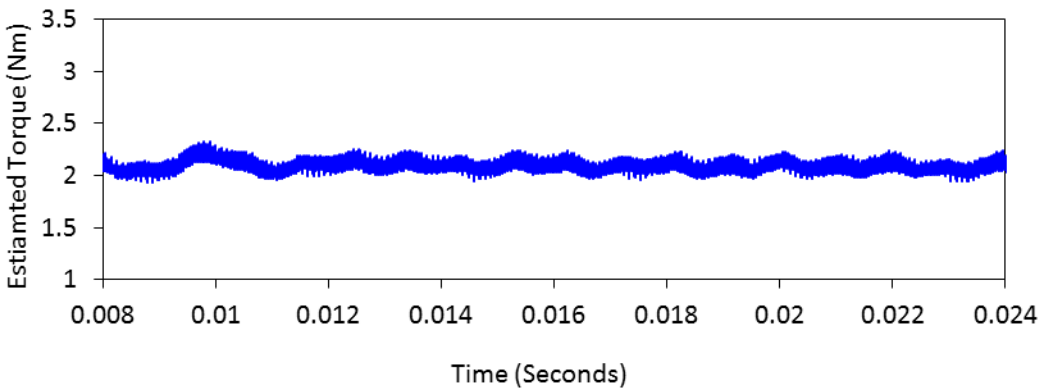

Figure D1.39: Estimated Output torque at 175 Hz and 2 Nm

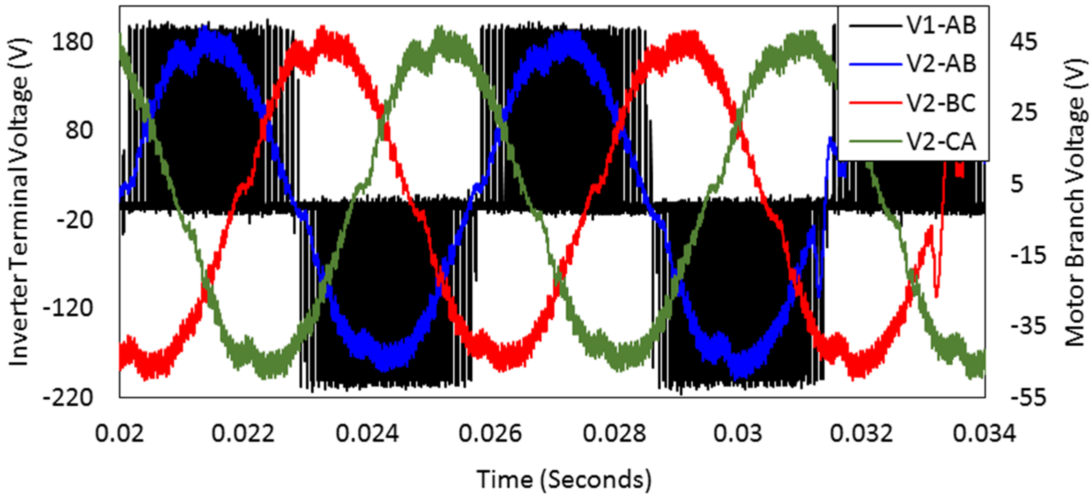

Figure D1.40: Line-to-line Inverter Terminals Voltage & Motor Branch Voltage at 175 Hz and 2.5Nm

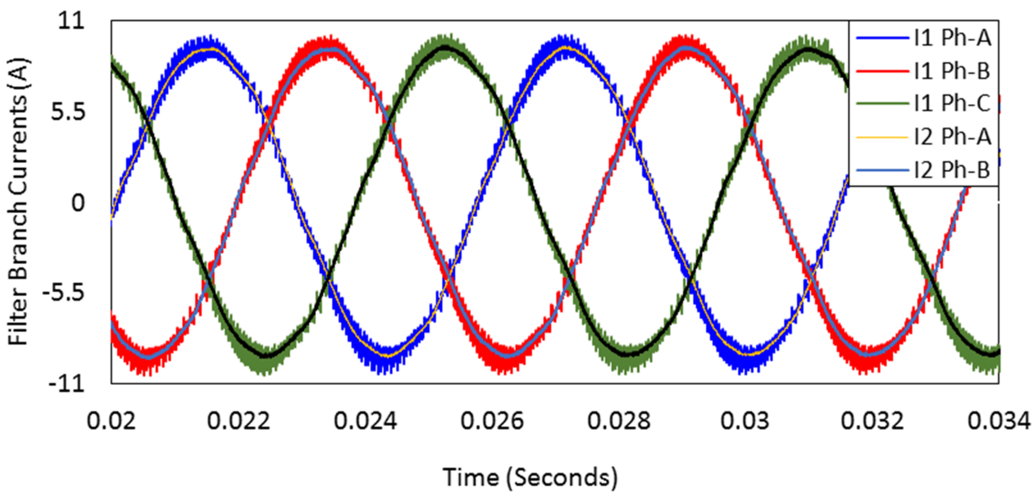

Figure D1.41: Line-to-line Filter & Motor Branch Currents at 175 Hz and 2.5 Nm

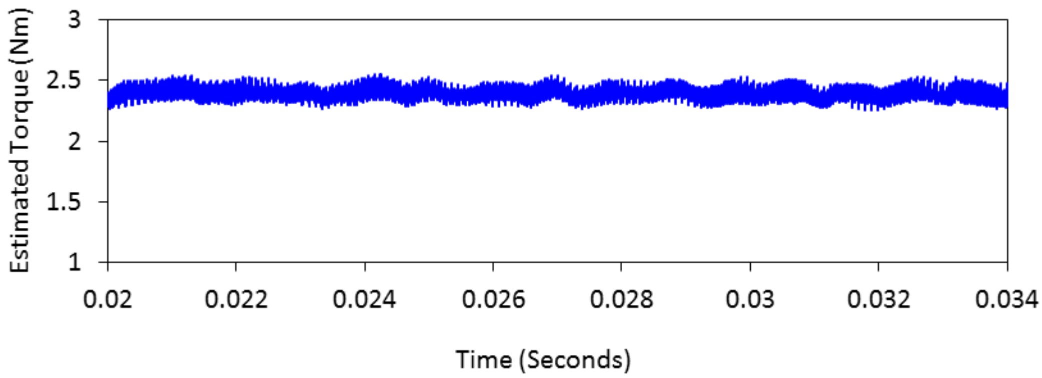

Figure D1.42: Estimated Output torque at 175 Hz and 2.5 Nm

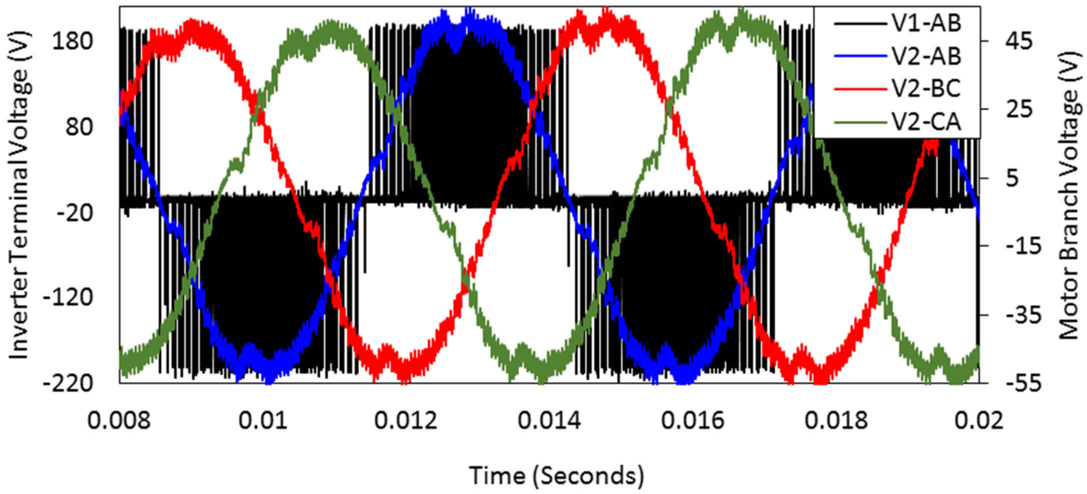

Figure D1.43: Line-to-line Inverter Terminals Voltage & Motor Branch Voltage at 175 Hz and 3Nm

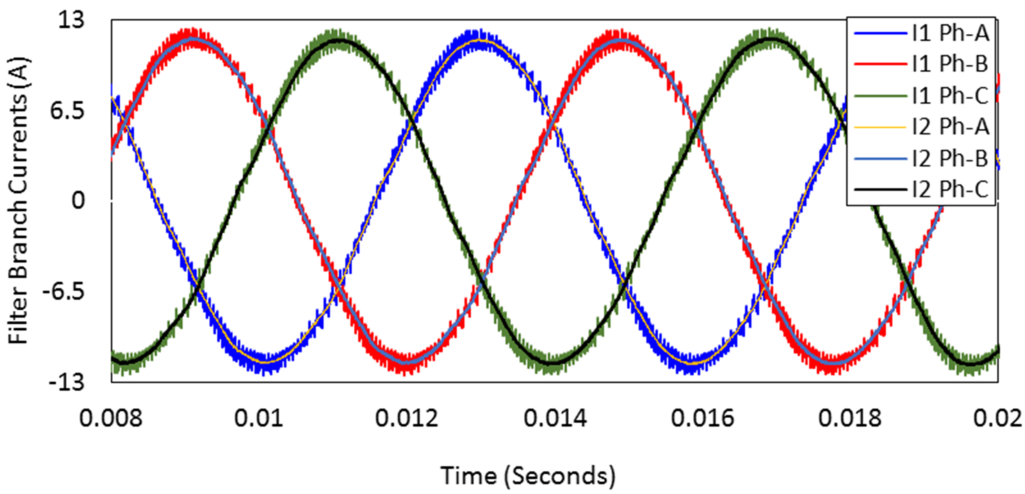

Figure D1.44: Line-to-line Filter & Motor Branch Currents at 175 Hz and 3 Nm

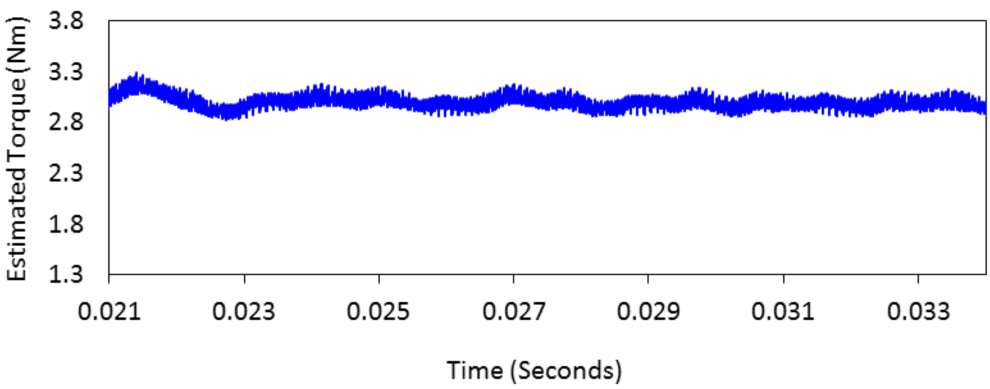

Figure D1.45: Estimated Output torque at 175 Hz and 3 Nm

Appendix D2: Experimental Results of the motor with External Inductor

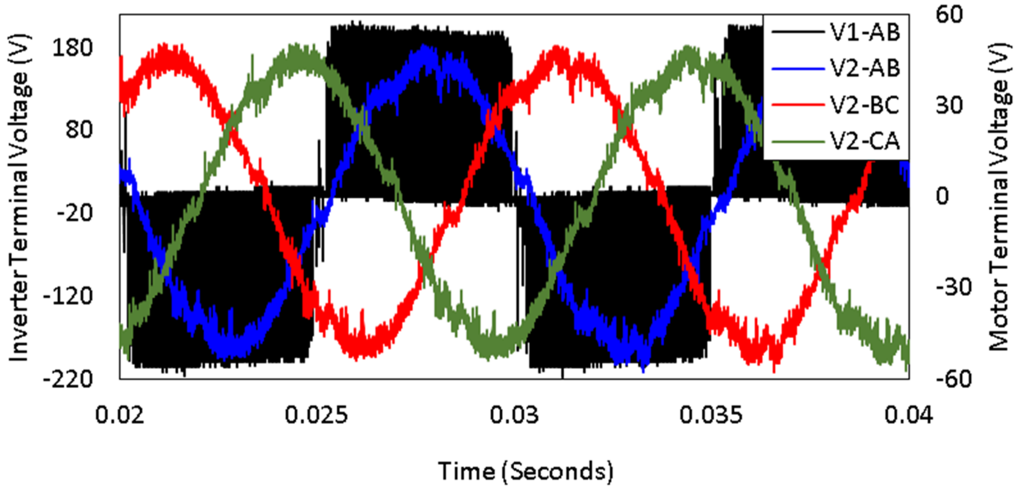

Figure D2.46: Line-to-line Inverter Terminals Voltage & Motor Branch Voltage at 100 Hz and 1.5Nm

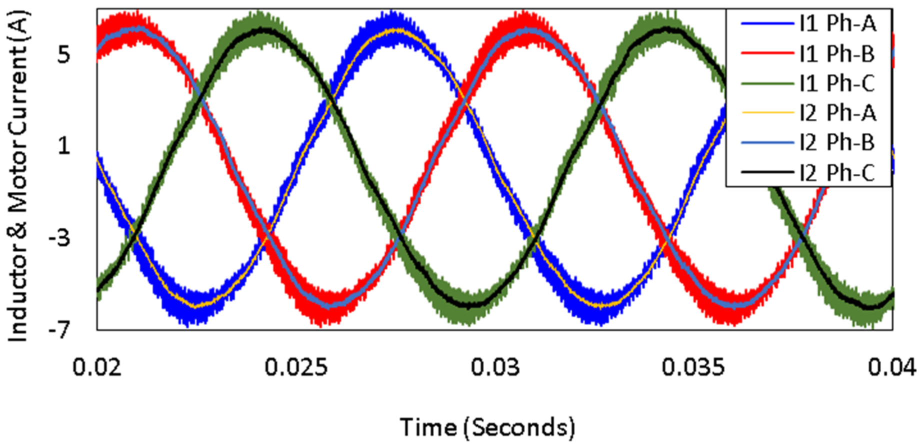

Figure D2.47: Line-to-line Filter & Motor Branch Currents at 100 Hz and 1.5 Nm

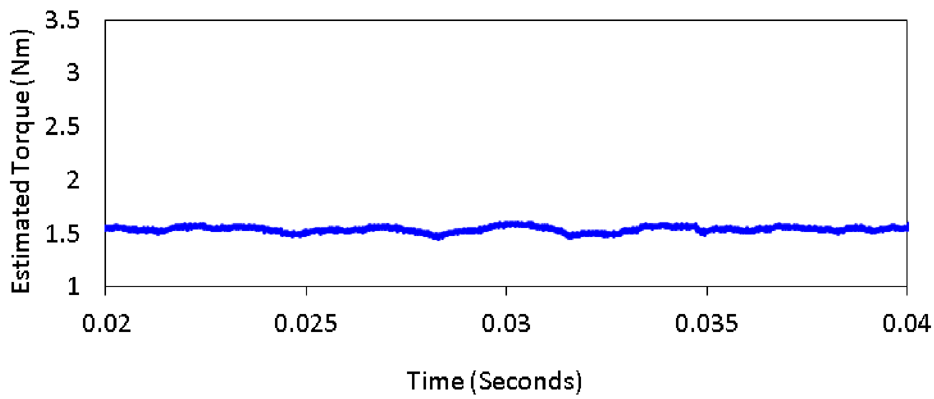

Figure D2.48: Estimated Output torque at 100 Hz and 1.5 Nm

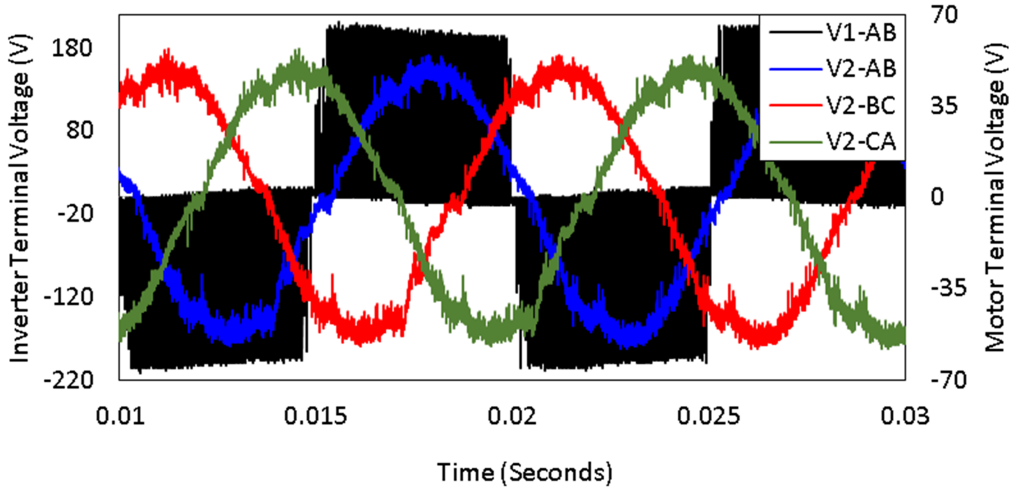

Figure D2.49: Line-to-line Inverter Terminals Voltage & Motor Branch Voltage at 100 Hz and 2Nm

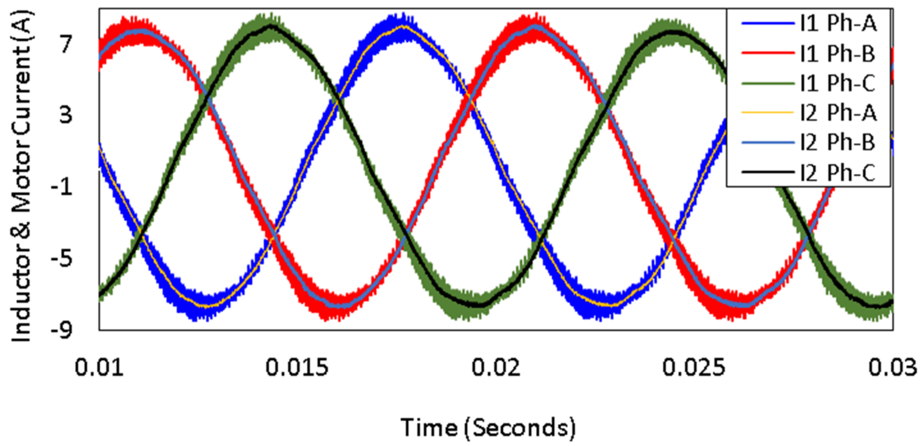

Figure D2.50: Line-to-line Filter & Motor Branch Currents at 100 Hz and 2 Nm

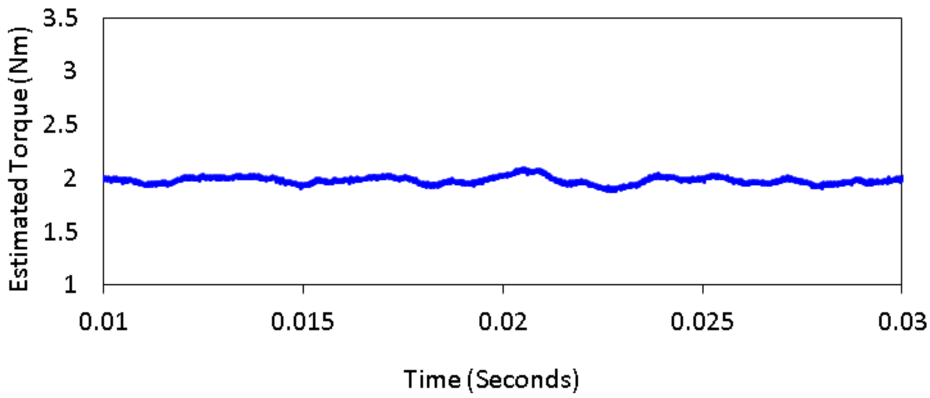

Figure D2.51: Estimated Output torque at 100 Hz and 2 Nm

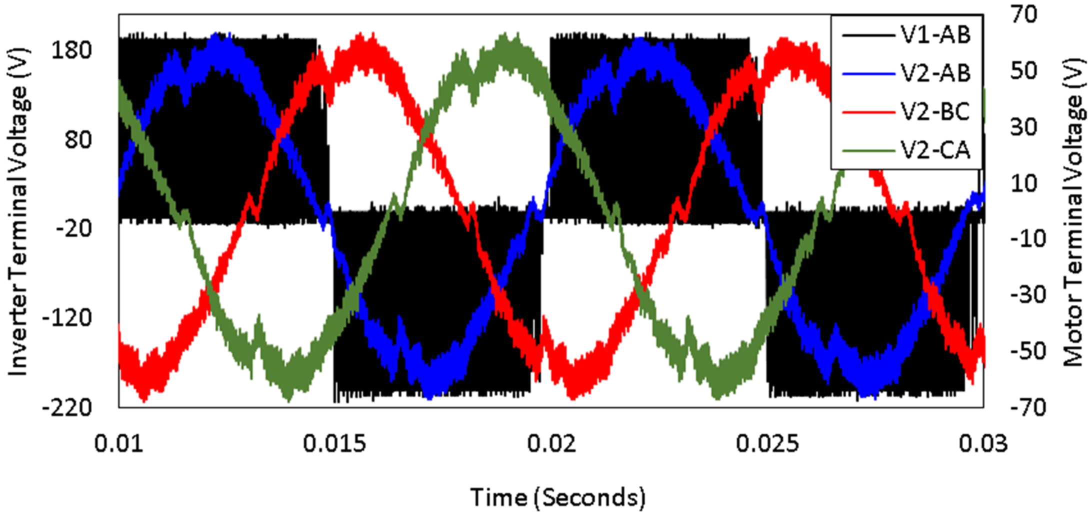

Figure D2.52: Line-to-line Inverter Terminals Voltage & Motor Branch Voltage at 100 Hz and 2.5Nm

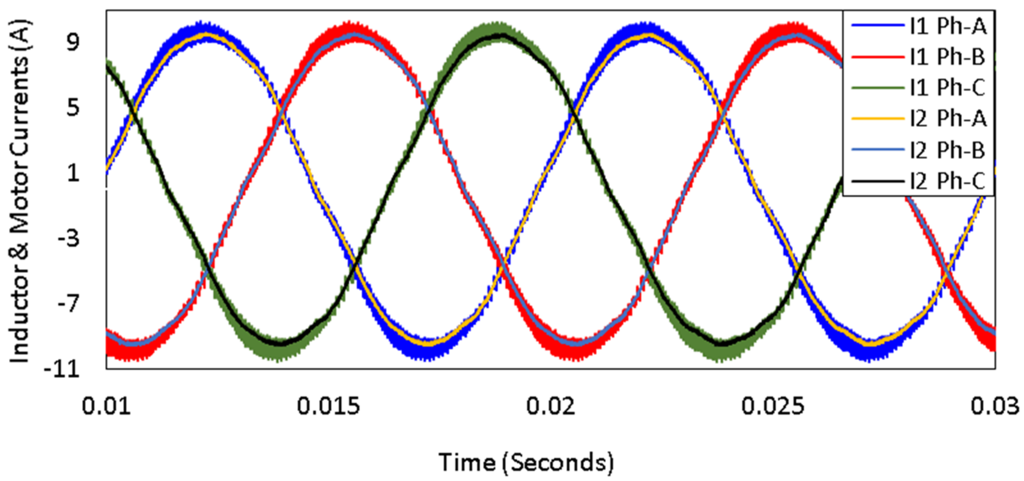

Figure D2.53: Line-to-line Filter & Motor Branch Currents at 100 Hz and 2.5 Nm

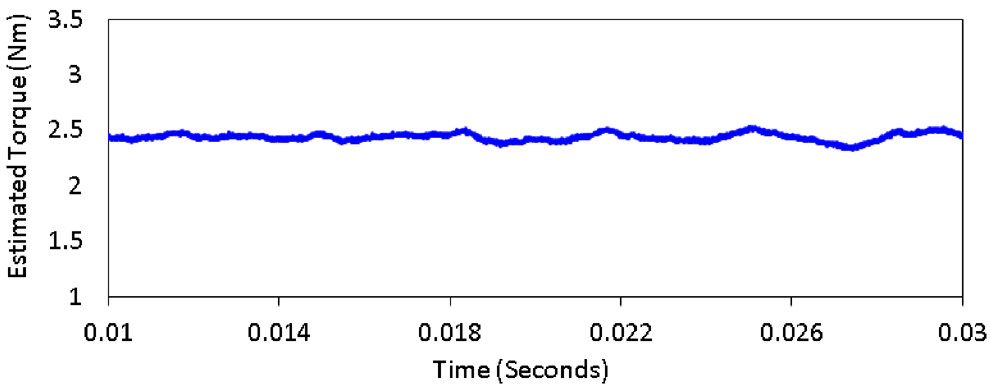

Figure D2.54: Estimated Output torque at 100 Hz and 2.5 Nm

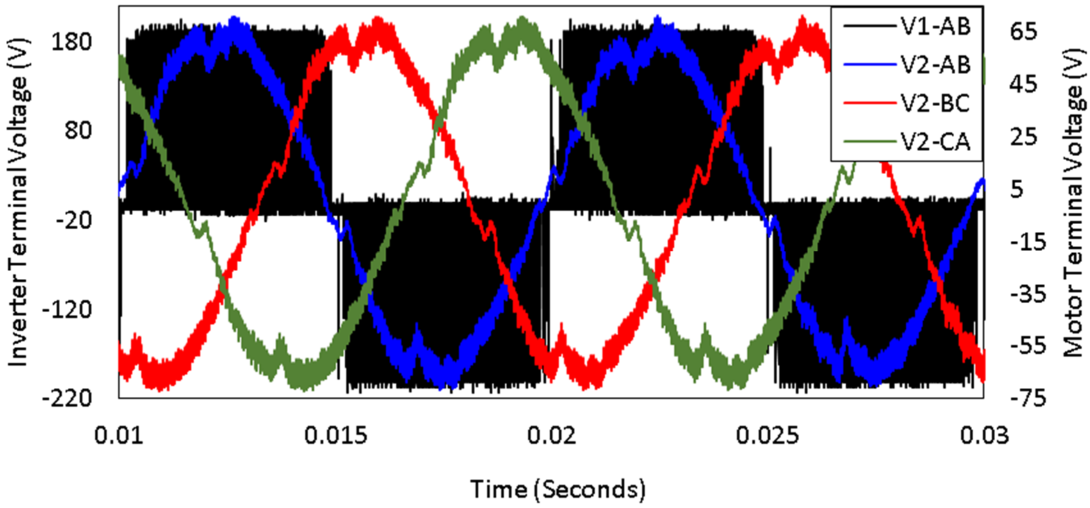

Figure D2.55: Line-to-line Inverter Terminals Voltage & Motor Branch Voltage at 100 Hz and 3Nm

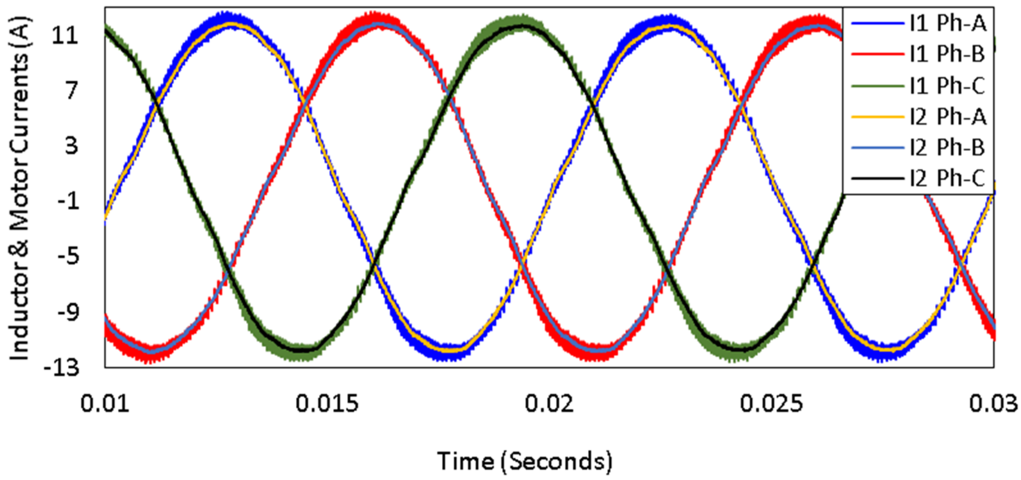

Figure D2.56: Line-to-line Filter & Motor Branch Currents at 100 Hz and 3 Nm

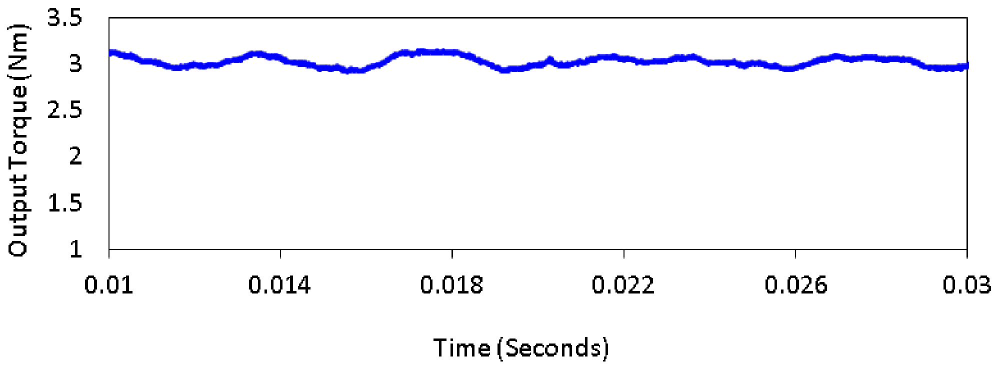

Figure D2.57: Estimated Output torque at 100 Hz and 3 Nm

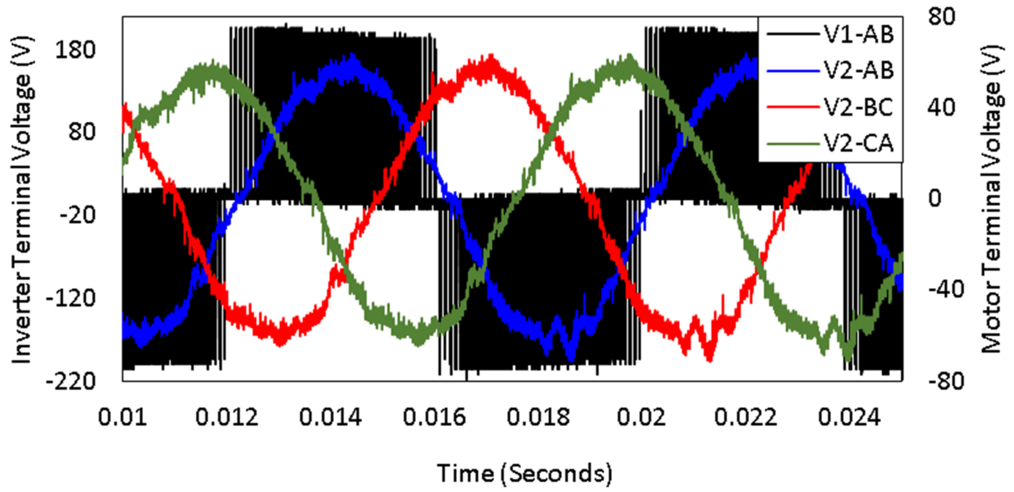

Figure D2.58: Line-to-line Inverter Terminals Voltage & Motor Branch Voltage at 125 Hz and 1.5Nm

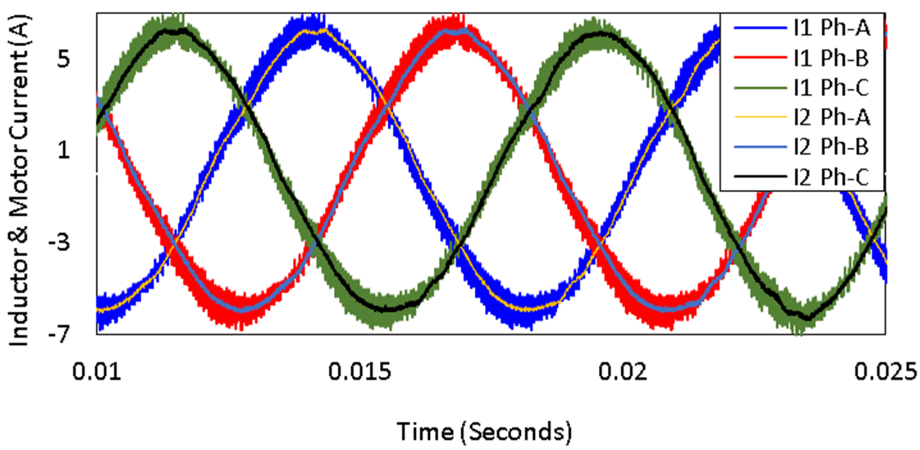

Figure D2.59: Line-to-line Filter & Motor Branch Currents at 125 Hz and 1.5 Nm

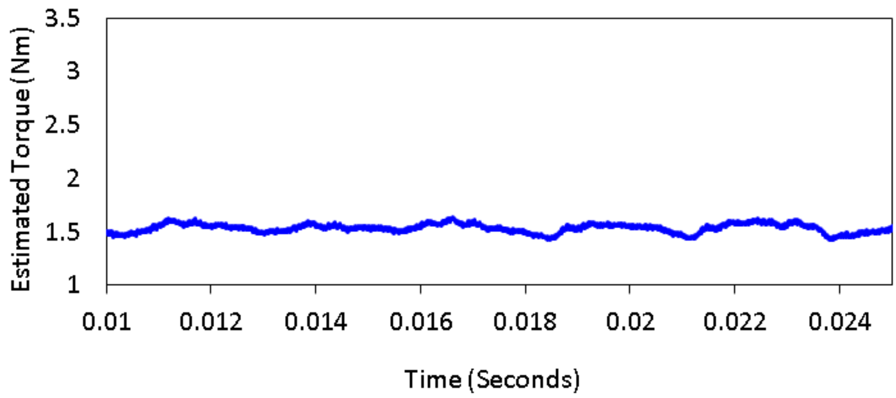

Figure D2.60: Estimated Output torque at 125 Hz and 1.5 Nm

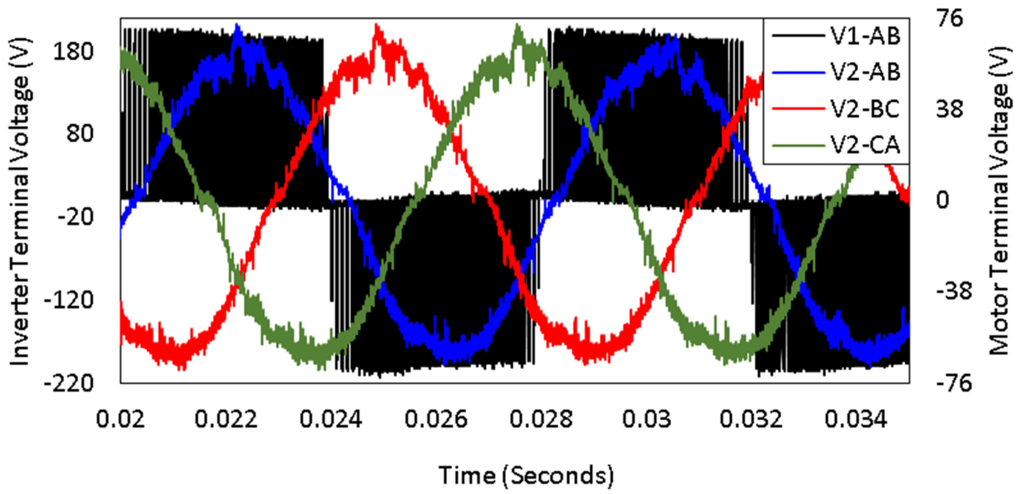

Figure D2.61: Line-to-line Inverter Terminals Voltage & Motor Branch Voltage at 125 Hz and 2Nm

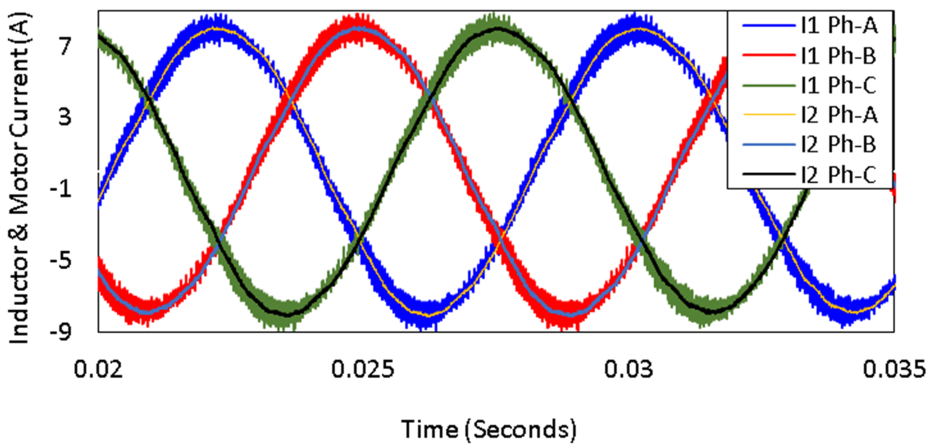

Figure D2.62: Line-to-line Filter & Motor Branch Currents at 125 Hz and 2 Nm

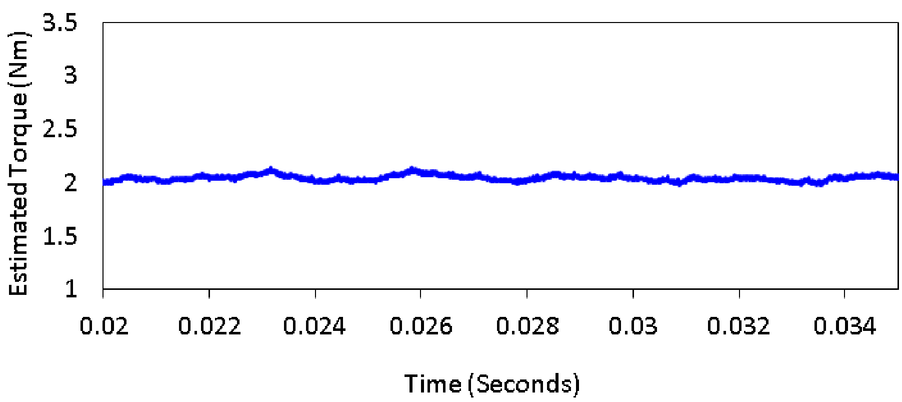

Figure D2.63: Estimated Output torque at 125 Hz and 2 Nm

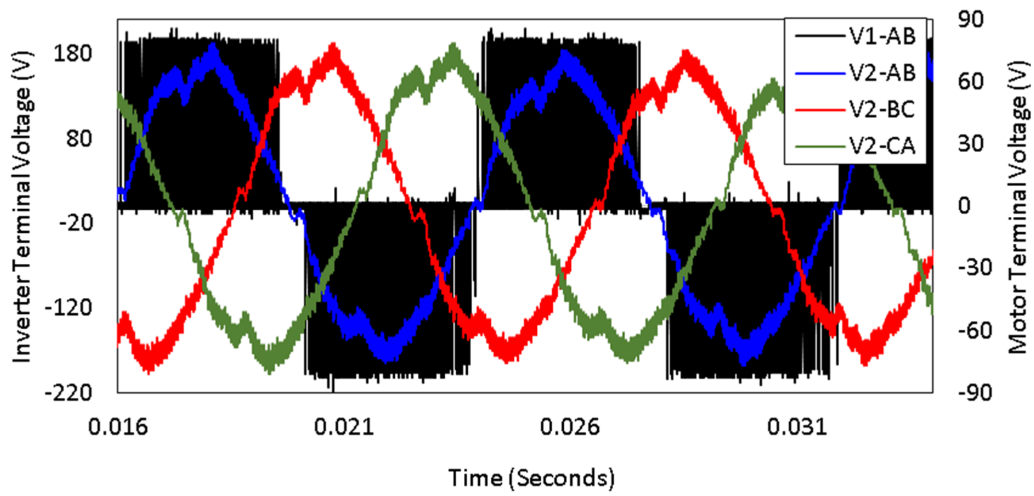

Figure D2.64: Line-to-line Inverter Terminals Voltage & Motor Branch Voltage at 125 Hz and 2.5Nm

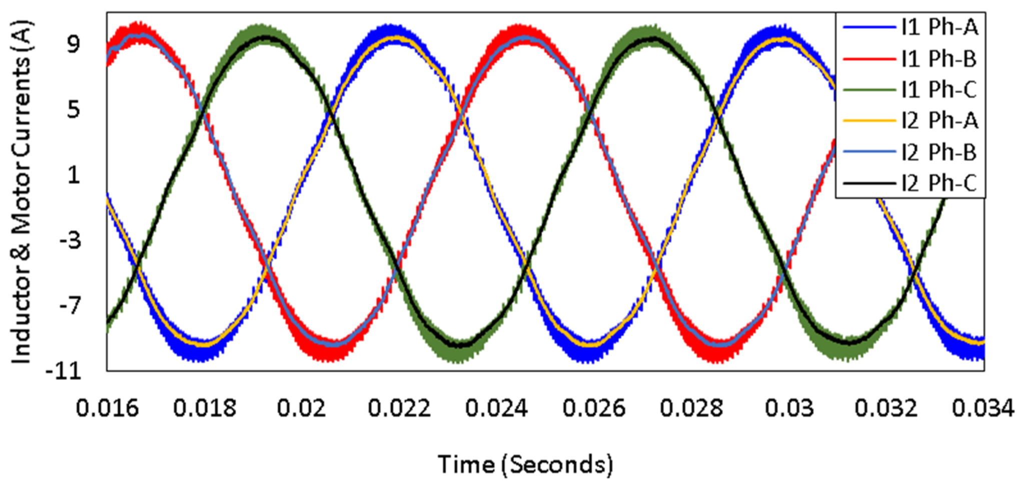

Figure D2.65: Line-to-line Filter & Motor Branch Currents at 125 Hz and 2.5 Nm

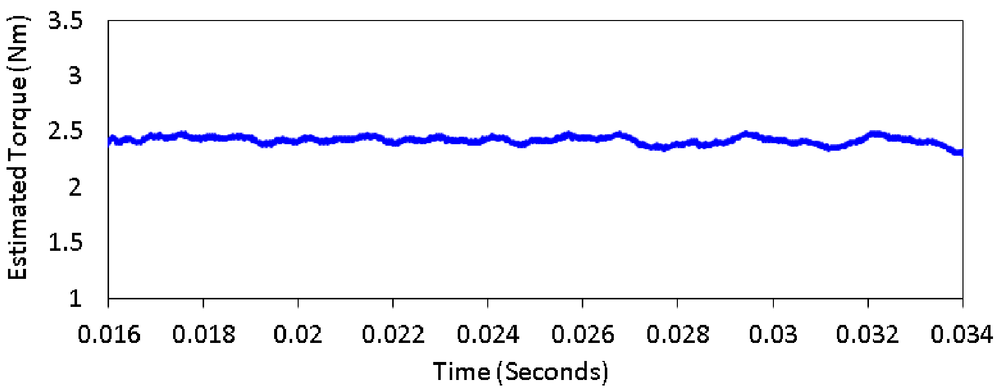

Figure D2.66: Estimated Output torque at 125 Hz and 2.5 Nm

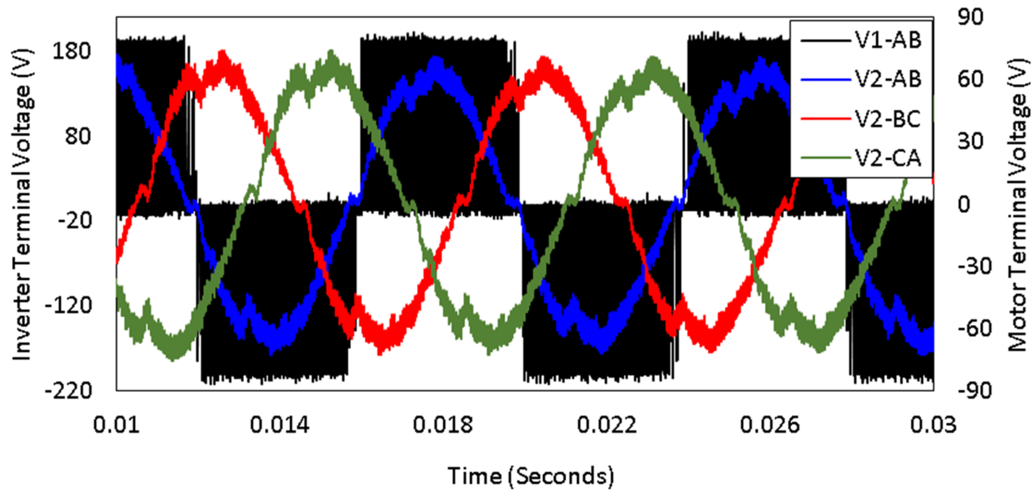

Figure D2.67: Line-to-line Inverter Terminals Voltage & Motor Branch Voltage at 125 Hz and 3Nm

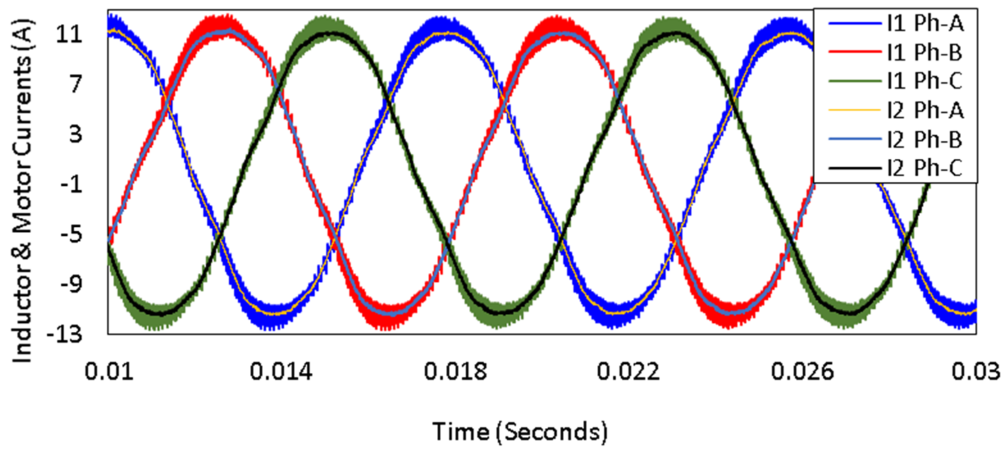

Figure D2.68: Line-to-line Filter & Motor Branch Currents at 125 Hz and 3 Nm

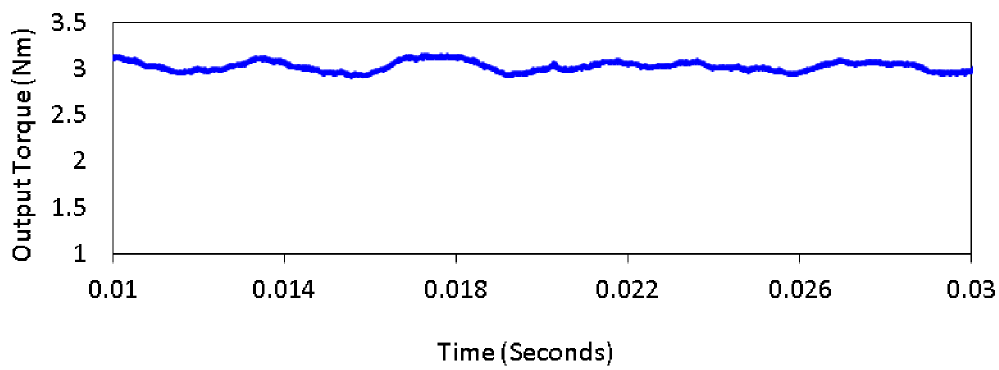

Figure D2.69: Estimated Output torque at 125 Hz and 3 Nm

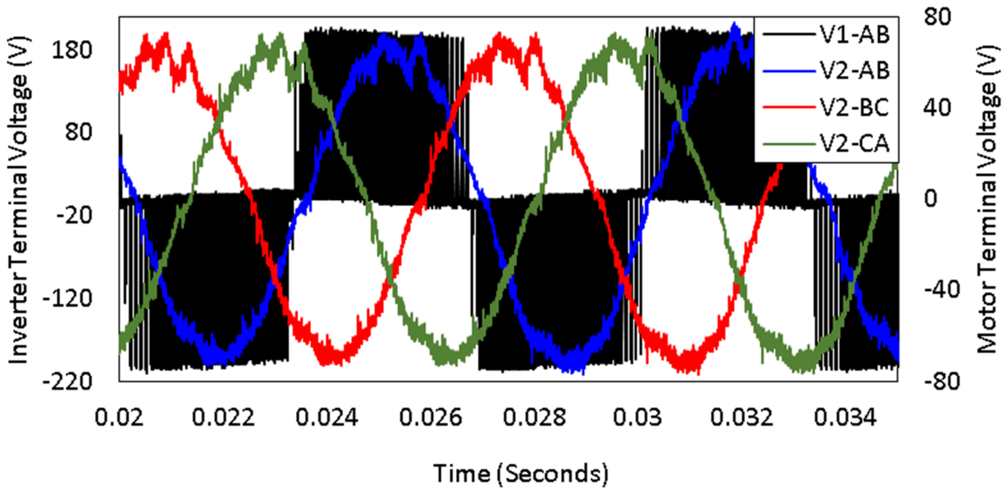

Figure D2.70: Line-to-line Inverter Terminals Voltage & Motor Branch Voltage at 150 Hz and 1.5Nm

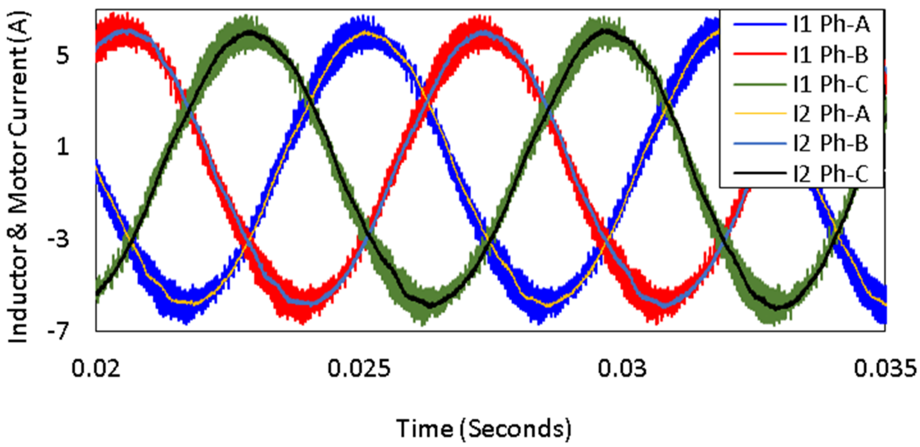

Figure D2.71: Line-to-line Filter & Motor Branch Currents at 150 Hz and 1.5 Nm

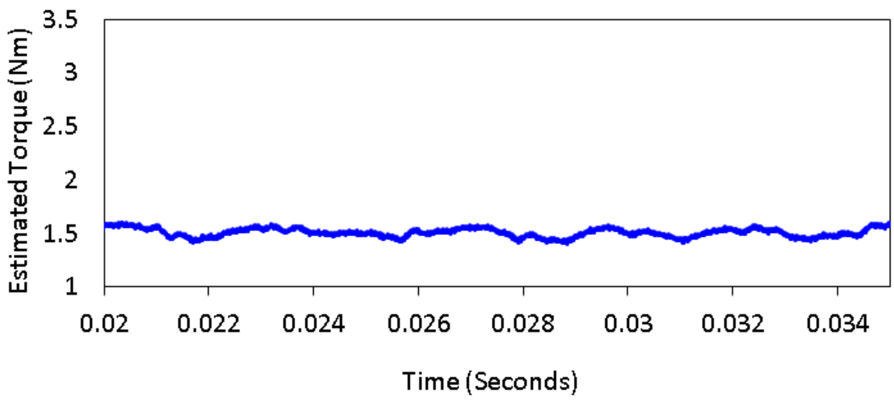

Figure D2.72: Estimated Output torque at 150 Hz and 1.5 Nm

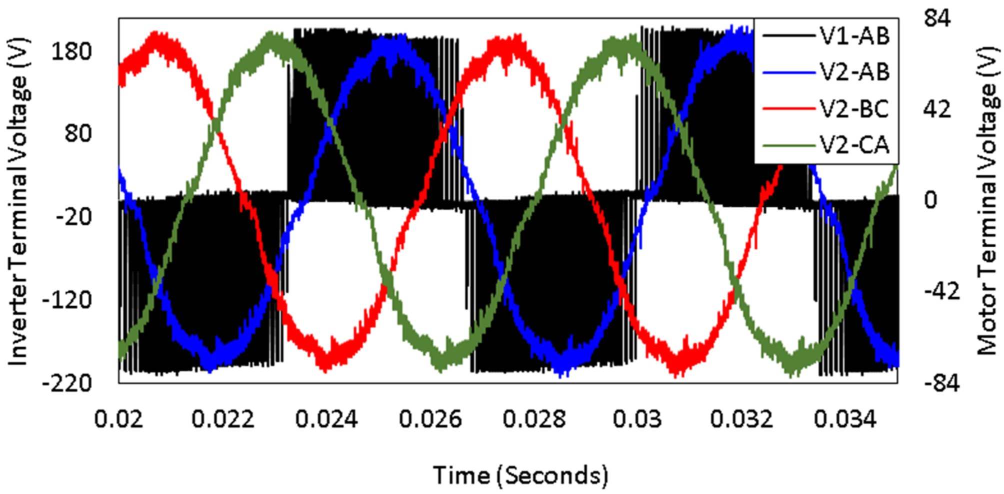

Figure D2.73: Line-to-line Inverter Terminals Voltage & Motor Branch Voltage at 150 Hz and 2Nm

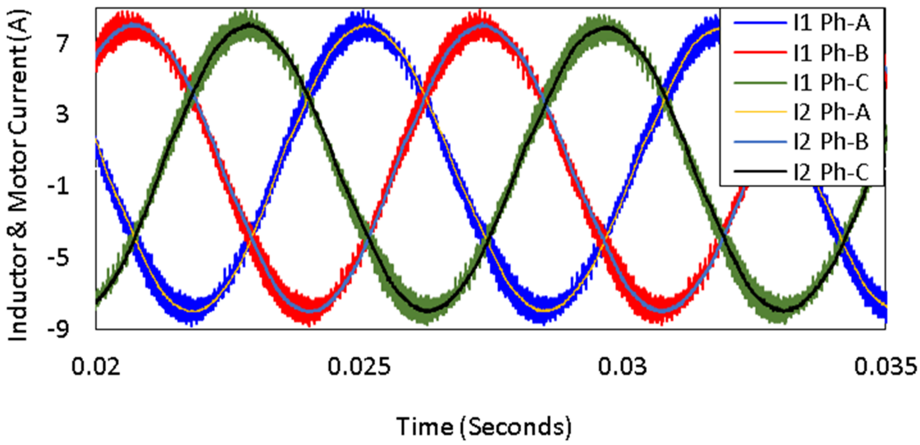

Figure D2.74: Line-to-line Filter & Motor Branch Currents at 150 Hz and 2 Nm

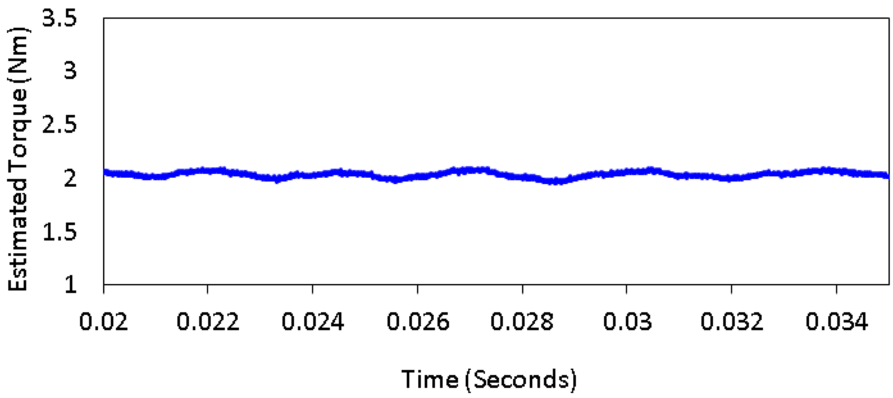

Figure D2.75: Estimated Output torque at 150 Hz and 2 Nm

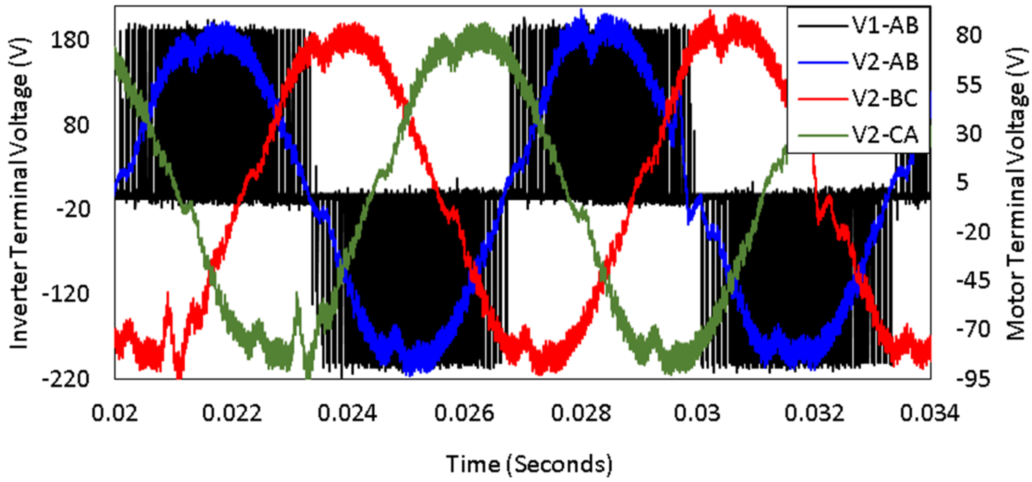

Figure D2.76: Line-to-line Inverter Terminals Voltage & Motor Branch Voltage at 150 Hz and 2.5Nm

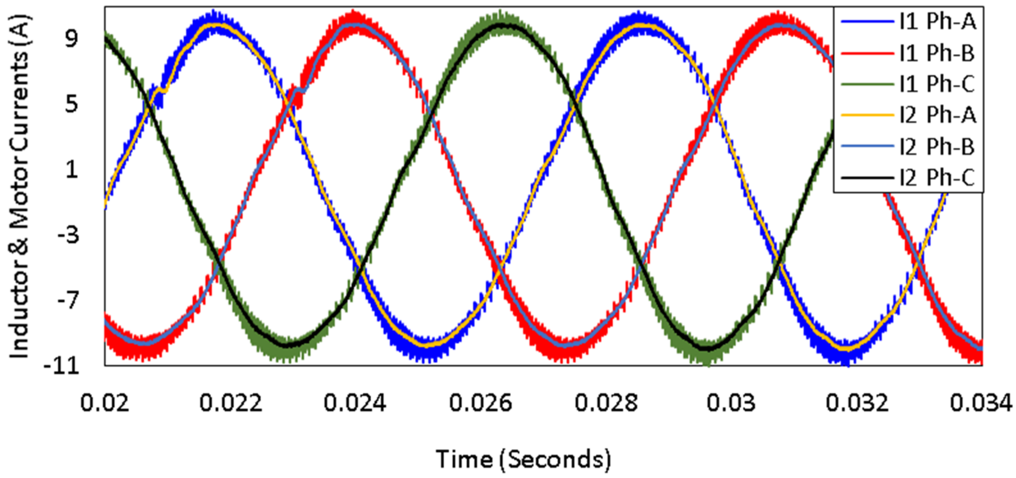

Figure D2.77: Line-to-line Filter & Motor Branch Currents at 150 Hz and 2.5 Nm

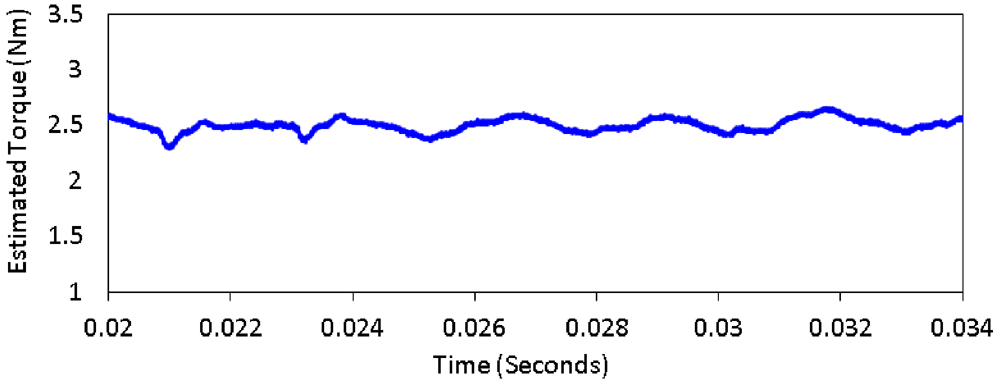

Figure D2.78: Estimated Output torque at 150 Hz and 2.5 Nm

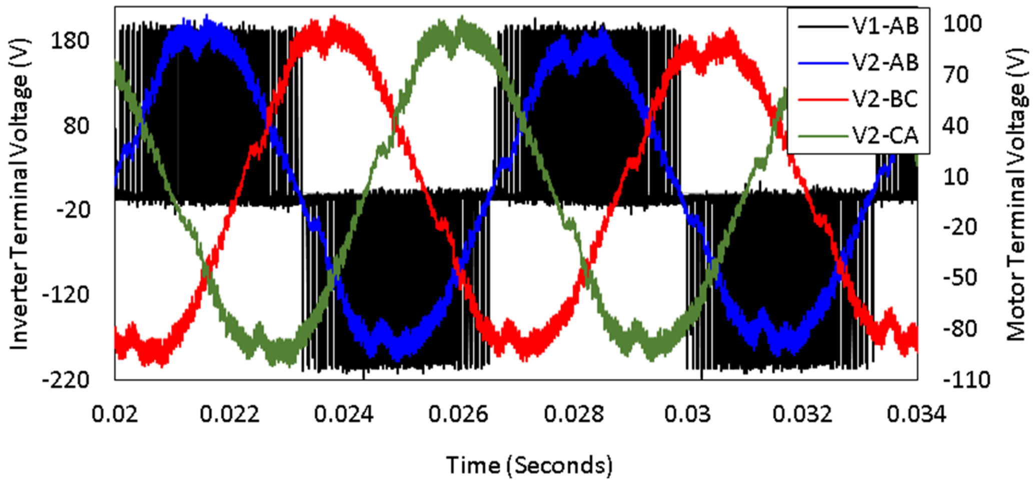

Figure D2.79: Line-to-line Inverter Terminals Voltage & Motor Branch Voltage at 150 Hz and 3Nm

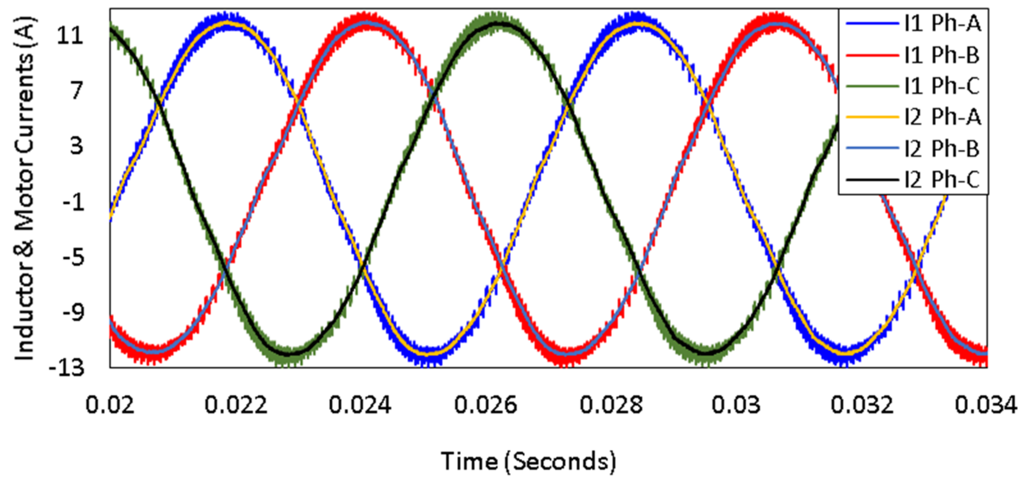

Figure D2.80: Line-to-line Filter & Motor Branch Currents at 150 Hz and 3 Nm

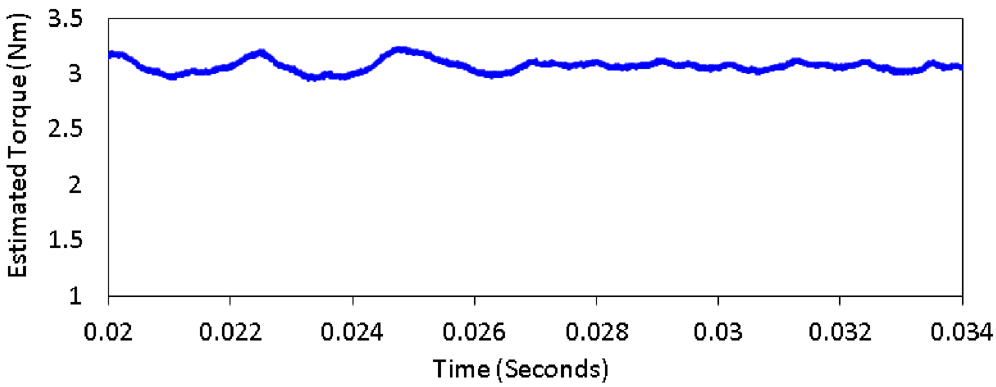

Figure D2.81: Estimated Output torque at 150 Hz and 3 Nm

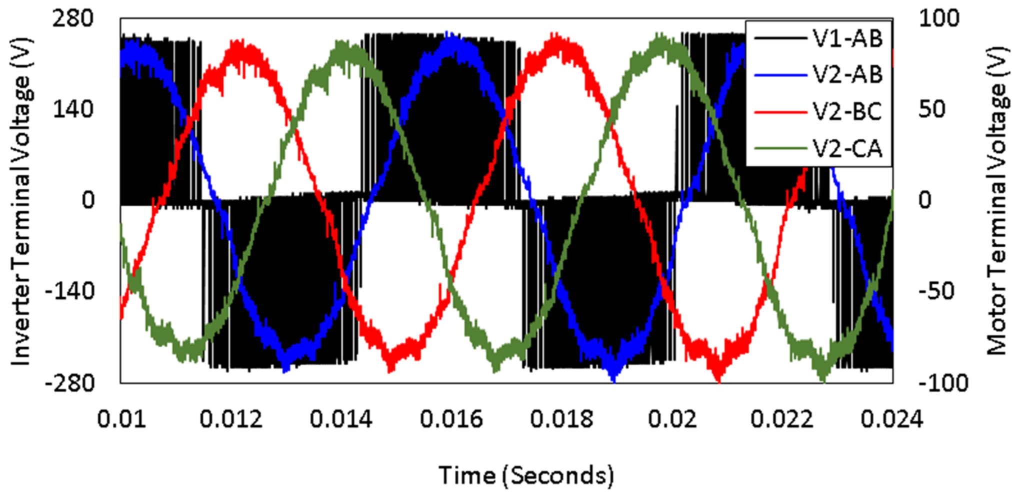

Figure D2.82: Line-to-line Inverter Terminals Voltage & Motor Branch Voltage at 175 Hz and 2Nm

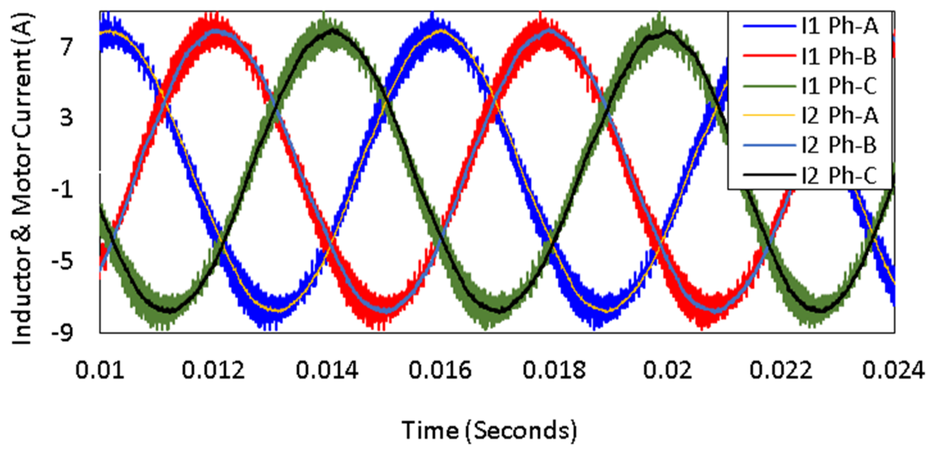

Figure D2.83: Line-to-line Filter & Motor Branch Currents at 175 Hz and 2 Nm

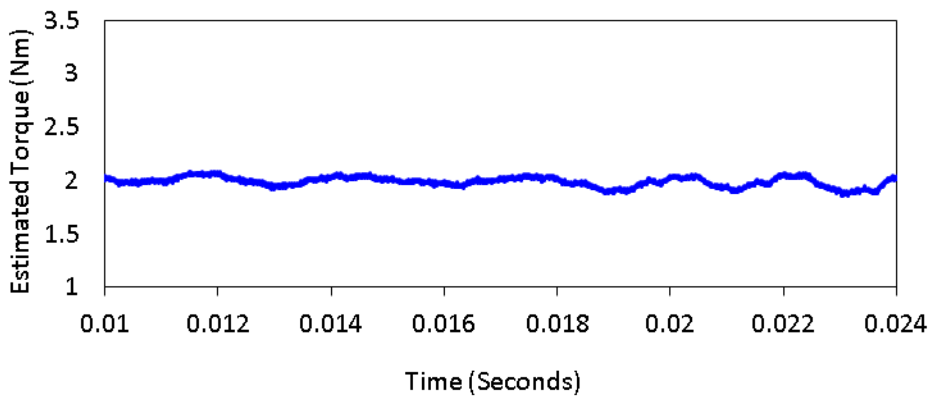

Figure D2.84: Estimated Output torque at 175 Hz and 2 Nm

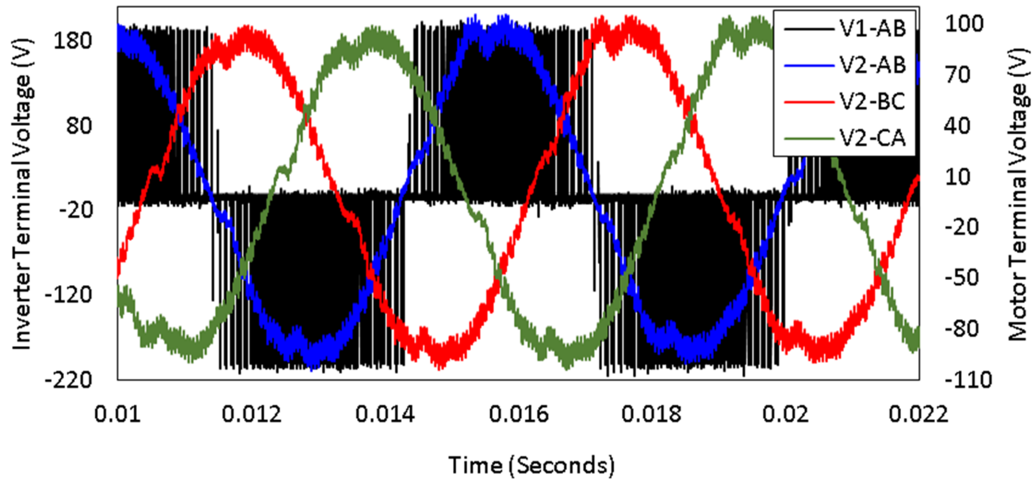

Figure D2.85: Line-to-line Inverter Terminals Voltage & Motor Branch Voltage at 175 Hz and 2.5Nm

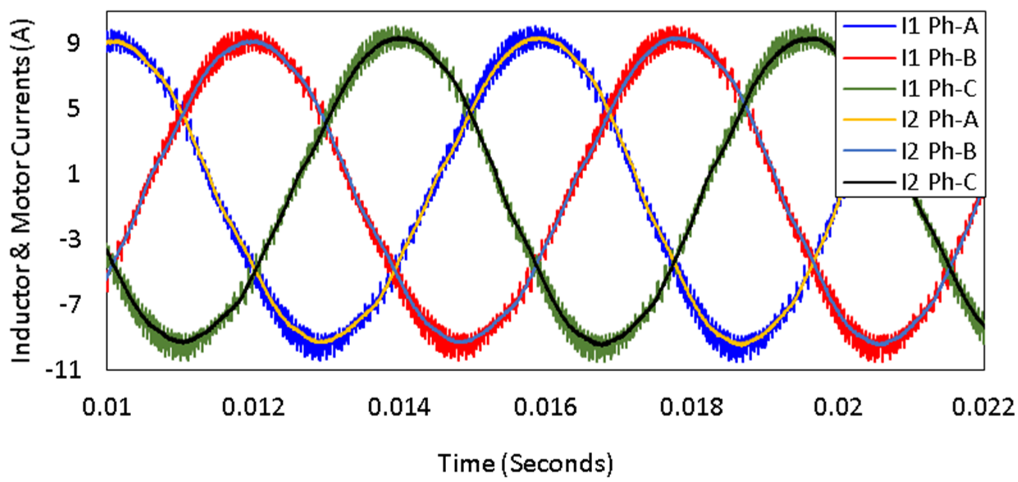

Figure D2.86: Line-to-line Filter & Motor Branch Currents at 175 Hz and 2.5 Nm

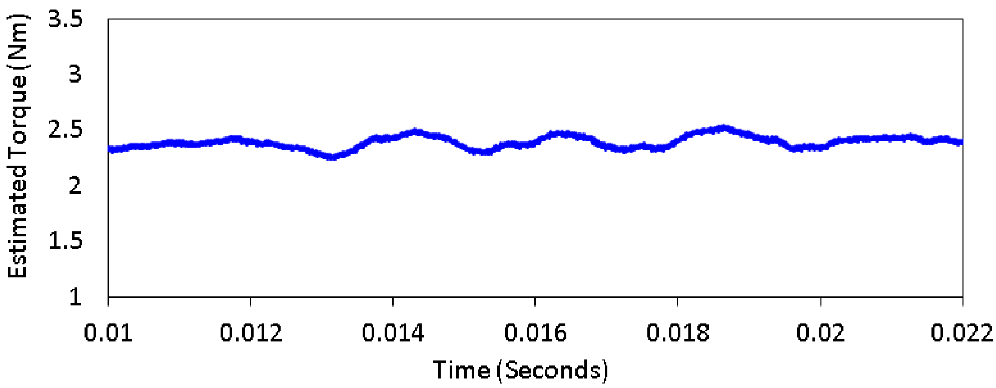

Figure D2.87: Estimated Output torque at 175 Hz and 2.5 Nm

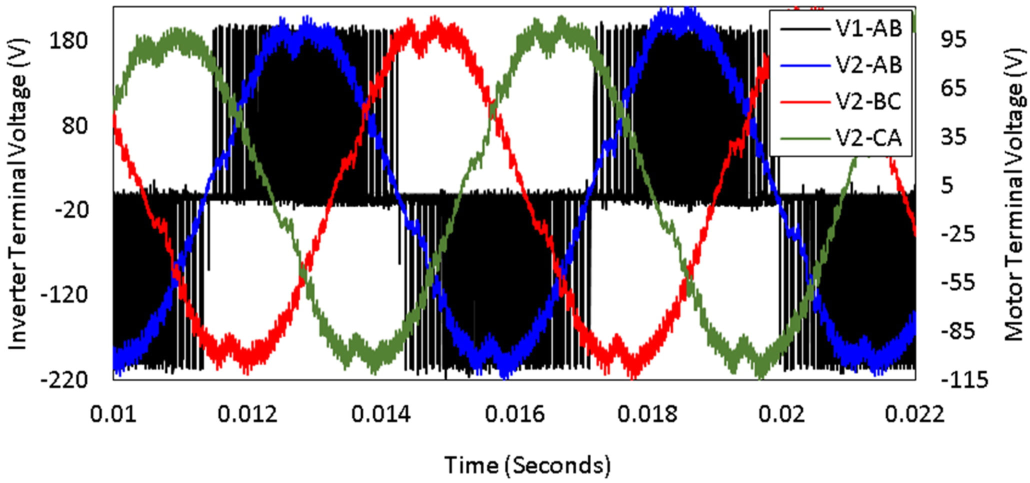

Figure D2.88: Line-to-line Inverter Terminals Voltage & Motor Branch Voltage at 175 Hz and 3Nm

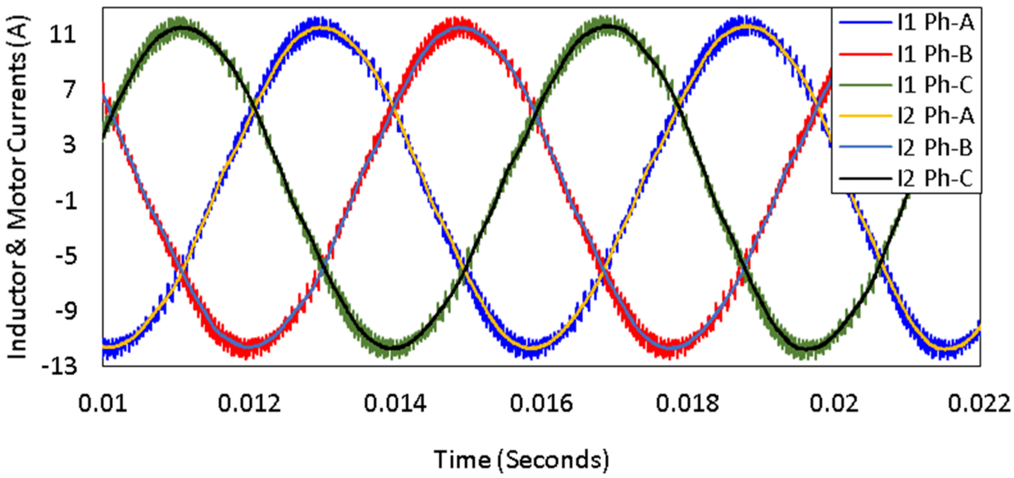

Figure D2.89: Line-to-line Filter & Motor Branch Currents at 175 Hz and 3 Nm

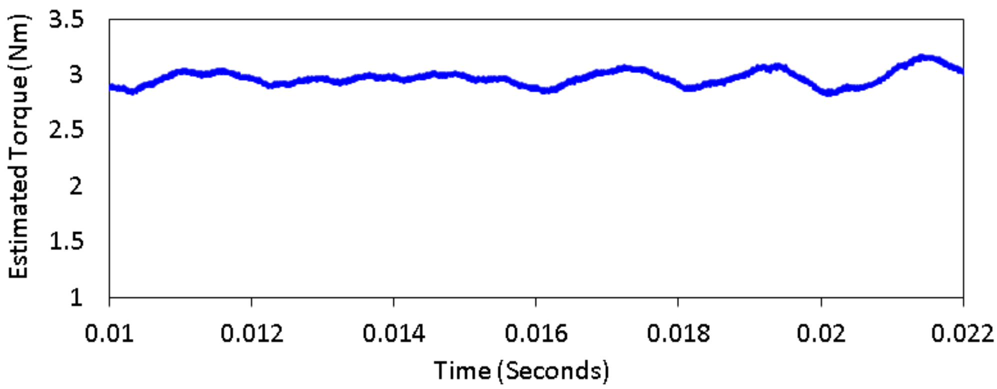

Figure D2.90: Estimated Output torque at 175 Hz and 3 Nm

APPENDIX E: WINDING CONFIGURATION AND FLUX DISTRIBUTION OF MOTOR-SHAPED INDUCTORS

E1. 4 Poles with 6, 12 and 18 slots Rotational Inductors

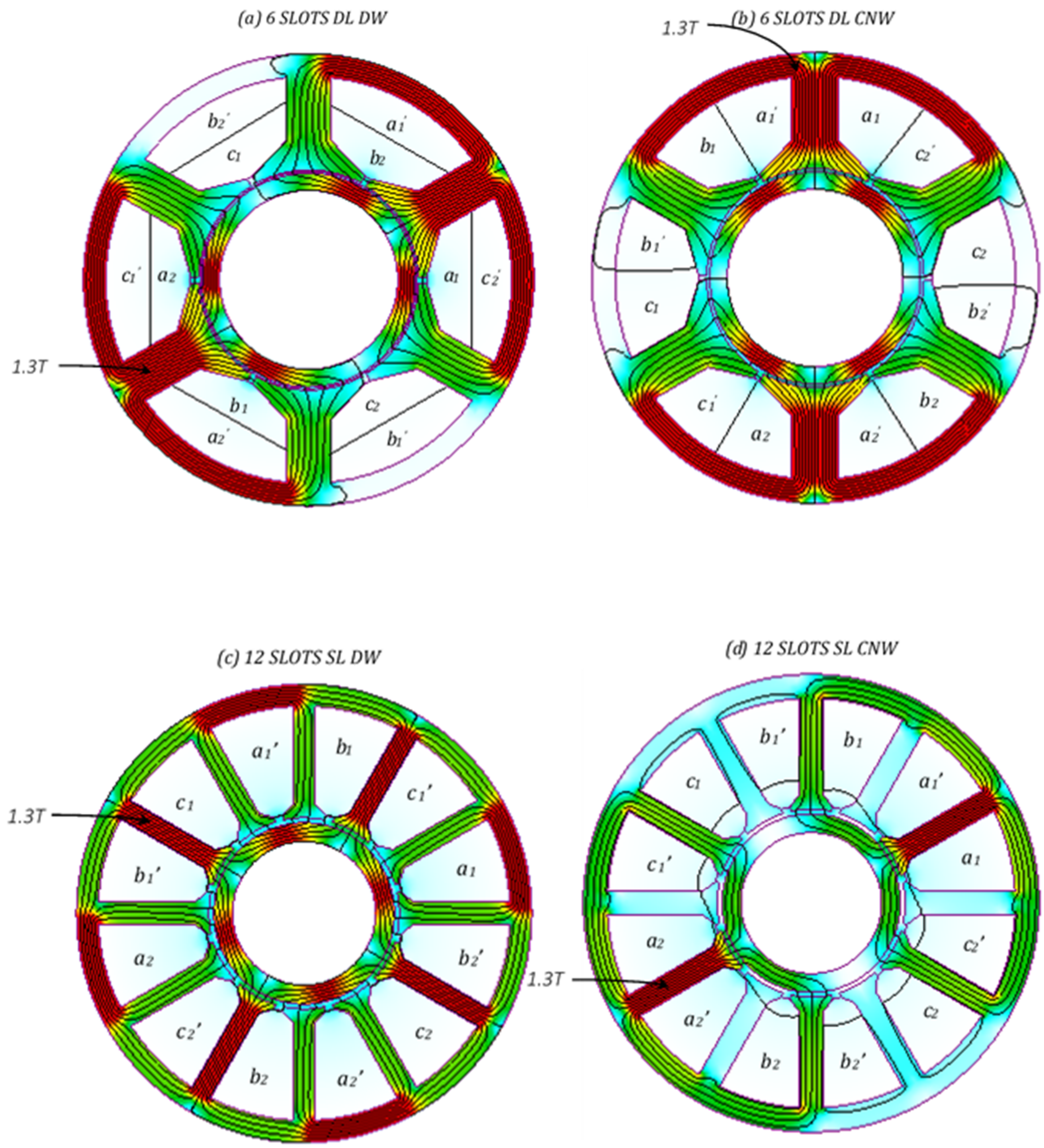

(e) 12 SLOTS DL DW

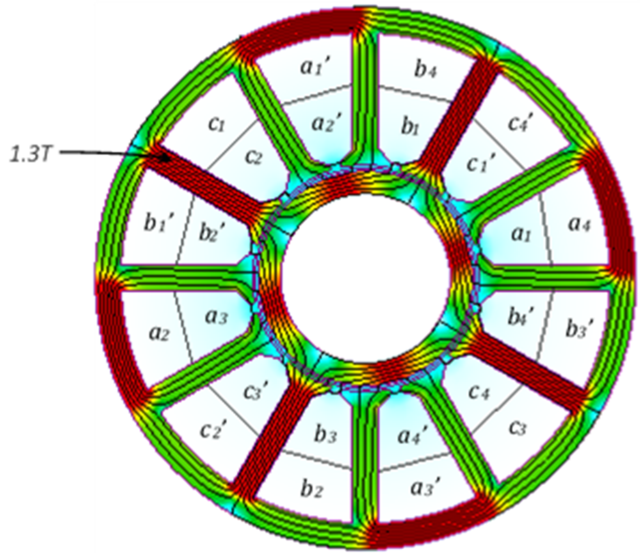

(f) 12 SLOTS DL CNW

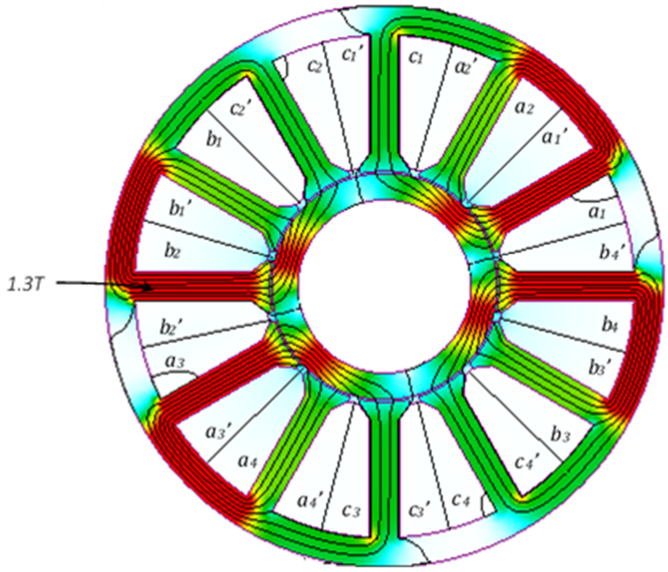

(g) 18 SLOTS DL DW

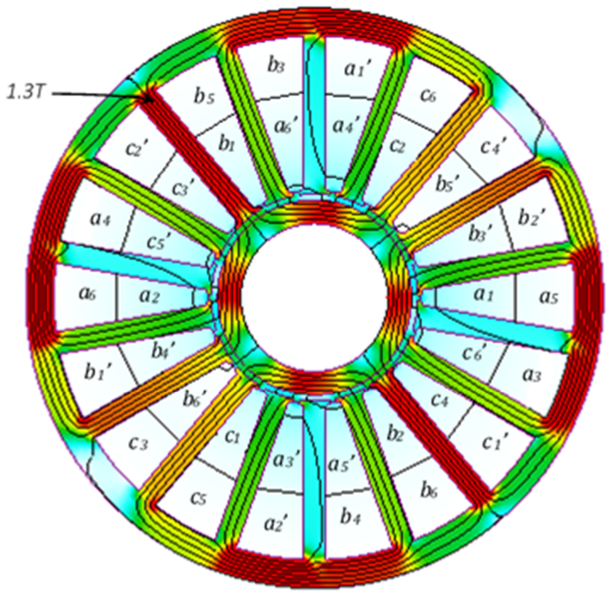

(h) 18 SLOTS DL CNW

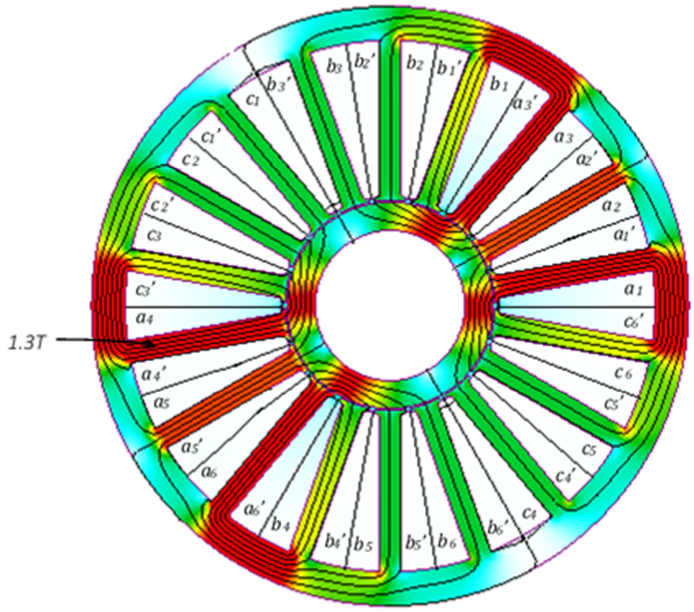

E2. 6 Poles with 18 slots Rotational Inductors

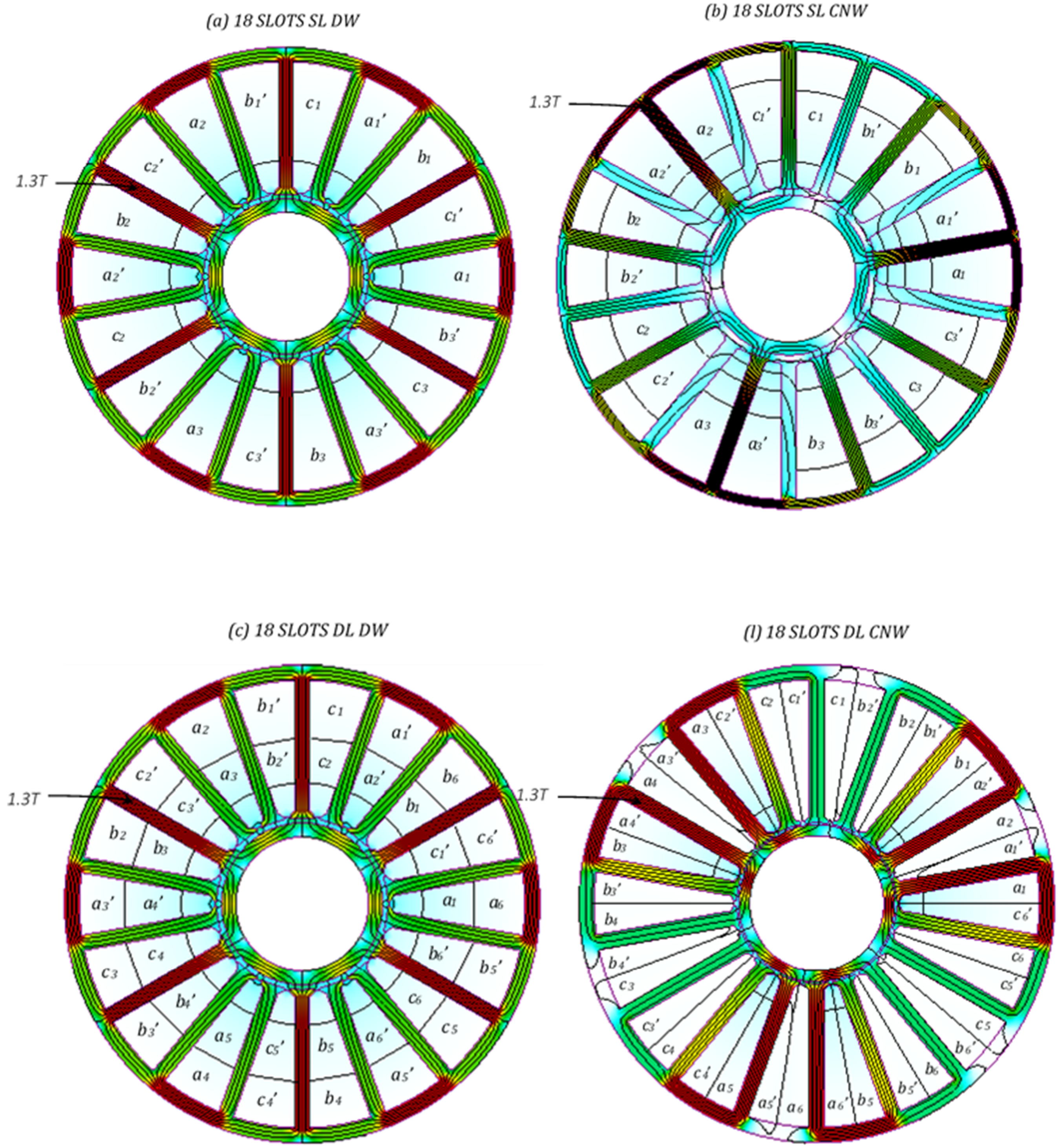

E3. 2 Poles with 6, 12 and 18 slots Rotor-less Inductors

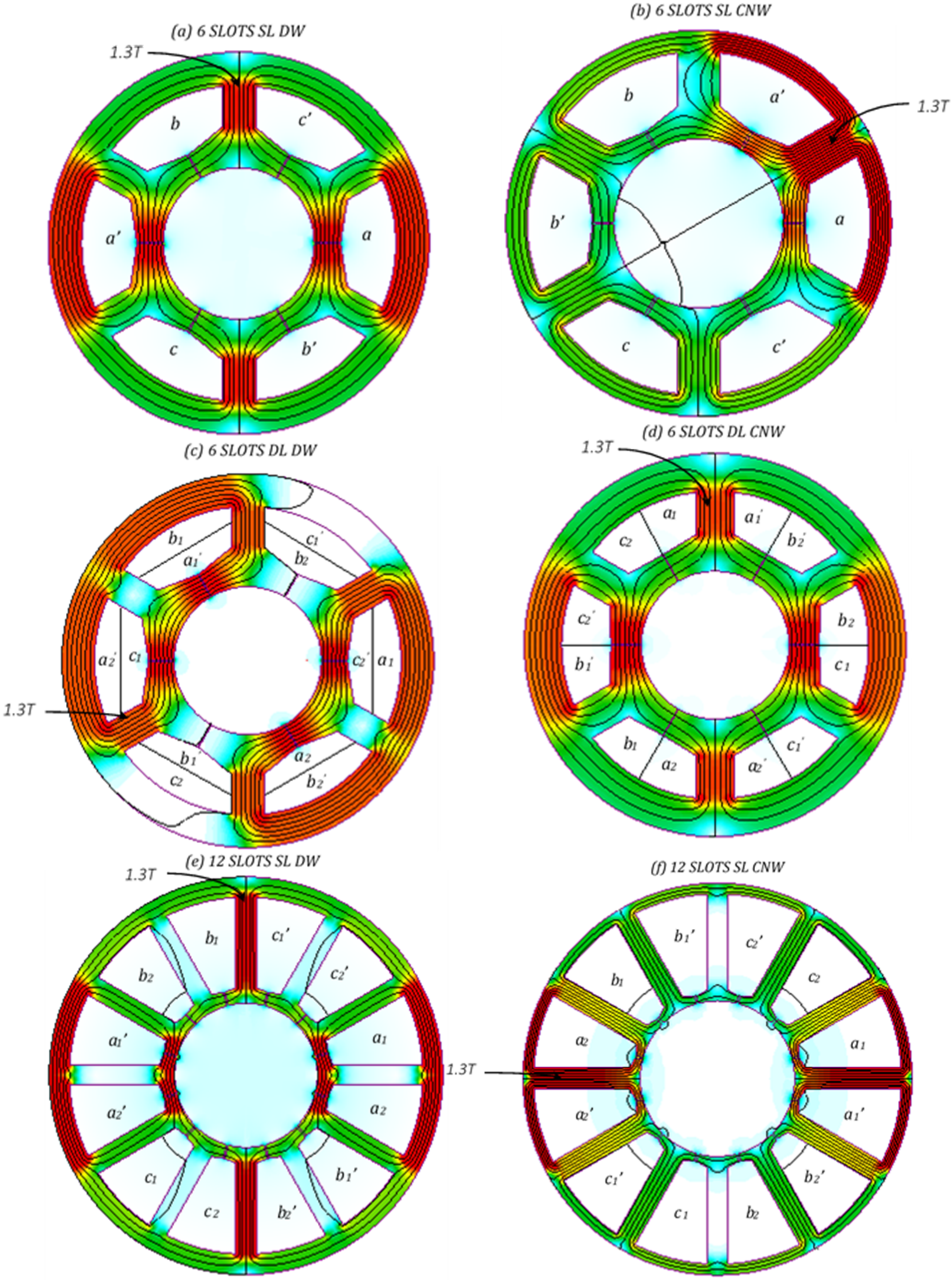

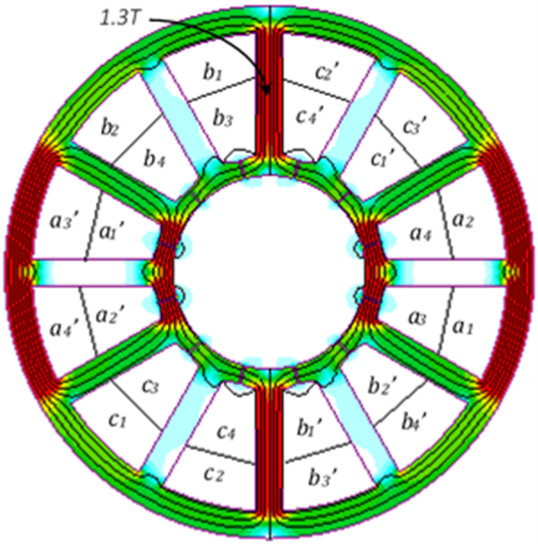

(g) 12 SLOTS DL DW

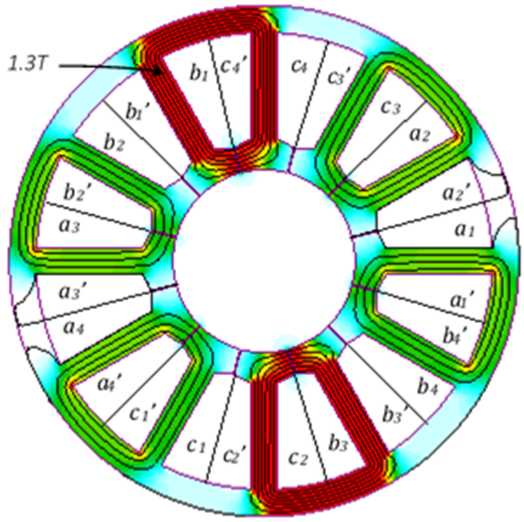

(h) 12 SLOTS DL CNW

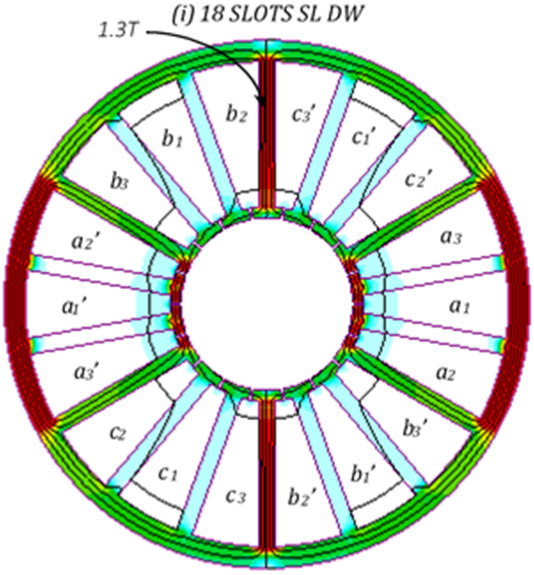

(i) 18 SLOTS SL DW

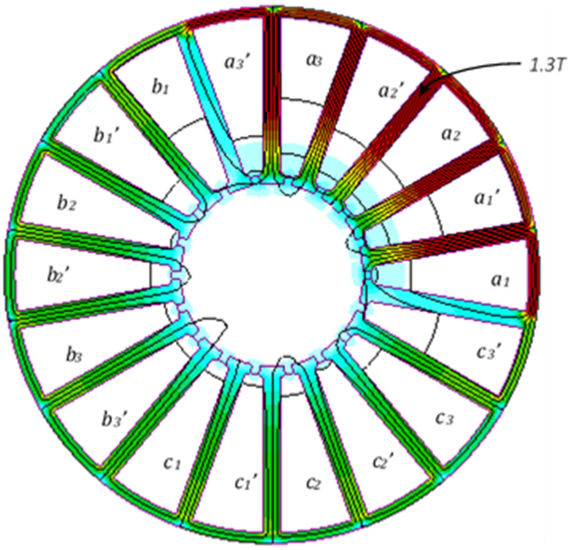

(j) 18 SLOTS SL CNW

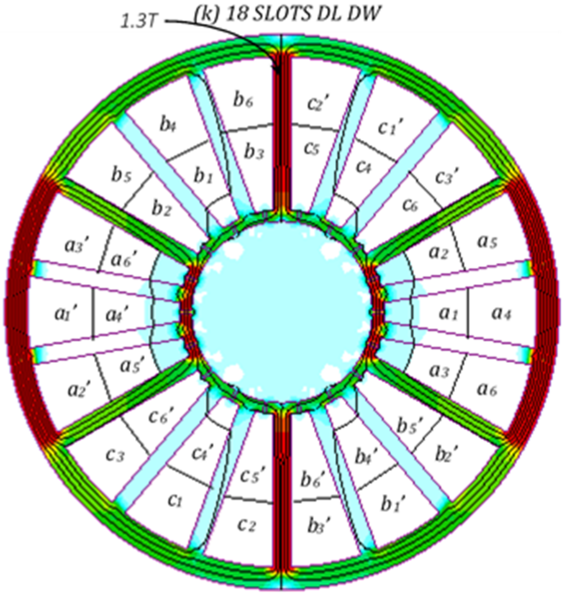

(k) 18 SLOTS DL DW

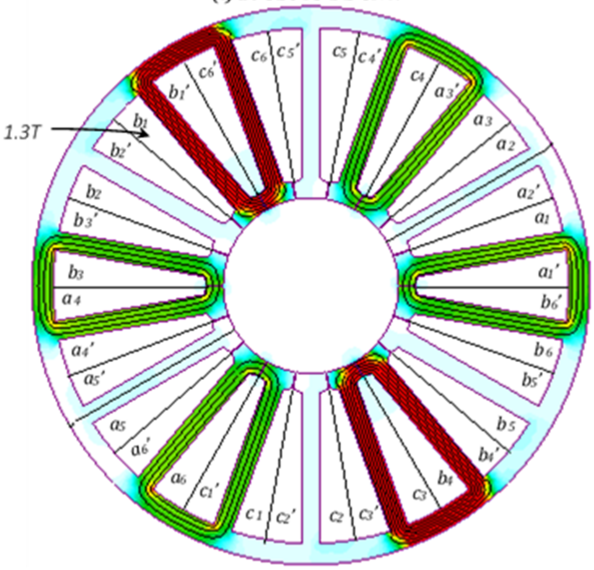

(l) 18 SLOTS DL CNW

E4. 4 Poles with 6, 12 and 18 slots Rotor-less Inductors

(a) 6 SLOTS DL DW

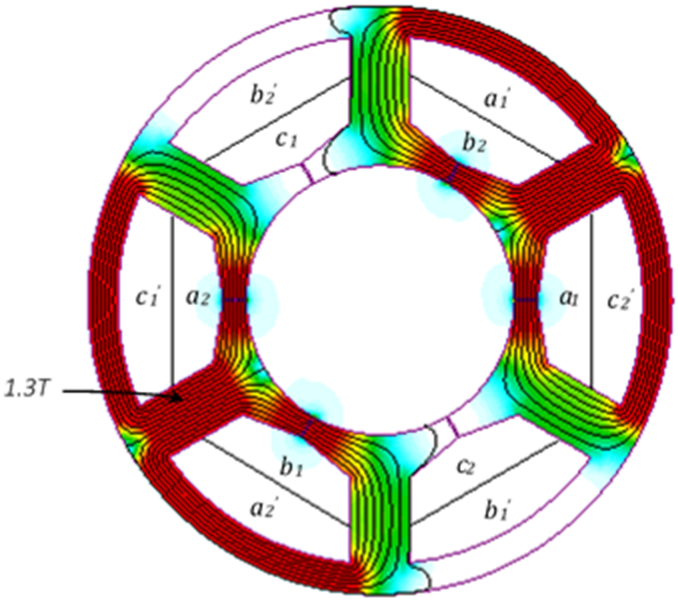

(b) 6 SLOTS DL CNW

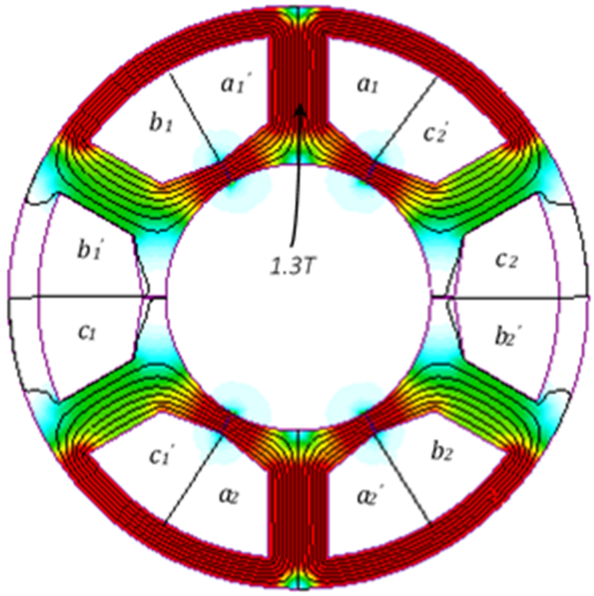

(c) 12 SLOTS SL DW

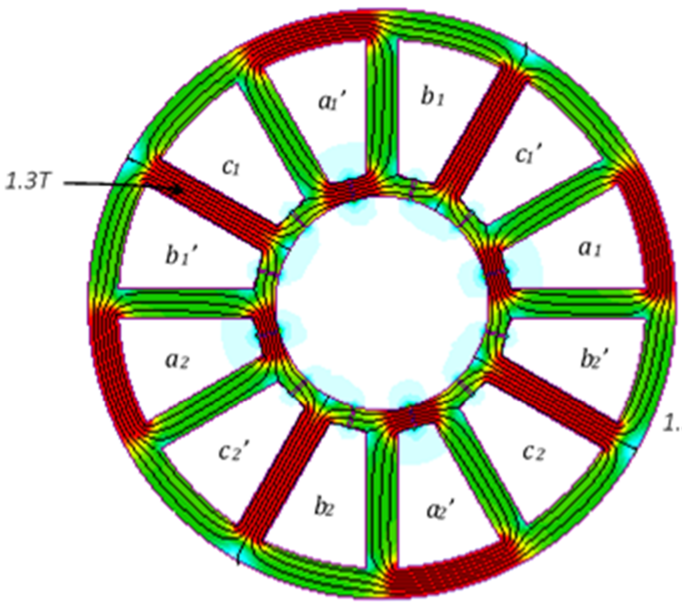

(d) 12 SLOTS SL CNW

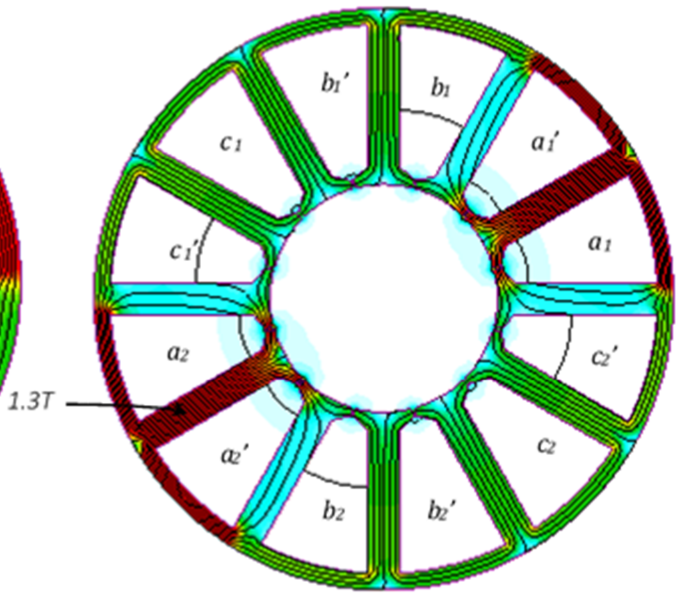

(e) 12 SLOTS DL DW

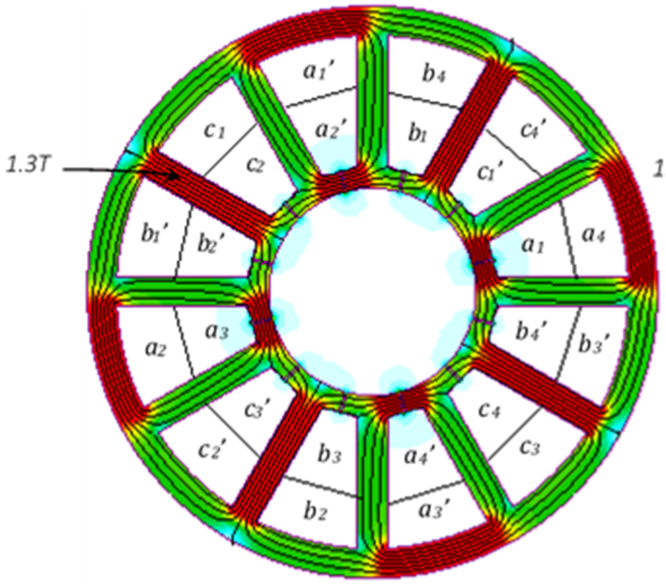

(f) 12 SLOTS DL CNW

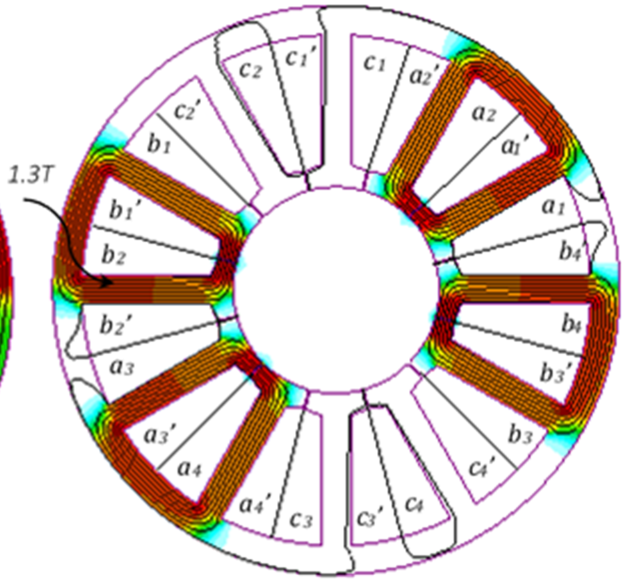

(f) 12 SLOTS DL CNW

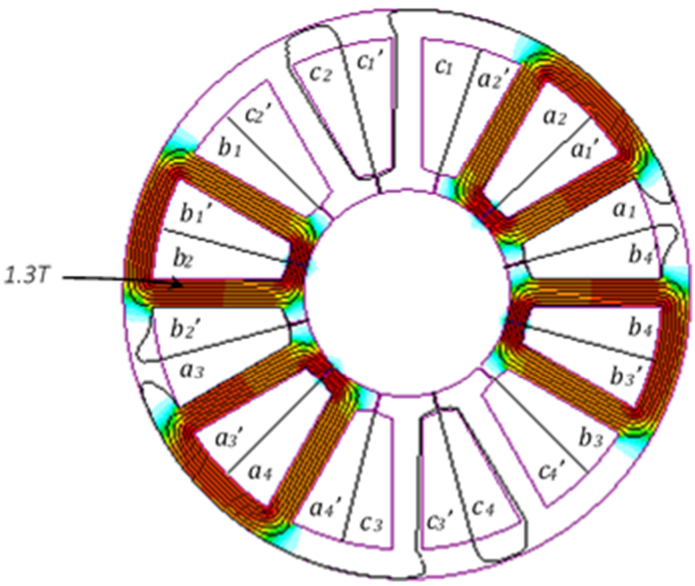

(g) 18 SLOTS DL DW

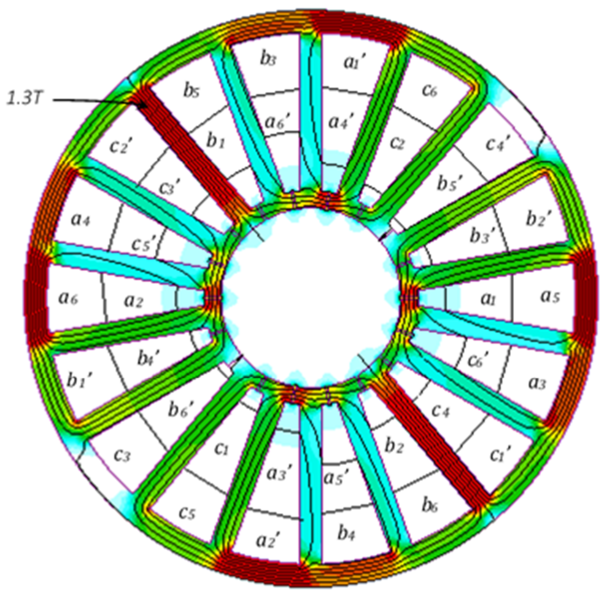

E5. 6 Poles with 18 slots Rotor-less Inductors

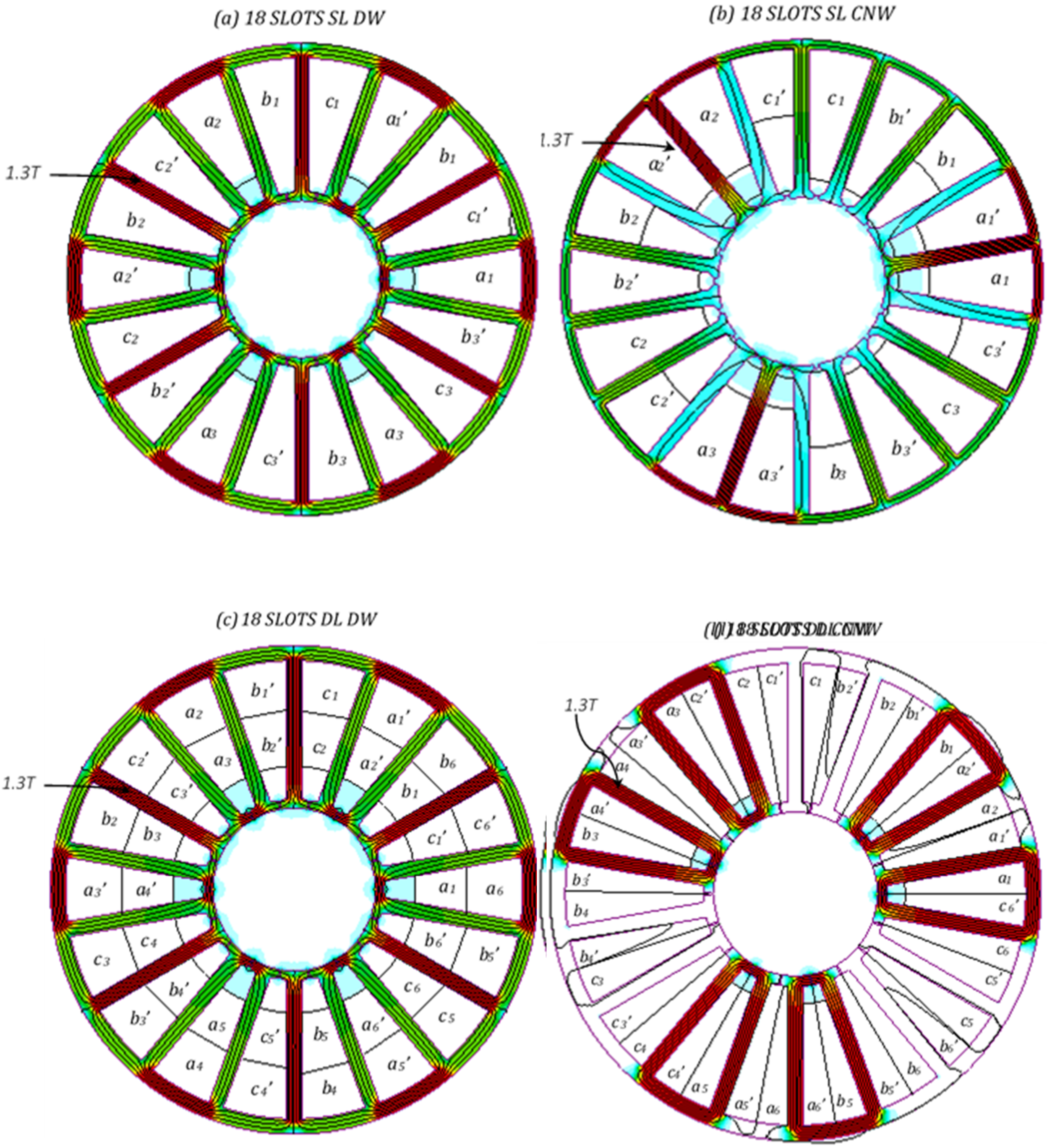

APPENDIX F: ESTIMATION OF SYNCHRONOUS INDUCTANCE

F1. EE Core Inductor

Figure F1: Input Power Measurement at 300 Hz

To estimate the synchronous inductance of EE core inductor RMS current of 1A is imposed by adjusting the voltage of the programmable AC power supply. The impedance of the EE core inductor is given as,

$$Z_{EE1} = \frac{V_{rms}}{I_{rms}} = \frac{2.2788}{1.1518} = 1.97846\ \Omega$$

The measured power factor is 0.0786 therefore, the angle between voltage and current is given as,

$$\theta = \cos^{-1}(0.0786) = 85.49\ degrees$$

The inductive reactance of the EE core inductor at 300 Hz is given as,

$$X_{EE1} = Z_{EE1} \cdot Sin\ (\theta) = \frac{2.2788}{1.1518}.Sin\ (85.49) = 1.97233\ \Omega$$

The synchronous inductance can be calculated as,

$$L_{EE1} = \frac{X_{EE1}}{2\pi f} = \frac{1.97233}{2\pi.300} = 1.04mH$$

Similarly, the synchronous inductance of phase 2 and 3 are,

$$L_{EE2} = 1.11mH$$

$$L_{EE3} = 1.13mH$$

F2. Rotational Inductor

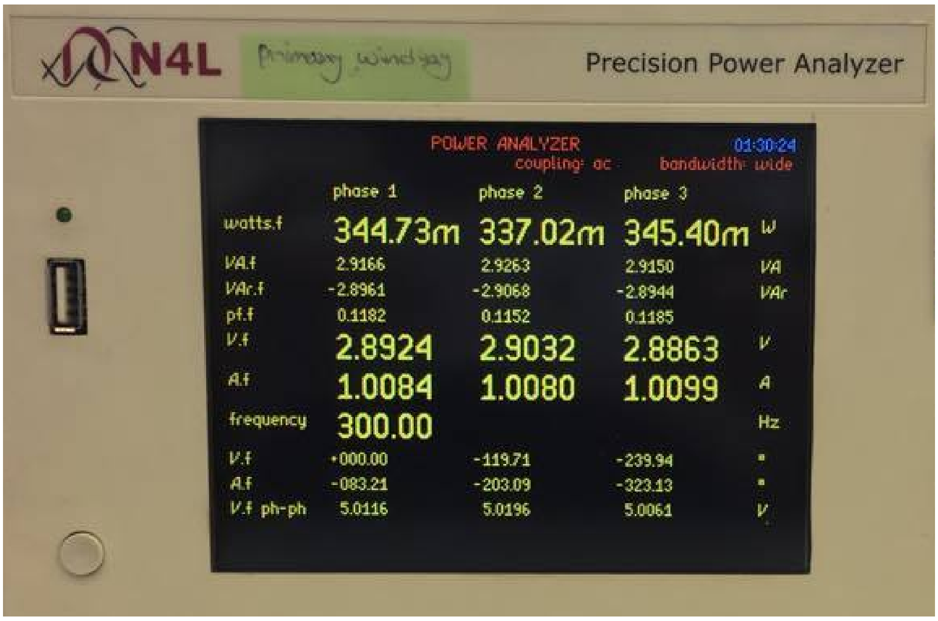

Figure F2: Input Power Measurement at 300 Hz

To estimate the synchronous inductance of EE core inductor RMS current of 1A is imposed by adjusting the voltage of the programmable AC power supply. The impedance of the EE core inductor is given as,

$$Z_{RT1} = \frac{V_{rms}}{I_{rms}} = \frac{2.8924}{1.0084} = 2.8683\ \Omega$$

The measured power factor is 0.1182 therefore, the angle between voltage and current is given as,

$$\theta = \cos^{-1}(0.1182) = 83.21\ degrees$$

The inductive reactance of the EE core inductor at 300 Hz is given as,

$$X_{RT1} = Z_{RT1} \cdot Sin\ (\theta) = \frac{2.8924}{1.0084} . Sin\ (83.21) = 2.8481\ \Omega$$

The synchronous inductance can be calculated as,

$$L_{RT1} = \frac{X_{RT1}}{2\pi f} = \frac{2.8481}{2\pi.300} = 1.52mH$$

Similarly, the synchronous inductance of phase 2 and 3 are,

$$L_{RT2} = 1.52mH$$

$$L_{RT3} = 1.52mH$$

APPENDIX G: Technical Specification and Construction Drawings

G1. Specification of Induction Motor Drive

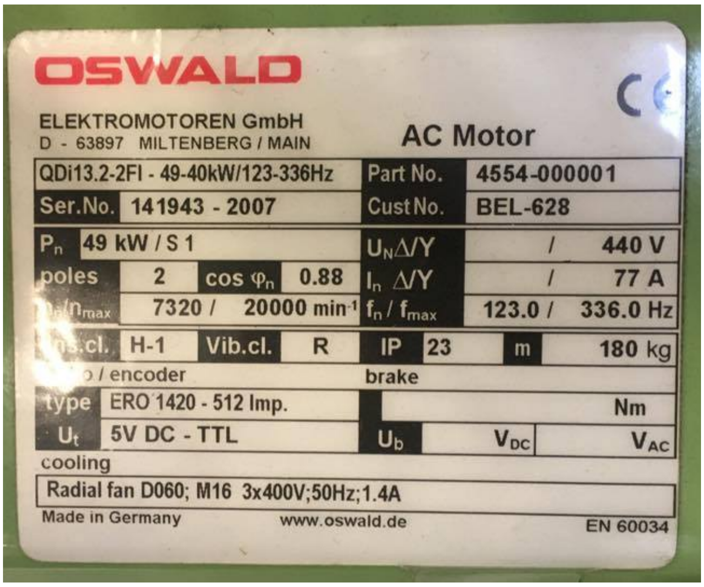

Figure G1: Specification of Induction Motor Drive

G2. Technical Drawings of Test Inductor (Rotational Inductor)

G2.1 Physical Layout

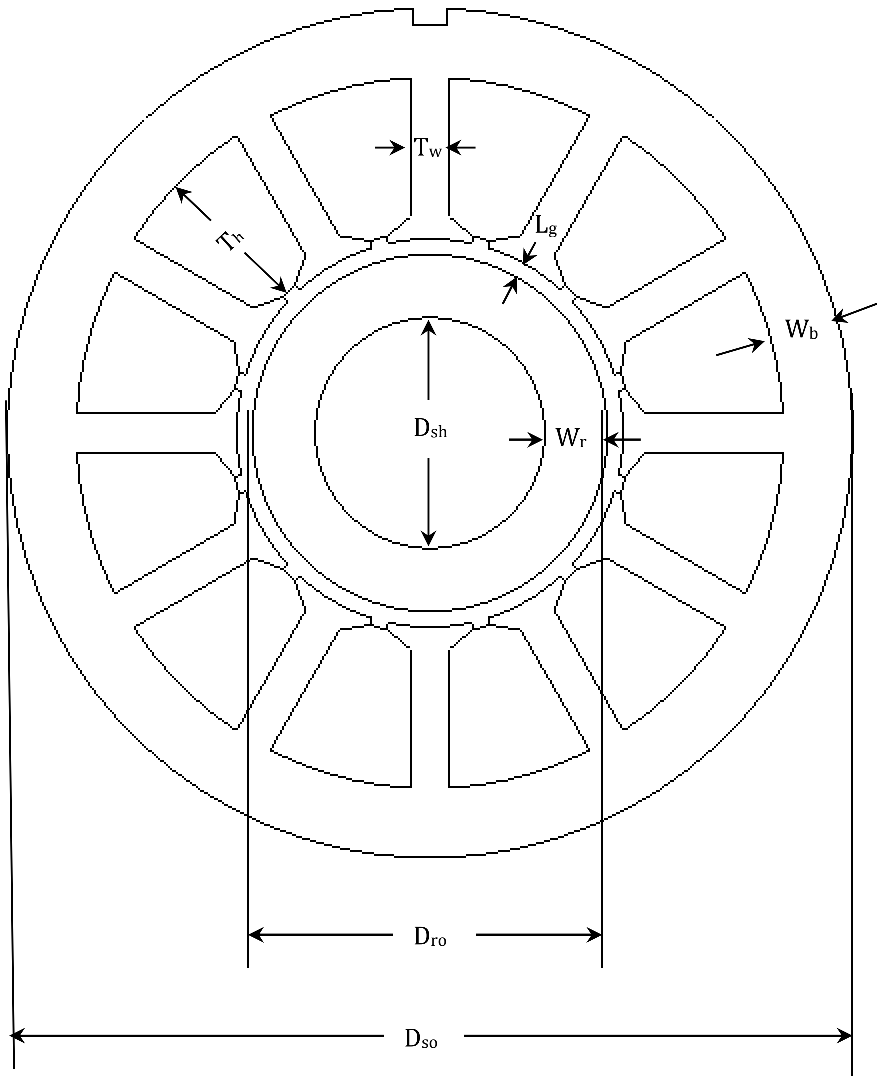

Figure G2: Physical Layout of Rotational Inductor

Table C1: Physical Dimensions of Rotational Inductor

PARAMETER	VALUE	UNIT
T_w	4.50	mm
T_h	16.0	mm
W_h	8.00	mm
W_r	7.30	mm
D_{so}	98.0	mm
D_{ro}	41.2	mm
D_{sh}	26.6	mm
L_g	1.80	mm
L_{st1}	30.0	mm
L_{st1} (with end-windings)	100.0	mm

G2.2 Stator Laminations (60 Laminations of 0.5mm thick stacked together – EDM Cut)

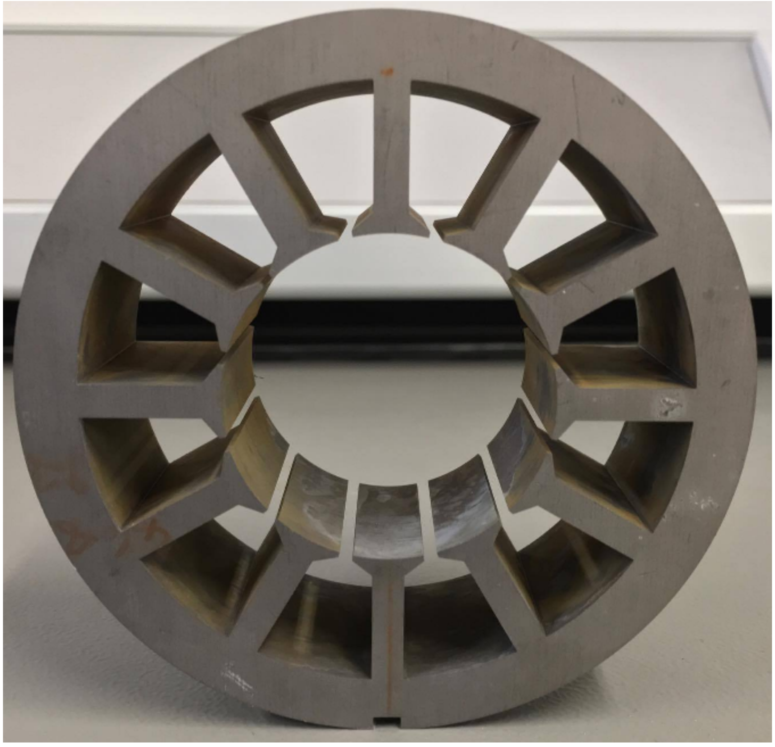

Figure G3: Stator Laminations (Radial Section)

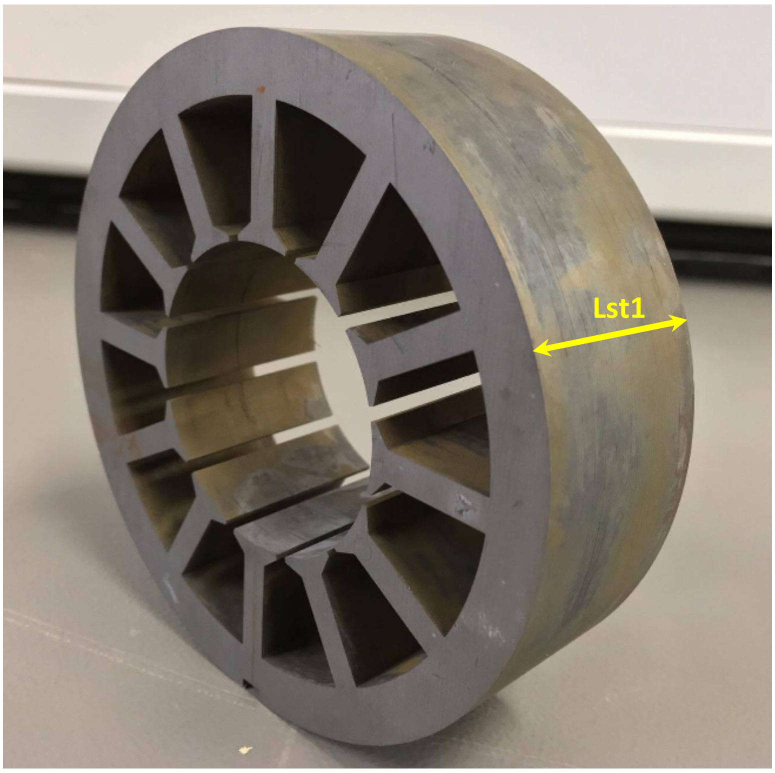

Figure G4: Stator Laminations (Radial & Axial Section)

G2.3 Rotor Laminations (60 Laminations of 0.5mm thick stacked together – EDM Cut)

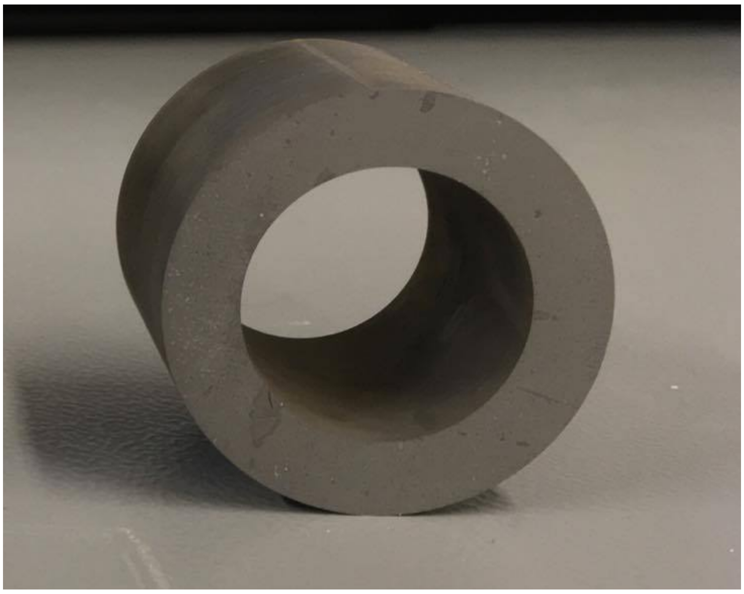

Figure G5: Rotor Laminations (Radial & Axial Section)

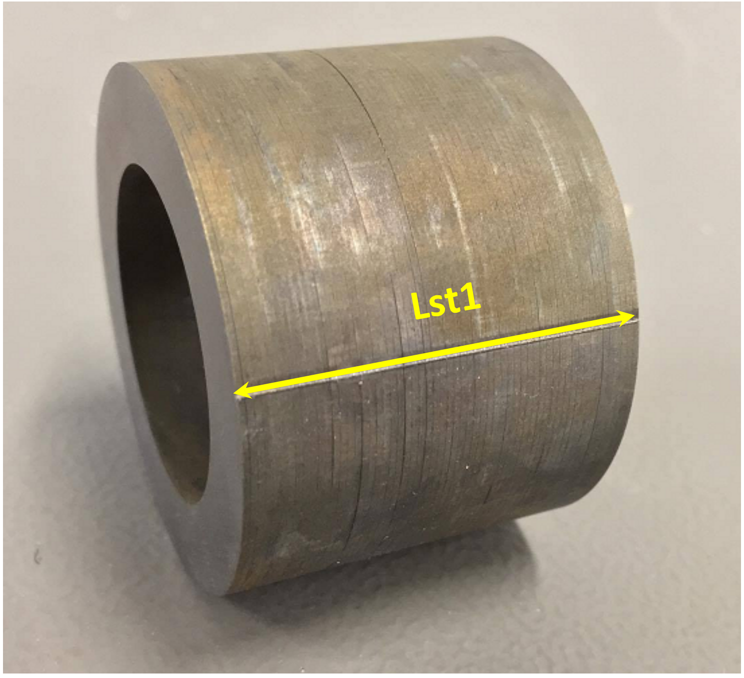

Figure G6: Rotor Laminations (Axial Section)

G3. Technical Drawings of Test Inductor (EE Core Inductor)

G3.1 Physical Layout

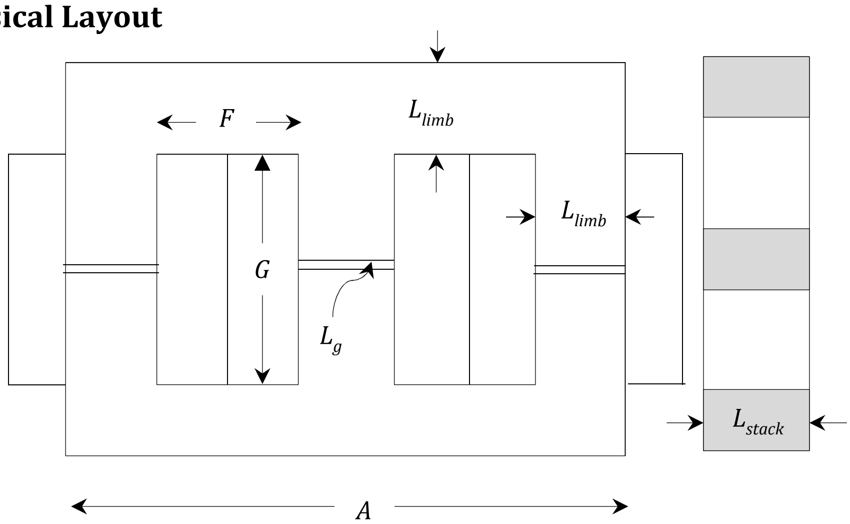

Figure G7: Physical Layout of Rotational Inductor

Table G2: Physical Dimensions of Rotational Inductor

PARAMETER	VALUE	UNIT
A	46.10	mm
F	11.90	mm
G	10.60	mm
L_{limb}	7.430	mm
L_{st2}	115.0	mm
L_{st2} (with end-windings)	134.2	mm
L_h	66.0	mm
L_w	56.0	mm
L_g	0.300	mm

G3.2 EE Core Laminations (230 Laminations of 0.5mm thick stacked together – EDM Cut)

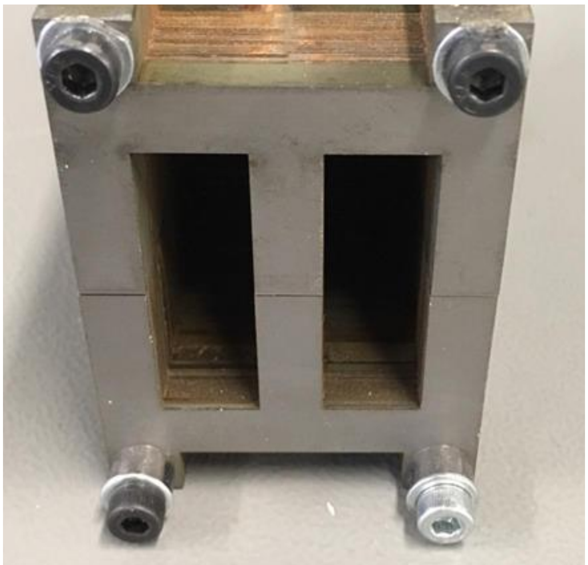

Figure G8: EE Core Laminations (Radial Section)

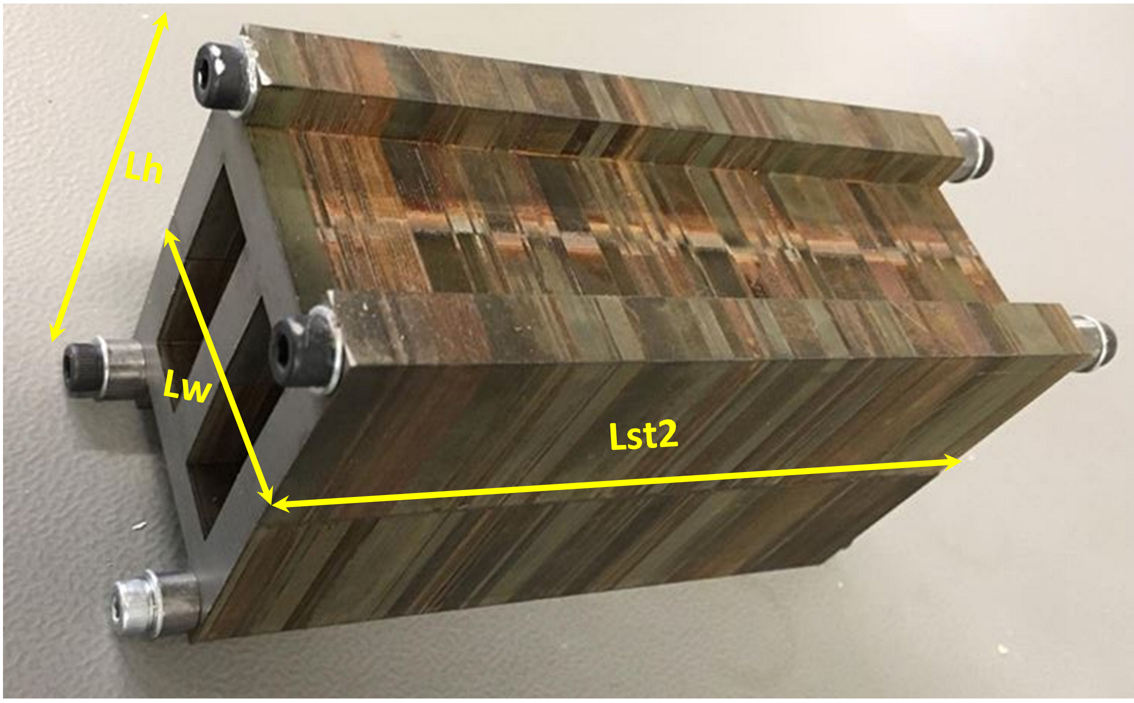

Figure G9: EE Core Laminations (Axial Section)

APPENDIX H: WEIGHT SCALING AND PHASE RESISTANCE MEASUREMENTS

H1. EE Core Inductor

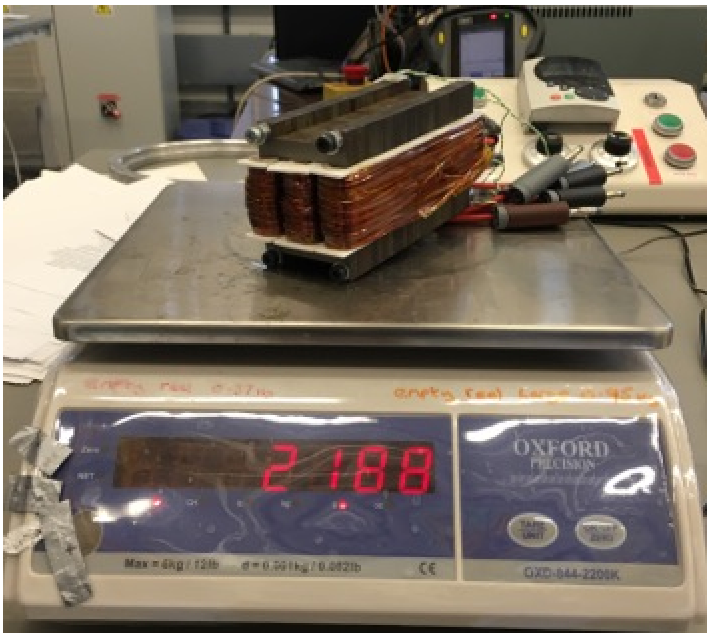

Figure H1: Active Weight of the EE Core Inductor (2188 grams)

H2. Rotational Inductor

Figure H2: Active Weight of the Stator (2023 grams)

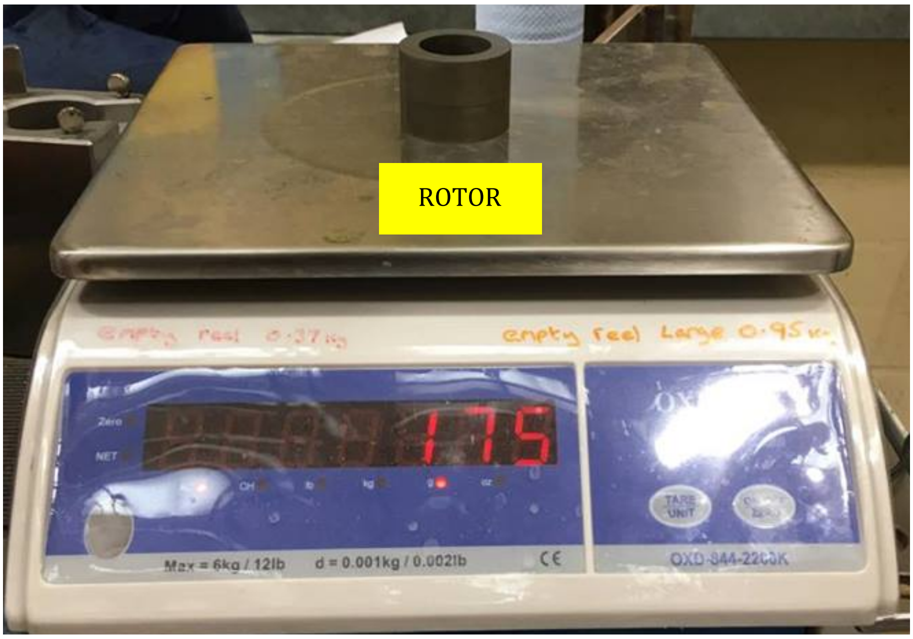

Figure H3: Active Weight of the Stator (175 grams)

H3. Phase Resistance Measurements of EE Core Inductor

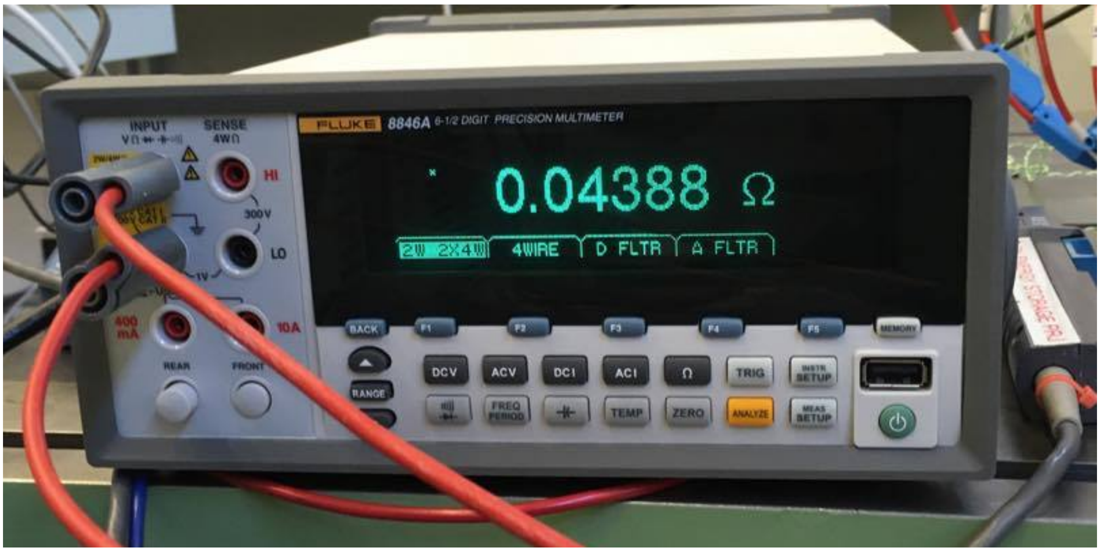

Figure H4: Resistance Measurement of EE Core Inductor

H4. Phase Resistance Measurements of Rotational Inductor

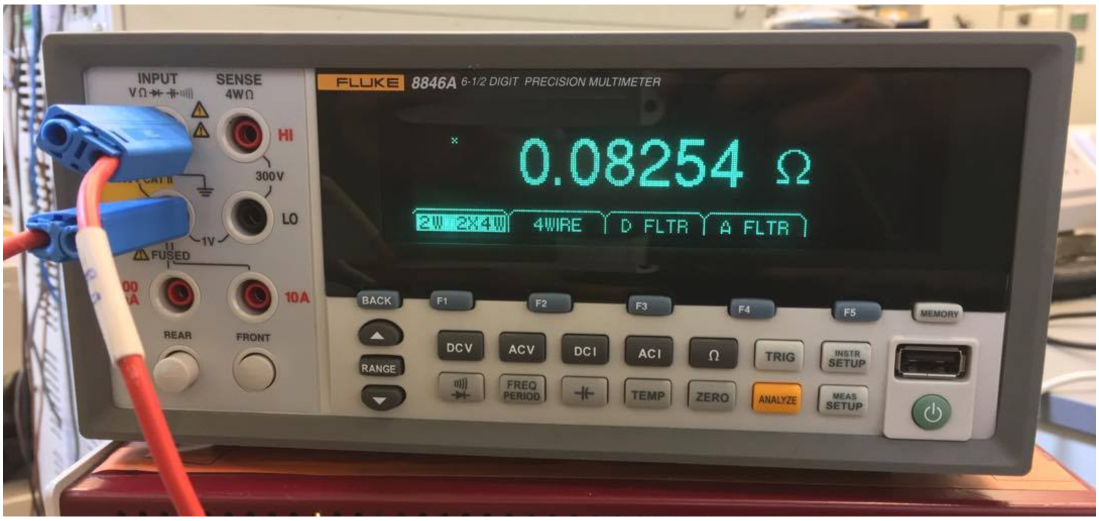

Figure H5: Resistance Measurement of Rotational Inductor